eman ta zabal zazu

Universidad del País Vasco
Euskal Herriko Unibertsitatea

DEVELOPMENT AND APPLICATIONS OF SEMICRYSTALLINE POLYMERS: FROM SHAPE MEMORY TO SELF-HEALING MATERIALS

MEMORIA para optar al Grado de Doctor por la Universidad del País Vasco
(UPV/EHU) presentada por

Nuria García Huete

Leioa, Diciembre 2016

eman ta zabal zazu

Universidad del País Vasco
Euskal Herriko Unibertsitatea

BCMATERIALS
BASQUE CENTER FOR MATERIALS, APPLICATIONS & NANOSTRUCTURES
ehugroup

DEVELOPMENT AND APPLICATIONS OF SEMICRYSTALLINE POLYMERS: FROM SHAPE MEMORY TO SELF-HEALING MATERIALS

MEMORIA para optar al Grado de Doctor por la Universidad del País Vasco (UPV/EHU) presentada por

Nuria García Huete

Leioa, Diciembre 2016

Abstract

Technological advances make the world a more and more automated place, increasing the interest in obtaining materials capable of acting on their own. In this sense, science plays an important role in the research and development of this kind of systems, resulting increasingly common the study and development of smart materials, which are those capable of modify some of their properties when they are subjected to a specific stimulus. An example of smart materials are shape memory polymers, in which this study is focused on, which can change their shape under the application of a certain stimulus.

Thus, in this work different systems have been developed based on a commercial polycyclooctene, a semicrystalline polymer which presents thermally-induced shape memory effect when it is crosslinked. Once the effectiveness of this polymer crosslinked with dicumyl peroxide has been demonstrated, gamma radiation crosslinking has been tested as an alternative, obtaining non-cytotoxic materials. In this way, after characterizing the thermo-mechanical properties, the shape memory behaviour has been analysed, as well as its relationship with the free volume. Additionally, polymeric blends with ionomers have been prepared, trying to obtain materials that retain the shape memory effect but with also self-healing capacity, thus to extend the useful life of the materials.

Therefore, the developed studies and the obtained results open the possibility of application of these polymers to various scientific and technological fields, as can be observed throughout the work, in order to satisfy the demands and comforts of the everyday life.

Resumen

Los avances tecnológicos hacen que el mundo en el que vivimos este cada vez más automatizado, siendo cada vez mayor el interés en obtener materiales capaces de actuar por sí mismos. En este sentido, la ciencia juega un papel importante en la investigación y desarrollo de este tipo de sistemas, resultando cada vez más habitual el estudio y desarrollo de materiales inteligentes, que son aquellos capaces de modificar alguna de sus propiedades al ser sometidos a un estímulo concreto. Un ejemplo son los polímeros con memoria de forma, que pueden cambiar su forma bajo la aplicación de un estímulo concreto, y que son los materiales objeto de este estudio.

Así, en este trabajo se han desarrollado diferentes sistemas basados en un mismo polímero semicristalino, un policicloocteno comercial, que presenta memoria de forma inducida térmicamente cuando se encuentra entrecruzado. Demostrada la efectividad de este polímero cuando es entrecruzado con peróxido de dicumilo, se ha probado como alternativa el entrecruzamiento con radiación gamma, obteniendo así materiales no citotóxicos. De este modo, una vez caracterizadas las propiedades mecánico-térmicas, se ha analizado el comportamiento de memoria de forma, relacionándolo con el volumen libre. Adicionalmente, se han preparado mezclas poliméricas con ionómeros, tratando de obtener materiales que conserven el efecto de memoria de forma y que además posean capacidad de autorreparación, para así alargar la vida útil de los materiales.

Por lo tanto, el conjunto de estudios realizados y los resultados obtenidos abren la posibilidad de aplicación de estos polímeros en diversos campos científico-tecnológicos, visibles a lo largo del trabajo, para así poder satisfacer las exigencias y comodidades del día a día.

Laburpena

Garapen teknologikoek mundua gero eta automatizatuago egotera eraman dute, beren kabuz jardun dezaketen materialek berebiziko garrantzia eskuratu dutelarik. Zentzu honetan, zientziak paper garrantzitsua jokatzen du sistema mota hauen ikerkuntzan, non material inteligenteen ikerketa eta garapena gero eta ohikoagoa bihurtzen ari den. Material hauek, beraien propietateren bat aldatzeko gaitasuna erakusten dute estimulu zehatz bataplikatzean. Forma memoria duten polimeroak horren adibide dira, beraien forma aldatzeko gaitasuna dute estimulu zehatz bat aplikatuz gero. Forma memoriadun polimero hauek ikerketa honen funtsa izan dira hain zuzen ere.

Lan honetan, polimero erdikristalino berean (poliziklookteno komertzial bat) oinarritutako hainbat sistema garatu dira. Polimero hau gurutzatuta dagoenean, termikoki induzitutako forma memoria aurkezten du. Poliziklooktenoa dikumilo peroxidoarekin gurutzatu ostean eta honen eraginkortasuna frogatu denean, gamma erradiazio bidezko gurutzaketa frogatu da alternatiba bezala, material ez-zitotoxikoak sintetizatzea lortu direlarik. Modu honetan, behin propietate mekaniko-termikoak karakterizatu direnean, forma memoria jokabidea aztertu da bolumen askearekin erlazionatuz. Osagarri modura, ionomeroekin nahaste polimerikoak prestatu dira, forma memoria efektua mantentzeaz gain, auto-konponketa ahalmena izango duten materialak lortzeko asmoz eta beraz beraien bizitza erabilgarria luzatzeko helburuarekin.

Ikerketa lan honetan egindako azterketa eta lortutako emaitzek, polimero hauek hainbat esparru zientifiko-teknologikotan aplikatzeko aukera zabala dela argi erakusten dute, eguneroko bizitzako behar eta erosotasun guztiak asetzeko helburuaz.

Samenvatting

Technologische vooruitgang zorgt ervoor dat de wereld steeds meer geautomatiseerd wordt. Dit vergroot de interesse in het verkrijgen van materialen die uit zichzelf kunnen functioneren. De wetenschap speelt een belangrijke rol in de ontwikkeling van dit soort systemen, wat resulteert in een verhoging van het aantal studies die gedaan worden op het gebied van slimme materialen die hun eigenschappen kunnen aanpassen wanneer ze worden blootgesteld aan een specifieke stimulus. Een voorbeeld van slimme materialen zijn 'shape memory'polymeren die hun vorm kunnen aanpassen na het krijgen van een bepaalde stimulus, hetgeen de focus is van deze studie.

Daarom zijn er in deze studie verschillende systemen ontwikkeld op basis van het commercieel verkrijgbare polycycloocteen, een semikristallijn polymeer dat een thermisch gestuurd 'shape memory'effect verkrijgt als het gecrosslinkt wordt. Nadat het effect van dit polymeer, gecrosslinkt met dicumylperoxide, aangetoond was, werd gammaradiatie crosslinking gestest als een alternatieve methode met niet-cytotoxische materialen als resultaat. Op deze manier, na karakterisatie van de thermomechanische eigenschappen, zijn het 'shape memory'gedrag en de relatie met het vrije volume geanalyseerd. Daarnaast zijn polymeermengsels met ionomeren gemaakt om zo materialen te verkrijgen die nog steeds 'shape memory'gedrag vertonen, maar tevens zelfherstellende eigenschappen hebben. Hierdoor wordt de effectieve levensduur van de materialen verlengd.

De ontwikkelde studies en de verkregen resultaten openen de mogelijkheid om deze polymeren toe te passen in verschillende wetenschappelijke en technologische velden. Daardoor draagt dit werk bij aan de ondersteuning van de eisen en gemakken van het alledaagse leven.

Contents

CHAPTER 1

Introduction

1.1. Smart materials

Smart, intelligent or adaptive systems are those capable of modify significantly one or more properties under controlled conditions. In other words, in response to specific stimulus input, they can change their physical properties in a specific manner [1], that is, they produce a predictable and repeatable response, or output.

Since smart materials first started to play an important role due to their capabilities to respond actively to environmental stimuli and allow significant potential applications, research on such materials has been progressively growing [2].

Smart materials include ceramics, polymers and metals, and the nature of the external stimulus and the corresponding property change can vary widely.

A possible way to classify these materials is by separating them by input (applied stimulus) and output (obtained response). Figure 1.1 links the input (left part) with the output (right part) for each material, allowing a user to know which materials are adapted to a predefined input or to a desired output [3].

Smart structures have some characteristics in common [4]:

- Immediacy: they react as soon as the stimuli appear, responding in real time.
- Transiency: they respond to more than one environmental state, and have different properties depending on these various environmental states.
- Self-actuation: the special properties are inherent to the materials, they are not produced by external actions on the materials.
- Selectivity: the response is predictable and replicable, meaning that a single environmental state can only lead to a unique and constant response of the material.
- Directness: the output is produced when the input is given, so the response is local.

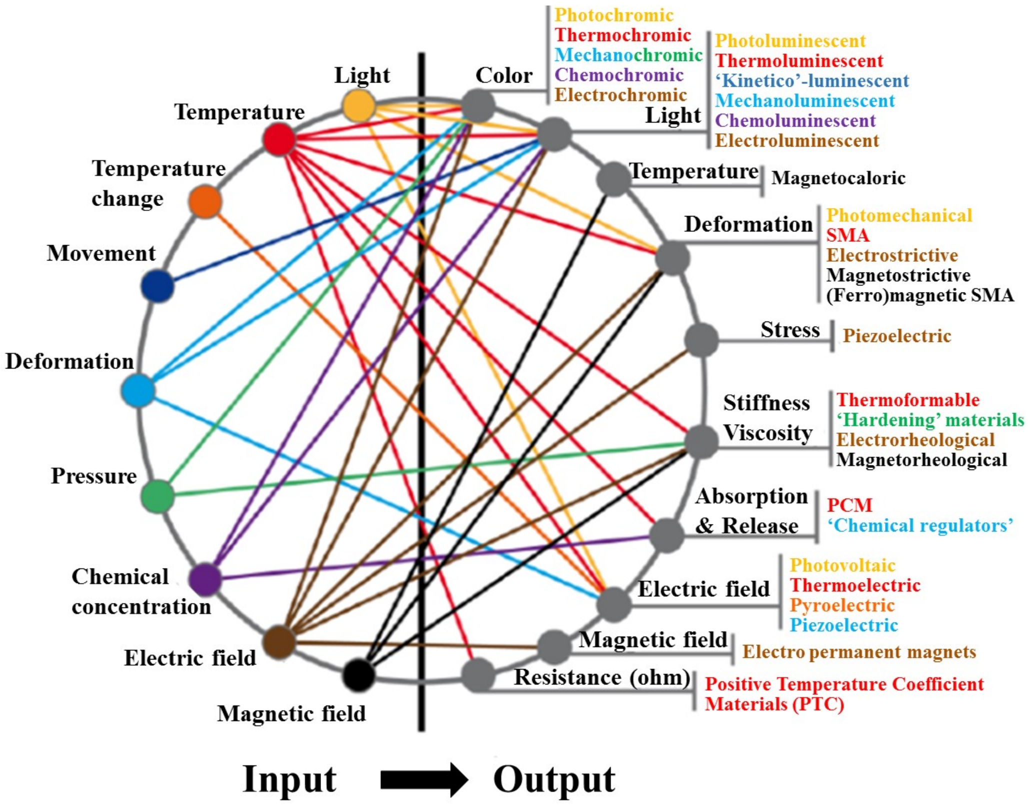

Figure 1.1. One possible classification of smart materials.

Because they response to a particular stimulus, they are usually called 'stimuli-responsive' materials, and there are a lot of types, as can be seen in Figure 1.1. Among others, they can be thermo-responsive materials (heat), mechano-responsive materials (stress/pressure), electro-responsive materials (electrical current/voltage), magneto-responsive materials (magnetic field), chemo-responsive materials (pH-change/solvent/moisture), and photo-responsive materials (light), based on the stimulus necessary to obtain the response. Additionally, the classification can be based on the obtained response having, for example, chromo-active materials, photo-active materials, electro-active, and magneto-active materials.

Thinking on making the sensorial properties of an object variable and interactive, several classes of materials become more interesting than others. It is especially the case for colour changing, light-emitting and shape changing materials, which variations affect directly the perceptions of the user.

Colour changing and light-emitting materials have a direct effect on the visual appearance of an object and present a large variety of possible inputs, making them appropriate to use in a wide variety of applications. For both type of materials, possible inputs are light (photochromic, photoluminescent), change in temperature (thermochromic and thermoluminescent), deformation or pressure (mechanochromic and mechanoluminescent), chemical concentration (chemochromic and chemoluminescent) and electricity (electrochromic, electroluminescent and LEDs). There are also some materials which can change colour when they are under pressure.

Commercially available examples for thermochromic and photochromic behaviours are represented in Figure 1.2. Figure 1.2a shows a mug which changes in colour when a hot liquid is inside it (thermochromic), whereas in Figure 1.2b glasses which changes in colour under exposition to solar radiation (photochromic) are represented.

An emerging class of smart materials are shape memory materials, which have the capability of changing their shape when the convenient external stimulus is applied [5,6]. This ability is known as shape memory effect (SME).

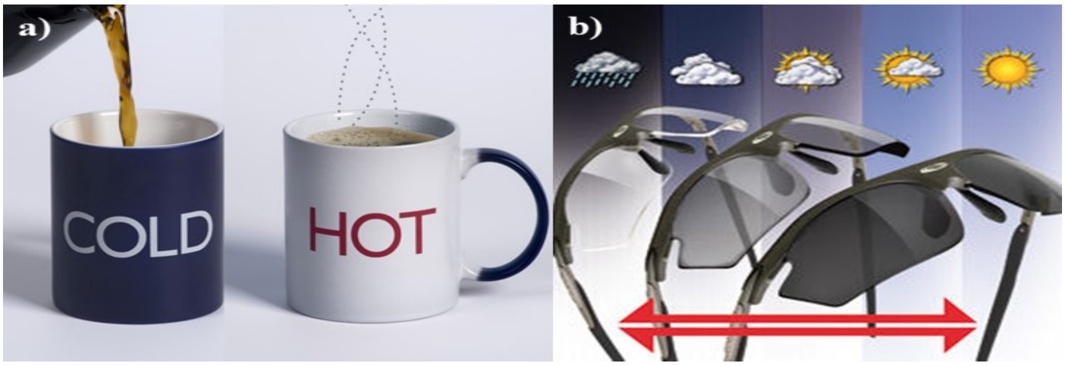

Figure 1.2. Possible applications of chromoactive materials. a) Thermochromic mug; b) photochromic glasses.

1.2. Shape memory materials

Shape memory materials have attracted the attention of scientist and engineers because their ability to remember two shapes at different conditions, giving to the materials a great potential for their application in sensors, actuators, smart devices, and media recorders [7]. As in other fields, one can find shape memory alloys (SMAs), shape memory ceramics (SMCs), and shape memory polymers (SMPs) [8].

(i) Shape memory alloys

Shape memory alloy was first discovered by Arne Ölander in 1932 in AuCd alloys. However, the importance of shape memory materials was not recognised until 1962, when William Buehler and Frederick Wang revealed the shape memory effect in a nickel-titanium alloy [9], also known as nitinol (derived from the material composition and the place of discovery, i.e. a combination of NiTi and Naval Ordnance Laboratory).

The shape memory effect in shape memory alloys is related to the presence of different internal structures at different temperatures. In this manner, the shape memory effect involves a change of phase inside of the material, called martensitic transformation: the material is in a phase or form, called martensitic when cold, and in an austenitic phase when heated at a certain temperature. The martensitic transformation is a shear-dominant diffusionless solid-state phase transformation occurring by nucleation and growth of the martensitic phase from the parent austenitic phase [10].

According to the stimulus, shape memory alloys can be catalogued in thermo-responsive and magneto-responsive SMAs. These last are also called ferromagnetic SMAs (FSMAs).

In this way, the first ones can only be activated by heating, whereas the last ones can also be activated by applying a static magnetic field (magneto-responsive) or an alternating magnetic field (inductive heating) to trigger the shape memory effect [11].

(ii) Shape memory ceramics

As in the case of alloys, there are ceramics which present shape memory properties. The first suggestion of the shape memory effect in ceramics dates on 1977, where Schurch and Ashbee presented a work where a mica glass-ceramic was capable of recover the original shape when it was heated [12]. Later, in 1986, Swain *et al.* reported the shape memory effect in magnesia-partially-stabilized zirconia [13], and in 1988 Reyes-Morel *et al.* suggest the same in a CeO_2-stabilized tetragonal zirconia polycrystal [14]. After that, several authors have investigated the shape memory effect in different ceramic materials [15,16].

These materials can be classified in terms of their shape memory mechanisms as martensitic ceramics, viscoelastic ceramics and ferroelectric and ferromagnetic ceramics.

- In martensitic ceramics, the mechanism is similar to the metallic alloys: the change in the shape comes from a change in the crystalline phase at a temperature higher than the transition temperature. Below T_{trans} the ceramic has a monoclinic crystalline structure, where the material is plastically deformable. When the temperature is higher than T_{trans}, the network becomes tetragonal, allowing the recovery of the original shape. An example of these ceramics are zirconia-based ceramics [13,17].
- Viscoelastic ceramics are composed of two phases, where one is crystalline and the other one is amorphous. The example of these materials is the ceramic described by Schurch and Ashbee [12], where the crystalline phase was mica, dispersed in the vitreous matrix. Above 300°C, thanks to stress

application, the mica was deformed, and the amorphous matrix was capable of fix the temporary shape cooling below that temperature maintaining the stress. Reheating above the transition temperature, the ceramic recovered the original shape.

- The last type of shape memory ceramics are ferroelectric and ferromagnetic ceramics, where it is possible to obtain the phase transitions, and thus the shape memory effect, by changing the temperature, leading to the development of paraelectric–ferroelectric [18] or paramagnetic–ferromagnetic ceramics [19].

(iii) Shape memory polymers

Shape memory polymers (SMPs) are those capable of recovering their original shape after having been deformed into a different one (temporary shape). In a way, they ‘remember’ the shape they were given when processed (permanent shape) on the basis of entropy changes with the ability of coming back to it several times (deformation cycles) from potential different temporary shapes when an external stimulus is applied. This ability, known as shape memory effect (SME), is supported on appropriate molecular structures [20], where several SMPs based on different structures and functionalities exist.

These materials will be deeper analysed throughout this chapter, because it is the topic of this thesis.

1.3. Shape memory polymers

The ‘shape memory’ concept in polymers appears for first time in 1941, where Vernon patented a dental material made of methacrylic acid ester resin, which poses ‘elastic memory’, recovering its original shape upon heating [21]. But it was in the 1960 decade when the ‘shape memory polymer’ term acquires an importance due to the investigations in the field of crosslinked polyethylene, obtaining heat shrinkable tubing and films [22–25]. After this, the number of different shape memory polymers has grown, appearing SMPs such as polynorbornene, poly(trans-isoprene), styrene-butadiene copolymers, and some polyurethane elastomers [7].

In a SMP, the SME is not a specific property of a single polymer. It results from the structure and morphology of the polymer, and is influenced by the programmed testing conditions [6]. The prerequisite to achieve a SME involves two aspects: netpoints (hard segments), which determine the permanent shape of the polymer; and switching components (soft segments), which are reversibly sensitive to certain external stimuli, controlling the shape fixity and recovery. Therefore, the entropic elasticity of the polymer network is the driving force for the strain recovery. Figure 1.3 represents the model proposed by Hu and Chen, valid for all shape memory polymers [26,27].

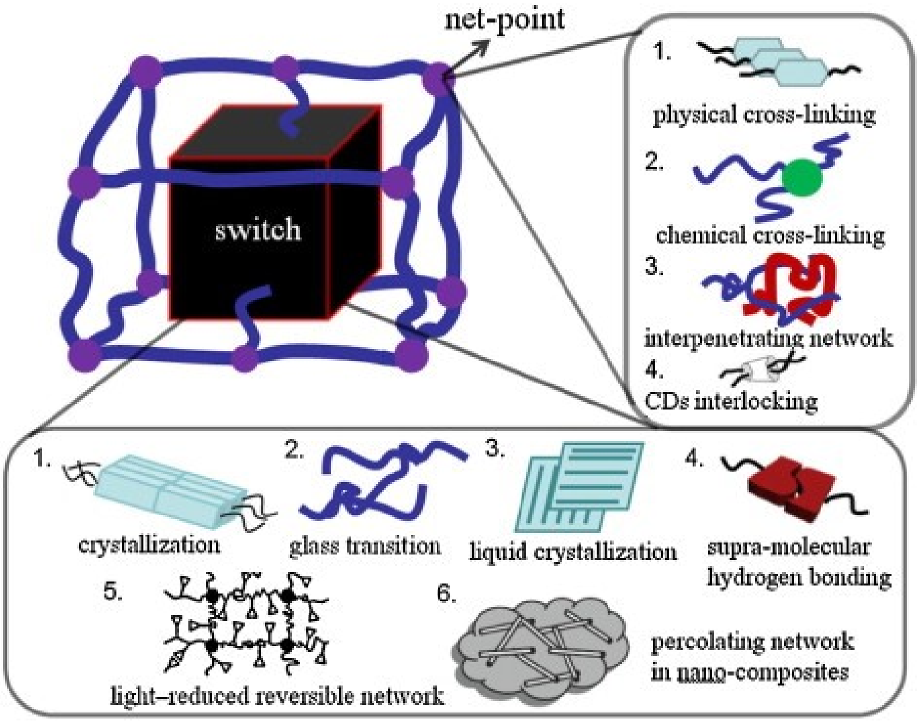

Figure 1.3. The overall architecture of shape memory polymers [27].

In general, in the permanent shape, the internal stress is zero or very low. If the SMP is subjected to deformation, the internal stress can be 'stored' in the polymer structure by following a suitable programming process. By exposing the polymer to a suitable stimulus, the SMP recovers its permanent shape as a result of releasing the internal stress stored in the crosslinking structure (Figure 1.4).

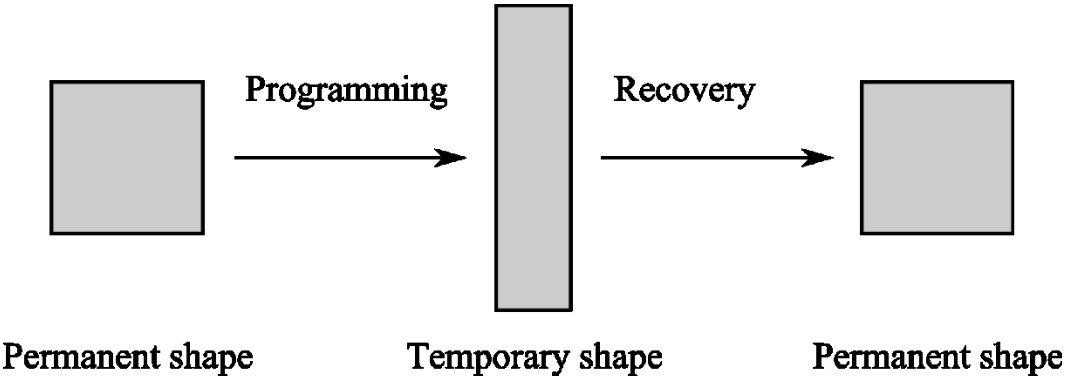

Figure 1.4. Scheme of the shape memory effect in polymers.

Shape memory polymers can be classified attending to the external stimulus, according to the nature of their netpoints, or attending to the functionality.

(i) External stimulus

- Electric field (electro-active SMPs). For example, Paik *et al.* designed an actuator based on shape-memory polyurethane composites, where multiwalled carbon nanotubes were incorporated [28]. Leng *et al.* prepared an electro-active SMP by filling a styrene-based shape-memory resin with carbon nanoparticles and/or short carbon fibers [29].
- Magnetic field (magnetic-sensitive SMPs). For example, Buckley *et al.* designed a prototype device capable to respond to a magnetic field by adding magnetic nanoparticles into a shape memory polyurethane [30]. He *et al.* created a multicomposite capable of recover controlled shapes by actuating remotely using two different radiofrequency fields [31].

- Light. There are shape memory polymers which are able to respond actively when irradiated by light at specified wavelengths, called photo-responsive SMPs. These kind of polymers must present chromophores capable of undergoing photochromic reactions [32–34].
- Chemo-responsive SMPs, pH-, redox- and moisture- and solvent-induced, are one of the barely studied systems in the literature. There are shape memory polymers which are sensitive to chemical changes [35–40].
- Temperature. Thermo-responsive shape memory polymers are the most common shape memory polymers, so different and several examples can be found in literature [41–45].

(ii) Nature of the netpoints. As explained before, it is necessary the presence of crosslinks on the polymer structure in order to have shape memory properties. These unions can be physical (thermoplastic polymers), and these shape memory polymers are, generally, linear block copolymers [46–48]. The bonds can be chemical (thermoset polymers), obtaining polymer networks [49–51].

(iii) Functionality

- Attending to the functionality, they can be one-way [43,44,52], two-way [53,54], triple-shape [41,55,56] or multi-shape memory polymers [57,58].

1.4. Thermally Sensitive Shape Memory Polymers

Most of the SMPs reported to date are activated by temperature changes, being labelled as thermally induced shape memory polymers. Polymers are, generally, intrinsically viscoelastic materials with at least one thermally reversible phase transition (glass transition temperature, T_g, or melting temperature, T_m). In this thermally sensitive SMP, the domains related to the highest transition temperature act as netpoints and the chain segments associated with the second highest transition temperature, T_{trans}, act as switches. Chemical or physical crosslinks are required to exhibit SME. An amorphous phase with a T_g, a semicrystalline phase with a T_m, and even a liquid crystalline (LC) phase with an isotropic temperature T_i can be used as switches to construct SMP. Based on the different phases of the switch, the SMP can be classified into three groups: T_g-type, T_m-type and LC-type SMP.

In the T_g-type SMP, a large rubber modulus can usually be maintained above the T_g, so this type of SMP requires a larger recovery force and have higher strength at low and high temperatures. Inside this classification, one can find both thermoplastic and thermoset SMP where the SME is based on a glass transition temperature. The working principle of T_g-based SMPs is schematically shown in Figure 1.5. As net points, remaining unaffected during deformation, molecular entanglements and entanglements along with crystalline domains act in linear (i.e. thermoplastic) amorphous and semicrystalline systems, respectively. The netpoints are structural units of the above physical networks. For example, polylactic acid is a T_g-based polymer, which can form both physical [46] or chemical [51] networks. When it is uncrosslinked, the crystallites and entanglements act as netpoints, whereas it can be crosslinked by using ionizing radiation. Different T_g-type polymers have been investigated due to their amorphous switching segments, such as epoxy [59,60], polyether ether ketone [52,61], acrylate-type polymers [62,63], polynorbornene and its derivatives [58,64], poly(lactic-co-glycolic) acid (PLGA) [65] and poly(glycerol-co-dodecanoate) [66].

In T_m-type, the crystallisation allows the fixation of the temporary shape, whereas the melting of this phase provides the greatest mobility to the entire polymer chain, being capable of recover the original shape. The advantage of this kind of polymers is that the temperature range where the transition occurs is smaller and easier to predict and control than the glass transition one [67]. Similar to T_g-based SMPs, chemical (covalent or thermoreversible) or physical crosslinking (through phase segregated domains), and their combinations, may be the ‘net points’ which guarantee the permanent shape. For example, polycaprolactone (PCL) is a suitable polymer to obtain both physical [48] and chemical [49,50] networks based on a melting temperature to activate the SME.

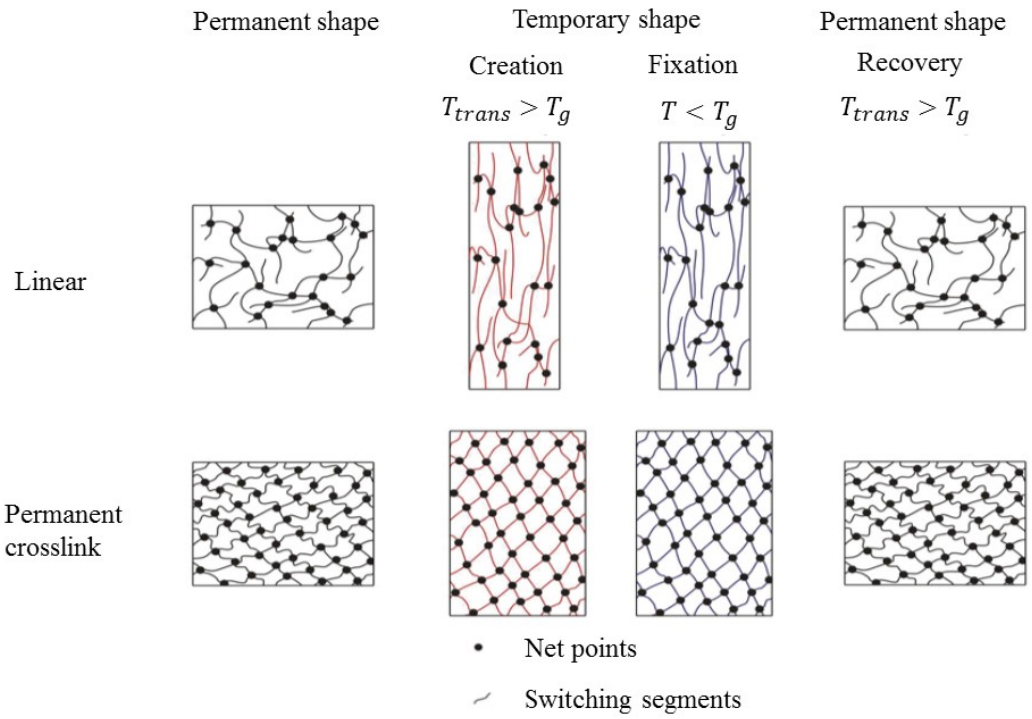

Figure 1.5. Shape memory effect in T_g-based SMPs [67].

The molecular mechanism, underlying the shape memory function in this type of SMPs, is schematically represented in Figure 1.6, where T_m and T_c represents the melting and the crystallisation temperatures, respectively.

Current polymeric segments used as semicrystalline-phase switches for SMP are polyolefins like poly(1,4-butadiene) [47], polyethers like polyethylene oxide (PEO) [68,69], and polyesters like poly(ε-caprolactone) (PCL) [70,71]. Polyolefin-based SMP have few hydrogen-bonds between the switches and netpoints due to the inherently non-polar nature of polyolefin, so they often form a more complete micro-phase separation structure compared with polyether- or polyester based SMP [72]. Additionally and as mentioned, chemical networks can be created in order to have more stable structures. This point will be deeper explained at section 1.5.

Liquid crystalline elastomers (LCE) show a first-order phase transition with an endothermic peak on heating curves, which shows the transition of the material from an anisotropic to an isotropic phase. LC-type SMP are accompanied by a significantly reversible change in orientation of the polymer chain, allowing the formation of reversible shape changes or two-way SME. Similar to the T_g- and T_m-type SMPs, chemical or physical crosslinks are also required in T_i-type SMPs made of LCEs to exhibit SMEs.

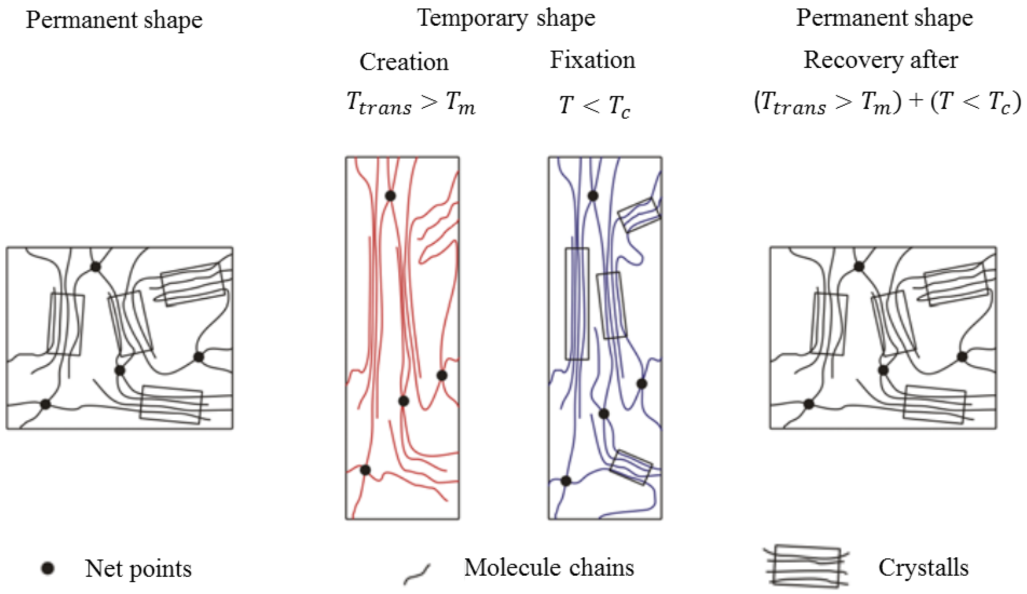

Figure 1.6. Shape memory effect in T_m-based SMPs [67].

1.5. Shape memory effect: types

As explained before, shape memory polymers are a class of smart materials that offer mechanical action triggered by an external stimulus. More specifically, SMPs are able to ‘memorise’ one or more shapes, each determined by network elasticity, but can be stored in temporary shapes by material immobilization, commonly by vitrification or crystallization.

Particularly, in covalent crosslinked semicrystalline shape memory polymers, the melting transition of the crystallites acts as the switching temperature of shape recovery. The crystallization process allows to fix the secondary shape, whereas the permanent shape is maintained by chemical crosslinks between polymer chains [7,8,73]. Figure 1.7 shows a scheme of the internal transformations during a shape memory cycle in a crosslinked semicrystalline polymer. At room temperature, the polymer in its primary shape (a) is heated, so the crystals melt (b), resulting in a compliant transparent material. Then, it is easy to stretch the sample to a deformed state (c) that is fixed to a secondary shape (d) by cooling and crystallization. Heating the secondary shape, a rapid sequence of melting, (d)-(c), and then elastic recovery, (c)-(b), occurs to yield the net effect of shape memory. Note that in Figure 1.7 depictions in bold frames (a, d) represent temperatures below the melting point, while the others (b, c) are above it. Crosslinking junctions are depicted as solid black circles.

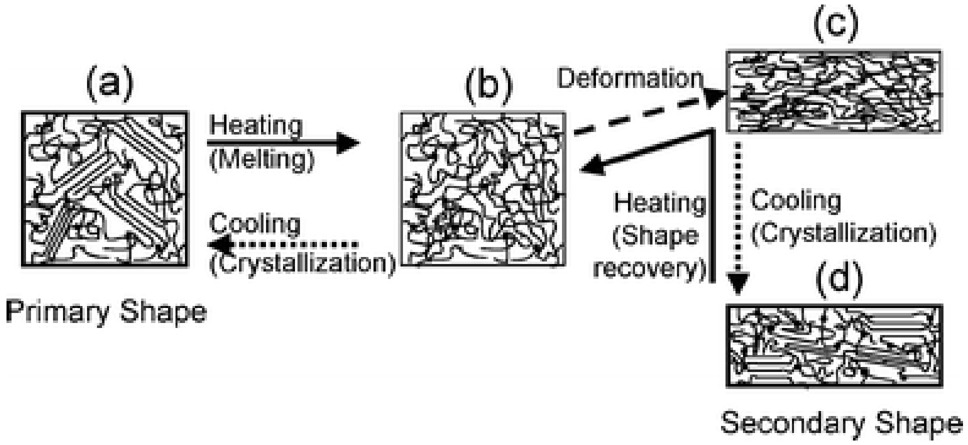

Figure 1.7. Schematic representation of the microstructural transformations of a chemically crosslinked shape memory polymer [7].

These kind of crosslinked structures can be obtained by following two strategies. The first of them is by copolymerization of monofunctional monomers with low molecular weight or oligomeric crosslinkers [74], whereas the second one consists in crosslink the linear polymers by using organic peroxides [75,76] or employing ionizing radiation [77,78].

Under different programming methods, various types of shape memory effects can be observed, as one-way, two-way, triple or multiple shape memory effect (Figure 1.8). According to the reversibility of the effect, we can find one-way shape memory polymers (irreversible effect), or two-way shape memory polymers (reversible effect).

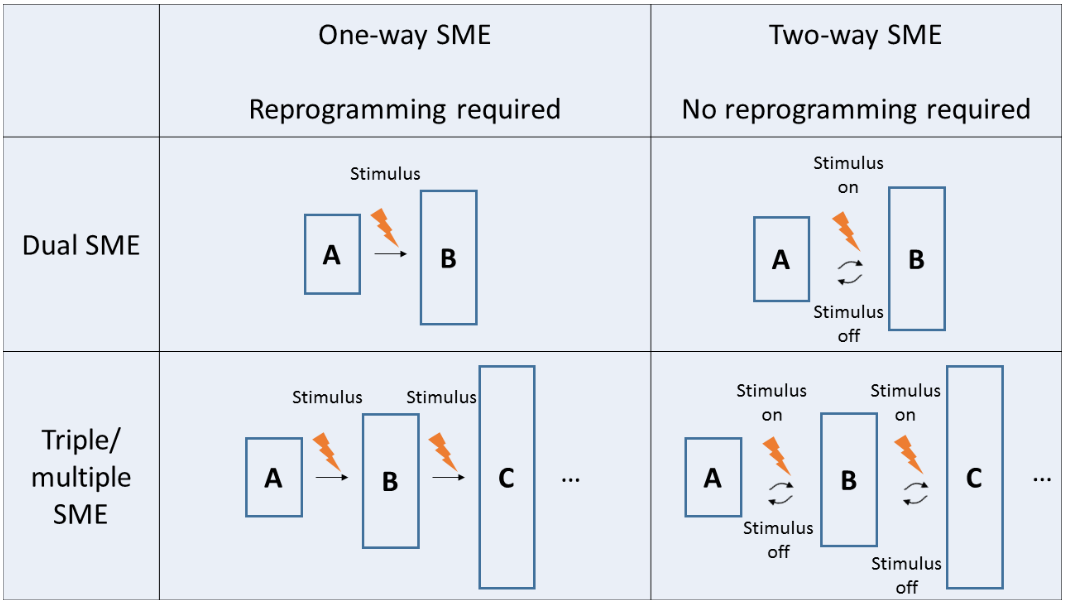

Figure 1.8. Shape memory functionality of shape memory polymers.

1.5.1. One-way shape memory effect

One-way shape memory polymer can retain a temporary shape when the stimulus is finished. The programming step consists on deform the sample by heating above T_m, and cooling the deformed specimen below the crystallisation temperature. Heating again above T_m, the sample can recover its initial shape.

1.5.1.1. Dual shape memory effect

This is the typical shape memory effect, represented in Figure 1.9. The thermally-induced dual shape memory effect consists of heating up the sample at a temperature higher than melting temperature ($T_m = T_{trans}$), so it is easy to deform the polymer. Subsequently, the temperature is decreased below the crystallization temperature. This immobilization of the SMP allows the fixation of the temporary shape, storing the mechanical energy at the same time. At this point, the material shows the temporary shape while the permanent shape is stored. Consequently, raising the temperature above T_{trans}, the shape memory effect takes place by the restoration of network conformational entropy, inducing the recovery of the stored permanent shape [79]. In other words, above the T_{trans}, the network mobility is regained, so the material will come back to its permanent conformation, and release the stored strain energy.

As this is the most common shape memory behaviour, we can find multiple and different examples in the literature, both in amorphous and in semicrystalline polymers.

1.5.1.2. Triple/multiple shape memory effect

Triple-shape memory polymers show two temporary shapes (A and B in Figure 1.8) besides the permanent one (C in Figure 1.8). In this way, the temporary shape B must be programmed, followed by the programming of the temporary shape A. Therefore, the polymer can switch from the temporary shape A to the temporary shape B and from there to the permanent shape C when they are stimulated by subsequent temperature increases. In these kind of polymers, shape C is determined by covalent netpoints, whereas shapes A and B are fixed temporarily by a respective switching domain which is assigned to a corresponding T_{trans} [80]. Based on this premise, in principle, we can obtain a multiple (n) shape memory polymer if we have multiple different transition temperatures, featuring one permanent shape and (n-1) temporary shapes.

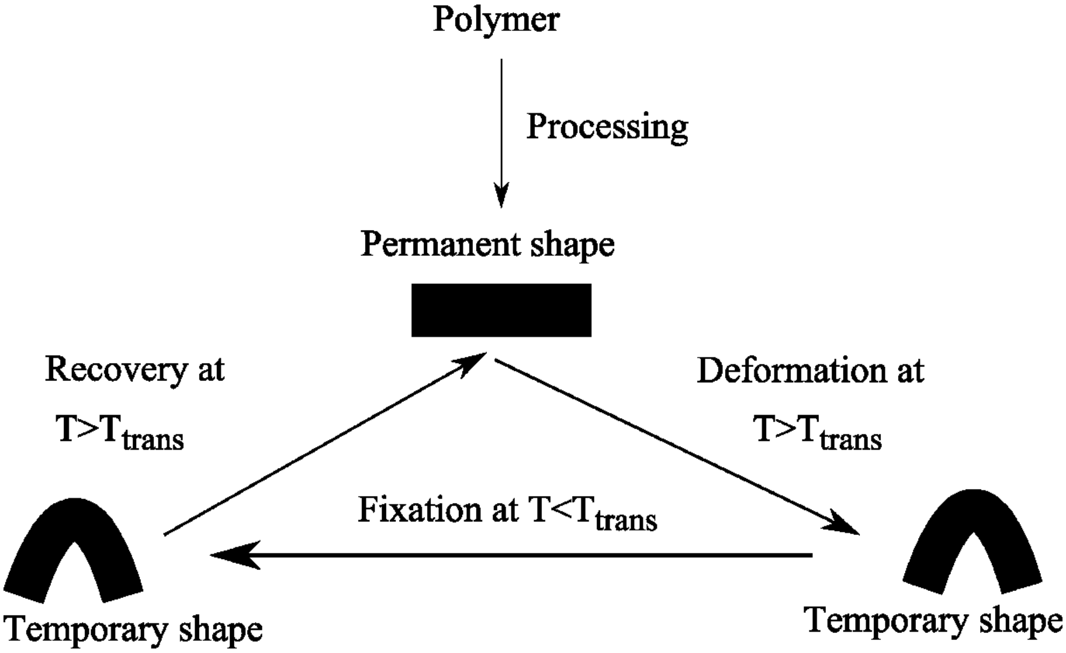

Figure 1.9. Thermally-induced dual shape memory effect.

Although triple-shape capability could be made by one-step programming [81,82], it is more typical to achieve triple-shape functionality by two-step programming [80], allowing the creation of the two independent A and B temporary shapes. For this, it is necessary to heat the polymer above the higher order temperature T_{high}, where the material is in the elastic state, and then deform it. Cooling down the system below T_{high} but above the T_{trans} of the second switching domain (the lower order transition temperature, T_{low}), physical crosslinks are established, forming the temporary shape B. To obtain the second temporary shape A, the shape B is deformed at that T between T_{high} and T_{low} (T_{high}>T>T_{low}), and fixed at T<T_{low}, forming a second set of physical netpoints, which stabilise the obtained shape A when the external stress is released. The recovery can be done by reheating to T>T_{high}, where shapes B and C are recovered sequentially, or by heating first to T_{high}>T>T_{low}, obtaining shape B, and then increasing the temperature until T>T_{high}, recovering the permanent shape C (Figure 1.10).

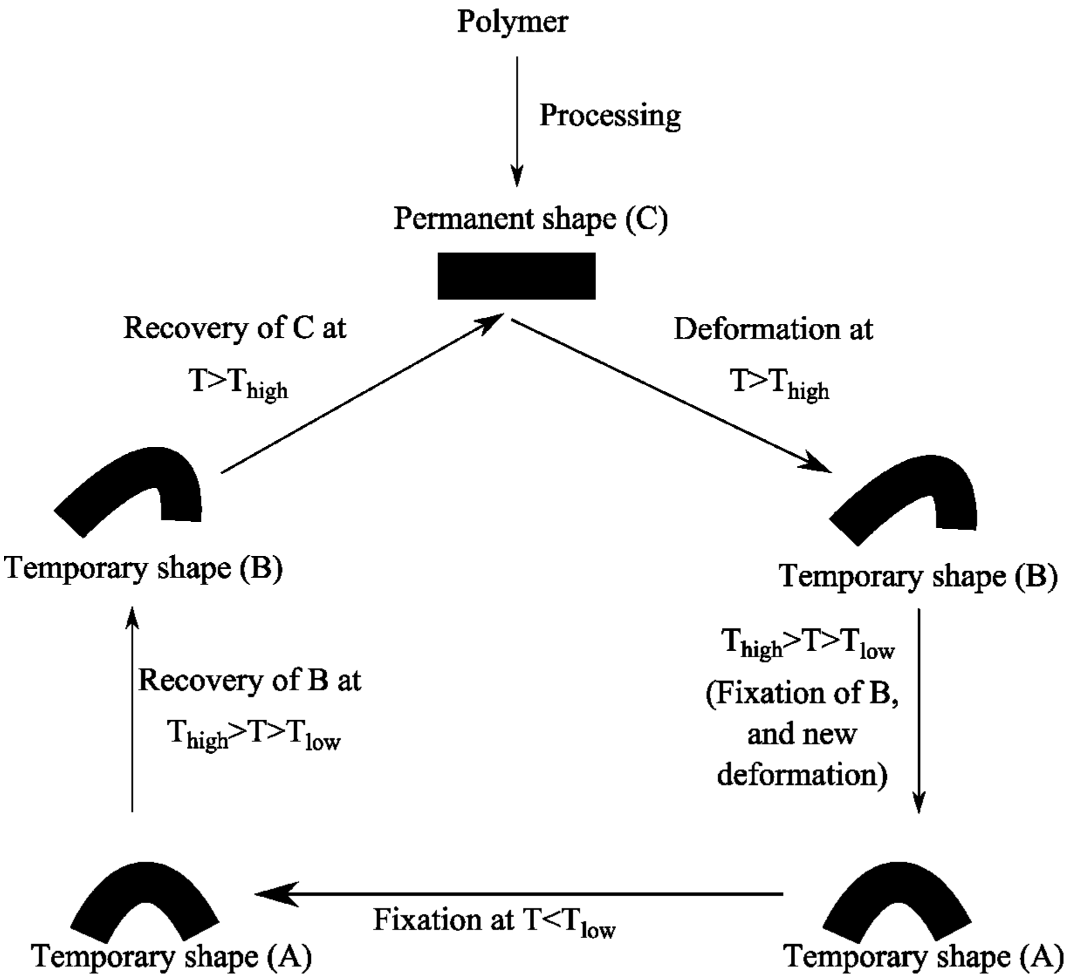

Figure 1.10. Thermally-induced triple shape memory effect.

The two principal approaches to design a triple SMP are the following:

(i) A very broad transition temperature (particularly a glass transition temperature). Examples of this type of triple SMP are persulphonic acid ionomer [57] or interpenetrating networks (IPNs) of poly(methyl methacrylate) and poly(ethylene oxide) [83].

(ii) Multiphase design, that is, different phases with different transition temperatures, such that each one is responsible for one part of the SME. A common polymer which shows triple-shape memory effect when mixed with other segment is polycaprolactone (PCL), as the investigations of Lendlein *et al.* [80], which shown two different triple-shape memory polymers consisting in PCL segments and poly(cyclohexyl methacrylate) (PCHMA) or polyethylene oxide segments, forming a polymeric network. While the first system works using as transition temperatures the T_g of the PCHMA and the T_m of the PCL, in the second one the triple-shape memory effect takes place using as switching temperatures the T_m of both segments. Another possibility is to have two interpenetrating networks with separate transition temperatures [55], or to make a sample with different phases, like a composite based in a dual SMP and shape memory fibres [84]. Additionally, it is possible to obtain blends using polyolefins with two separate transition temperatures [56,85].

1.5.2. Two-way shape memory effect

One-way SMP can satisfy the requirements of a wide variety of applications when they need a unique cycle to be carried out. If we want an additional shape memory cycle, an extra programming step is required. To solve this problem, it is interesting to develop materials with reversible shape memory properties, that is, two-way shape memory polymers, where the polymer recovers its original shape from the temporary one when the stimulus is removed (or reversed) [53]. This reversible behaviour takes place during heating and cooling, in the presence [86] or absence [54] of external stress. The two-way shape memory effect can fulfill the requirements of applications such as sensors or actuators.

As mentioned in section 1.4, liquid crystalline elastomers are widely used as two-way shape memory polymers, as it has been reported by different authors [87–90], but there are other polymers and systems capable of present this kind of shape memory effect, like poly(ethylene-vinyl acetate) –EVA- [54,86], or polycyclooctene [91].

In the same way as in the one-way effect, for two-way shape memory effect we can find dual shape, triple shape or multi shape memory polymers. For example, based in a previous study performed by Chung *et al*. using a commercial polycylooctene [91], a shape memory copolymer with two-way shape memory effect was designed [92]. These authors show how the polymer can adopt one shape or another depending if the sample is heated or cooled. Zotzmann *et al*. developed a multiphase polymer networks containing two different crystallisable segments [93,94]. This polymer, based on polypentadecalactone and polycaprolactone, shows reversible triple-shape memory behaviour under constant stress.

1.6. Shape memory characterization techniques

In this section, the typical procedures to characterise the shape memory behaviour are exposed.

1.6.1. Cyclic, thermomechanical characterization

The shape memory effect can be quantified by cyclic, thermomechanical investigations. A single cycle includes programming the test piece and recovering its permanent shape. The typical test protocol is as follows: first, the sample is heated up to a temperature $T_{high} > T_{trans}$ and then it is stretched to the maximum strain ε_m. The specimen is cooled down below T_{trans} under constant strain to a temperature T_{low} in order to fix the temporary shape. After heating the sample up to $T_{high} > T_{trans}$, it contracts and the permanent shape is recovered. The cycle then begins again.

This experiment can be performed varying different parameters, such the temperature in the programming process (it is possible to make the test at $T < T_{trans}$ -cold drawing- or at $T > T_{trans}$) or the control mode (stress or strain controlled).

The representation of a strain controlled thermomechanical cycle in a shape memory polymer can be observed in Figure 1.11 [95].

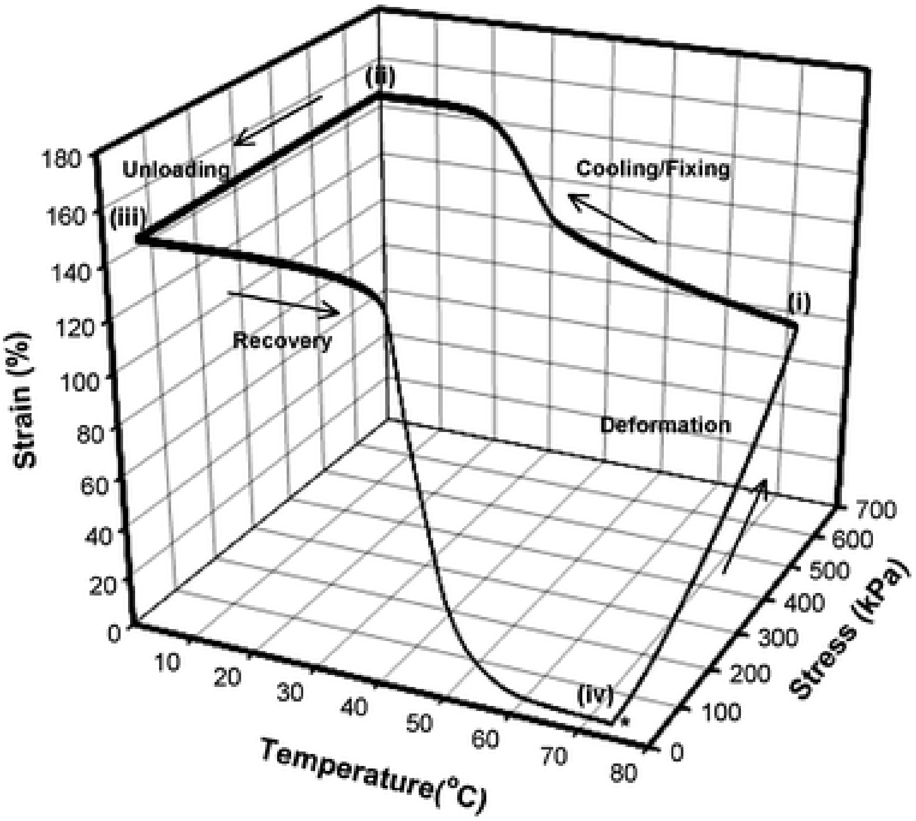

Figure 1.11. Thermomechanical cycle of a SMP [95].

1.6.2. Bending tests

There are two types of tests to characterize the SME where a sample bending is involved: bending test and three-point flexural test.

Bending test consists in bending the sample at a given angle θ_i at a temperature above the switching transition temperature. This deformed sample is then cooled down to a temperature $T_{low} < T_{trans}$ and the deforming stress is released. Finally, the sample is heated up to the measuring temperature $T_{high} > T_{trans}$, recording the recovery of the permanent shape. The deformation angle θ_f varies as a function of time, and it is possible to calculate the shape recovery rate R from the ratio of the different angles before and after recovery and the deformation angle in the temporary shape by the following equation [96]:

$$R\ (\%) = \frac{\theta_i - \theta_f}{\theta_i} \times 100 \tag{1.1}$$

Three point flexural test is based on the previous one and provides values for the modulus of elasticity in bending, flexural stress, flexural strain, and the flexural stress-strain response of the tested material, i.e. the determination of strain recovery and stress recovery ratio. The setup and the scheme of SME is shown in Figure 1.12 [97].

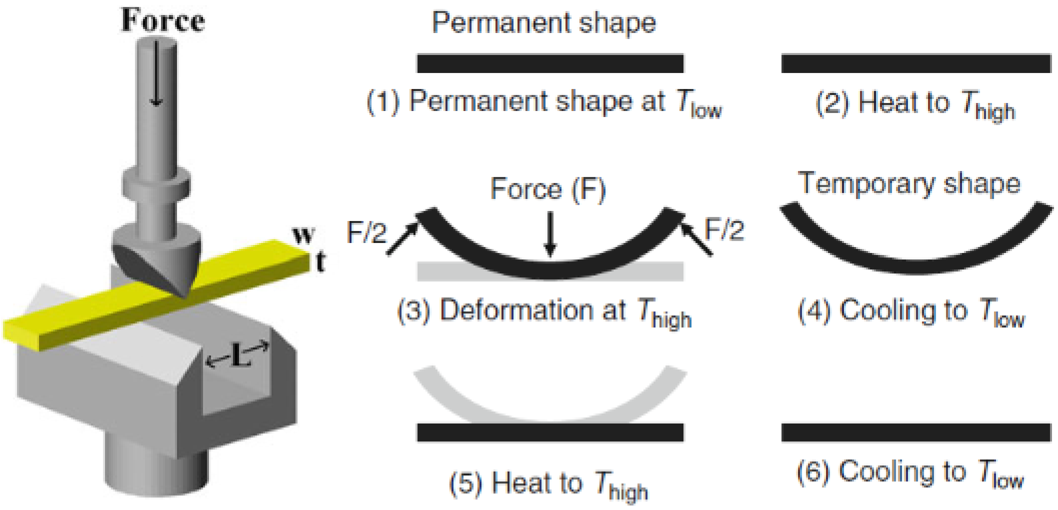

Figure 1.12. Three point flexural test [97].

The sample, of known dimensions width (w) x thickness (t), is placed on two supporting pins separated a fixed length (L), and a third loading pin is lowered with a known force (F) from above at a constant rate until sample failure. The flexural stress (σ_f) can be calculated by equation 1.2.

$$\sigma_f = \frac{3FL}{2wt^2} \tag{1.2}$$

1.7. Applications

The impressing property of shape memory polymers makes them interesting candidates for several applications. It is common to use them in their bulk form, but also seems interesting to make patterns on the surface in order to employ them for surface tuning, as wrinkling [98] or wetting [99], for example.

It is easy to obtain shape memory fibres [100], so it is possible to obtain smart textiles by knitting fabrics [26]. Additionally, it is possible to transfer the shape memory properties from polymers to fabrics on a process called shape memory finishing, using a shape memory polymer solution as finishing agent, so for example wrinkle-free clothes can be fabricated (Figure 1.13) [101]. There are commercially available clothes made with shape memory membranes like Diaplex® and Dermizax®, which can control the moisture permeability based on the temperature [102]. While Diaplex® shows high permeability in its rubber state and low permeability below the glass transition temperature, Dermizax® consists in an ultrathin monolithic membrane where the openings between the polymer molecules expand, increasing the fabric moisture permeability, when the microclimate rises, whereas a dropping in the temperature causes the closing of the pores, trapping the heat.

Due to their versatility, an emerging field of application is the automobile and aerospace world, where they can be used to make from deployable devices to morphing structures. In this way, Composite Technology Development (CTD), Inc. has experience in the fabrication of different deployable devices based in an epoxy SMP reinforced with carbon fibre, where hinges have attracted especial attention

[103]. Another shape memory polymer devices are trusses, booms, antennas or optical reflectors [104,105]. On the other hand, changes in the structures could be of interest to improve the performance and efficiency. Thinking in how birds change their flight posture according to the air flow, researchers are trying to introduce the shape memory concept in this field, creating folding wings and variable camber wings (Figure 1.14) [104].

Figure 1.13. Wrinkle-free effect of fabric treated with water-borne SMPU in comparison with that of the fabric not treated with SMPU [101].

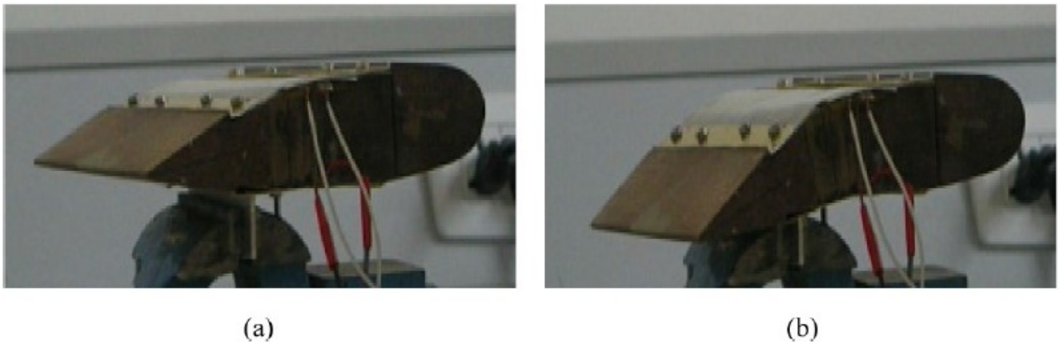

Figure 1.14. Variable-camber wing: (a) the original configuration (0º) and (b) the morphing configuration (15º) [104].

Because of different advantages of shape memory polymers, like the light weight, high strain/shape-recovery ability, easy processability, biocompatibility, and biodegradability, they could be promising materials for biomedical applications. For example, they can be used in minimally invasive surgery for clot removal [106], aneurysm occlusion [107], and vascular stents [108], among others. They can also been employed as orthopaedic devices, as their use as orthodontic wires (Figure 1.15) [109] or artificial muscles [110]. If the needed stimulus to the shape memory change is the temperature, one can design devices based on polymers where the transition temperature of the shape memory effect is near human body temperature, so the polymer can have different shapes depending if it is at room temperature or if it is inside the body.

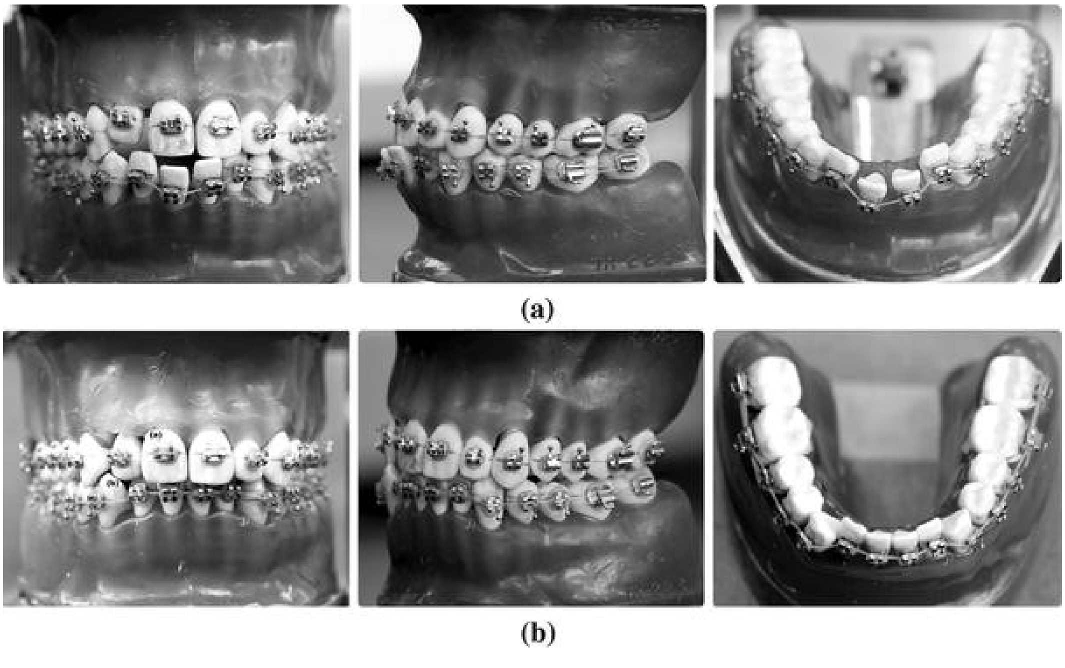

Figure 1.15. Comparison of (a) before and (b) after orthodontic treatment using a SMP wire, where it can be seen the movement of the misaligned teeth due to a lateral force originating from the shape recovery.

1.8. Objectives

The objective of this work is to obtain shape memory polymers based on a commercial polycyclooctene. In this manner, we want to demonstrate the shape memory capabilities of this polymer in different fields. The thesis is divided in three big experimental chapters, where each one is dedicated to a different polycyclooctene system (in Chapter 2, the polycyclooctene is crosslinked with peroxide, in Chapter 3 it is crosslinked with radiation, and in Chapter 4 blends of polycyclooctene are presented) which at the same time are subdivided in different sections for an easier understanding. Additionally, each section presents its own introduction, specific for the studied topic; a materials part, mentioning the employed reagents; the preparation of samples, specifying the procedure to make the substrates; experimental part, where the protocols, results and discussion are treated; and all the sections finalise with the most important extracted conclusions.

Particularly, the polycyclooctene (PCO) is a semicrystalline polymer that exhibits shape memory properties when its macromolecular chains are crosslinked. It is a thermally-induced shape memory polymer, where the transition temperature of the shape memory effect is the melting temperature of the crystallites [79,91].

The most common way to obtain the required chemically crosslinked structure in this polymer is by employing a monofunctional peroxide, which originates free radicals able to pull out an hydrogen atom from the polymer, so polymeric macroradicals can react and recombine to obtain a crosslinked network [111].

It is usual to find in the literature different studies about polycycloctene crosslinked with dicumyl peroxide (DCP). Particularly, this was the main objective of a doctoral thesis in the 'Laboratorio de Química Macromolecular' research group, where the shape memory properties of a commercial polycyclooctene crosslinked with different amounts of DCP were evaluated [112]. As a direct consequence of this doctoral thesis, and to complete the work, we decided to study the behaviour of the surface in these kind of materials, explained in Chapter 2. In the section 2.1 different indentations were made in the surfaces, and the recovery of the original surface was evaluated. On the other hand, in section 2.2 micropillars were performed in the surface of the material by means of laser ablation, which were deformed and recovered by means of shape memory effect, changing both the depth and the wettability of the system.

It is well known that the peroxide originates side products, so it would be interesting to obtain another alternative way to crosslink the macromolecular chains of the PCO in order to its potential use in the promising field of biomedicine. Other polyolefins, like the polyethylene, have been crosslinked by using high energy radiations [78,113], so we thought about the possibility of the use of gamma rays to crosslink our polymer. In this way, Chapter 3 is dedicated to polycyclooctene crosslinked by means of gamma radiation. It is subdivided in different sections. In section 3.1, thermal and mechanical characterisation of the different samples is presented. In section 3.2, the shape memory behaviour, as well as the self-repairing properties of selected samples are analysed. In the section 3.3, a relationship between the free volume and the shape memory effect of different samples is presented.

As the possibility of use these materials in advanced sectors, it seems interesting to have new materials that not only been capable of recover deformations, but restore breakages. In this way, and trying to obtain self-healing polymers, we thought appropriately to blend our well-known-SMP with well-known-molecules that are able to restore damages, named ionomers. In Chapter 4 the properties of some polycyclooctene/ionomer blends are presented. In section 4.1, PCO is blended with two ionomers in a 50/50 ratio (with and without peroxide), and thermal, mechanical and shape memory properties are evaluated. In section 4.2, blends in different PCO/ionomer proportions with a new ionomer are obtained, and a relationship between the blend ratio and the final mechanical and healing behaviour was established.

Finally, once the goals outlined are achieved, Chapter 5 summarizes the main conclusions of the work and gives future perspectives in this area.

1.9. References

1. Kamila, S. Introduction, classification and applications of smart materials: An overview. *Am. J. Appl. Sci.* **2013**, *10*, 876–880.

2. Hu, J. *Shape memory polymers and textiles*; Woodhead Publishing Limited and CRC Press LLC: Cambridge, 2007.

3. Lefebvre, E.; Piselli, A.; Faucheu, J.; Delafosse, D.; Del Curto, B. Smart materials: development of new sensory experiences through stimuli responsive materials. *5th STS Ital. Conf. A Matter Des. Mak. Soc. through Sci. Technol.* **2014**, 10.

4. Addington, M.; Schodek, D. *Smart materials and new technologies for the architecture and design professions*; Elsevier: Oxford, 2005; Vol. 1.

5. Huang, W. M.; Ding, Z.; Wang, C. C.; Wei, J.; Zhao, Y.; Purnawali, H. Shape memory materials. *Mater. Today* **2010**, *13*, 54–61.

6. Lendlein, A.; Kelch, S. Shape-memory polymers. *Angew. Chemie Int. Ed.* **2002**, *41*, 2034–2057.

7. Liu, C.; Qin, H.; Mather, P. T. Review of progress in shape-memory polymers. *J. Mater. Chem.* **2007**, *17*, 1543–1558.

8. Otsuka, K.; Wayman, C. M. *Shape memory materials*; Cambridge University Press: Cambridge, 1999.

9. Buehler, W. J.; Gilfrick, J. V.; Wiley, R. C. Effects of low temperature phase changes on the mechanical properties of alloys near composition TiNi. *J. Appl. Phys.* **1963**, *34*, 1475–1477.

10. Olson, G. B.; Cohen, M. Stress-assisted isothermal martensitic transformation: Application to TRIP steels. *Metall. Trans. A* **1982**, *13*, 1907–1914.

11. Sun, L.; Huang, W. M.; Ding, Z.; Zhao, Y.; Wang, C. C.; Purnawali, H.; Tang,

C. Stimulus-responsive shape memory materials: A review. *Mater. Des.* **2012**, *33*, 577–640.

12. Schurch, K. E.; Ashbee, K. H. G. A near perfect shape-memory ceramic material. *Nature* **1977**, *266*, 706–707.

13. Swain, M. V. Shape memory behaviour in partially stabilized zirconia ceramics. *Nature* **1986**, *322*, 234–236.

14. Reyes-Morel, P. E.; Cherng, J.-S.; Chen, I.-W. Transformation plasticity of CeO2-stabilized tetragonal zirconia polycrystals: II, pseudoelasticity and shape memory effect. *J. Am. Ceram. Soc.* **1988**, *71*, 648–657.

15. Gao, P. X.; Mai, W.; Wang, Z. L. Superelasticity and nanofracture mechanics of ZnO nanohelices. *Nano Lett.* **2006**, *6*, 2536–2543.

16. Du, Z.; Zeng, X. M.; Liu, Q.; Lai, A.; Amini, S.; Miserez, A.; Schuh, C. A.; Gan, C. L. Size effects and shape memory properties in ZrO2 ceramic micro- and nano-pillars. *Scr. Mater.* **2015**, *101*, 40–43.

17. Heuer, A. H.; Ruhle, M.; Marshall, D. B. On the thermoelastic martensitic transformation in tetragonal zirconia. *J. Am. Ceram. Soc.* **1990**, *73*, 1084–1093.

18. Pandit, P.; Gupta, S. M.; Wadhawan, V. K. Effect of electric field on the shape-memory effect in Pb[(Mg 1/3 Nb 2/3) 0.70 Ti 0.30]O 3 ceramic. *Smart Mater. Struct.* **2006**, *15*, 653–658.

19. Polosan, S.; Negrea, R.; Ciobotaru, I. C.; Schinteie, G.; Kuncser, V. Ferromagnetic behaviour of bismuth germanate oxides glass-ceramic materials. *J. Alloys Compd.* **2015**, *623*, 192–196.

20. Behl, M.; Lendlein, A. Shape-memory polymers. *Mater. Today* **2007**, *10*, 20–28.

21. Vernon, L. B.; Vernon, H. M. Process of manufacturing articles of thermoplastic synthetic resins 1941, US 2234993 A.

22. Hitov, J. J.; Rainer, W. C.; Redding, E. M.; Sloan, A. W.; Stewart, W. D. Polyethylene product and process 1964, US 3144398 A.

23. Cook, P. M.; Muchmore, R. W. Process and apparatus for producing materials having plastic memory 1963, US 3086242 A.

24. Edward, W. P. Process and apparatus for producing plastic memory articles 1968, US 3370112 A.

25. Arditti, S. J.; Avedikian, S. Z.; Bernstein, B. S. Articles with polymeric memory and method of constructing same 1971, US 3563973 A.

26. Hu, J.; Chen, S. A review of actively moving polymers in textile applications. *J. Mater. Chem.* **2010**, *20*, 3346.

27. Hu, J.; Zhu, Y.; Huang, H.; Lu, J. Recent advances in shape-memory polymers: Structure, mechanism, functionality, modeling and applications. *Prog. Polym. Sci.* **2012**, *37*, 1720–1763.

28. Goo, N. S.; Paik, I. H.; Jung, Y. C.; Cho, J. W. Development and application of conducting shape memory polyurethane actuators. *Smart Mater. Struct.* **2006**, *15*, 1476–1482.

29. Leng, J.; Lv, H.; Liu, Y.; Du, S. Electroactivate shape-memory polymer filled with nanocarbon particles and short carbon fibers. *Appl. Phys. Lett.* **2007**, *91*, 144105/1–144105/3.

30. Buckley, P. R.; McKinley, G. H.; Wilson, T. S.; Small, W.; Benett, W. J.; Bearinger, J. P.; McElfresh, M. W.; Maitland, D. J. Inductively heated shape memory polymer for the magnetic actuation of medical devices. *Biomed. Eng. IEEE Trans.* **2006**, *53*, 2075–2083.

31. He, Z.; Satarkar, N.; Xie, T.; Cheng, Y. T.; Hilt, J. Z. Remote controlled multishape polymer nanocomposites with selective radiofrequency actuations. *Adv. Mater.* **2011**, *23*, 3192–3196.

32. Lendlein, A.; Jiang, H.; Junger, O.; Langer, R. Light-induced shape-memory polymers. *Nature* **2005**, *434*, 879–882.

33. Jiang, H. Y.; Kelch, S.; Lendlein, A. Polymers move in response to light. *Adv. Mater.* **2006**, *18*, 1471–1475.

34. Long, K. N.; Scott, T. F.; Jerry Qi, H.; Bowman, C. N.; Dunn, M. L. Photomechanics of light-activated polymers. *J. Mech. Phys. Solids* **2009**, *57*, 1103–1121.

35. Lv, H.; Leng, J.; Liu, Y.; Du, S. Shape-memory polymer in response to solution. *Adv. Eng. Mater.* **2008**, *10*, 592–595.

36. Boyle, A. J.; Weems, A. C.; Hasan, S. M.; Nash, L. D.; Monroe, M. B. B.; Maitland, D. J. Solvent stimulated actuation of polyurethane-based shape memory polymer foams using dimethyl sulfoxide and ethanol. *Smart Mater. Struct.* **2016**, *25*, 075014.

37. Du, H.; Zhang, J. Solvent induced shape recovery of shape memory polymer based on chemically cross-linked poly(vinyl alcohol). *Soft Matter* **2010**, *6*, 3370–3376.

38. Dong, Z. Q.; Cao, Y.; Yuan, Q. J.; Wang, Y. F.; Li, J. H.; Li, B. J.; Zhang, S. Redox- and glucose-induced shape-memory polymers. *Macromol. Rapid Commun.* **2013**, *34*, 867–872.

39. Han, X. J.; Dong, Z. Q.; Fan, M. M.; Liu, Y.; Li, J. H.; Wang, Y. F.; Yuan, Q. J.; Li, B. J.; Zhang, S. pH-induced shape-memory polymers. *Macromol. Rapid Commun.* **2012**, *33*, 1055–1060.

40. Fang, Y.; Ni, Y.; Choi, B.; Leo, S. Y.; Gao, J.; Ge, B.; Taylor, C.; Basile, V.; Jiang, P. Chromogenic photonic crystals enabled by novel vapor-responsive shape-memory polymers. *Adv. Mater.* **2015**, *27*, 3696–3704.

41. Ji, S.; Wang, J.; Olah, A.; Baer, E. Triple-shape-memory polymer films created

by forced-assembly multilayer coextrusion. *J. Appl. Polym. Sci.* **2016**.

42. Wei, W.; Shi, A.; Wu, T.; Wei, J.; Guo, J. Thermo-responsive shape and optical memories of photonic composite films enabled by glassy liquid crystalline polymer networks. *Soft Matter* **2016**, *42*, 2528.

43. Raidt, T.; Hoeher, R.; Meuris, M.; Katzenberg, F.; Tiller, J. C. Ionically cross-linked shape memory polypropylene. *Macromolecules* **2016**, *49*, 6918–6927.

44. Zhao, Q.; Zou, W.; Luo, Y.; Xie, T. Shape memory polymer network with thermally distinct elasticity and plasticity. *Sci. Adv.* **2016**, *2*, e1501297.

45. Chan, B. Q. Y.; Low, Z. W. K.; Heng, S. J. W.; Chan, S. Y.; Owh, C.; Loh, X. J. Recent advances in shape memory soft materials for biomedical applications. *ACS Appl. Mater. Interfaces* **2016**, acsami.6b01295.

46. Lu, X. L.; Cai, W.; Gao, Z.; Tang, W. J. Shape memory effects of poly(L-lactide) and its copolymer with poly(ε-caprolactone). *Polym. Bull.* **2007**, *58*, 381–391.

47. Sakurai, K.; Tanaka, H.; Ogawa, N.; Takahashi, T. Shape-memorizable styrene-butadiene block copolymer. I. Thermal and mechanical behaviors and structural change with deformation. *J. Macromol. Sci. Part B* **1997**, *36*, 703–716.

48. Luo, H.; Liu, Y.; Yu, Z.; Zhang, S.; Li, B. Novel biodegradable shape memory material based on partial inclusion complex formation between α-cyclodextrin and poly(ϵ-caprolactone). *Biomacromolecules* **2008**, *9*, 2573–2577.

49. Pandini, S.; Passera, S.; Messori, M.; Paderni, K.; Toselli, M.; Gianoncelli, A.; Bontempi, E.; Ricc, T. Two-way reversible shape memory behaviour of crosslinked poly(ε-caprolactone). *Polymer* **2012**, *53*, 1915–1924.

50. Pandini, S.; Baldi, F.; Paderni, K.; Messori, M.; Toselli, M.; Pilati, F.; Gianoncelli, A.; Brisotto, M.; Bontempi, E.; Riccò, T. One-way and two-way shape memory behaviour of semi-crystalline networks based on sol-gel cross-linked

poly(ε-caprolactone). *Polymer* **2013**, *54*, 4253–4265.

51. Ninaya, Z. H. A.; Hamid, Z. A. A.; Ahmad, Z.; Jaafar, M.; Yahaya, B. H. Development and evaluation of surface modified poly (lactic acid) microsphere via irradiation techniques for drug delivery system. *Procedia Chem.* **2016**, *19*, 373–380.

52. Wu, X. L.; Huang, W. M.; Ding, Z.; Tan, H. X.; Yang, W. G.; Sun, K. Y. Characterization of the thermoresponsive shape-memory effect in poly(ether ether ketone) (PEEK). *J. Appl. Polym. Sci.* **2014**, *131*, doi: 10.1002/app.39844.

53. Wu, Y.; Hu, J.; Han, J.; Zhu, Y.; Huang, H.; Li, J.; Tang, B. Two-way shape memory polymer with "switch–spring" composition by interpenetrating polymer network. *J. Mater. Chem. A* **2014**, *2*, 18816–18822.

54. Fu, C. Q. and Y. D. and Y. Z. and Y. Two-way shape memory behavior of semi-crystalline elastomer under stress-free condition. *Smart Mater. Struct.* **2016**, *25*, 85023.

55. Chatani, S.; Wang, C.; Podgórski, M.; Bowman, C. N. Triple shape memory materials incorporating two distinct polymer networks formed by selective thiol-Michael addition reactions. *Macromolecules* **2014**, *47*, 4949–4954.

56. Zhao, J.; Chen, M.; Wang, X.; Zhao, X.; Wang, Z.; Dang, Z. M.; Ma, L.; Hu, G. H.; Chen, F. Triple shape memory effects of cross-linked polyethylene/polypropylene blends with cocontinuous architecture. *ACS Appl. Mater. Interfaces* **2013**, *5*, 5550–5556.

57. Xie, T. Tunable polymer multi-shape memory effect. *Nature* **2010**, *464*, 267–270.

58. Shao, Y.; Lavigueur, C.; Zhu, X. X. Multishape memory effect of norbornene-based copolymers with cholic acid pendant groups. *Macromolecules* **2012**, *45*, 1924–1930.

59. Rousseau, I. a.; Xie, T. Shape memory epoxy: Composition, structure, properties and shape memory performances. *J. Mater. Chem.* **2010**, *20*, 3431.

60. Santhosh Kumar, K. S.; Biju, R.; Reghunadhan Nair, C. P. Progress in shape memory epoxy resins. In *Reactive and Functional Polymers*; 2013; Vol. 73, pp. 421–430.

61. Shi, Y.; Yoonessi, M.; Weiss, R. A. High temperature shape memory polymers. *Macromolecules* **2013**, *46*, 4160–4167.

62. Barwood, M. J.; Breen, C.; Clegg, F.; Hammond, C. L. The effect of organoclay addition on the properties of an acrylate based, thermally activated shape memory polymer. *Appl. Clay Sci.* **2014**, *102*, 41–50.

63. Muschenborn, A. D.; Hearon, K.; Volk, B. L.; Conway, J. W.; Maitland, D. J. Feasibility of crosslinked acrylic shape memory polymer for a thrombectomy device. *Smart Mater Struct* **2014**, *2014*, 971087.

64. Yang, D.; Huang, W.; Yu, J.; Jiang, J.; Zhang, L.; Xie, M. A novel shape memory polynorbornene functionalized with poly(ε-caprolactone) side chain and cyano group through ring-opening metathesis polymerization. *Polymer* **2010**, *51*, 5100–5106.

65. Kusmierczuk, M.; Nöchel, U.; Baudis, S.; Behl, M.; Kratz, K.; Lendlein, A. Shape-memory polymer networks prepared from star-shaped poly[(L-lactide)-co-glycolide] precursors. *Macromol. Symp.* **2014**, *345*, 98–104.

66. Migneco, F.; Huang, Y. C.; Birla, R. K.; Hollister, S. J. Poly(glycerol-dodecanoate), a biodegradable polyester for medical devices and tissue engineering scaffolds. *Biomaterials* **2009**, *30*, 6479–6484.

67. Karger-Kocsis, J.; Kéki, S. Biodegradable polyester-based shape memory polymers: Concepts of (supra)molecular architecturing. *Express Polym. Lett.* 2014, *8*, 397–412.

68. Wei, H.; Zhang, F.; Zhang, D.; Liu, Y.; Leng, J. Shape-memory behaviors of electrospun chitosan/poly(ethylene oxide) composite nanofibrous membranes. *J. Appl. Polym. Sci.* **2015**, *132*.

69. Wang, M.; Luo, X.; Zhang, X.; Ma, D. Shape memory properties in poly(ethylene oxide)–poly(ethylene terephthalate) copolymers. *Polym. Adv. Technol.* **1997**, *8*, 136–139.

70. Ping, P.; Wang, W.; Chen, X.; Jing, X. Poly(ε-caprolactone) polyurethane and its shape-memory property. *Biomacromolecules* **2005**, *6*, 587–592.

71. Kim, B. K.; Lee, S. Y.; Xu, M. Polyurethanes having shape memory effects. *Polymer* **1996**, *37*, 5781–5793.

72. Sun, X.; Ni, X. Block copolymer of trans-polyisoprene and urethane segment: Crystallization behavior and morphology. *J. Appl. Polym. Sci.* **2004**, *94*, 2286–2294.

73. Mather, P. T.; Luo, X.; Rousseau, I. A. Shape memory polymer research. *Annu. Rev. Mater. Res.* **2009**, *39*, 445–471.

74. Lin, X. K.; Chen, L.; Zhao, Y. P.; Dong, Z. Z. Synthesis and characterization of thermoresponsive shape-memory poly(stearyl acrylate-co-acrylamide) hydrogels. *J. Mater. Sci.* **2010**, *45*, 2703–2707.

75. Li, F.; Zhu, W.; Zhang, X.; Zhao, C.; Xu, M. Shape memory effect of ethylene–vinyl acetate copolymers. *J. Appl. Polym. Sci.* **1999**, *71*, 1063–1070.

76. Alonso-Villanueva, J.; Cuevas, J. M.; Laza, J. M.; Vilas, J. L.; León, L. M. Synthesis of poly(cyclooctene) by ring-opening metathesis polymerization: Characterization and shape memory properties. *J. Appl. Polym. Sci.* **2010**, *115*, 2440–2447.

77. Zhu, G.; Liang, G.; Xu, Q.; Yu, Q. Shape-memory effects of radiation crosslinked poly(ϵ-caprolactone). *J. Appl. Polym. Sci.* **2003**, *90*, 1589–1595.

78. Basfar, A. A. Flammability of radiation cross-linked low density polyethylene as an insulating material for wire and cable. *Radiat. Phys. Chem.* **2002**, *63*, 505–508.

79. Liu, C.; Chun, S. B.; Mather, P. T.; Zheng, L.; Haley, E. H.; Coughlin, E. B. Chemically cross-linked polycyclooctene: synthesis, characterization, and shape memory behavior. *Macromolecules* **2002**, *35*, 9868–9874.

80. Bellin, I.; Kelch, S.; Langer, R.; Lendlein, A. Polymeric triple-shape materials. *Proc. Natl. Acad. Sci. U. S. A.* **2006**, *103*, 18043–18047.

81. Zotzmann, J.; Behl, M.; Feng, Y.; Lendlein, A. Copolymer networks based on poly(ω-pentadecalactone) and poly(ε-caprolactone)segments as a versatile triple-shape polymer system. *Adv. Funct. Mater.* **2010**, *20*, 3583–3594.

82. Behl, M.; Bellin, I.; Kelch, S.; Wagermaier, W.; Lendlein, A. One-step process for creating triple-shape capability of AB polymer networks. *Adv. Funct. Mater.* **2009**, *19*, 102–108.

83. Li, J.; Liu, T.; Xia, S.; Pan, Y.; Zheng, Z.; Ding, X.; Peng, Y. A versatile approach to achieve quintuple-shape memory effect by semi-interpenetrating polymer networks containing broadened glass transition and crystalline segments. *J. Mater. Chem.* **2011**, *21*, 12213–17.

84. Luo, X.; Mather, P. T. Triple-shape polymeric composites (TSPCs). *Adv. Funct. Mater.* **2010**, *20*, 2649–2656.

85. Hoeher, R.; Raidt, T.; Krumm, C.; Meuris, M.; Katzenberg, F.; Tiller, J. C. Tunable Multiple-Shape Memory Polyethylene Blends. *Macromol. Chem. Phys.* **2013**, *214*, 2725–2732.

86. Li, J.; Rodgers, W. R.; Xie, T. Semi-crystalline two-way shape memory elastomer. *Polymer* **2011**, *52*, 5320–5325.

87. Ahir, S. V.; Tajbakhsh, A. R.; Terentjev, E. M. Self-assembled shape-memory

fibers of triblock liquid-crystal polymers. *Adv. Funct. Mater.* **2006**, *16*, 556–560.

88. Ohm, C.; Brehmer, M.; Zentel, R. Liquid crystalline elastomers as actuators and sensors. *Adv. Mater.* **2010**, *22*, 3366–3387.

89. Rousseau, I. A.; Mather, P. T. Shape memory effect exhibited by smectic-c liquid crystalline elastomers. *J. Am. Chem. Soc.* **2003**, *125*, 15300–15301.

90. Martínez-Gómez, A.; Fernández-Blázquez, J. P.; Bello, A.; Pérez, E. Preparation and Properties of a Main-Chain Smectic Liquid-Crystalline Elastomer with Shape-Memory Ability. *Macromolecules* **2016**, *49*, 5306–5314.

91. Chung, T.; Romo-Uribe, A.; Mather, P. T. Two-way reversible shape memory in a semicrystalline network. *Macromolecules* **2008**, *41*, 184–192.

92. Westbrook, K. K.; Mather, P. T.; Parakh, V.; Dunn, M. L.; Ge, Q.; Lee, B. M.; Qi, H. J. Two-way reversible shape memory effects in a free-standing polymer composite. *Smart Mater. Struct.* **2011**, *20*, 65010.

93. Zotzmann, J.; Behl, M.; Hofmann, D.; Lendlein, A. Reversible triple-shape effect of polymer networks containing polypentadecalactone- and poly(ε-caprolactone)-segments. *Adv. Mater.* **2010**, *22*, 3424–3429.

94. Behl, M.; Kratz, K.; Zotzmann, J.; Nöchel, U.; Lendlein, A. Reversible bidirectional shape-memory polymers. *Adv. Mater.* **2013**, *25*, 4466–4469.

95. Kunzelman, J.; Chung, T.; Mather, P. T.; Weder, C. Shape memory polymers with built-in threshold temperature sensors. *J. Mater. Chem.* **2008**, *18*, 1082.

96. Li, F.; Larock, R. C. New soybean oil-styrene-divinylbenzene thermosetting copolymers. V. Shape memory effect. *J. Appl. Polym. Sci.* **2002**, *84*, 1533–1543.

97. Gall, K.; Yakacki, C. M.; Liu, Y.; Shandas, R.; Willett, N.; Anseth, K. S. Thermomechanics of the shape memory effect in polymers for biomedical applications. *J. Biomed. Mater. Res. - Part A* **2005**, *73*, 339–348.

98. Li, J.; An, Y.; Huang, R.; Jiang, H.; Xie, T. Unique aspects of a shape memory polymer as the substrate for surface wrinkling. *ACS Appl. Mater. Interfaces* **2012**, *4*, 598–603.

99. Turner, S. A.; Zhou, J.; Sheiko, S. S.; Ashby, V. S. Switchable micropatterned surface topographies mediated by reversible shape memory. *ACS Appl. Mater. Interfaces* **2014**, *6*, 8017–8021.

100. Zhu, Y.; Hu, J.; Yeung, L.-Y.; Liu, Y.; Ji, F.; Yeung, K. Development of shape memory polyurethane fiber with complete shape recoverability. *Smart Mater. Struct.* **2006**, *15*, 1385–1394.

101. Hu, J.; Meng, H.; Li, G.; Ibekwe, S. I. A review of stimuli-responsive polymers for smart textile applications. *Smart Mater. Struct.* **2012**, *21*, 053001.

102. Gök, M. O.; Bilir, M. Z.; Gürcüm, B. H. Shape-memory applications in textile design. *Procedia - Soc. Behav. Sci.* **2015**, *195*, 2160–2169.

103. Barrett, R.; Francis, W.; Abrahamson, E.; Lake, M. S.; Scherbarth, M.; Duncan, L. C. Qualification of elastic memory composite hinges for spaceflight applications. *Proceedings* **2006**, 1–4.

104. Liu, Y.; Du, H.; Liu, L.; Leng, J. Shape memory polymers and their composites in aerospace applications: a review. *Smart Mater. Struct.* **2014**, *23*, 023001.

105. Santo, L.; Quadrini, F.; Accettura, A.; Villadei, W. Shape memory composites for self-deployable structures in aerospace applications. In *Procedia Engineering*; 2014; Vol. 88, pp. 42–47.

106. Small IV, W.; Metzger, M. F.; Wilson, T. S.; Maitland, D. J. Laser-activated shape memory polymer microactuator for thrombus removal following ischemic stroke: Preliminary in vitro analysis. *IEEE J. Sel. Top. Quantum Electron.* **2005**, *11*, 892–901.

107. Small IV, W.; Buckley, P. R.; Wilson, T. S.; Benett, W. J.; Hartman, J.;

Saloner, D.; Maitland, D. J. Shape memory polymer stent with expandable foam: A new concept for endovascular embolization of fusiform aneurysms. *IEEE Trans. Biomed. Eng.* **2007**, *54*, 1157–1160.

108. Yakacki, C. M.; Shandas, R.; Lanning, C.; Rech, B.; Eckstein, A.; Gall, K. Unconstrained recovery characterization of shape-memory polymer networks for cardiovascular applications. *Biomaterials* **2007**, *28*, 2255–2263.

109. Jung, Y. C.; Cho, J. W. Application of shape memory polyurethane in orthodontic. *J. Mater. Sci. Mater. Med.* **2010**, *21*, 2881–2886.

110. Marshall, J. E.; Gallagher, S.; Terentjev, E. M.; Smoukov, S. K. Anisotropic colloidal micromuscles from liquid crystal elastomers. *J. Am. Chem. Soc.* **2014**, *136*, 474–479.

111. Tamboli, S. M.; Mhaske, S. T.; Kale, D. D. Crosslinked polyethylene. *Indian J. Chem. Technol.* **2004**, *11*, 853–864.

112. Cuevas Zarraga, J. M. Desarrollo y caracterización de la capacidad de memoria de forma en polímeros semicristalinos (Doctoral thesis), UPV/EHU, 2011.

113. Barkhudaryan, V. G. Alterations of molecular characteristics of polyethylene under the influence of γ-radiation. *Polymer* **2000**, *41*, 2511–2514.

CHAPTER 2

Polycyclooctene (PCO) crosslinked with peroxide

2.1. Recovering surface damages on polymer substrates

2.1.1. Introduction

Most of the polymeric systems are susceptible to damage from environmental stresses, which can cause loss in its mechanical, physical and aesthetic properties, so interest in developing and characterizing self-healing materials has grown considerably due to broad applicability in innumerable industrial sectors. Self-healing in materials, where damage is detected and repaired in situ [1,2], is the result of a new and innovative approach to tailor the structure/property relations in materials to extend their lifetime and their reliability in use. Therefore, providing self-healing properties to these polymeric materials is enormously attractive from the industrial viewpoint. In recent years, different types of developed systems demonstrate the ability to heal, which are mainly based on microcapsule dispersions [3–5], particle segregation [6,7], microvascular networks [8–10], or gels [11–14], among others, where shape memory polymers (SMP) can play an outstanding role in the field of self-repairing features [15].

As explained in Chapter 1, the shape memory effect in thermo-responsive SMPs consists of heating up the sample above the transition temperature of the shape memory effect (T_{trans}), deforming, and cooling the sample below that temperature. The recovery of the permanent shape can be observed heating up the sample above T_{trans}. Furthermore, the deformation force may also be applied to a non-heated SMP, i.e. draw the sample at a low temperature. In this case, the permanent shape was recovered at an elevated temperature under a stress free condition [16]. Mather *et al.* [17] called it ‘reversible plasticity shape memory effect (RP-SME)’ and the deformation step is usually called ‘cold drawing programming process’ because it consists in working at temperatures below T_{trans} [18,19], that is, deforming the SMP at glassy or crystalline state. This procedure has different benefits, such as lower recovery temperatures and largely enhanced recovery stress [20].

This RP-SME can be used to repair surfaces. The surface of the plastic-made objects may be damaged during its lifetime. These damages are mainly plastic deformations, which can be recovered according to RP-SME mechanism, although just in case of non-permanent damages such as surface scratches or indents. If permanent damages such cracking occur, heating would reduce crack width but not heal it [21] since surface scratches are material deformations related with entropy changes, whereas cracking implies a macroscopical material separation. Thus, shape memory polymers can be used to partially repair structural damage [22].

The present chapter describes the potential thermally activated self-repair features of developed polyalkenamer based shape memory materials faced to thermomechanical and shape memory properties, as a function of the degree of selective crosslinking of the semi-crystalline network. Therefore, these polymers can recover its original shape upon heating above its melting temperature (T_m), due to its autonomous conformational entropy driven shape recovery mechanism, which is demonstrated by different techniques, such as surface profilometry, and confocal and optical microscopy.

2.1.2. Materials

All the employed materials were used as received without any previous purification step.

2.1.2.1. Polycyclooctene (PCO)

This work has been performed employing the commercially available polycyclooctene Vestenamer® 8012, from Evonik Industries (some properties of Vestenamer® 8012 technical datasheet's are listed in Table 2.1).

Vestenamer® 8012 is presented in cylindrical white pellets (see Figure 2.1) with a length less than 6 mm, where the 80% of its double bonds are in *trans* configuration. The degree of purity of the polymer is higher than 99.5%.

It is produced by polymerisation of cyclooctene, which is in turn synthesised from 1,3-butadiene via conversion into 1,5-cyclooctadiene. The cyclooctene is polymerized to octenamer by Ring Opening Metathesis Polymerization (ROMP), where the double bond of the monomer is preserved so that the resulting polyoctenamer contains a double bond at every eight carbon atom, producing linear and cyclic macromolecules (Figure 2.2). The *cis/trans* ratio determines the crystallinity of the polycyclooctene.

Table 2.1. Properties of Vestenamer® 8012 supplied by the manufacturer.

Property	Method	Value
Molecular weight, M_w	GPC (DIN 55672-1)	90000 g/mol
Glass transition temperature, T_g	DSC (ISO 11357)	-65 ºC
Crystallinity at 23 ºC	DSC (ISO 11357)	About 30%
Melting point, T_m (2nd heating)	DSC (ISO 11357)	54 ºC
Thermal decomposition	TGA (ISO 11357)	275 ºC
Double bonds cis/trans ratio	IR (SOP 0188)	20/80%
Density	ISO 1183	0.91 g/cm^3

Figure 2.1. Pellets of Vestenamer ® 8012.

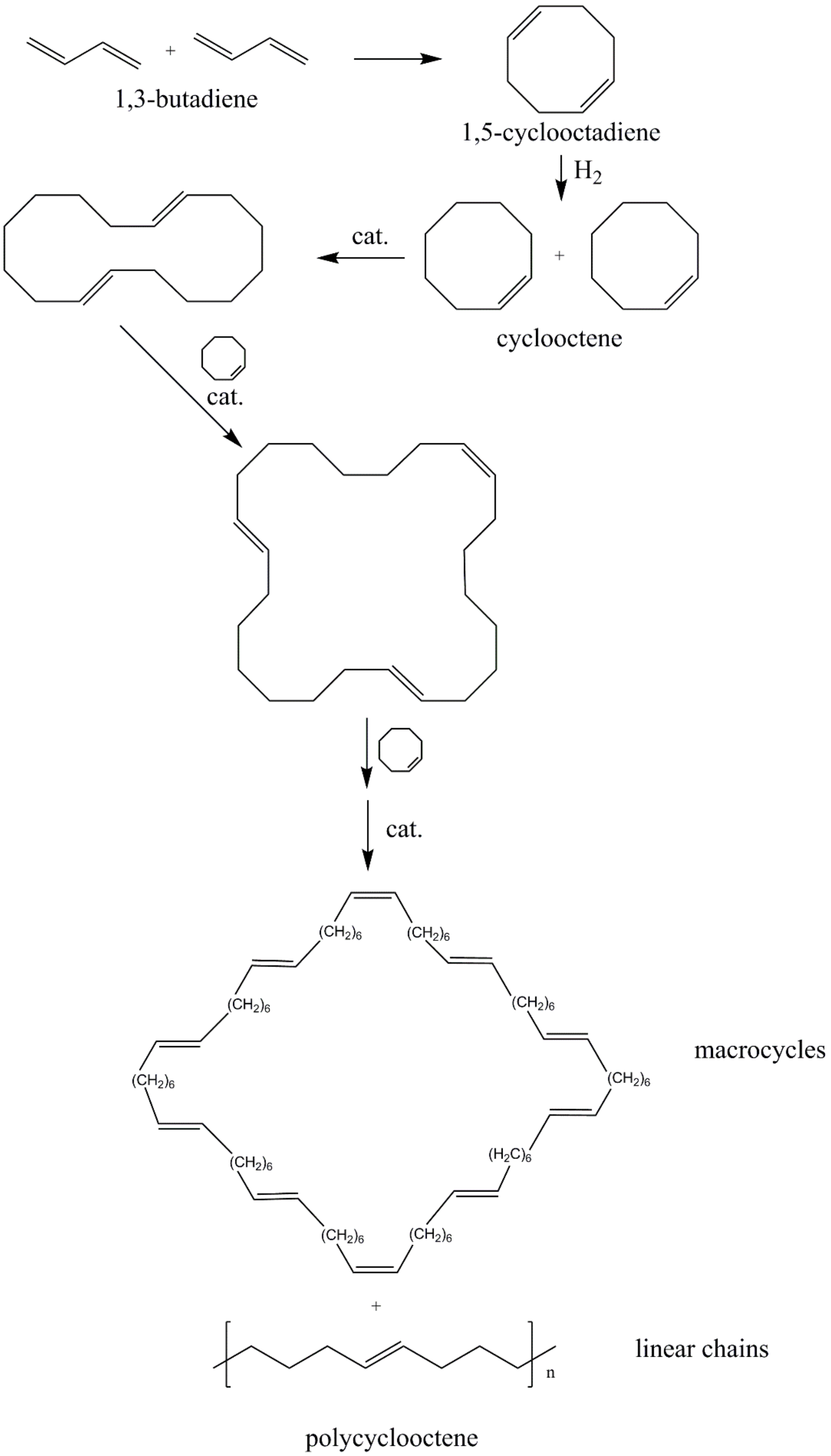

Figure 2.2. Synthesis of polycyclooctene (PCO).

2.1.2.2. Dicumyl peroxide (DCP)

The crosslinking agent used was dicumyl peroxide (DCP) from Aldrich, which is a 98.0% purity solid crystalline monofunctional peroxide, which decomposes at 90 ºC. The chemical structure can be seen in Figure 2.3.

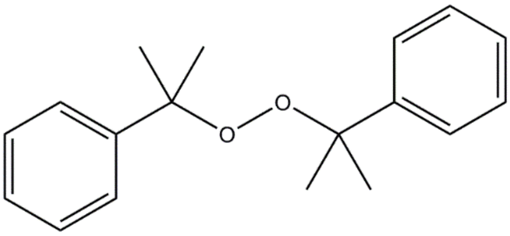

Figure 2.3. Dicumyl peroxide (DCP)

2.1.3. Preparation of samples

Polycyclooctene-based shape memory formulations were prepared by a melt-blending protocol varying the DCP content from 1 to 3 wt% using a Haake Rheomix 600 mixing chamber (Figure 2.4) at 70 ºC. When the temperature was stabilized at 70 ºC, the dried polycyclooctene (PCO) Vestenamer® 8012 was extruded until suitable melting and, subsequently, dicumyl peroxide was fed into the mixing chamber to form a homogeneous blend of components without significant induced crosslinking (see Figure 2.5). Subsequently, the obtained homogeneous blends were crosslinked at 180 ºC for 20 min by compression moulding (Figure 2.6) under a pressure of 925 bar in a 2 mm thickness flat mould (Figure 2.7). Two Teflon sheets were placed on both sides of the mould to reduce the surface roughness of the PCO-DCP specimens obtained. After curing, the obtained 50 mm × 50 mm × 2 mm specimens were cooled to room temperature in the mould under constant pressure. In order to provide an identical thermal history, the neat PCO (0 wt% of peroxide) was also processed under the same described conditions. Table 2.2 summarizes all the developed PCO samples, whereas Figure 2.8 shows the different performed samples.

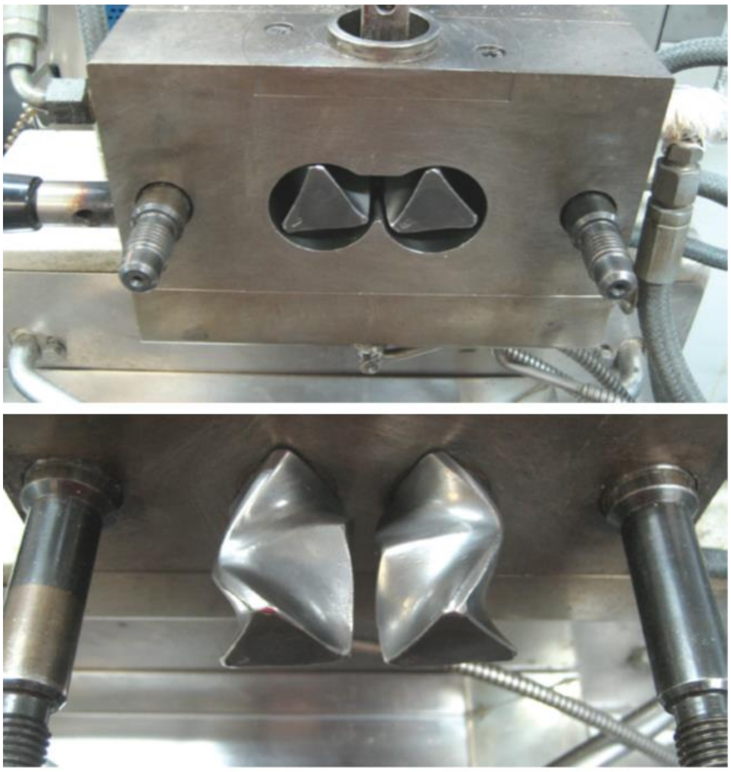

Figure 2.4. Haake Rheomix 600 mixing chamber and mixing screws.

Figure 2.5. Blend obtained by extrusion process.

Figure 2.6. Hydraulic press.

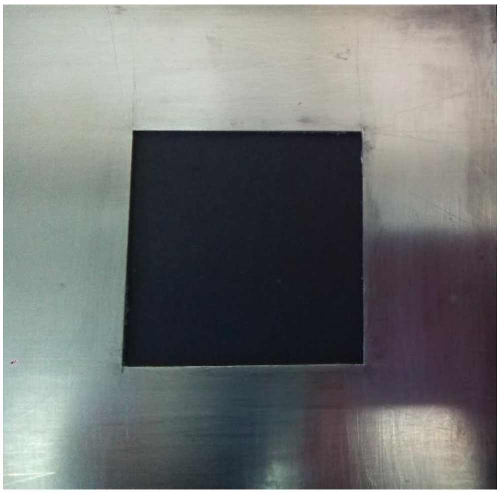

Figure 2.7. Mould.

Table 2.2. Thermal properties and Shore D hardness values of the PCO-DCP samples studied.

Sample	DCP wt%	T_g (ºC)	T_m (ºC)	T_{rec} (ºC)	Crystallinity (%)	Shore D hardness
PCO-0	0	-76.3	57.0	80	26.4	36.5
PCO-1	1	-75.5	52.6	70	24.8	35.3
PCO-2	2	-73.6	42.0	60	22.2	32.6
PCO-3	3	-73.5	37.8	55	20.7	28.6

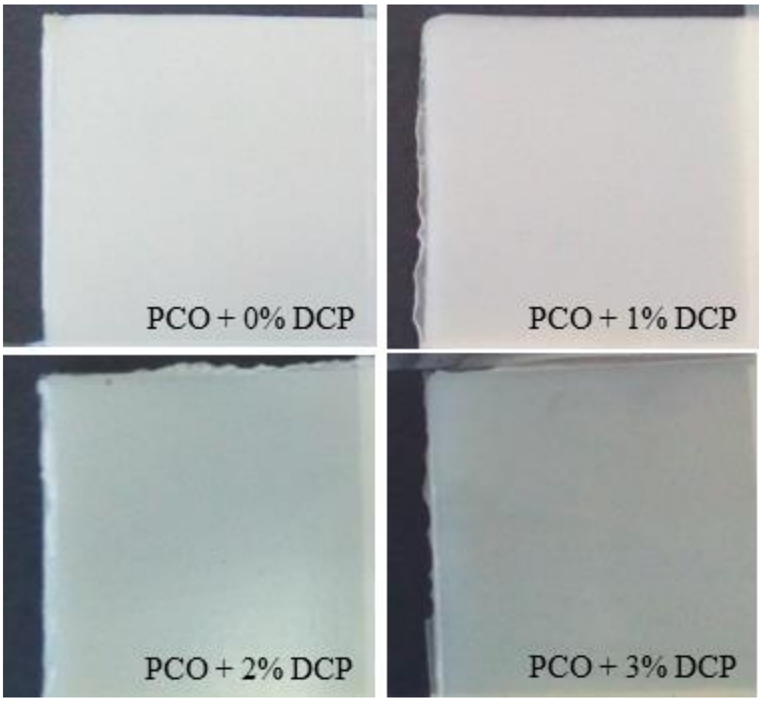

Figure 2.8. PCO samples with different amount of DCP.

Crosslinking the macromolecular chains of the polymer using organic peroxides is a reported method to obtain shape memory polymers, as it has been explained in Chapter 1. Here, the crosslinking process of the thermoplastic matrix promoted by dicumyl peroxide may occur via two main different reactions [23,24] (Figure 2.9). On the one hand, the free radicals from thermal decomposition of functional peroxide generate, by hydrogen abstraction, polymeric macroradicals able to react and recombine (Figure 2.9a) in a crosslinked network. Besides, another process can occurs from combining the peroxide radical with the double bond of the polymer chain (Figure 2.9b).

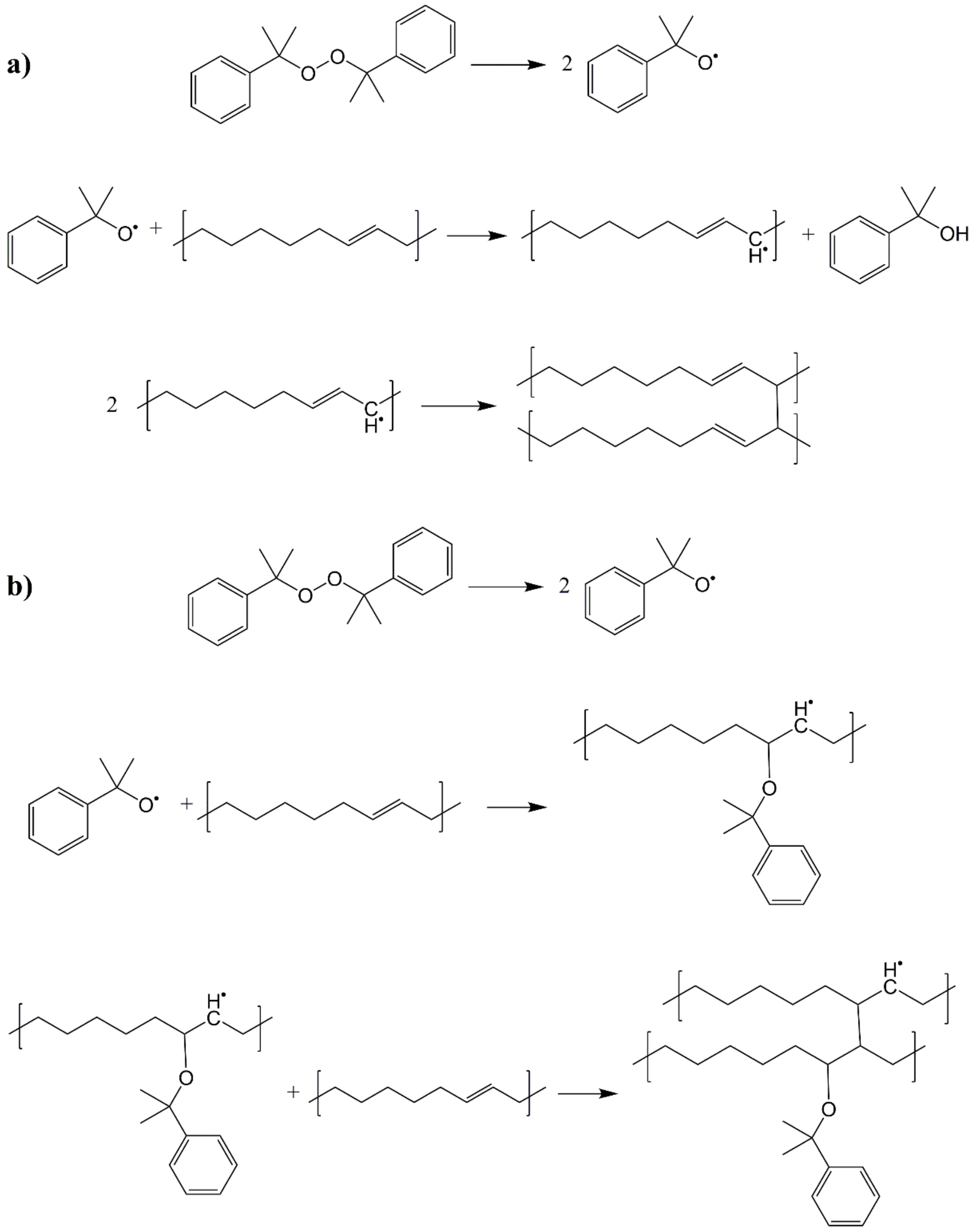

Figure 2.9. Schematic representation of crosslinking reaction between PCO and DCP.

2.1.4. Experimental section

2.1.4.1. Thermal Properties

Thermal properties of neat PCO and crosslinked PCO samples were measured by Differential Scanning Calorimetry (DSC 822e from Mettler Toledo) to identify thermal actuation temperatures. Samples in aluminium pans were characterized under constant nitrogen flow (50 ml·min^{-1}). First, samples were heated from −100 to 150 ºC at a rate of 10 ºC·min^{-1}, followed by a cooling scan from 150 to −100 ºC at a rate of −10 ºC·min^{-1}. Subsequently, a second heating scan to 150 ºC was conducted at the same heating rate. In all cases, samples around 5–10 mg were used.

The DSC analysis indicated that the peroxide concentration, and the associated crosslinking density, has an impact on the crystallinity of the materials. Crystallinity values were also shown in Table 2.2. These crystallinity values were calculated employing equation 2.1, where the enthalpy of a 100% crystalline polycyclooctene was 230 J g^{-1} [25].

$$\%\, crystallinity = \frac{\Delta H_{m2}\,(PCO\ sample)}{\Delta H_m\,(100\%\ crystalline\ PCO)} \times 100 \qquad (2.1)$$

Figure 2.10 shows the respective DSC curves, as well as Table 2.2 listed the corresponding melting temperatures. As can be observed in Figure 2.10, the peaks corresponding to the melting and crystallization temperatures for the different PCO-DCP samples switched to lower temperatures as the DCP wt% increases. Increasing peroxide concentration, thus, promotes crosslinking density, and the degree of crystallinity decreases as result of the lower chain mobility from crosslinking knots, which are responsible for a lower diffusion and limited conformational order of the polymer chains.

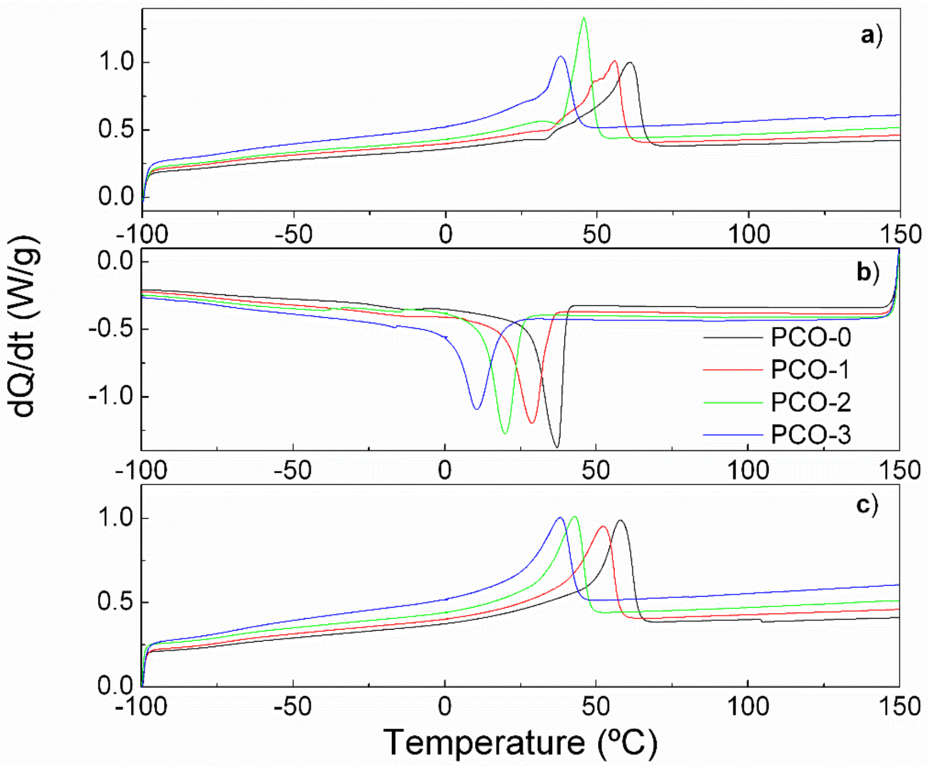

Figure 2.10. DSC curves for all the PCO-DCP samples: a) first heating, b) cooling and c) second heating.

Since slight differences in the DSC curves can be observed between consecutive heating cycles due to variations in the thermal history of the samples, the transition temperature of shape memory effect (T_{trans}) was defined from melting temperature measured in the second heating cycle (T_m in Table 2.2).

In conclusion, it is possible to tailor the melting temperature of the PCO-DCP crosslinked samples, and thus the transition temperature of shape memory (T_{trans}), simply by controlling the degree of crosslinking of the samples by the concentration of peroxide.

2.1.4.2. Shore D Hardness

Shore test measures the resistance of plastics toward indentation. Thus, Shore D hardness of different PCO samples was measured by pressing a 30º cone indenter tip of 1.4 mm extension with a spring force of 44.48 N on the surface with a Shore D mechanical hardness tester, assembled on test stand BS 61 from Bareiss Prüfgerätebau Gmbh, and reading the scale after 15 s holding the presser foot in contact. Five measurements of hardness were performed and the median value was determined (Table 2.2).

Hardness of semicrystalline polymers depends on numerous microestructural parameters related to crystallinity degree, conformational alternating lamellae regions and disordered layers, defects in the stereoregularity, chain entanglements and folds, and other conformational irregularities [26,27]. However, hardness is often correlated to the yield stress, being a direct relationship between yield stress and degree of crystallinity, in agreement with data in Figure 2.11 [28].

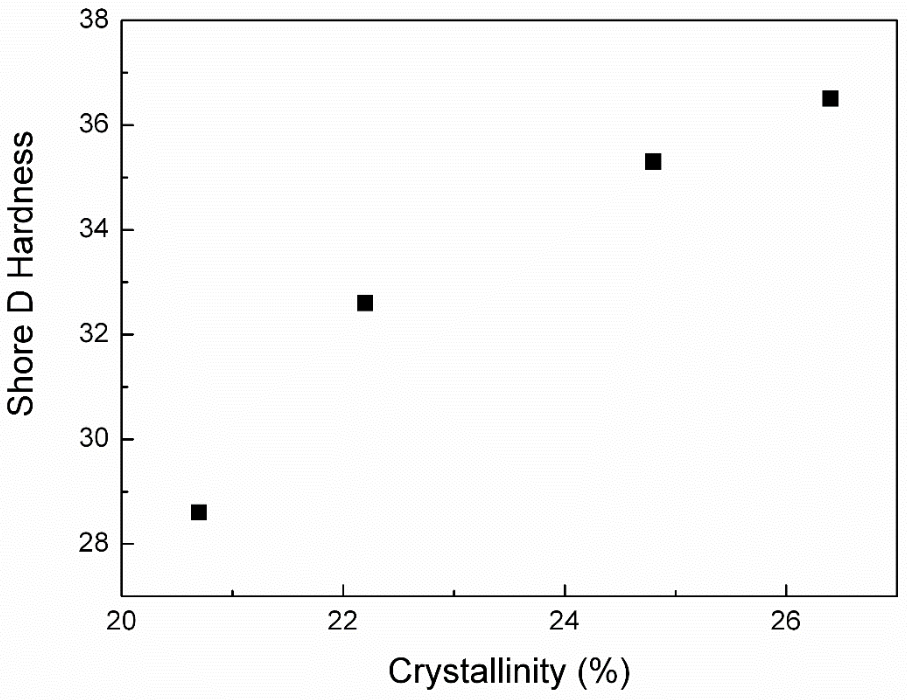

Figure 2.11. Relationship between crystallinity and Shore D Hardness for PCO samples.

2.1.4.3. Self-repair behaviour

The protocol to evaluate correctly the shape memory properties of the PCO samples, related to its self-repair behaviour, consists in measure their surface at different stages of the process: i) before mark the surface, ii) after marking, iii) after 24 hours at room temperature and, finally, iv) after heating. To emphasize the potentiality of self-repairing capabilities in PCO samples, two kinds of marks were performed: a) holes and, b) 30 mm line marks.

a. Holes

Holes were performed using a Hardness Test Pencil Model 318 from Erichsen (Figure 2.12) by marking the surface of the samples with a known force (5, 10 and 15 N). Once the required spring tension is set, the Test Pencil was held upright and placed its point on the test surface to draw a hole. The length of contact time under load was very short (1-2 s) in order to minimise the effect of loading cycle time on final permanent deformation. Therefore, the deformation was applied to a non-heated samples and could be recovered at elevate temperature under stress free conditions [16] through the reversible shape memory plasticity effect described by Mather [17].

Self-repair properties of crosslinked PCO samples were evaluated using surface profilometry (Alpha-Step D-100 profilometer from KLA-Tencor), and non-contact confocal optical 3D profilometry (PLμ NEOX microscope from SENSOFAR). A surface profilometer can measure small surface variations in vertical stylus displacement as a function of position. A diamond stylus is moved vertically in contact with the sample at the same time that is moved laterally across the sample a specific distance with a determined contact force. In contrast, the confocal profilometry is an optical imaging technique for increasing optical resolution and contrast of a micrograph by means of adding a spatial pinhole placed at the confocal plane of the lens to eliminate out-of-focus light. It enables the reconstruction of three-dimensional structures from the obtained images because of the horizontal scanning.

Figure 2.12. Hardness test pencil.

After measuring the surface roughness of the PCO specimens by optical-confocal profilometry test, three different holes with known forces (5, 10, 15 N) were performed in each sample. The measured depths in the centre of the holes evaluated by both profilometry techniques are collected in Table 2.3. Furthermore, the profiles obtained with the profilometry technique are illustrated in Figure 2.13 for PCO-1, PCO-2 and PCO-3 samples.

The measured surfaces, as well as the corresponding profiles, are shown in Figure 2.14 to Figure 2.22, for all samples (PCO-1, PCO-2, PCO-3) and all forces (5, 10, 15 N). Only the 10 N hole in all samples was measured 24 hours later (Figure 2.15, Figure 2.18 and Figure 2.21), and no differences were observed. So in the rest of the holes (5 and 15 N) the measurements were performed in the initial stage, when the sample was holed, and once the sample was recovered; that is, the measurement 24 hours later was not performed.

Table 2.3. Hole depth marks in the PCO-DCP samples.

Sample	**Marking force (N)**	**Hole depth measured (μm)**	
		Surface profilometry	**Confocal profilometry**
PCO-1	15	196	181
	10	79	86
	5	34	36
PCO-2	15	188	191
	10	130	133
	5	44	54
PCO-3	15	117	105
	10	106	100
	5	48	42

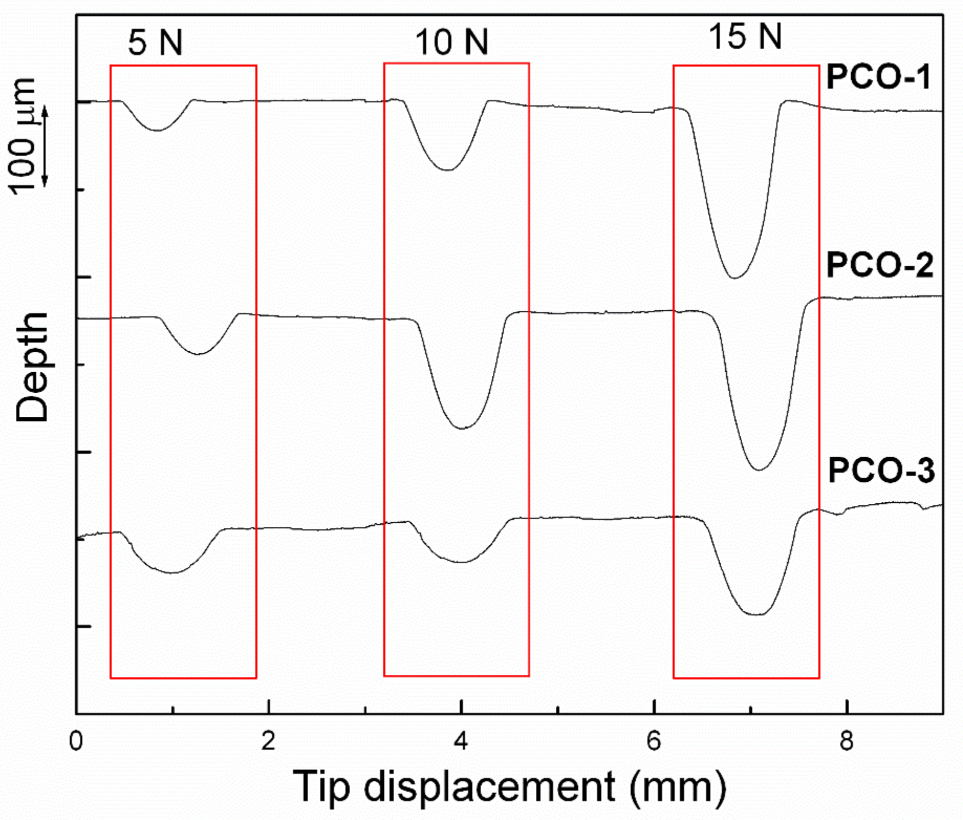

Figure 2.13. Measured profiles of holes for all PCO samples.

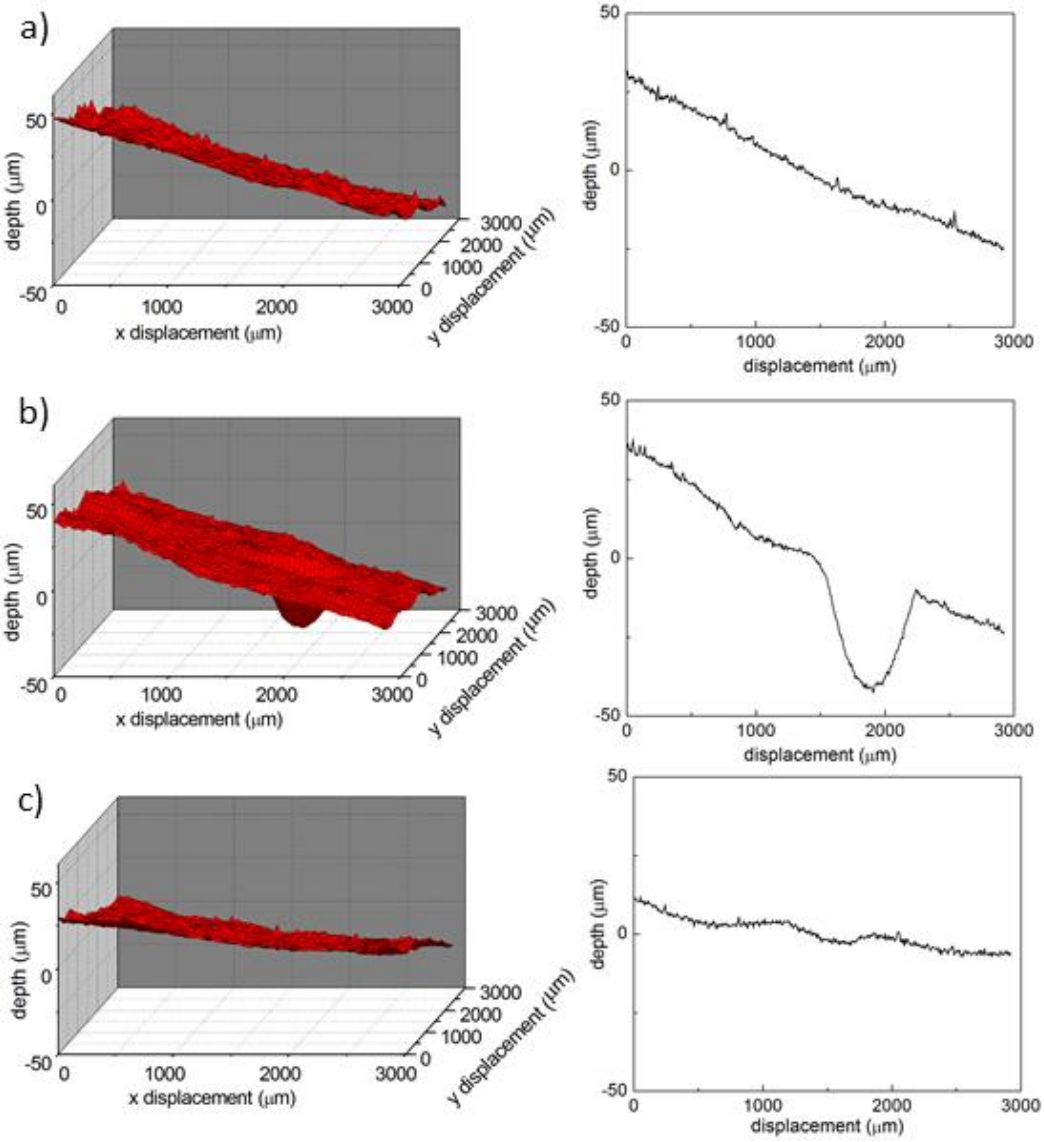

Figure 2.14.Measured surfaces (left) and profiles (right) for 5 N hole in PCO-1 sample: (a) without hole, (b) hole, (c) recovered.

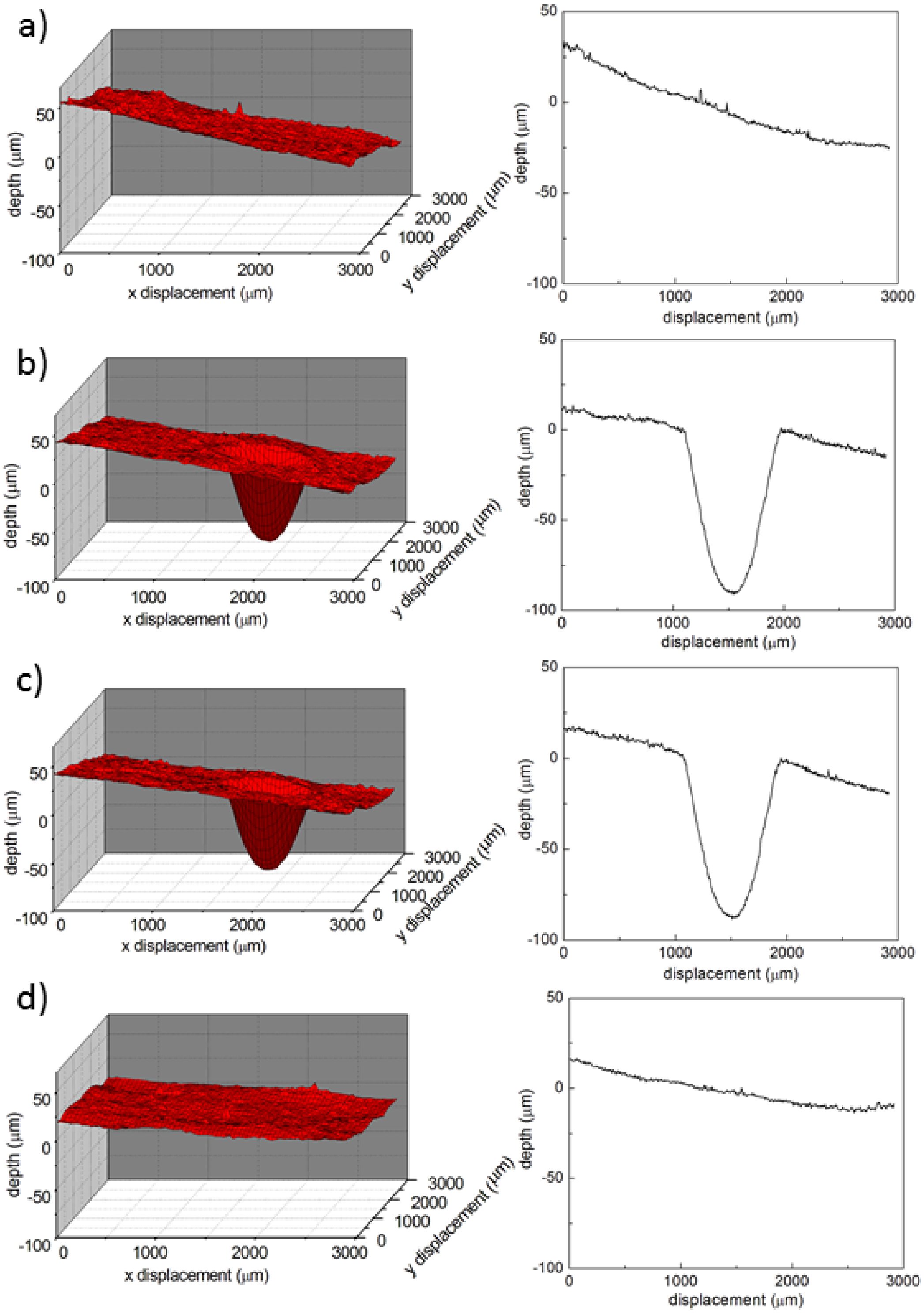

Figure 2.15. Measured surfaces (left) and profiles (right) for 10 N hole in PCO-1 sample: (a) without hole, (b) hole, (c) measured 24 h later and (d) recovered.

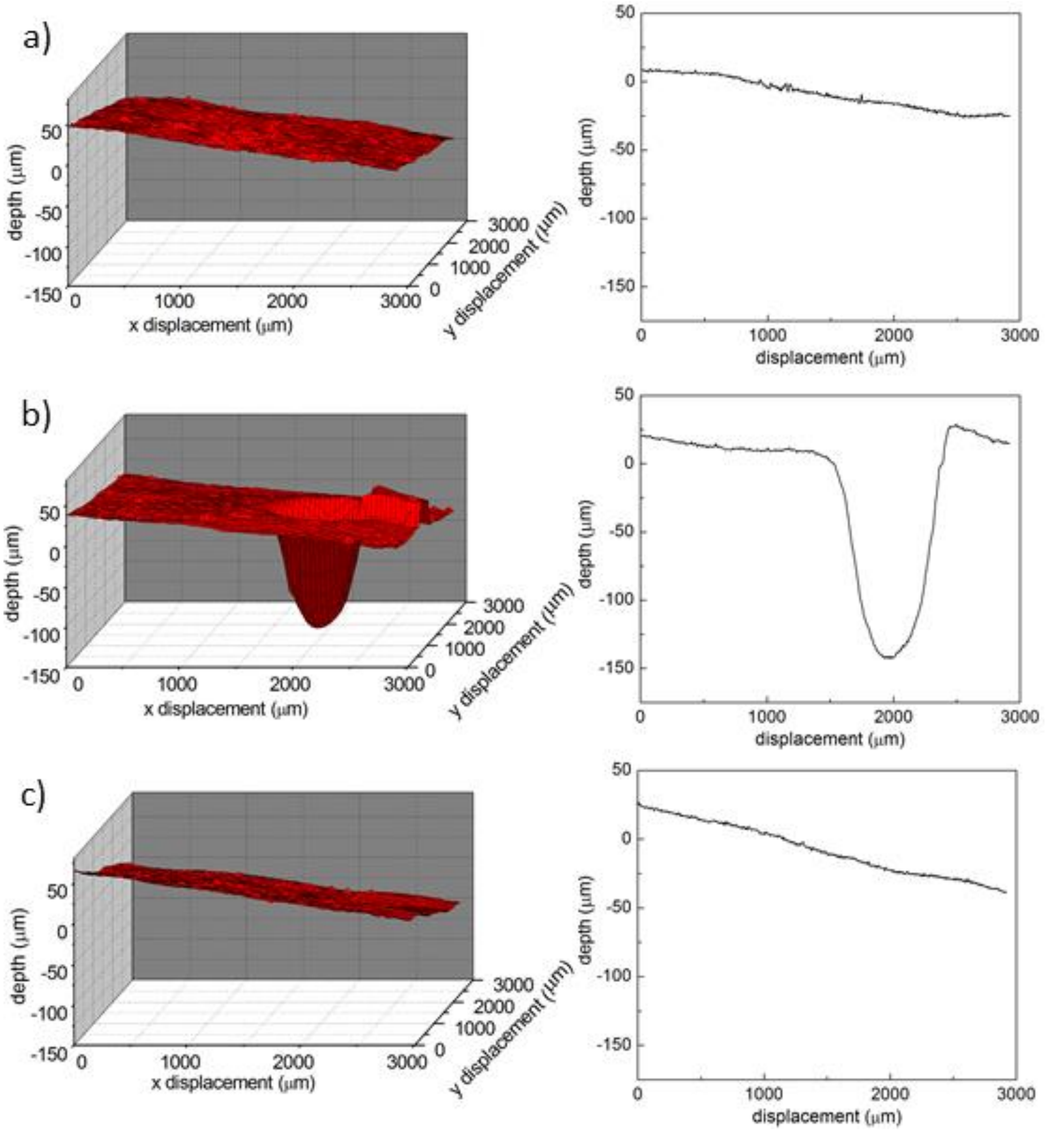

Figure 2.16. Measured surfaces (left) and profiles (right) for 15 N hole in PCO-1 sample: (a) without hole, (b) hole, (c) recovered.

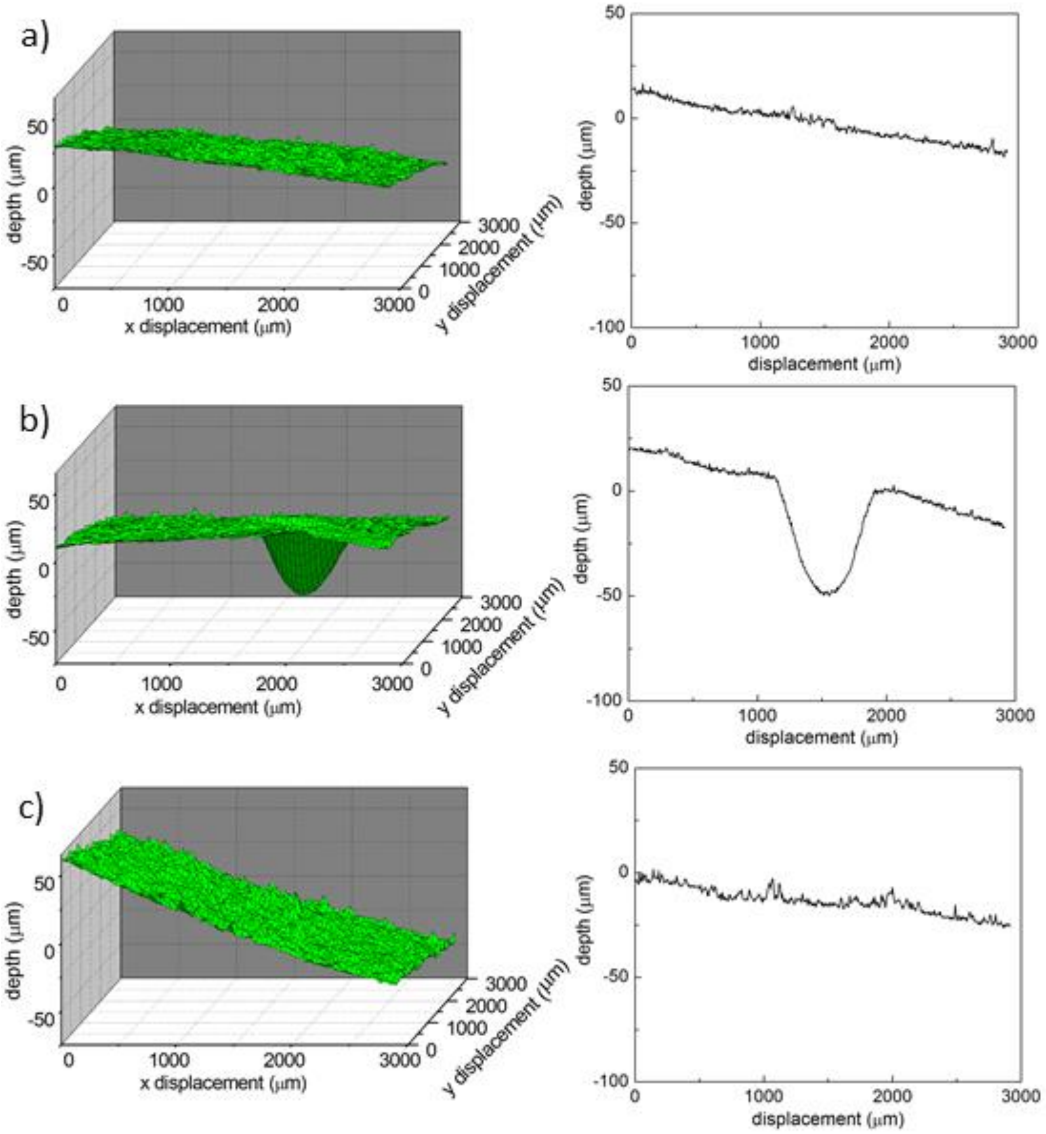

Figure 2.17. Measured surfaces (left) and profiles (right) for 5 N hole in PCO-2 sample: (a) without hole, (b) hole, (c) recovered.

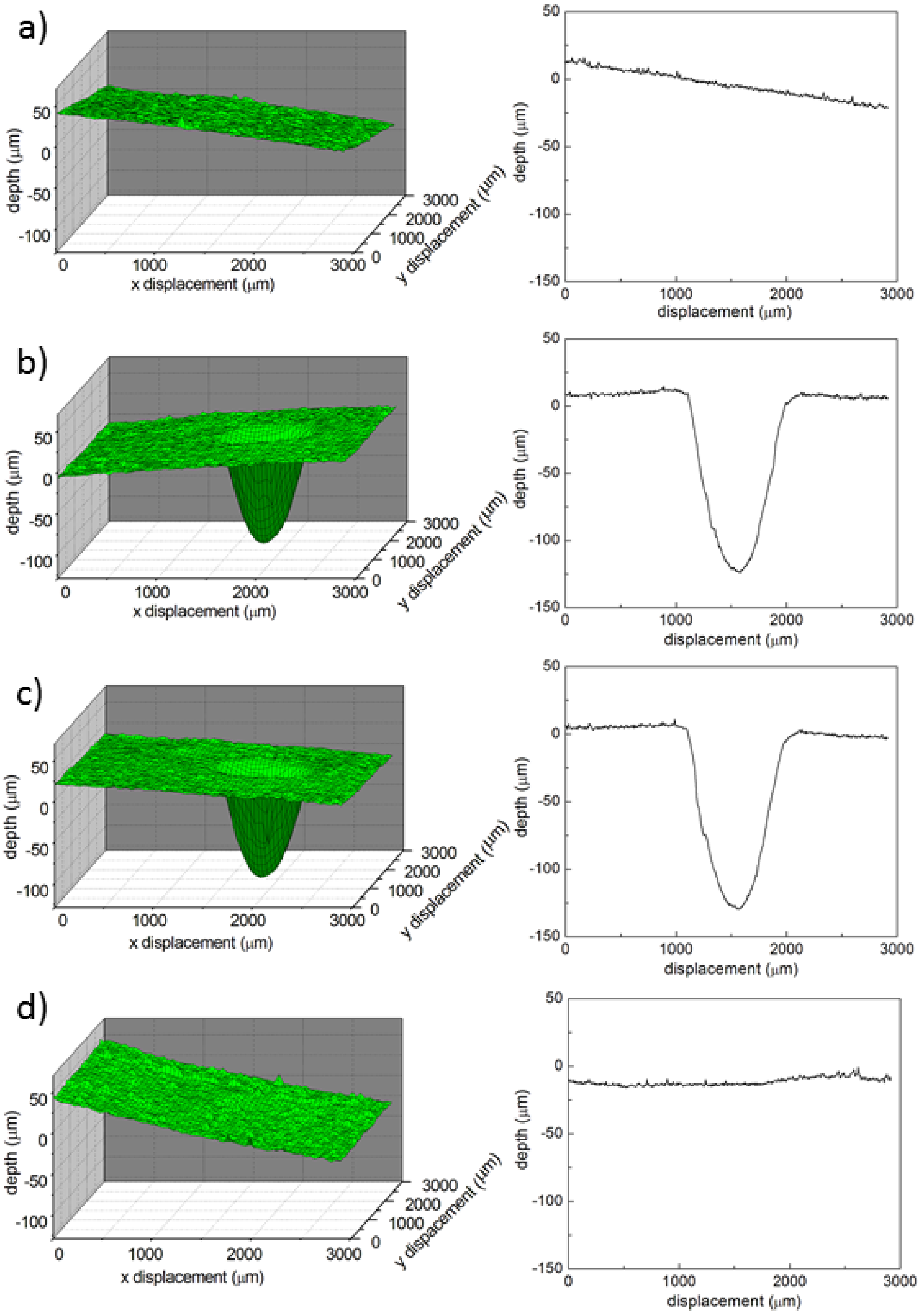

Figure 2.18. Measured surfaces (left) and profiles (right) for 10 N hole in PCO-2 sample: (a) without hole, (b) hole, (c) measure 24 h later and (d) recovered.

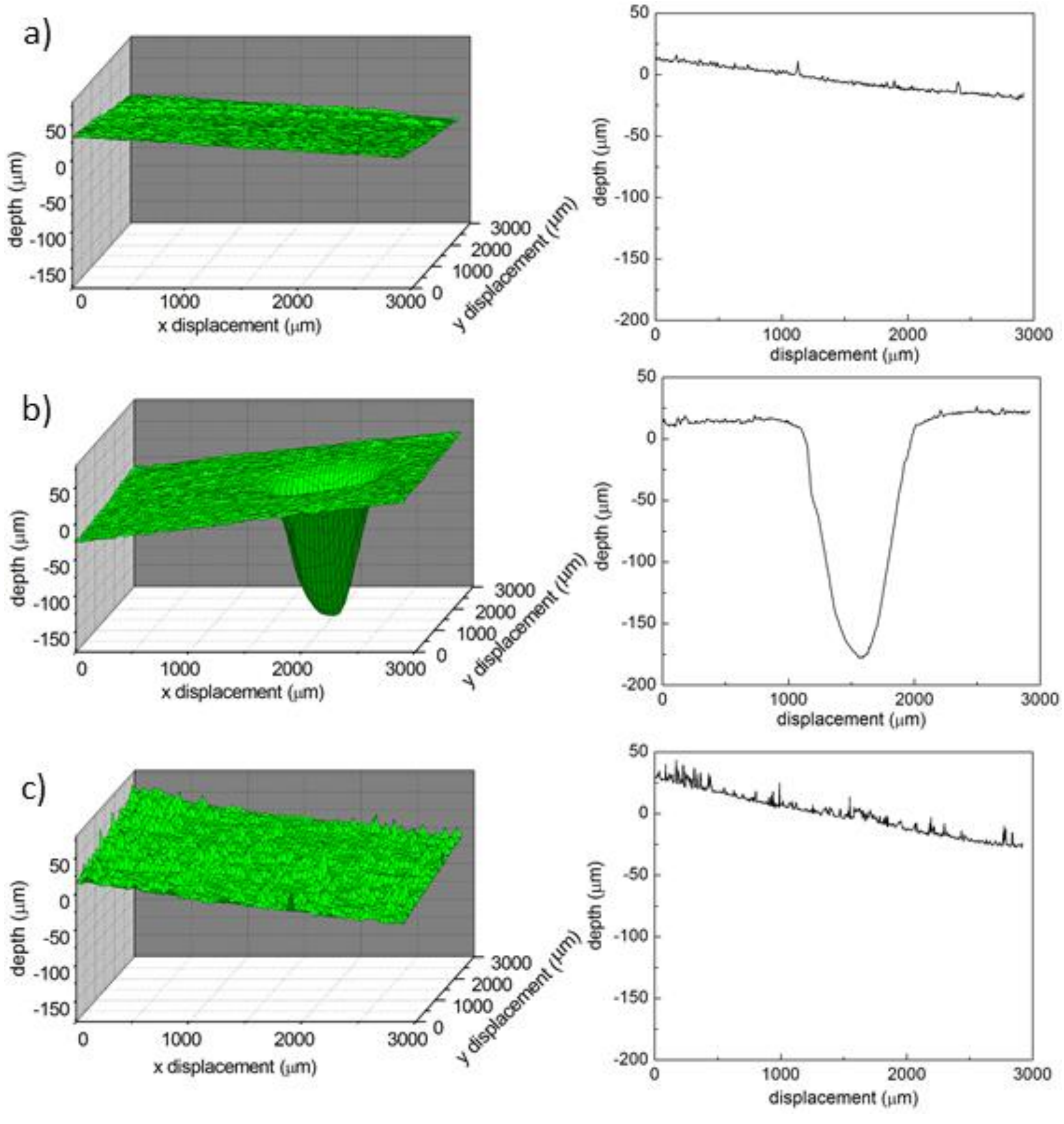

Figure 2.19. Measured surfaces (left) and profiles (right) for 15 N hole in PCO-2 sample: (a) without hole, (b) hole, (c) recovered.

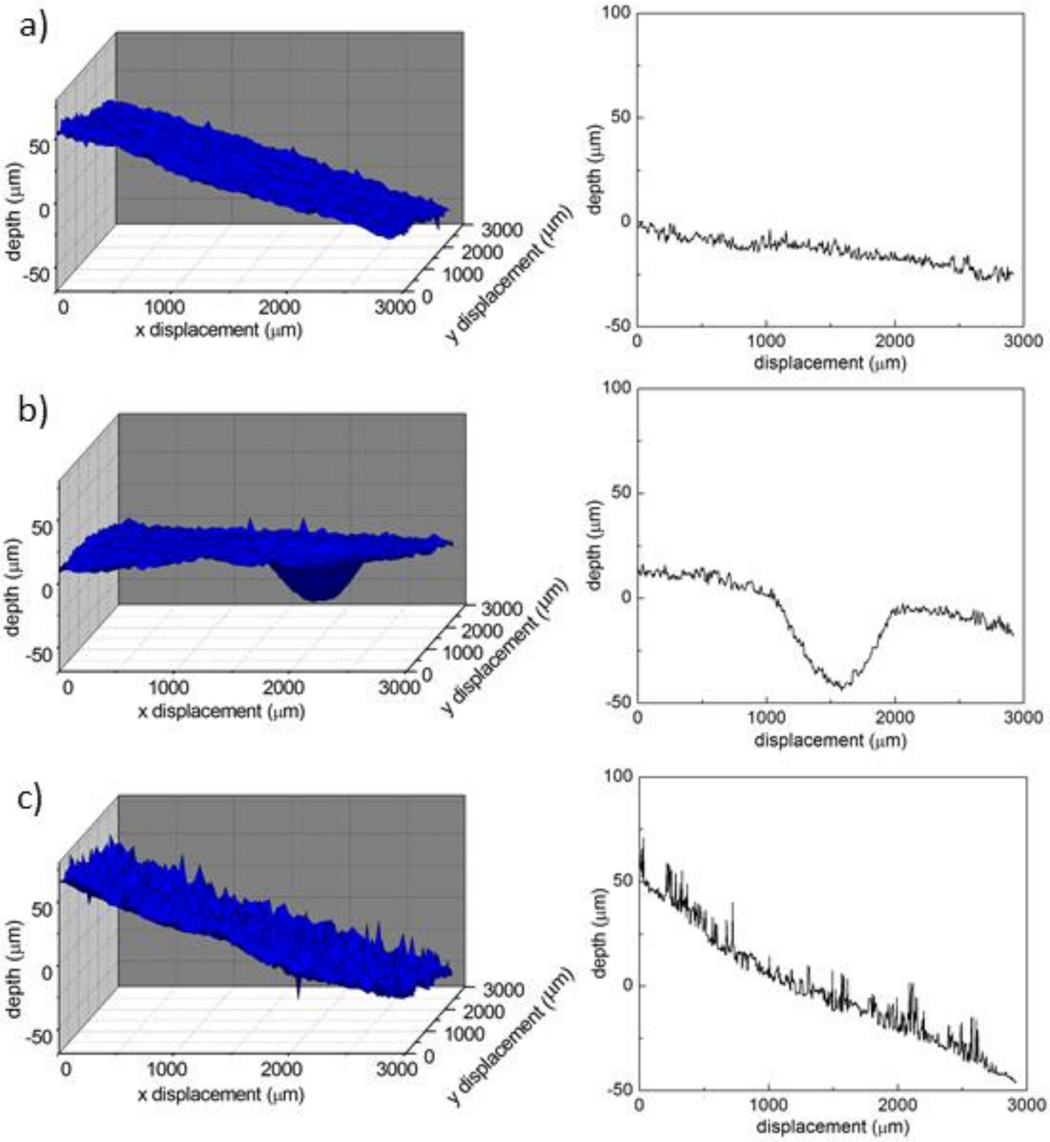

Figure 2.20. Measured surfaces (left) and profiles (right) for 5 N hole in PCO-3 sample: (a) without hole, (b) hole, (c) recovered.

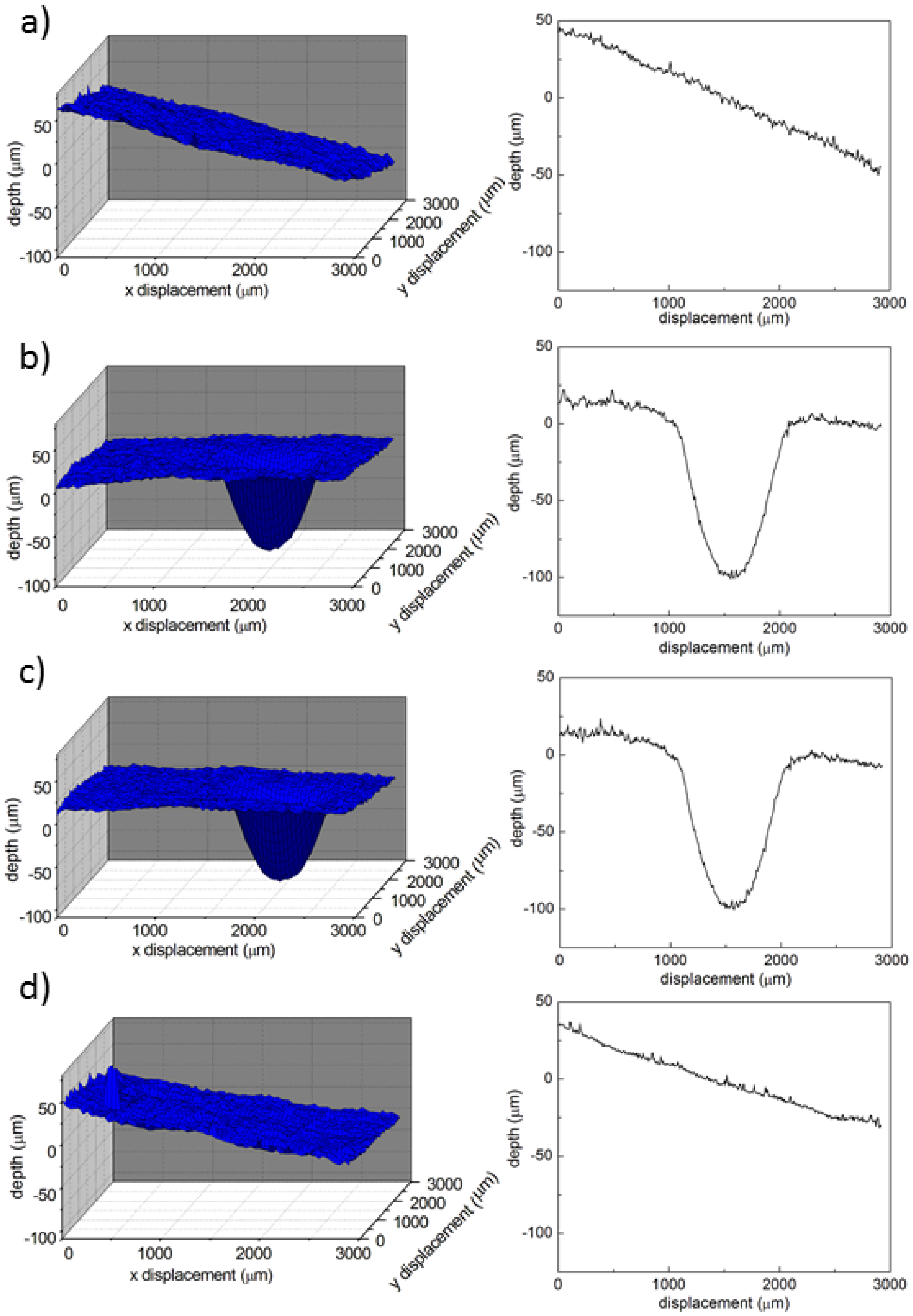

Figure 2.21. Measured surfaces (left) and profiles (right) for 10 N hole in PCO-3 sample: (a) without hole, (b) hole, (c) measure 24 h later and (d) recovered.

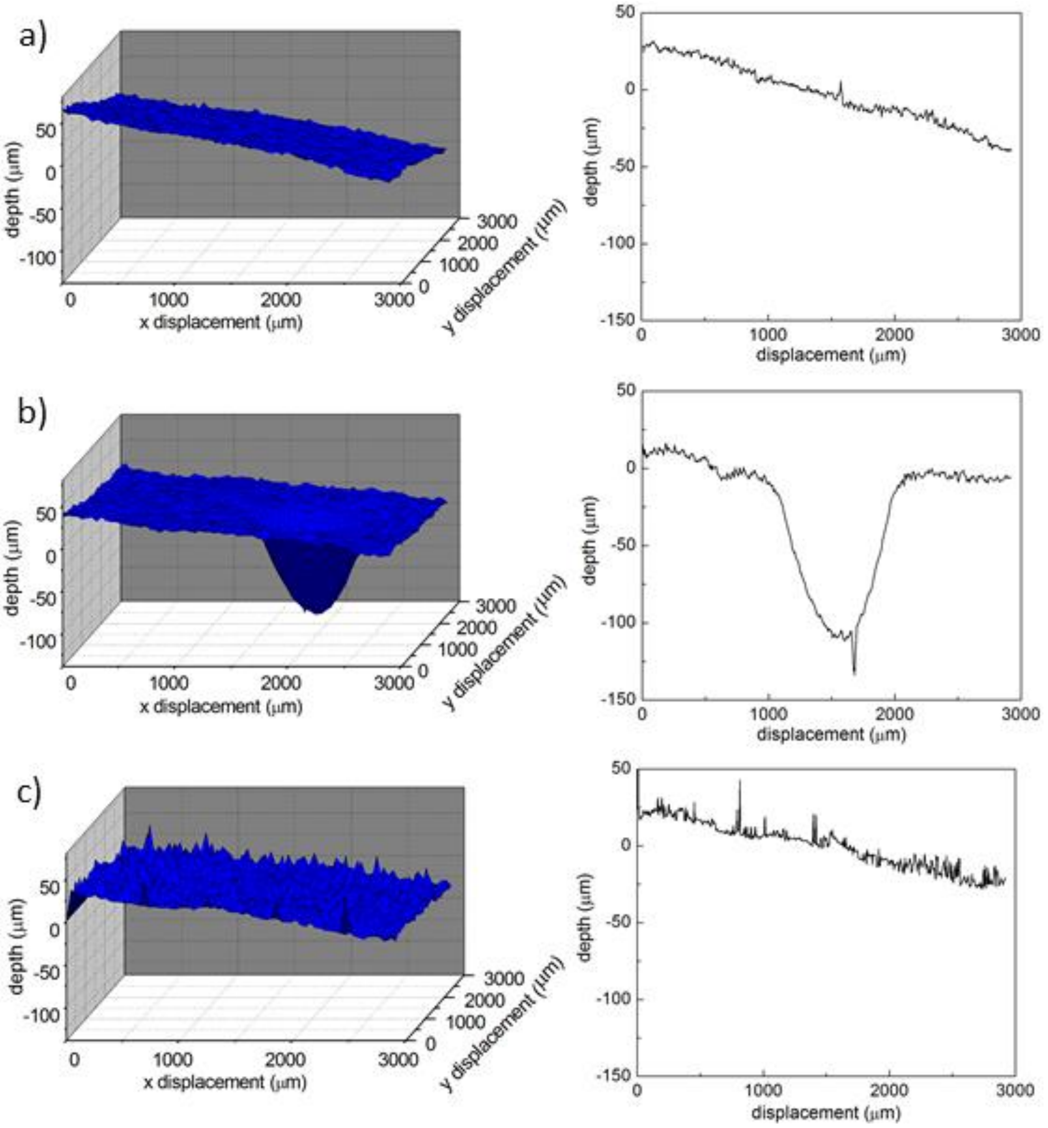

Figure 2.22. Measured surfaces (left) and profiles (right) for 15 N hole in PCO-3 sample: (a) without hole, (b) hole, (c) recovered.

The depth values obtained by the two techniques (profilometry and confocal microscopy) are very similar following the same trend, which demonstrates that indentation depth increases with applied load for all cases (Figure 2.23), and that both measurement techniques are appropriated for evaluating the subsequent self-repair behaviour.

Considering the hardness as a measurement of the resistance of the samples towards indentation, it could be expected lower indentation marks with higher hardness, as occurs for low indentation loads and related minor marking depths or deformations (Figure 2.23). However, at the same time that applied load and subsequent depth increase, this trend reverses.

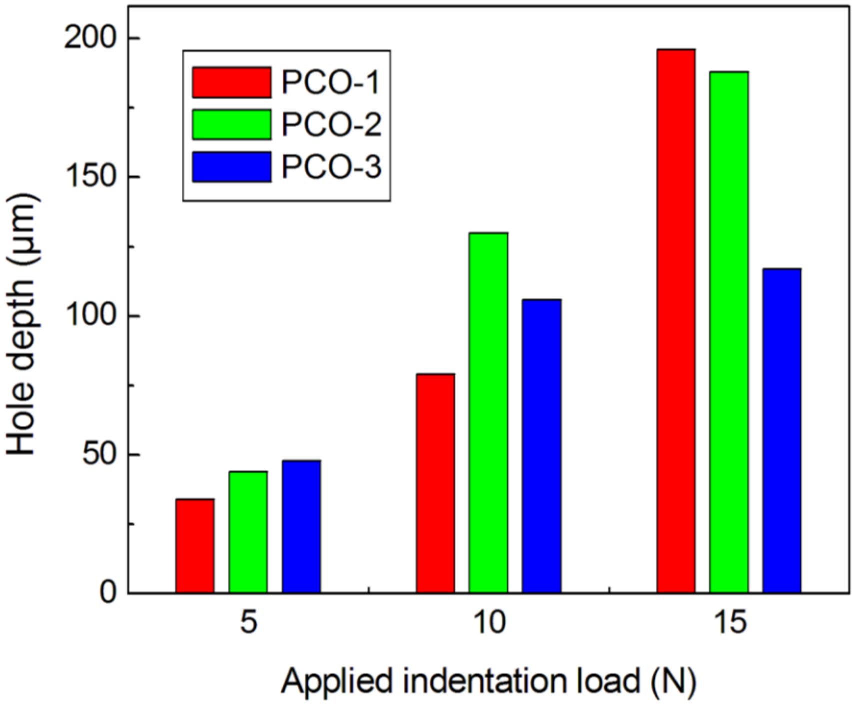

Figure 2.23. Indentation depth vs. applied load for different crosslinked samples.

In semicrystalline polymers, the relationship between morphological characteristics and hardness is extremely complex and is dependent on many variables controlled by molecular weight, chain structure, degree of crystallinity, crystalline structure, thickness distribution of crystallites, interfacial interaction with non-crystalline region and structure of amorphous phase, among others [27].

Crosslinked PCO consists of separate and mechanically distinct ‘hard’ crystalline elements and ‘soft’ amorphous regions. Therefore, when indented, the material is compressed and a complex combination of effects influences the produced local deformation, being the prevalent mechanism dependent on the strain/stress field depth round the indent and on the morphology of the polymer [26]. Therefore, it is suspected that for low strains from low-moderate applied loads, probably prior to the yield point, deformation modes and strength of crystalline phase governs the observed performance. However, as the fraction of amorphous phase increases from lower crystallinity degree, when indentation involves yielding of crystalline regions and partial destruction of surface crystallites from higher strains, intrinsic flexibility and elastic storage properties of amorphous crosslinked chains prevails. Therefore, for high loads, when the applied stress is removed, the rubber-elastic behaviour of crosslinked molecules in the amorphous phases leads to elastic recovery and relax back of a fraction of indentation strain, which is higher when DCP content increases and produces lower remaining hole depths (Figure 2.23) [26–28].

Additionally, the evolution of recovery process with temperature was monitored by optical microscopy. The employed microscope was a Nikon SMZ-2T optical microscope equipped with a CCTV camera, Jenoptik C10 Plus model. The sample was placed at room temperature on a heating plate under the microscope and series of photos of the hole were taken when temperature was increasing until recovery process was finished. Finally, the sample was slowly cooled down to room temperature. Variations in the brightness in photos come from melting process of crystallites and turning the samples into transparent. Nevertheless, when cooled down they return to original translucent white colour. Figure 2.24, Figure 2.25 and Figure 2.26 show the evolution of the 10 N hole with temperature for the PCO-1, PCO-2 and PCO-3 samples, respectively, assessing surface-repairing features from the shape memory properties of this kind of SMPs.

In parallel, in order to evaluate the shape recovery ratios faced to temperature, the variation in the hole depths were measured following the recovery phase under heating process of perpendicular cuts of the performed holes on replicas by optical microscopy. The recovery process for the 10 N hole in the three crosslinked samples can be appreciate in Figure 2.27, Figure 2.28 and Figure 2.29.

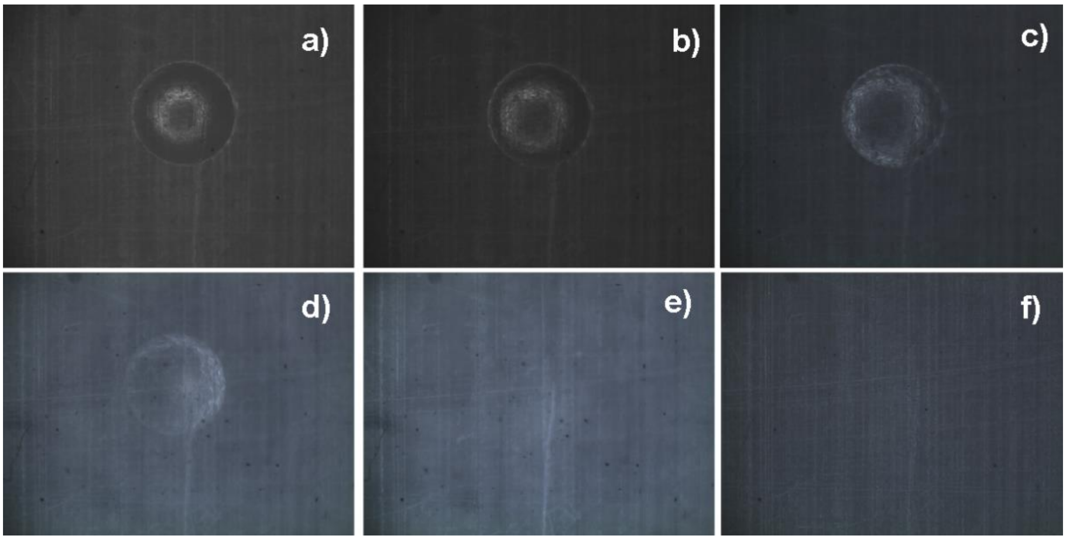

Figure 2.24. Recovery process for 10 N hole in PCO-1 at: (a) 22.9 ºC, (b) 36 ºC, (c) 43 ºC, (d) 46 ºC, (e) 51 ºC, (f) cooled (recovered).

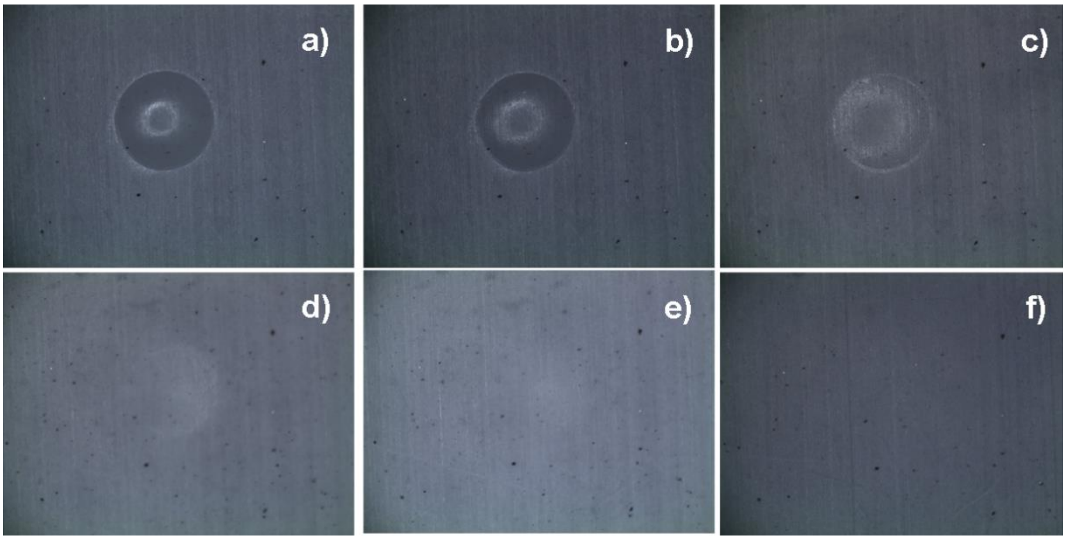

Figure 2.25. Recovery process for 10 N hole in PCO-2 at: (a) 23.8 ºC, (b) 32 ºC, (c) 37 ºC, (d) 41 ºC, (e) 43 ºC, (f) cooled (recovered).

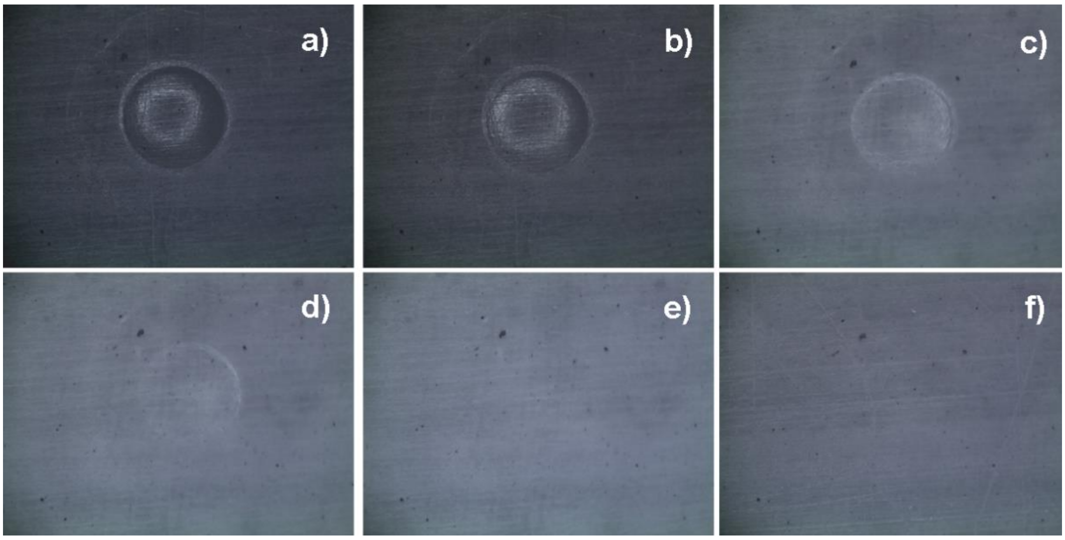

Figure 2.26. Recovery process for 10 N hole in PCO-3 at: (a) 23.9 ºC, (b) 29 ºC, (c) 33 ºC, (d) 35 ºC, (e) 37 ºC, (f) cooled (recovered).

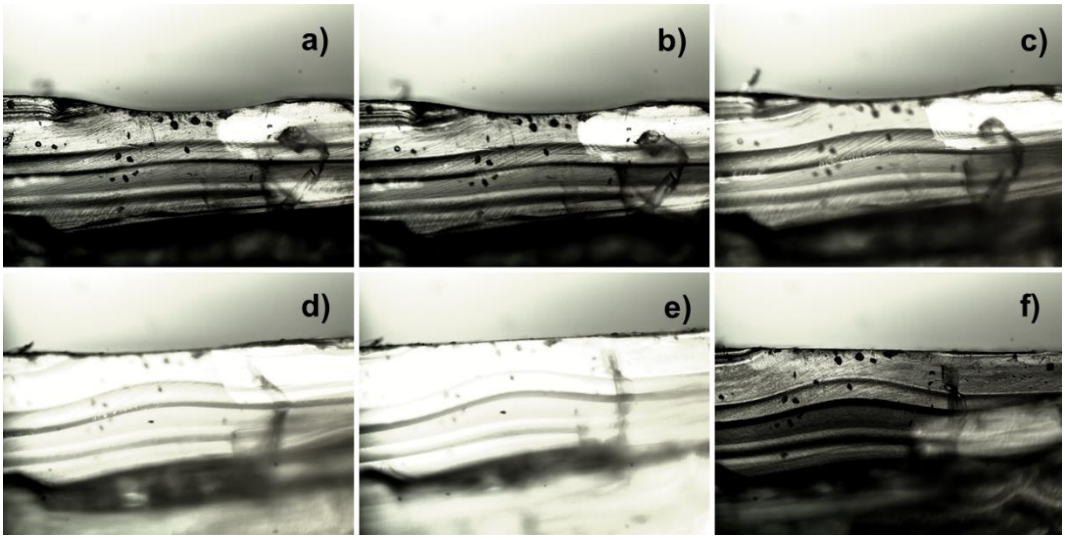

Figure 2.27. Edgewise view of the recovery process for 10 N hole in PCO-1 at: (a) 24.2 ºC, (b) 38 ºC, (c) 45 ºC, (d) 49 ºC, (e) 52 ºC, (f) cooled (recovered).

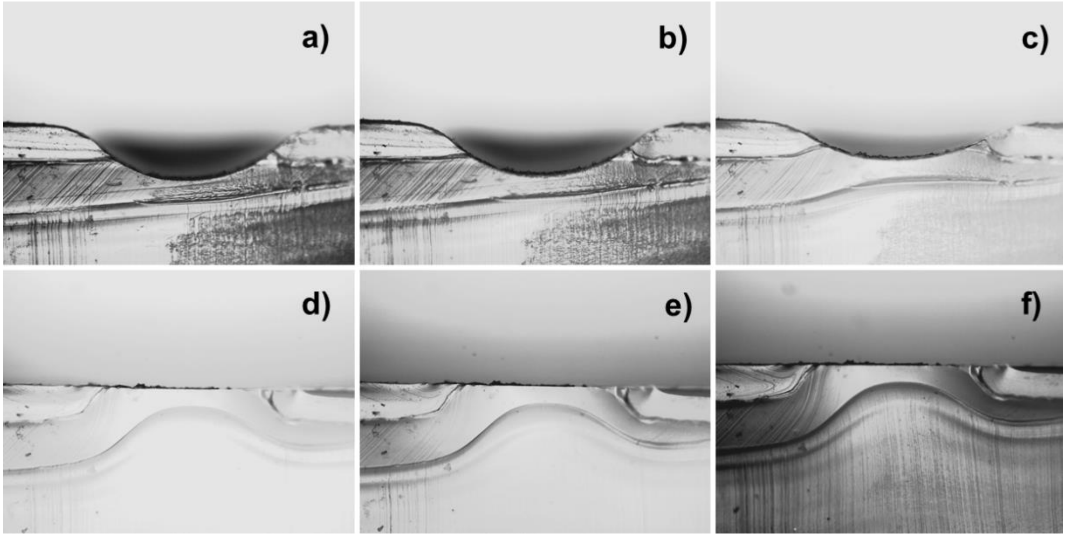

Figure 2.28. Edgewise view of the recovery process for 10 N hole in PCO-2 at: (a) 24 ºC, (b) 31 ºC, (c) 36 ºC, (d) 42 ºC, (e) 44 ºC, (f) cooled (recovered).

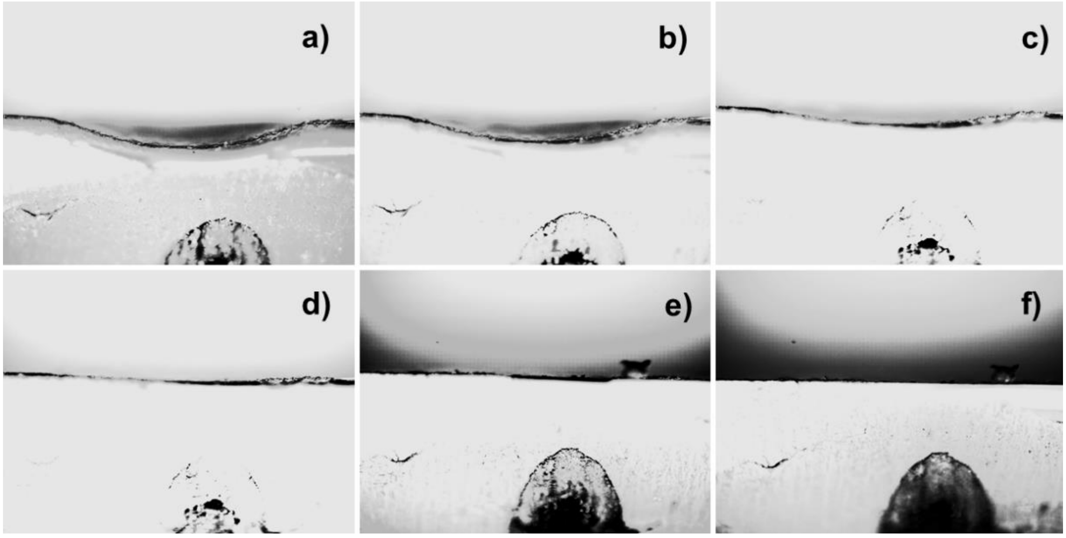

Figure 2.29. Edgewise view of the recovery process for 10 N hole in PCO-3 at: (a) 22.9 ºC, (b) 30 ºC, (c) 33 ºC, (d) 35 ºC, (e) 40 ºC, (f) cooled (recovered).

Furthermore, the respective shape recoveries with temperature, calculated by equation 2.2, are represented in Figure 2.30, where it can be observed the described shape recovery ratios of 100%.

$$recovery\,\% = (D_T - D_0)/D_0 \times 100$$

$$\{D_0 = initial\ depth;\ D_T = depth\ at\ each\ temperature\} \tag{2.2}$$

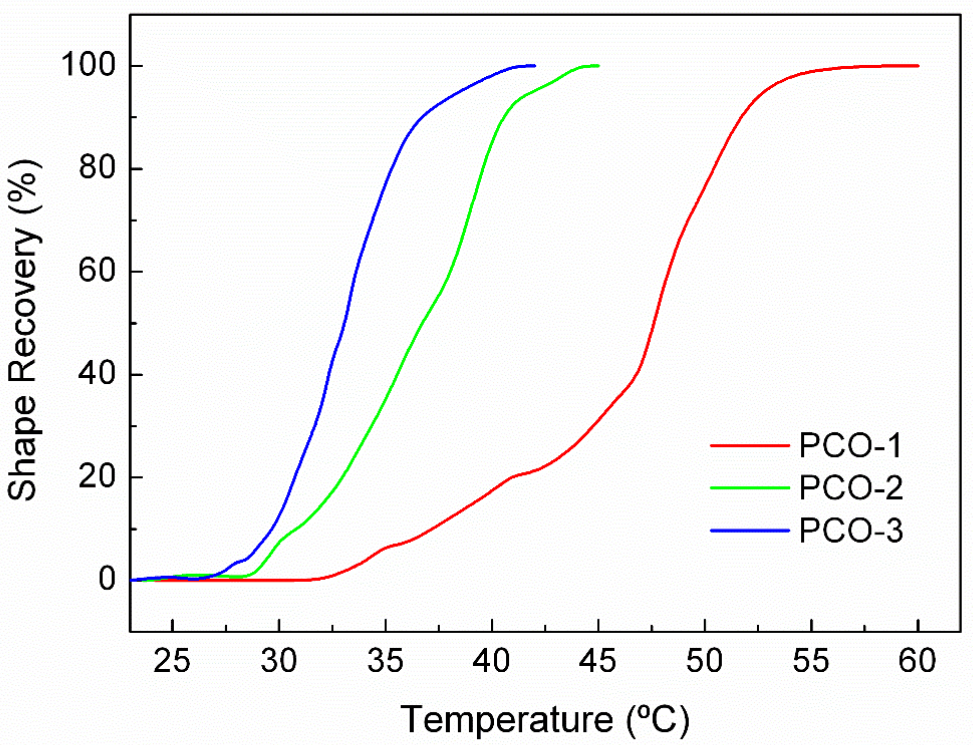

Figure 2.30. Shape recovery with temperature.

b. Line marks

Moreover, another test was effectuated by performing 30 mm line marks in PCO samples at a rate of approximately 10 mm·sec^{-1} with each force (5, 10 and 15 N) using the same Hardness Test Pencil. Measurements were made with the surface profilometer, again, before and after marking, 24 hours later and after heating the sample in an oven during 10 minutes at approximately 20 ºC above its melting temperature (T_{rec} in Table 2.2) and cooling down.

Self-repair of the scratch-marked samples was demonstrated by surface profilometry (both measuring techniques were demonstrated as suitable tools for evaluation and it is faster and easier to use than confocal microscopy).

Figure 2.31 to Figure 2.34 shows the profiles measured with the profilometry technique for all the PCO samples (PCO without crosslink and PCO crosslinked with different amounts of DCP) when they are line-marked. As can been observed in Figure 2.31, the PCO-0 sample has no shape memory properties, as well as losses dimensional stability from null crosslinking preventing specimens from flowing like a viscous liquid. However, in Figure 2.32, Figure 2.33 and Figure 2.34, it can be seen that the sample with covalent bonds in polymer network is characterized by shape memory features and subsequent exhibited self-repairing properties.

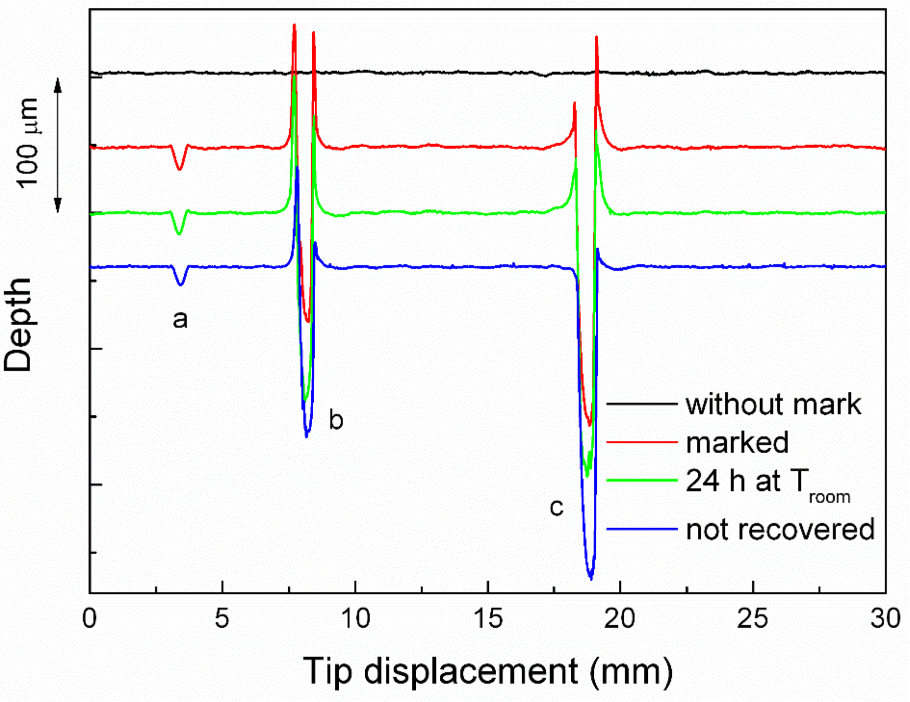

Figure 2.31. Measured profiles for PCO-0 sample for (a) 5 N, (b) 10 N and (c) 15 N lines.

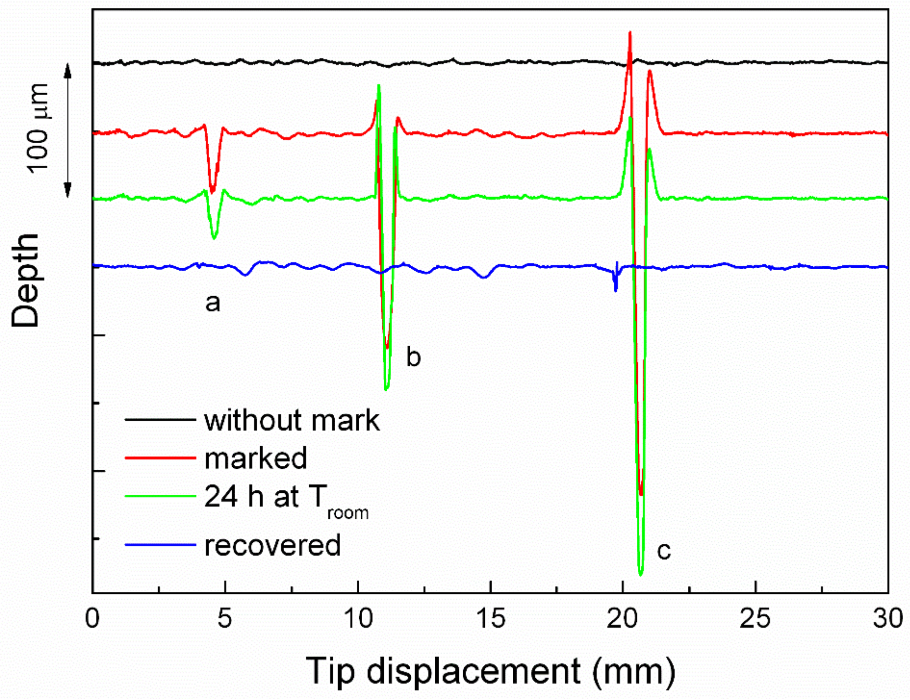

Figure 2.32. Measured profiles for PCO-1 sample for (a) 5 N, (b) 10 N and (c) 15 N lines.

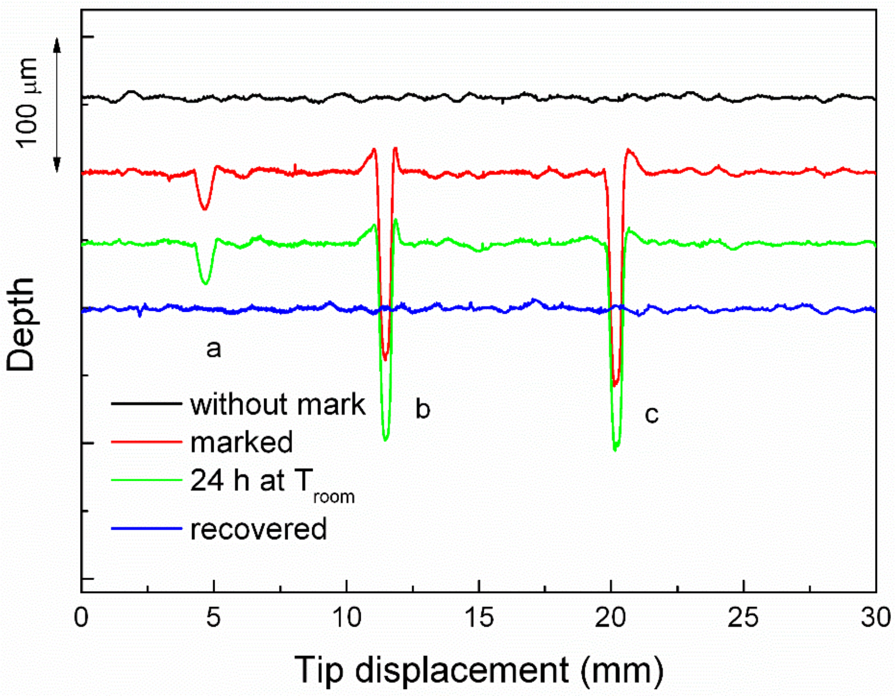

Figure 2.33. Measured profiles for PCO-2 sample for (a) 5 N, (b) 10 N and (c) 15 N lines.

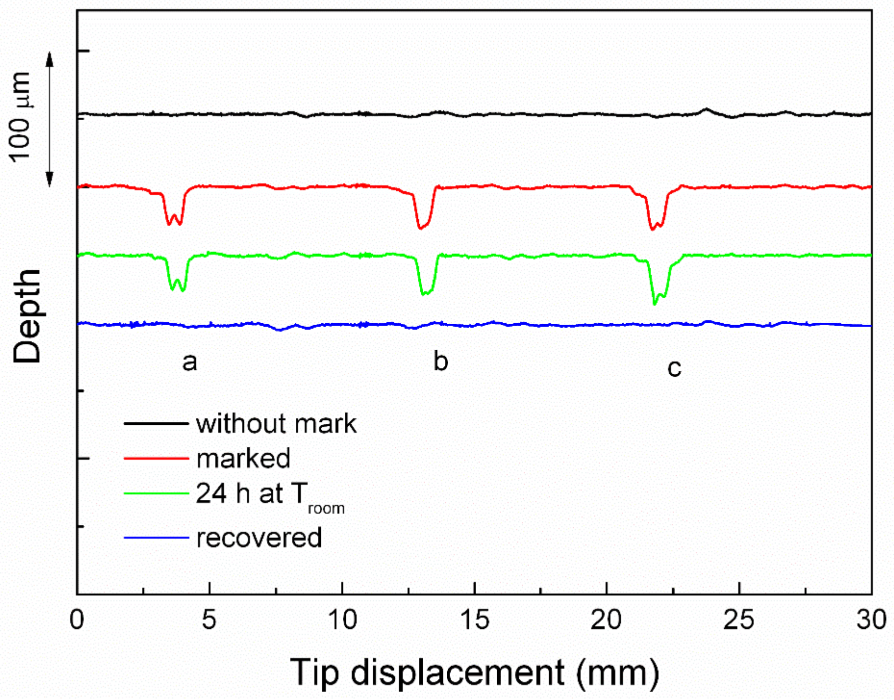

Figure 2.34. Measured profiles for PCO-3 sample for (a) 5 N, (b) 10 N and (c) 15 N lines.

Additionally, the original sample, the sample after mark and the sample after the heat treatment is shown in Figure 2.35 for the non-crosslinked sample (PCO-0) and in Figure 2.36 for a crosslinked one (PCO-2). Here is clear that the sample with shape memory properties is capable of recover its original shape (the surface is recovered by means of shape memory effect), whereas in the sample without peroxide the marks remain after the heat treatment (no shape memory effect and no recovery properties).

In conclusion, when the PCO-DCP crosslinked samples were heated above its transition temperature the surface defects disappear (holes or lines/scratches), which demonstrates the potential self-repair response under temperature of these new polymeric materials, based on their shape memory behaviour, with functional or aesthetic applications.

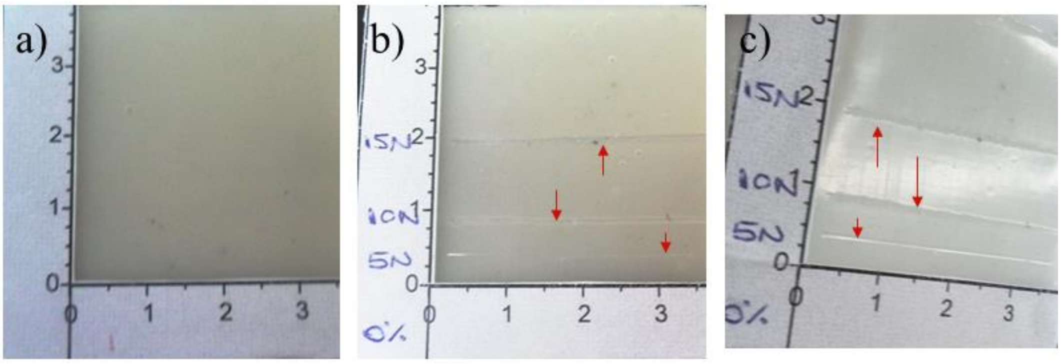

Figure 2.35. PCO-0 sample: a) original; b) marked; c) after heat treatment.

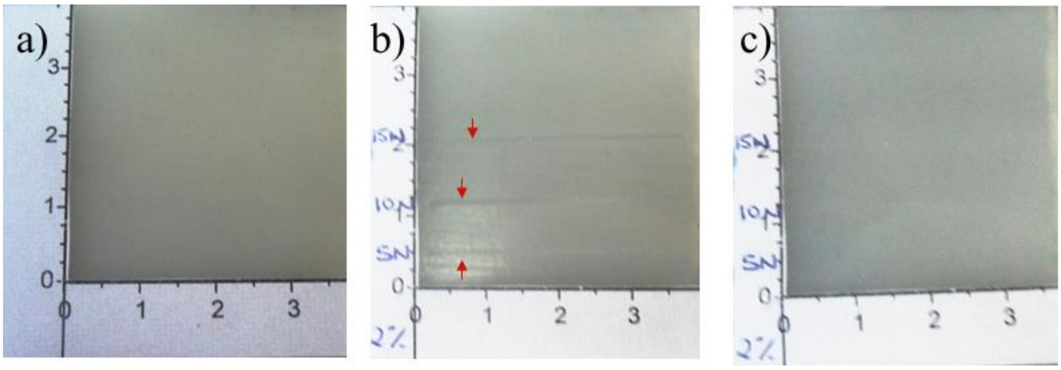

Figure 2.36. PCO-2 sample: a) original; b) marked; c) after heat treatment.

2.1.5. Conclusions

Thermal-activated self-repair features of a series of crosslinked PCO samples were demonstrated by evaluating the recovery of plastic deformations performed with different indentation and scratching forces. The correlation of the influence of crosslinking density on thermal properties of these shape memory semi-crystalline polymers with thermal-induced surface self-repairing was evaluated. Thus, different marking processes and recovery features were monitored by surface and optical-confocal profilometry, together with optical microscopy, to demonstrate potential applications of this smart performance in, for example, aesthetic or functional related purposes, apart from other temperature-sensing elements.

2.2. Polymeric shape memory micropillars

2.2.1. Introduction

Micro-/nano-topography on surfaces has an outstanding effect on wetting regimes, as it is described by different models dealing with the wettability of patterned surfaces by considering topography [29–32]. For the last years, this approach based on structured surfaces has been used for tailor-made wetting regimes in order to create superhydrophobic, superhydrophilic or superolephobic surfaces, among others [33–35]. Moreover, it is well known that both surface chemistry and surface topography play an important role on the wettability of a material [36], and it can be modified by applying an external stimulus.

Attending to responsive surface chemistry, it can be found light-induced and pH-responsive surfaces. For example, polymers containing acid or basic functional groups (such as amine and carboxyl groups) usually exhibit pH-responsive wetting behaviour [37] because their morphologies and/or charges are dramatically influenced by the pH of solution. Among the light-induced surfaces, azobenzene derivatives are very representative, where the wettability varies in presence of light thanks to a *cis–trans* transformation [38,39]. Additionally, these type of materials have been employed to cover a patterned surface in order to obtain superhydrophobic surfaces using light as stimulus [40].

Concerning active surface topography, some examples of patterned surfaces from shape memory polymers by replica moulding can be found [41–47] where the recoverability of the patterned structure after being deformed has been demonstrated. Thereby, Xu *et al.* [41] used a semi-crystalline shape memory elastomer to obtain deformable, programmable, and shape-memorizing micro-optical devices. Some authors studied the adhesion properties evaluating it in the different stages of the shape memory process [42–44]. For example, Reddy *et al.* [43] employed a thermoplastic elastomer with thermal shape memory properties to fabricate a switchable adhesive surface. Other authors [45–47] studied if the differences in the wettability of the original and deformed states can be appreciated.

For example, Chen and Yang [45] fabricated recoverable tilted pillars from shape memory polymers (an epoxy resin) by replica moulding in order to manipulate the surface wettability for potential applications such as directional water shedding and collection.

In this chapter, micropillars based surface structure on crosslinked PCO were designed by laser ablation [48], and interesting variations in water contact angles were observed by means of shape memory features of the PCO micropillars under heating, as seen in Figure 2.37. Thus, laser ablation allows fabricating this kind of responsive periodic patterns with high accuracy and reproducibility over large areas, and its combination with handily developed shape memory surface means a broadly applicable and flexible tool to manipulate wettability by heating for platforms where control of fluids is a key facet.

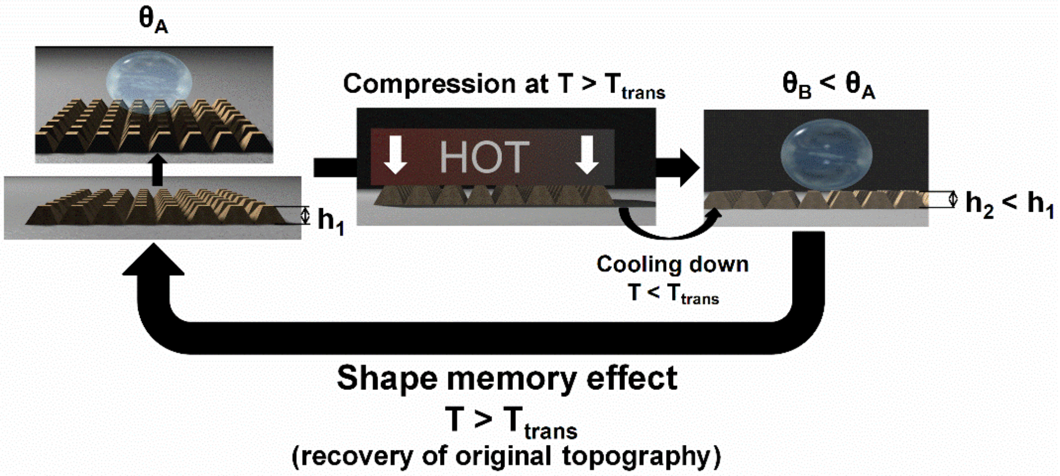

Figure 2.37. Schematic illustration of switching wettability from thermally induced surface shape memory recovery (from water contact angle θ_A to θ_B by compression, and recovery of the original θ_A by heating).

2.2.2. Materials

2.2.2.1. Polycyclooctene (PCO)

The employed polycyclooctene is the commercial PCO from Evonik, explained at section 2.1.2.1.

2.2.2.2. Dicumyl peroxide (DCP)

The dicumyl peroxide used was the same aforementioned at section 2.1.2.1.

2.2.3. Preparation of the sample

Polycyclooctene (PCO) and 2 wt % dicumyl peroxide (DCP) were blended as explained in section 2.1.3 in a Haake Rheomix 600 mixing chamber at 70 ºC. Subsequently, the samples were crosslinked at 160 ºC for 20 min by compression moulding under a pressure of 100 bar in a 1.5 mm thickness flat mould coated with two Teflon sheets to reduce the roughness of the specimens. After curing, the 50 mm × 50 mm × 1.5 mm specimens were cooled down to room temperature in the mould under constant pressure.

Micropillars on crosslinked PCO were manufactured by means of ultrashort pulse laser microprocessing. Femtosecond laser pulses were generated by a Ti:Sapphire oscillator-regenerative amplifier system (1 kHz, 4.0 mJ, 35 fs pulses at 800 nm, Coherent Inc.). The pulse energy is controlled with a variable neutral density filter in the 1-40 µJ range. The light is focused onto the sample, which is mounted in a computer controlled 3D translation stage (1 µm precision, Thorlabs) at atmospheric pressure, using a fused silica lens (f = 150 mm). The diameter of the spot (FW1/e^2M) is 40 µm. A nozzle injecting pressurized dry air was placed next to specimens to remove debris. A demonstrative 1 cm^2 surface was structured using 10 µJ/pulse energy and a scanning speed of 0.25 mm/s. In particular, a pattern of lines in two perpendicular directions was generated, with an interval between lines of 46 µm (Figure 2.38).

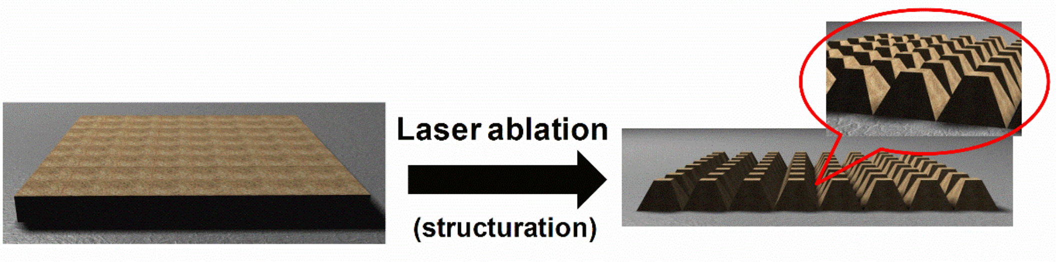

Figure 2.38. Structuration forming micropillars by laser ablation.

2.2.4. Experimental section

2.2.4.1. Dynamic Mechanical Thermal Analysis

Dynamic Mechanical Thermal Analysis (DMTA) allows obtaining characteristic temperatures of polymers such as glass transition temperature, T_g, and melting temperature, T_m. DMTA was performed in tension mode using a DMA-1 from Mettler Toledo. A rectangular sample with a cross-section area of 4 mm x 1.5 mm and initial clamps distance of 10 mm was directly cut from the PCO + 2%DCP sheet and measured from −100 to 80 ºC, at a deformation frequency of 10 Hz, a strain of 100 µm and a heating rate of 2 ºC min^{-1}.

Figure 2.39 shows both the storage modulus (E') and the loss factor ($\tan\delta = E''/E'$) measured for that sample. It can be observed that initially the polymer is in the glassy state at −100 ºC, showing high values of storage modulus and low values of $\tan\delta$. As the temperature increases, the storage modulus decreases progressively and a peak appears in $\tan\delta$ at −50 ºC, which corresponds to T_g. Once T_g has been overcome, at temperatures near to the melting transition, the storage modulus decreases sharply, whereas $\tan\delta$ increases reaching a *plateau* due to the crosslinks in the PCO + 2%DCP preventing the sample to flow like a viscous liquid.

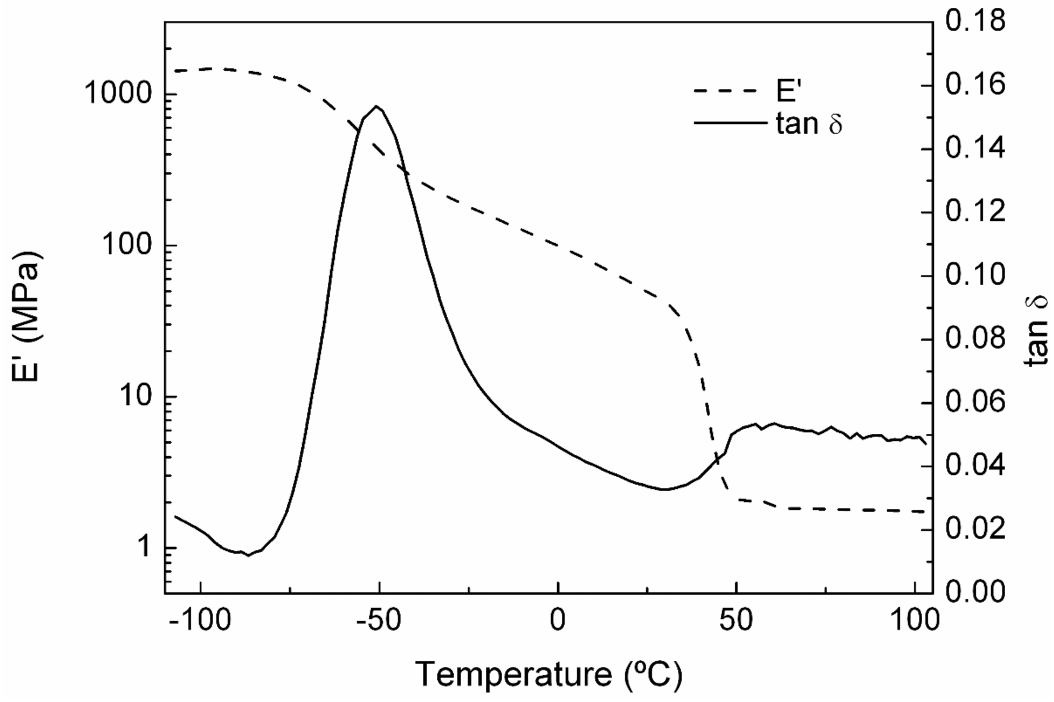

Figure 2.39. Evolution of tanδ and E' with temperature for PCO+2%DCP sample.

2.2.4.2. Cyclic Thermomechanical Shape Memory Properties

As PCO is a thermally induced shape memory polymer, where the transition temperature corresponds with the melting temperature (T_m), a cyclic thermomechanical experiment was designed in the stress-controlled mode according to Garle *et al.* [49] in order to evaluate the shape memory behaviour.

For thermomechanical analysis (TMA), samples shaped as strips (width = 4 mm, thickness = 1.5 mm and free length = 10 mm) cut from the PCO + 2%DCP sheet were employed. TMA was also conducted in tension mode on the DMA-1 from Mettler Toledo in the temperature range of −10 to 80 ºC at a heating rate of 4 ºC min^{-1}. This temperature range was selected according to the melting temperature of the sample, calculated from calorimetric analysis and equal to 42.0 ºC, as it is listed in Table 2.2. TMA measurements were made following the procedure depicted at Figure 2.40, where the increase of the sample length was recorded as a function of temperature. Previously, the sample was heated without force to 80 ºC in order to allow relaxation of the polymer chains, so initial conditions were fixed (sample dimensions and temperature).

The different performed experiments can be appreciate in Table 2.4, were deformation force or cooling rate were modified in order to study how these parameters affect the fixation of the temporary shape.

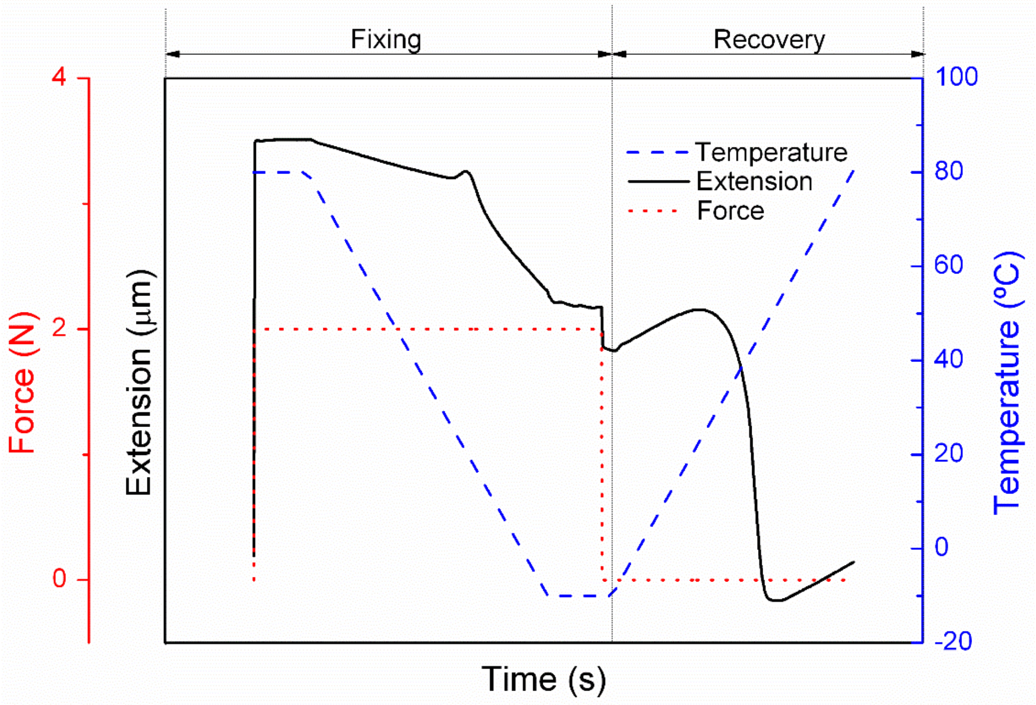

Figure 2.40. Procedure of the cyclic thermomechanical experiment: extension, temperature and force.

Table 2.4. Experimental conditions to perform shape memory experiments in bulk material.

Experiment	Force (N)	Cooling rate (ºC/min)	Heating rate (ºC/min)
1	1	4	4
2	2	4	4
3	2.5	4	4
4	2.5	20	4

Shape fixity ratio (R_f) and shape recovery ratio (R_r) for all performed experiments were calculated according to equations 2.3 and 2.4, and the obtained values are listed in Table 2.5. In Figure 2.41, several thermomechanical cycles for PCO+2%DCP sample are represented. Here, the same cooling rate was used, 4 ºC min^{-1}, whereas the deformation force varies from 1 to 2.5 N.

$$R_f(\%) = \left(\frac{\varepsilon_u(N)}{\varepsilon_m(N)}\right) \times 100 \tag{2.3}$$

$$R_r(\%) = \left(\frac{\varepsilon_m(N) - \varepsilon_p(N)}{\varepsilon_m(N) - \varepsilon_p(N-1)}\right) \times 100 \tag{2.4}$$

Table 2.5. Shape fixity and shape recovery ratios for a PCO+2%DCP sample tested at different conditions.

Experiment	R_f (%)	R_r (%)
1	-	100
2	50.6	100
3	65.0	100
4	71.2	100

Thermomechanical cycles demonstrate that higher tensile force involves higher deformation (240 μm for 1 N, 479 μm for 2 N and 604 μm for 2.5 N). The PCO+2%DCP sample was also tested to 3 N but the deformation obtained with this force exceeded the measurement limit of the equipment (1 mm).

After maintaining the stress for 5 min at 80 ºC, the sample is cooled down under the same deformation force and shrinkage occurs. It can be observed that too low fixing force (1 N) cannot counteract the contraction stress under cooling (R_f< 0), which causes the almost total recovery of original dimensions (0.8% shorter probably from thermal history) before thermal fixing. Therefore, as deformation force increases (2 N and 2.5 N), this one counteracts more efficiently the shrinkage stress and the fixing ratio increases with the applied force.

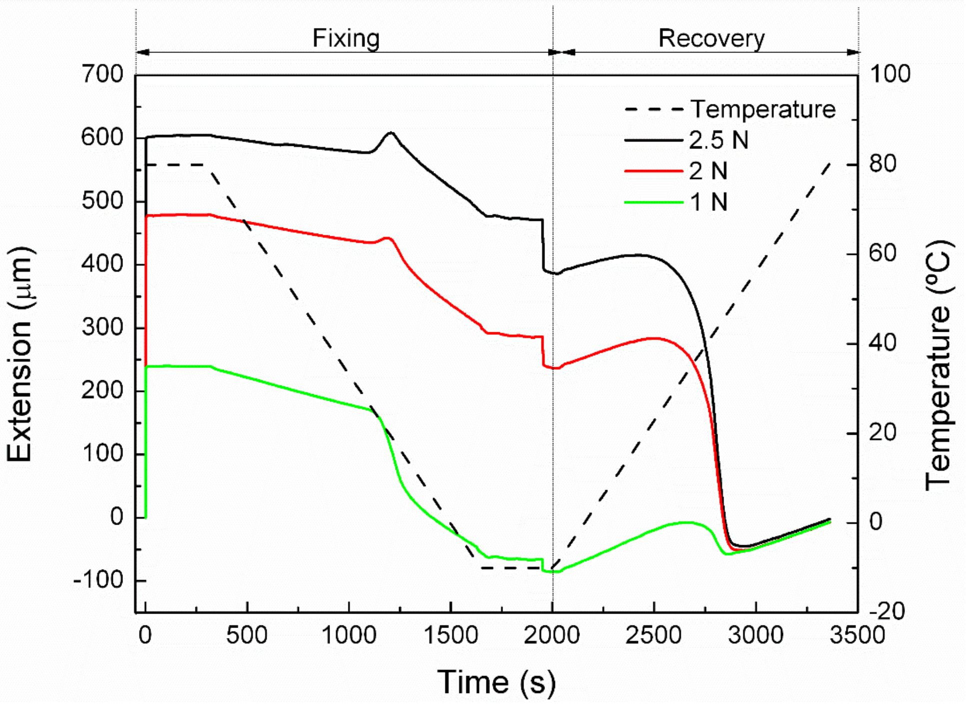

Figure 2.41. Cyclic thermomechanical response of PCO+2%DCP sample elongated at different forces.

When the sample is kept at −10 ºC for 5 min the deformation stabilizes, stress is removed (leading to springback of the specimen) and temporary shape is fixed (about 1960 s), where higher fixation ratio is observed from increased deformation force. It can be observed that at higher force of deformation, higher is the fixation (R_f with 2 N force = 50.6% and R_f with 2.5 N force = 65.0%, as seen in Table 2.5).

Finally, the sample is maintained stress-free at -10 ºC for 1 min before the recovery process begins by heating the PCO + 2%DCP sample to 80 ºC, so when temperature reaches T_m, the recovery process takes place and the primary shape is recovered. In all cases, independently of the applied force and thus the generated deformation, the recovery is total.

Therefore, the most remarkable difference between the thermomechanical curves with different tensile forces (1, 2 and 2.5 N) lies in the achieved fixing ratio from higher counteracting shrinkage stress in cooling by higher force (2.5 N). Once the effect of deformation force on the shape memory behavior is analyzed, the next step is to study how the cooling rate affects the fixation process and therefore the shape memory capabilities of the PCO + 2%DCP sample.

Therefore, a new thermomechanical cycle is performed by deforming the sample with 2.5 N (maximum deformation and fixing capacity) and cooling at 20 °C min^{-1}. Figure 2.42 compares the two thermomechanical curves with the two different used cooling rates, 4 and 20 °C min^{-1}, respectively.

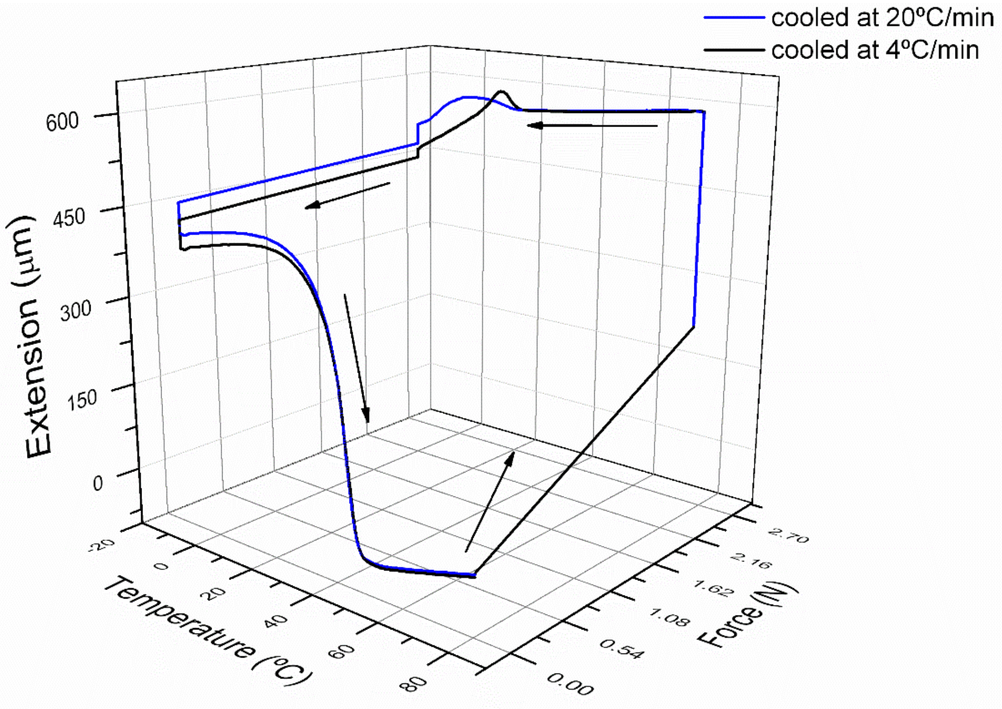

Figure 2.42. Thermomechanical cycle of PCO+2%DCP sample elongated at 2.5 N force and cooled at different rates.

It can be observed that the two samples elongate equally due to the same deformation force applied. However, when the cooling process takes place faster (20 ºC min^{-1}), the sample fixes slightly better the temporary shape, which seems to indicate that the cooling speed has little effect on shape fixity (65.0% *vs.* 71.2%, as seen in Table 2.5).

Consequently, thermomechanical cycle with a 2.5 N tensile force and 20 ºC min^{-1} cooling rate can be considered suitable experimental conditions to study the shape memory behavior of the PCO + 2%DCP sample. This thermomechanical cycle was repeated three times (Figure 2.43), and PCO + 2%DCP sample showed a good shape memory behavior, with the ability of coming back to its permanent shape several times (deformation cycles) from potential different temporary shapes.

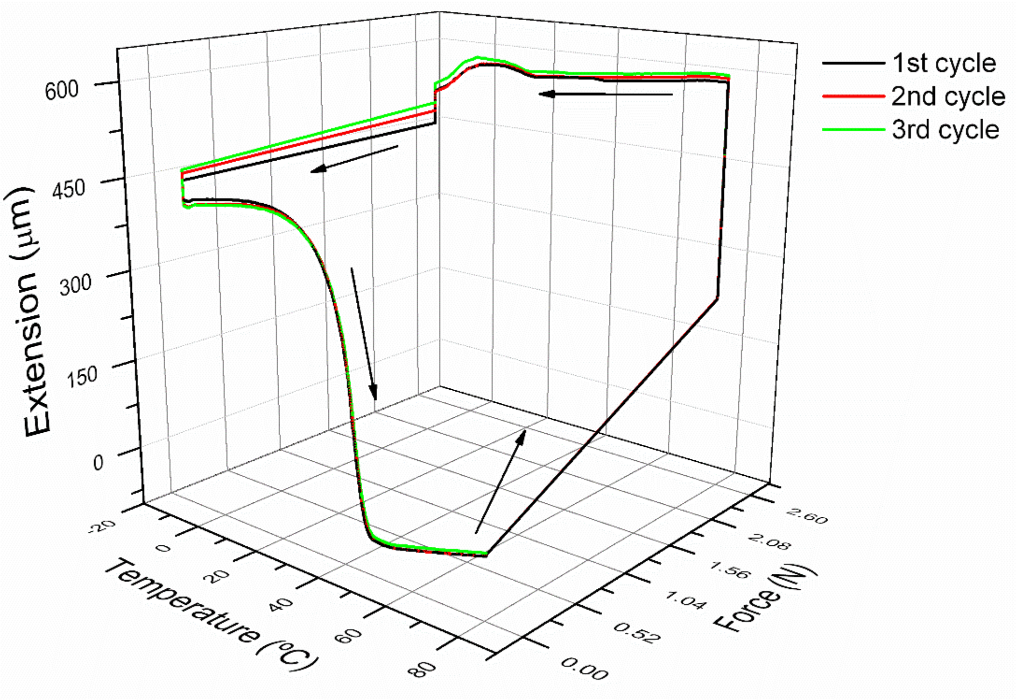

Figure 2.43. Shape memory capabilities in tension mode of PCO+2%DCP sample.

2.2.4.3. Shape Memory Micropillars

To evaluate the shape memory properties of the micropillars, it is necessary to measure the height of the micropillars by means of confocal microscopy (Leica LCS SP2 AOBS confocal microscope in reflection mode) at different stages in the deformation–fixation–recovery process: i) original micropillars, ii) deformed micropillars and iii) recovered micropillars. This procedure was performed twice (two cycles). Additionally, the wettability of the system at each step can be analysed measuring the water contact angle using a video-based optical contact angle measuring system (OCA 15EC from Dataphysics Instruments).

Previous to make the micropillars, the static water contact angle on the original unstructured PCO surface was measured as reference (Figure 2.44). All measurements were performed at room temperature with a water drop with approximately 2 µL volume, and resulted from an average of three individual measurements at different positions on the specimen. The different experimental data (water contact angle and height measurements) are summarized in Table 2.6.

Starting from a hydrophobic unstructured surface characterized by a water contact angle of θ = 95°, the achieved micro-structured surface after femtosecond laser ablation resulted in an outstanding increase of 40° in water contact angle from up to 16 µm height micropillars (Figure 2.45a). As surface analysis (3D representations and XY projections) demonstrated, the obtained micropillars were flat top pyramid-like structures with dissimilar geometry depending on the direction (Figure 2.45). Thus, the height in Table 2.6 was calculated, in all cases, in X direction.

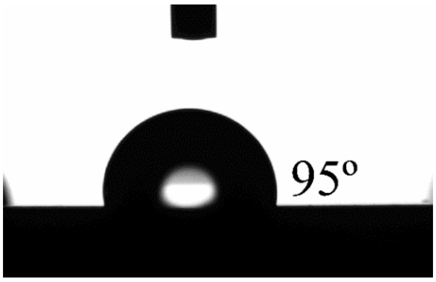

Figure 2.44. Water contact angle on unstructured crosslinked polycyclooctene surface.

Table 2.6. Height of the micropillars and contact angle on the surface of the PCO+2%DCP sample at the different steps in the shape memory process, Cycle 1 and Cycle 2.

Measured parameters	Initial	Cycle 1		Cycle 2	
		Deformed	Recovered	Deformed*	Recovered
Height (µm)	15.9±0.4	13.1±0.2	15.8±0.4	12.0±0.5	16.2±0.5
Contact angle (º)	136±1.2	124±1.2	135±0.5	120±1.0	136±1.5

***** Initial shape in the second cycle corresponds to the recovered shape from the first cycle.

In the first deformation cycle, surface micropillars were deformed by compression between two neodymium magnets with a pressure of approximately 0.6 MPa on the structured area at 100 ºC (a temperature well above T_{trans}), whereas the achieved deformation was fixed immediately by cooling down at room temperature maintaining the pressure. So, after the height of the surface micropillars dropped up to 17% as a consequence of the compression stage (Figure 2.45b), the water contact angle decreased 8.8% approximately, resulting in a less hydrophobic surface than original structured PCO (θ = 124°). Subsequently, this temporally stable less hydrophobic surface, under heating at 70 ºC (well above T_{trans}), recovers the original topography taking advantage of the shape memory properties of crosslinked PCO. Consequently, the total recovery of the original height of micropillars, from 100% recovery rate of PCO, restores the higher starting water contact angle (θ = 135°) (Figure 2.45c).

The second deformation-recovery cycle was performed in the same way (Figure 2.46), varying the deformation temperature (in the first cycle, T= 100 ºC; in the second cycle, T=130 ºC). The system was cooled until room temperature, and higher deformation was achieved resulting in micropillars 24% shorter than the original laser ablated surface and, consequently, causing a reduction in the water contact angle up to 11.1%, θ = 120° (Figure 2.46a). Once again, after heating the sample above the shape memory switching temperature, a 100% recovery of the original topography was observed. Besides, the contact angle returned to the highest value observed from the original structured surface (Figure 2.46b).

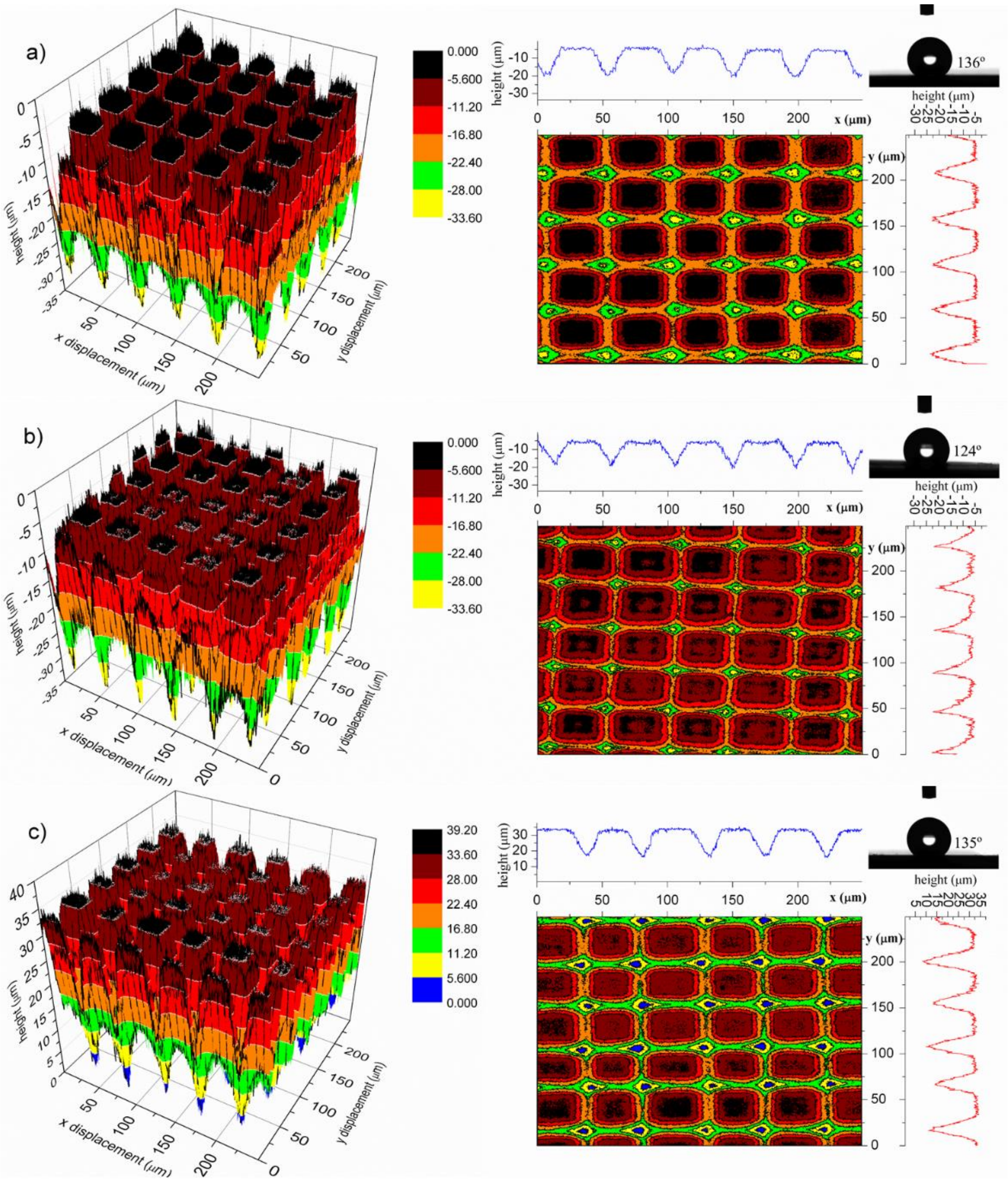

Figure 2.45. Topography and water contact angle for the first shape memory cycle: (a) original; (b) deformed (temporal shape); and (c) recovered.

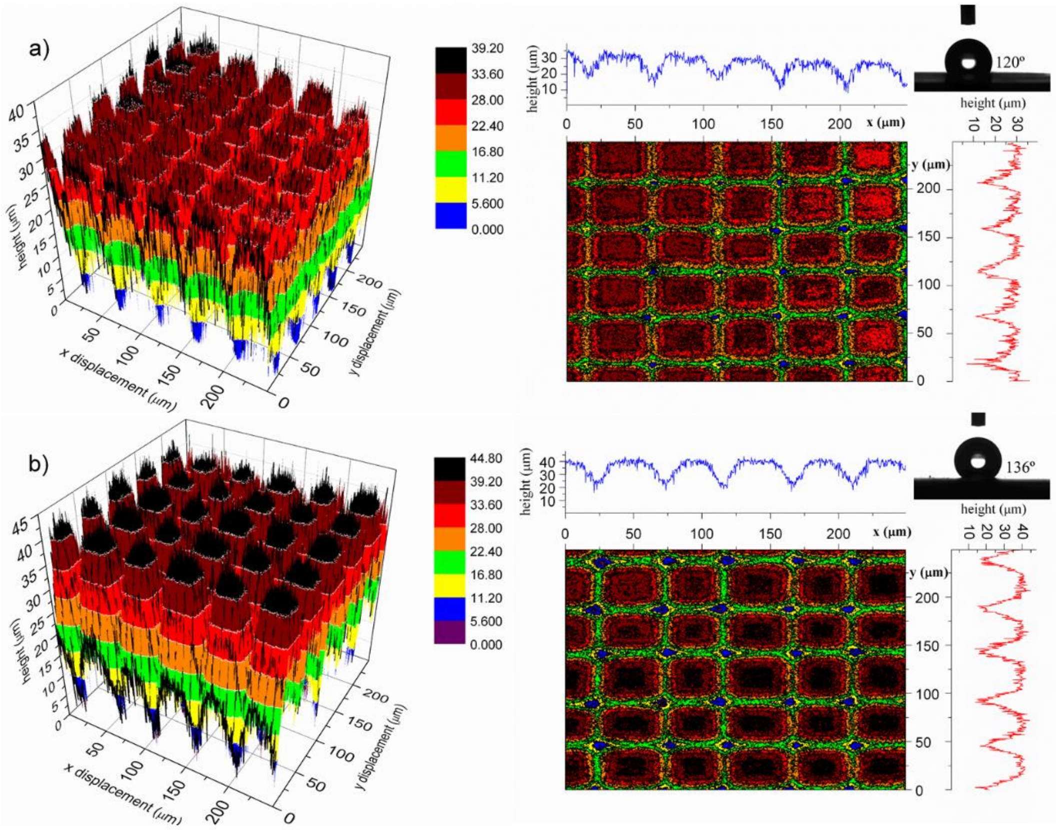

Figure 2.46. Surface topography and contact angle during the second shape memory cycle: (a) deformed (temporal shape) and (b) recovered surfaces.

The basic effect of surface roughness can easily be understood by the Wenzel equation [50,51]. The Wenzel's model is usually employed to study the wettability of a rough surface, which is defined by the following equation:

$$\cos\theta_w = r\cos\theta_i \qquad (2.5)$$

In equation 2.5, θ_w is the apparent contact angle (corresponds to the stable equilibrium state) and θ_i is the Young's intrinsic contact angle defined for an ideal surface. The roughness ratio, *r*, is a measure of how surface roughness affects a homogeneous surface, defined as the ratio of true area of the solid surface to the apparent area. Based on this, Shastry *et al.* [52] extracted the equation for a surface of rectangular pillars, shown below:

$$r = \frac{4\,bh + (a+b)^2}{(a+b)^2} \tag{2.6}$$

In equation 2.6, a corresponds to the distance between pillars, b is the pillar width and h is the pillar height. Therefore, from Shastry equation, it can be conclude that the roughness, and then the wettability, depends on the geometry of the pillars and the distance between them.

In this work, the PCO micropillars obtained are not rectangular (the obtained micropillars are flat top pyramid-like structures). Moreover, this equation cannot be applied exactly due to the pillar height varying considerably (up to 24%) when the PCO pillars are deformed, whereas the pillar width and the interpillar distances are, practically, constants (see Figure 2.45 and Figure 2.46).

However, this equation can be employed as a simplification to explain the obtained results where a and b can be considered constant. That is, from Shastry equation, the roughness ratio, r, is directly proportional to the pillar height h. Therefore, as in the deformed state, the height decreases, the roughness factor diminishes and the contact angle value is lower. In conclusion, the wettability of a polymeric nanostructured surface can be altered simply by modifying the height of the pillars, as is done in this work through the shape memory behaviour.

Considering the three thermomechanical cycles previously made (Figure 2.43), it could be expected that this deformation–recovery process could repeated an undetermined number of cycles. Furthermore, the variation of wettability with temperature from shape memory recovery of polymer surface topography could be extended to more intermediate scales, unidirectional or reversibly, based on multi-shape memory polymers able to memorize correlated reversible topographies [53,54].

2.2.5. Conclusions

The shape memory features of a PCO sample crosslinked with dicumyl peroxide (PCO+2%PDC) have been characterized by TMA in tension mode. On the one hand, the fixing capability of the temporary shape is strongly affected by the deformation force that is mainly responsible for counteracting the thermal shrinkage during cooling at presented low strains. Therefore, higher deformation is retained as applied force increases. However, on the other hand, just a slight effect on fixation is observed with regards to cooling rate.

After performing consecutive TMA cycles (tensile mode) at suitable testing conditions, crosslinked PCO demonstrates outstanding shape memory properties with repeatable behaviour as a thermo-responsive polymer.

Once the shape memory response was evaluated, nanostructuring by means of laser ablation has been presented as a suitable method in order to modify the wettability of the polymer surface with high accuracy and reproducibility over large areas (cm^2). As the PCO belongs to the group of thermo-active shape memory polymers with shape memory response based on heating a previously deformed shape above a switching temperature (transition temperature), it is demonstrated that the hydrophobicity (wettability) of this micropatterned polymeric surface can be controlled by means of the thermally induced shape memory effect. Thus, in this work, the wettability measured by water contact angle changes up to 10% when the shape memory behaviour takes place for this monofunctional peroxide based crosslinked commercial polyolefin (PCO+2%DCP).

In particular, the process has been performed twice (two cycles), but it could be expected that this deformation–recovery process could be repeated an undetermined number of cycles taking into account the cyclic TMA results. Definitively, it is possible to control the wettability of the surface by the shape memory effect in a smart way, a fact that could be interesting in different fields such as microfluidics and actuators, among others.

2.3. References

1. Schmets, A. J. M.; van der Zaken, G.; van der Zwaag, S. *Self healing materials: an alternative approach to 20 centuries of materials science*; Springer: Dordrecht, The Netherlands, 2007; Vol. 100.

2. Wu, D. Y.; Meure, S.; Solomon, D. Self-healing polymeric materials: A review of recent developments. *Prog. Polym. Sci.* **2008**, *33*, 479–522.

3. White, S. R.; Sottos, N. R.; Geubelle, P. H.; Moore, J. S.; Kessler, M. R.; Sriram, S. R.; Brown, E. N.; Viswanathan, S. Autonomic healing of polymer composites. *Nature* **2001**, *409*, 794–797.

4. Rule, J. D.; Brown, E. N.; Sottos, N. R.; White, S. R.; Moore, J. S. Wax-protected catalyst microspheres for efficient self-healing materials. *Adv. Mater.* **2005**, *17*, 205–208.

5. Cho, S. H.; Andersson, H. M.; White, S. R.; Sottos, N. R.; Braun, P. V Polydimethylsiloxane-based self-healing materials. *Adv. Mater.* **2006**, *18*, 997–1000.

6. Gupta, S.; Zhang, Q.; Emrick, T.; Balazs, A. C.; Russell, T. P. Entropy-driven segregation of nanoparticles to cracks in multilayered composite polymer structures. *Nat. Mater.* **2006**, *5*, 229–233.

7. Kolmakov, G. V; Matyjaszewski, K.; Balazs, A. C. Harnessing labile bonds between nanogel particles to create self-healing materials. *ACS Nano* **2009**, *3*, 885–892.

8. Toohey, K. S.; Sottos, N. R.; Lewis, J. A.; Moore, J. S.; White, S. R. Self-healing materials with microvascular networks. *Nat. Mater.* **2007**, *6*, 581–585.

9. Toohey, K. S.; Hansen, C. J.; Lewis, J. A.; White, S. R.; Sottos, N. R. Delivery of two-part self-healing chemistry via microvascular networks. *Adv. Funct. Mater.* **2009**, *19*, 1399–1405.

10. Hansen, C. J.; Wu, W.; Toohey, K. S.; Sottos, N. R.; White, S. R.; Lewis, J. A. Self-healing materials with interpenetrating microvascular networks. *Adv. Mater.* **2009**, *21*, 4143–4147.

11. South, A. B.; Lyon, L. A. Autonomic self-healing of hydrogel thin films. *Angew. Chemie* **2010**, *122*, 779–783.

12. Mukhopadhyay, P.; Fujita, N.; Takada, A.; Kishida, T.; Shirakawa, M.; Shinkai, S. Regulation of a real-time self-healing process in organogel tissues by molecular adhesives. *Angew. Chemie Int. Ed.* **2010**, *49*, 6338–6342.

13. Amamoto, Y.; Kamada, J.; Otsuka, H.; Takahara, A.; Matyjaszewski, K. Repeatable photoinduced self-healing of covalently cross-linked polymers through reshuffling of trithiocarbonate units. *Angew. Chemie* **2011**, *123*, 1698–1701.

14. He, L.; Fullenkamp, D. E.; Rivera, J. G.; Messersmith, P. B. pH responsive self-healing hydrogels formed by boronate – catechol complexation. *Chem. Commun.* **2011**, *47*, 7497–7499.

15. Lai, S.-M.; Lan, Y.-C. Shape memory properties of melt-blended polylactic acid (PLA)/thermoplastic polyurethane (TPU) bio-based blends. *J. Polym. Res.* **2013**, *20*, 1–8.

16. Xie, T. Recent advances in polymer shape memory. *Polymer* **2011**, *52*, 4985–5000.

17. Rodriguez, E. D.; Luo, X.; Mather, P. T. Linear/network poly(ε-caprolactone) blends exhibiting Shape Memory Assisted Self-Healing (SMASH). *ACS Appl. Mater. Interfaces* **2011**, *3*, 152–161.

18. Wang, W.; Jin, Y.; Ping, P.; Chen, X.; Jing, X.; Su, Z. Structure evolution in segmented poly(ester urethane) in shape-memory process. *Macromolecules* **2010**, *43*, 2942–2947.

19. Lendlein, A.; Kelch, S. Shape-memory polymers. *Angew. Chemie Int. Ed.* **2002**,

41, 2034–2057.

20. Ping, P.; Wang, W.; Chen, X.; Jing, X. Poly(ε-caprolactone) polyurethane and its shape-memory property. *Biomacromolecules* **2005**, *6*, 587–592.

21. Xiao, X.; Xie, T.; Cheng, Y.-T. Self-healable graphene polymer composites. *J. Mater. Chem.* **2010**, *20*, 3508–3514.

22. Li, G.; Nettles, D. Thermomechanical characterization of a shape memory polymer based self-repairing syntactic foam. *Polymer* **2010**, *51*, 755–762.

23. Céspedes, R. I. N.; Gámez, J. F. H.; Velázquez, M. G. N.; Belmontes, F. Á.; de León, R. E. D.; Fernández, O. S. R.; Orta, C. A. Á.; Hernández, E. H. Thermoplastic elastomers based on high-density polyethylene, ethylene–propylene–diene terpolymer, and ground tire rubber dynamically vulcanized with dicumyl peroxide. *J. Appl. Polym. Sci.* **2014**, *131*, 39901/1–39901/8.

24. Nakayama, K.; Watanabe, T.; Ohtake, Y.; Furukawa, M. Influence of residual peroxide on the degradation of peroxide-crosslinked ethylene–propylene–diene rubber. *J. Appl. Polym. Sci.* **2008**, *108*, 2578–2586.

25. Schneider, W. A.; Müller, M. F. Crystallinity of trans-polyoctenamer: characterization and influence of sample history. *J. Mol. Catal.* **1988**, *46*, 395–403.

26. Baltá-Calleja, E. J.; Kilian, H. G. A novel concept in describing elastic and plastic properties of semicrystalline polymers: polyethylene. *Colloid Polym. Sci.* **1985**, *263*, 697–707.

27. Deslandes, Y.; Rosa, E. A.; Brisse, F.; Meneghini, T. Correlation of microhardness and morphology of poly (ether-ether-ketone) films. *J. Mater. Sci.* **1991**, *26*, 2769–2777.

28. Calleja, F. J. B.; Salazar, J. M.; Čačković, H.; Loboda-Čačković, J. Correlation of hardness and microstructure in unoriented lamellar polyethylene. *J. Mater. Sci.* **1981**, *16*, 739–751.

29. Marmur, A. Wetting on hydrophobic rough surfaces: To be heterogeneous or not to be? *Langmuir* **2003**, *19*, 8343–8348.

30. Patankar, N. A. On the modeling of hydrophobic contact angles on rough surfaces. *Langmuir* **2003**, *19*, 1249–1253.

31. Takeshita, N.; Paradis, L. A.; Öner, D.; McCarthy, T. J.; Chen, W. Simultaneous tailoring of surface topography and chemical structure for controlled wettability. *Langmuir* **2004**, *20*, 8131–8136.

32. Forward, K. M.; Moster, A. L.; Schwartz, D. K.; Lacks, D. J. Contact angles of submillimeter particles: connecting wettability to nanoscale surface topography. *Langmuir* **2007**, *23*, 5255–5258.

33. Jabbarzadeh, A. Effect of nano-patterning on oleophobic properties of a surface. *Soft Matter* **2013**, *9*, 11598.

34. Jo, H. B.; Choi, J.; Byeon, K. J.; Choi, H. J.; Lee, H. Superhydrophobic and superoleophobic surfaces using ZnO nano-in-micro hierarchical structures. *Microelectron. Eng.* **2014**, *116*, 51–57.

35. Drelich, J.; Chibowski, E. Superhydrophilic and superwetting surfaces: Definition and mechanisms of control. *Langmuir* **2010**, *26*, 18621–18623.

36. Zhang, P.; Wang, S.; Wang, S.; Jiang, L. Superwetting surfaces under different media: effects of surface topography on wettability. *Small* **2015**, *11*, 1939–1946.

37. Zhang, X.; Shi, F.; Niu, J.; Jiang, Y.; Wang, Z. Superhydrophobic surfaces: from structural control to functional application. *J. Mater. Chem.* **2008**, *18*, 621–633.

38. Oh, S.-K.; Nakagawa, M.; Ichimura, K. Photocontrol of liquid motion on an azobenzene monolayer. *J. Mater. Chem.* **2002**, *12*, 2262–2269.

39. Delorme, N.; Bardeau, J. F.; Bulou, A.; Poncin-Epaillard, F. Azobenzene-containing monolayer with photoswitchable wettability. *Langmuir* **2005**, *21*,

12278–12282.

40. Jiang, W.; Wang, G.; He, Y.; Wang, X.; An, Y.; Song, Y.; Jiang, L. Photo-switched wettability on an electrostatic self-assembly azobenzene monolayer. *Chem. Commun. (Camb).* **2005**, 3550–2.

41. Xu, H.; Yu, C.; Wang, S.; Malyarchuk, V.; Xie, T.; Rogers, J. A. Deformable, programmable, and shape-memorizing micro-optics. *Adv. Funct. Mater.* **2013**, *23*, 3299–3306.

42. Chen, C.-M.; Chiang, C.-L.; Lai, C.-L.; Xie, T.; Yang, S. Buckling-based strong dry adhesives via interlocking. *Adv. Funct. Mater.* **2013**, *23*, 3813–3823.

43. Reddy, S.; Arzt, E.; del Campo, A. Bioinspired surfaces with switchable adhesion. *Adv. Mater.* **2007**, *19*, 3833–3837.

44. Li, W.; Gong, T.; Chen, H.; Wang, L.; Li, J.; Zhou, S. Tuning surface micropattern features using a shape memory functional polymer. *RSC Adv.* **2013**, *3*, 9865.

45. Chen, C. M.; Yang, S. Directed water shedding on high-aspect-ratio shape memory polymer micropillar arrays. *Adv. Mater.* **2014**, *26*, 1283–1288.

46. Zheng, Y.; Li, J.; Lee, E.; Yang, S. Light-induced shape recovery of deformed shape memory polymer micropillar arrays with gold nanorods. *RSC Adv.* **2015**, *5*, 30495–30499.

47. Turner, S. A.; Zhou, J.; Sheiko, S. S.; Ashby, V. S. Switchable micropatterned surface topographies mediated by reversible shape memory. *ACS Appl. Mater. Interfaces* **2014**, *6*, 8017–8021.

48. Huang, H.; Zheng, H. Y.; Lim, G. C. Femtosecond laser machining characteristics of Nitinol. *Appl. Surf. Sci.* **2004**, *228*, 201–206.

49. Garle, A.; Kong, S.; Ojha, U.; Budhlall, B. M. Thermoresponsive semicrystalline poly(ε-caprolactone) networks: exploiting cross-linking with

cinnamoyl moieties to design polymers with tunable shape memory. *ACS Appl. Mater. Interfaces* **2012**, *4*, 645–657.

50. Gennes, P.-G. de; Brochard-Wyart, F.; Quere, D. *Capillarity and Wetting Phenomena: Drops, Bubbles, Pearls, Waves*; Springer: New York, 2004.

51. Wenzel, R. N. Resistance of solid surfaces to wetting by water. *J. Ind. Eng. Chem. (Washington, D. C.)* **1936**, *28*, 988–994.

52. Shastry, A.; Case, M. J.; Bohringer, K. F. Engineering surface roughness to manipulate droplets in microfluidic systems. *18th IEEE Int. Conf. Micro Electro Mech. Syst. 2005. MEMS 2005.* **2005**.

53. Cuevas, J. M.; Rubio, R.; German, L.; Laza, J. M.; Vilas, J. L.; Rodriguez, M.; Leon, L. M. Triple-shape memory effect of covalently crosslinked polyalkenamer based semicrystalline polymer blends. *Soft Matter* **2012**, *8*, 4928–4935.

54. Xie, T. Tunable polymer multi-shape memory effect. *Nature* **2010**, *464*, 267–270.

CHAPTER 3

Polycyclooctene (PCO) crosslinked with radiation

3.1. Thermal and mechanical characterization

3.1.1. Introduction

High-energy radiation is one of the most effective ways to modify the performance of polymers [1,2]. The irradiation of polymeric materials with ionizing radiation (gamma rays, X-rays, accelerated electrons, ion beams) leads to the formation of very reactive intermediates, free radicals, ions and excited states [3]. These intermediates can follow several reaction paths that result in molecular chains crosslinking, and/or destruction and degradation of the macromolecules with the simultaneous formation of molecules of smaller chain lengths and change in the number and nature of double bonds [4]. The degree of these transformations depends on the structure of the polymer and the conditions of treatment before, during and after irradiation. Those factors may be controlled in order to facilitate the modification of polymers by radiation processing. Therefore, the field of ionizing radiations is an interesting field of research as an approach for the preparation of materials with enhanced properties.

Most of the polymers undergo crosslinking reaction upon exposure to radiation, like electron beam [5–7] or gamma radiation [8–10]. Thus, different authors have studied the involved crosslinking mechanism [11–13]. The polyolefins belong to the group of radiation crosslinking polymers. The most commonly polyolefin studied is polyethylene. For example, Barkhudaryan studied the effect of γ-radiation on the molecular characteristics of low density polyethylene (LDPE) [9,14]; Basfar measured the mechanical properties of polyethylene/ethylene vinyl acetate blends [15]; and the mechanical and physical properties of nitrile butadiene rubber/high density polyethylene (HDPE) blends were studied by Elshereafy [16]. Other polymers that have been crosslinked by radiation are polyvinyl alcohol/polyethylene glycol blends [17], polyamides [18,19], polytetrafluoroethylene [20,21], and poly(ethylene oxide) [22].

When a polymer is irradiated, chain scission and crosslinking will occur simultaneously [23]. The ratio of chain scission and crosslinking can be determined using the classical Charlesby–Pinner equation [24] shown in equation 3.1.

$$S + S^{1/2} = \frac{p_0}{q_0} + \frac{1}{q_0 + \mu_1 + D} \tag{3.1}$$

In equation 3.1, S is the sol fraction ($1 - g = S$, where g is the gel fraction); p_0 and q_0 are the fractions of the polymer chain units undergoing scission and crosslinking, respectively, per unit absorbed dose; and k is a constant ($k = f(\mu_1)$, where μ_1 represents the number-average degree of polymerization of the polymer before irradiation); and D is the radiation dose. Thus, the plot of the dependence of $S + S^{1/2}$ on $1/D$ makes it possible to obtain the value of p_0/q_0 by extrapolating to the ordinate, as well as to establish whether only crosslinking takes place in the polymer (in this case, the straight line pass through the origin) or whether scission also occurs (in this case, an intercept is formed with the ordinate) [25].

The aim of this section is to crosslink the polycyclooctene (PCO) using gamma radiation and study how thermal and mechanical properties vary with the radiation dose (25-1000 kGy). In this way, high-energy ionizing radiation raises as an effective alternative to peroxides for crosslinking the PCO, which avoids related contaminants from non-reacted peroxide or side products. After gamma irradiation, gel content was determined by Soxhlet extraction in cyclohexane, whereas thermal and mechanical properties were evaluated by means of Thermogravimetric Analysis (TGA), Differential Scanning Calorimetry (DSC), and Dynamic Mechanical Thermal Analysis (DMTA).

3.1.2. Materials

3.1.2.1. Polycyclooctene (PCO)

This work has been performed employing the same commercially available polycyclooctene Vestenamer® 8012 (from Evonik Industries), already described at section 2.1.2.1.

3.1.3. Preparation of samples

PCO sheets were manufactured by compression moulding under pressure of 100 bars (using a hydraulic press with thermostatically controlled platens) in a 1.5 mm thickness flat mould, at 160 ºC for 20 min. Two Teflon sheets were placed on both sides of the mould to reduce the surface roughness of the PCO sheets obtained. The obtained 50 mm × 50 mm × 1.5 mm sheets were cooled to room temperature in the mould under constant pressure.

Rectangular-shaped samples (length = 50 mm, width = 40 mm, and thickness = 1.5 mm) were cut from moulded sheets, packaged and sealed under vacuum (Figure 3.1). These PCO sheets were irradiated by gamma rays in a ^{60}Co radiation facility (NÁYADE Irradiation Plant of CIEMAT, Madrid, Spain). The irradiation was always performed at room temperature. A first group of samples were irradiated at a dose rate of 6.44 kGy/h. Total doses of 25, 50, 75, 100, 125, 150, 175 and 200 kGy were applied to each set of samples. A second group of samples were irradiated at a dose rate of 6.25 kGy/h, applying total doses of 300, 500, 750 and 1000 kGy. In both cases the error in dose is estimated to be ± 6-7%.

One sheet of raw PCO (50 mm × 10 mm × 1.5 mm) was used as reference (PCO-0) for comparing with corresponding irradiated samples. Table 3.1 summarizes all the developed PCO samples.

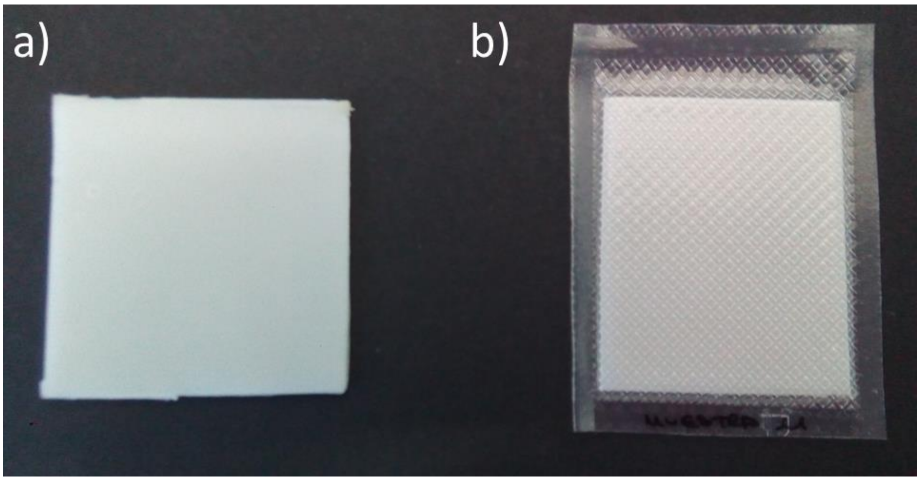

Figure 3.1. a) 50 mm × 50 mm × 1.5 mm PCO moulded sample; b) 50 mm × 40 mm × 1.5 mm cut and sealed under vacuum sample.

3.1.4. Experimental section

3.1.4.1. Gel content determination

As known, upon exposure to radiation, most of the polymers undergo crosslinking reactions [3], and the degree of crosslinking can be easily obtained measuring the gel content by Soxhlet extraction (Figure 3.2) [26,27]. The gel fraction (wt%) shows the insoluble fraction of the irradiated PCO samples (Table 3.1).

The gel content of irradiated PCO samples was determined gravimetrically using 10 Soxhlet extraction cycles with boiling cyclohexane as solvent (~10 h). Approximately 0.2 g of irradiated sample were cut into small pieces and placed in a cellulose cartridge. After extraction, the PCO samples were washed and vacuum dried at 50 ºC to constant weight. A non-irradiated PCO sample was also measured in the same conditions. The gel fraction was calculated using equation 3.2, where W_0 is the initial weight of sample and W_1 is the weight of sample after extraction. For each PCO sample, gel fraction determination was repeated three times and results reported typically varied no more than 5 wt%. The results are listed in Table 3.1.

Figure 3.2. Soxhlet extraction.

Table 3.1. Irradiated PCO samples and gel fraction determination results.

Sample	Radiation dose (kGy)	Gel fraction (wt %)
PCO-0	0	0
PCO-25	25	21.3
PCO-50	50	47.6
PCO-75	75	83.7
PCO-100	100	86.9
PCO-125	125	79.7
PCO-150	150	92.4
PCO-175	175	91.0
PCO-200	200	94.6
PCO-300	300	97.0
PCO-500	500	97.5
PCO-750	750	96.9
PCO-1000	1000	98.7

$$gel\ fraction\ (wt\%) = \frac{W_1}{W_0} \times 100 \tag{3.2}$$

Figure 3.3 illustrates the influence of radiation dose on the degree of crosslinking, expressed as gel content obtained by cyclohexane extraction. As expected, there is no gel formed in non-irradiated PCO sample. However, with radiation doses greater than 25 kGy, a sharp increase in the gel content occurs together with a moderated increment and a tendency to stabilization for the higher doses. Thus, for example the gel content is about 84 wt% for 75 kGy dose and over 90 wt% for 150 kGy dose (Table 3.1). The increase in the gel fraction values can be attributed to the radiation crosslinking in the PCO chains. In fact, a higher radiation dose implies higher gel content, although only with small differences between PCO-200 and PCO-1000 samples (4 wt%), which could suggest chain scission reactions from gamma radiation above 200 kGy. Therefore, 200 kGy seem to be sufficient from the viewpoint of gel content in the PCO samples.

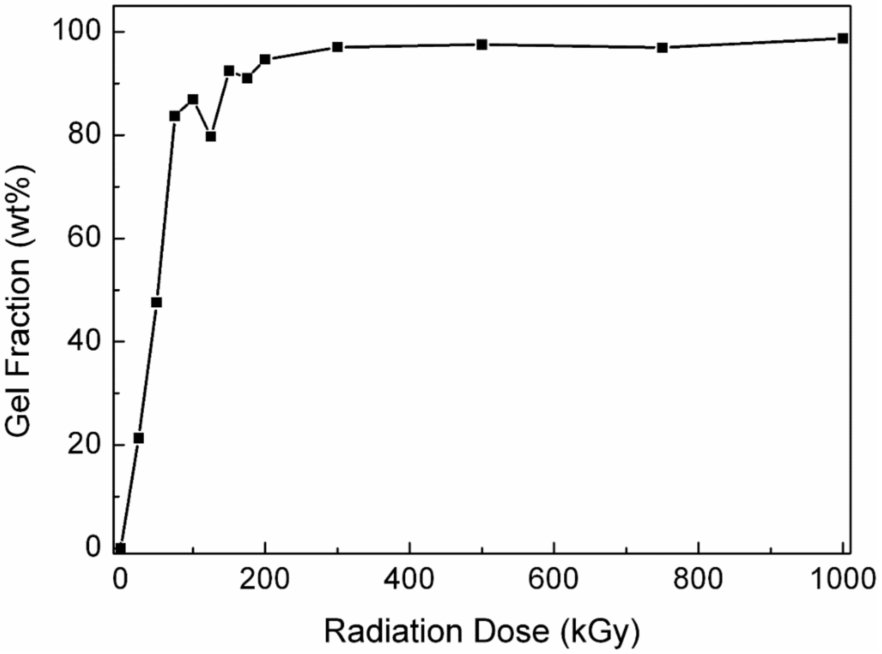

Figure 3.3. Variation of gel content of irradiated PCO samples versus radiation dose.

The Charlesby-Pinner equation was applied in order to estimate the probability of crosslinking or chain scission in gamma irradiated PCO. A linear relationship is obtained (Figure 3.4) considering all the PCO irradiated samples, where a value of p_0/q_0 equal to 0.13 is extrapolated, indicating that crosslinking process is predominant comparing with scission one.

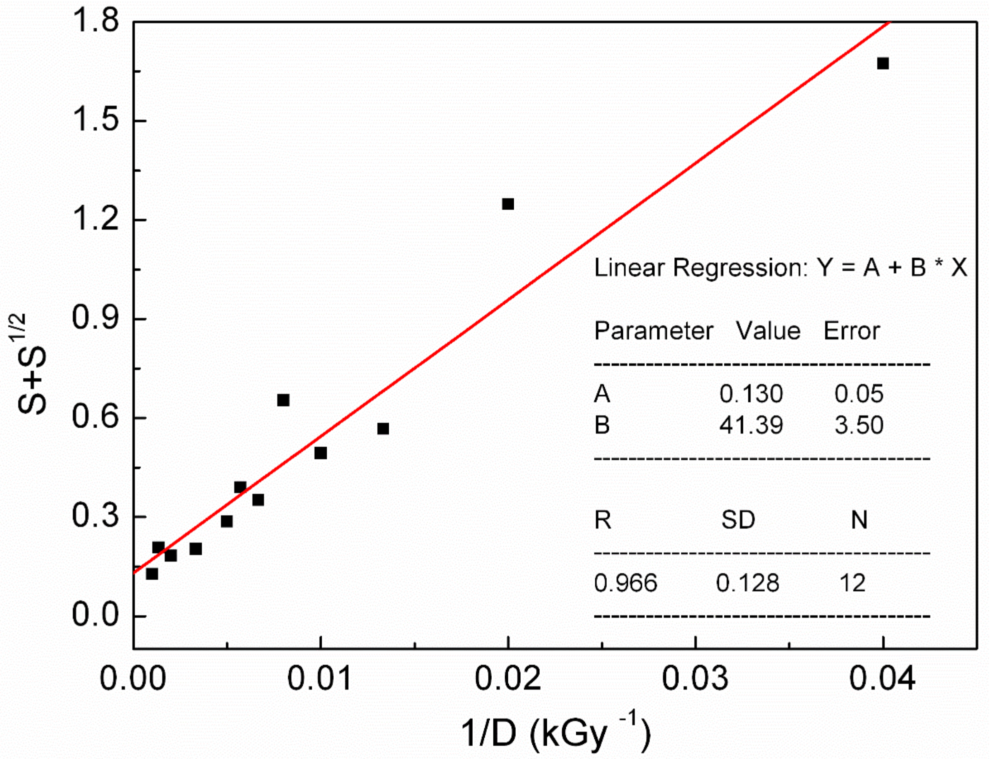

Figure 3.4. Representation of Charlesby-Pinner equation for gamma irradiated PCO samples (25-1000 kGy).

3.1.4.2. Thermogravimetric Analysis

Thermogravimetric (TGA) and Derivative Thermogravimetric (DTG) analysis gives information of the weight loss process, as well as of its degradation rate (dw/dt), respectively.

Thermal stability of non-irradiated and irradiated samples was evaluated by Thermogravimetric Analysis with a Mettler Toledo TGA/SDTA 851e thermobalance. The measurements were carried out from 25 to 800 ºC with a heating rate of 10 ºC·min^{-1} under nitrogen atmosphere. For irradiated PCO samples, this characterization was realized for each sample before and after Soxhlet extraction.

TGA and DTG analyses were performed before Soxhlet extraction for all non-irradiated and irradiated PCO samples as can be observed in Figure 3.5, Figure 3.6 and Figure 3.7. All PCO samples decompose in one main breakdown stage. Table 3.2 collects the temperature (T_d) at the maximum degradation rate (dw/dt) from DTG thermograms for all non-irradiated and irradiated samples.

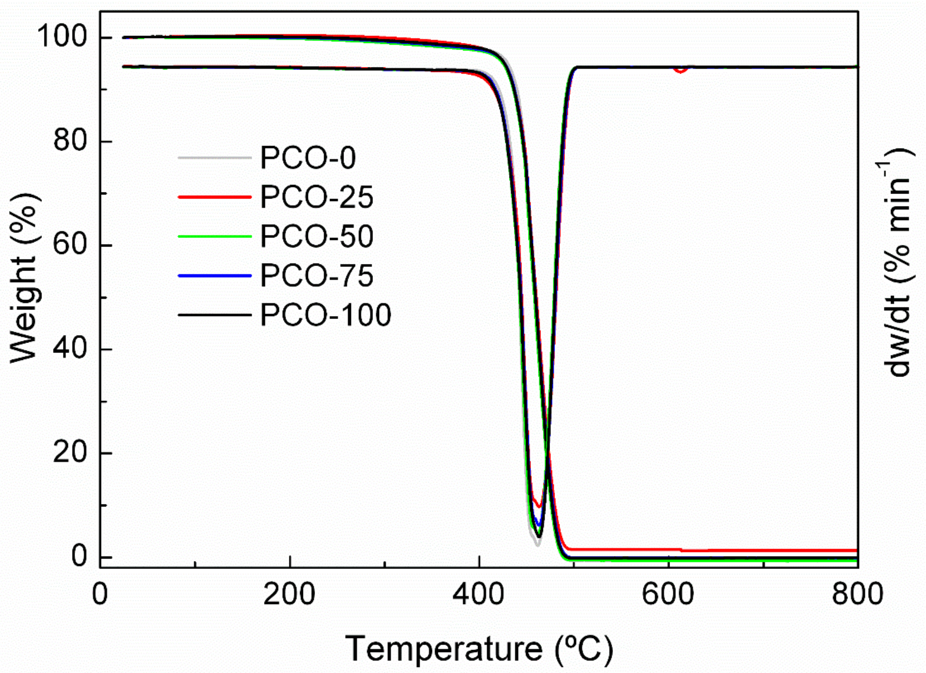

Figure 3.5. TGA and DTG curves for irradiated PCO samples (0-100 kGy) studied before Soxhlet extraction.

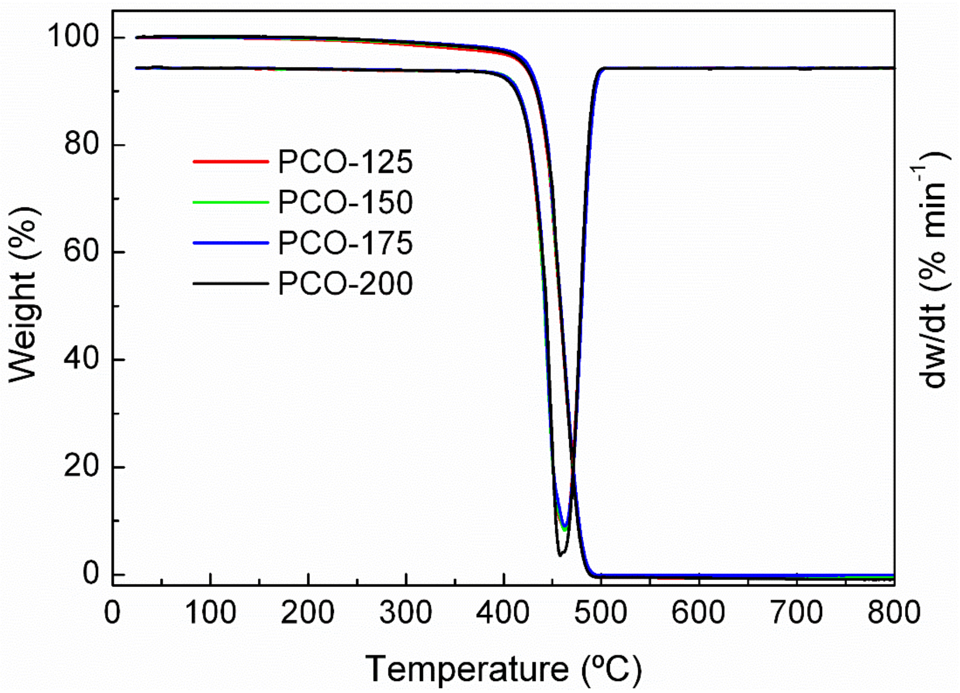

Figure 3.6. TGA and DTG curves for irradiated PCO samples (125-200 kGy) studied before Soxhlet extraction.

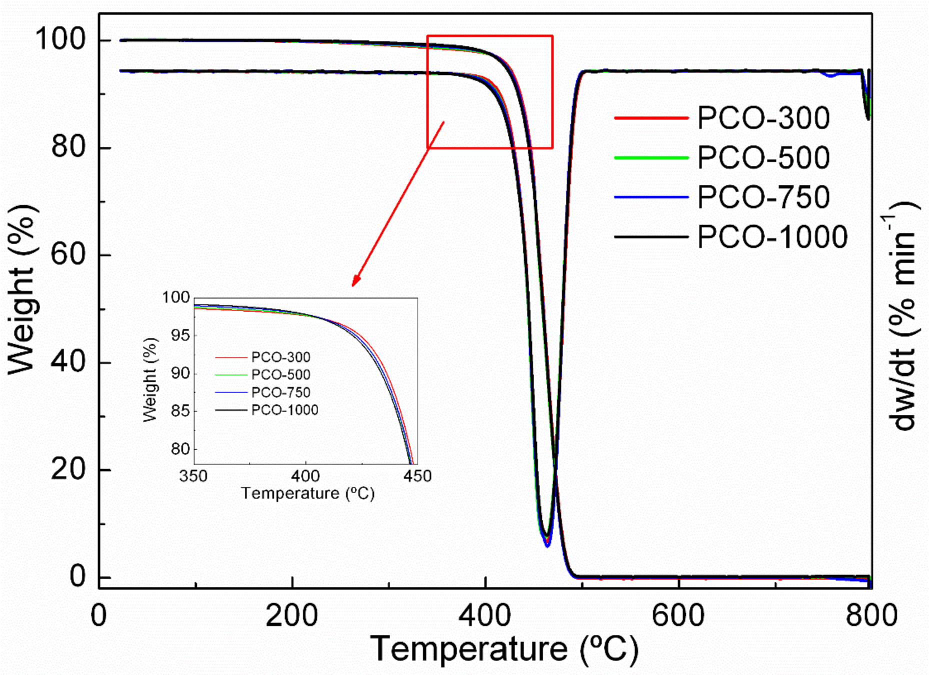

Figure 3.7. TGA and DTG curves for irradiated PCO samples (300-1000 kGy) studied before Soxhlet extraction.

Table 3.2. Thermal properties for irradiated PCO samples (0-1000 kGy) studied before Soxhlet extraction.

Sample	T_{m1} **(ºC)**	ΔH_{m1} **(J/g)**	T_c **(ºC)**	ΔH_c **(J/g)**	T_{m2} **(ºC)**	ΔH_{m2} **(J/g)**	**Crystallinity (%)**	T_d **(ºC)**
PCO-0	60.7	65.1	37.0	-66.0	57.5	69.7	30.3	461.8
PCO-25	60.0	67.5	34.1	-64.1	57.6	69.7	30.3	463.7
PCO-50	60.6	67.0	32.3	-63.3	58.3	64.3	28.0	462.4
PCO-75	60.8	61.8	30.7	-55.7	56.3	62.6	27.2	463.1
PCO-100	60.1	65.6	30.0	-55.5	54.6	59.7	25.9	463.4
PCO-125	59.4	65.0	31.0	-56.2	54.3	58.9	25.6	462.5
PCO-150	60.1	66.6	28.9	-54.1	52.6	57.0	24.8	462.7
PCO-175	61.1	63.0	25.8	-52.5	55.4	56.1	24.4	462.8
PCO-200	59.6	62.1	27.7	-49.0	52.5	52.6	22.8	458.1
PCO-300	60.8	76.0	30.2	-57.9	53.2	55.8	24.3	463.5
PCO-500	60.5	69.2	33.8	-52.1	51.9	48.3	21.0	462.5
PCO-750	59.1	62.0	37.1	-52.0	51.4	41.9	18.2	464.1
PCO-1000	57.1	60.3	40.1	-50.3	48.9	42.5	18.5	463.5

In general, the thermal stability of the irradiated samples was slight increased, from T_d = 461.8 ºC for neat PCO to T_d = 464.1 ºC for PCO-750 sample. The already reported improvement of mechanical and thermal properties from crosslinking process in polymer irradiation [28–30] explains this slight increase in the thermal stability of the irradiated PCO samples.

The same thermogravimetric analysis (TGA and DTG) was performed for all irradiated PCO samples after Soxhlet extraction in cyclohexane. The curves are illustrated in Figure 3.8, Figure 3.9 and Figure 3.10, whereas the values of the temperature (T_d) at the maximum degradation rate (dw/dt), calculated from DTG curves are listed in Table 3.3. For lower radiation doses, after the extraction of non-crosslinked fraction and scissed polyalkenamer chains from macromolecular network, the T_d increases (increased thermal stability). However, above 200 kGy, where crosslinked gel content is very high, the T_d values (Table 3.2 and Table 3.3) are practically equal before and after Soxhlet extraction, or slightly lower.

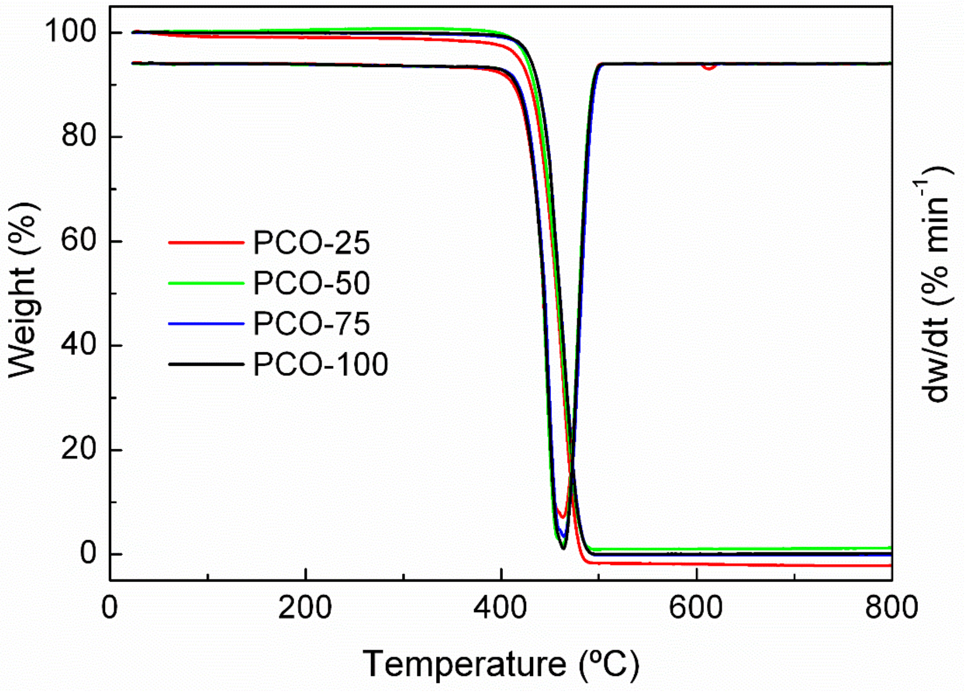

Figure 3.8. TGA and DTG curves for irradiated PCO samples (25-100 kGy) studied after Soxhlet extraction.

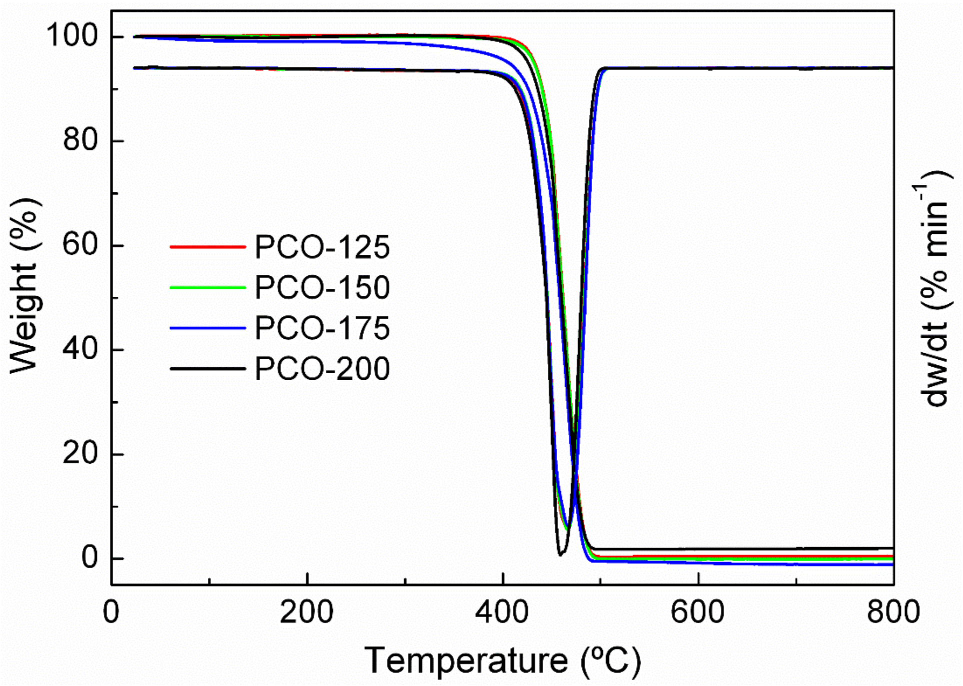

Figure 3.9. TGA and DTG curves for irradiated PCO samples (125-200 kGy) studied after Soxhlet extraction.

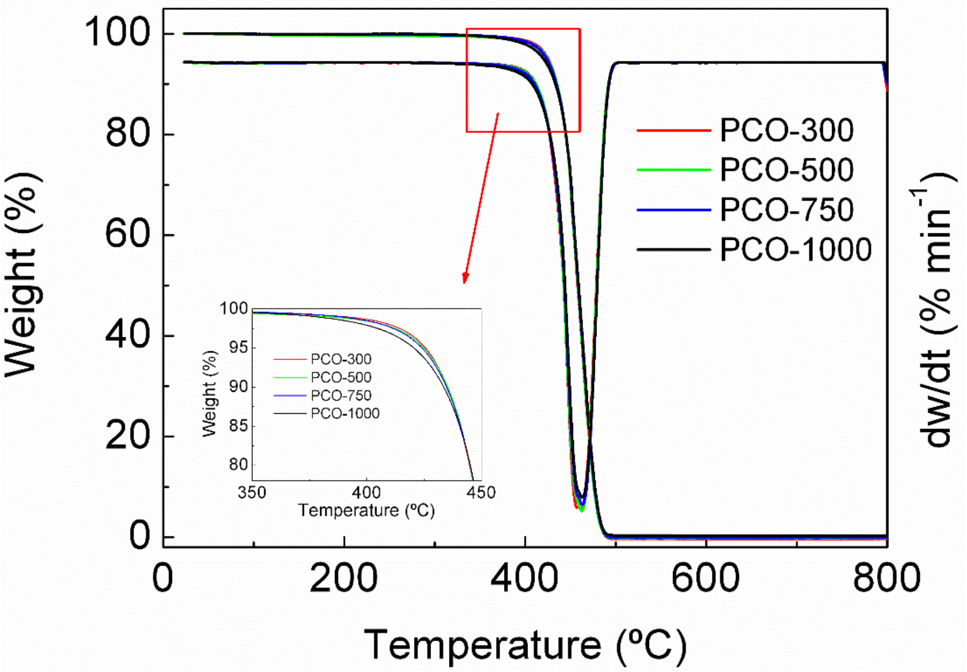

Figure 3.10. TGA and DTG curves for irradiated PCO samples (300-1000 kGy) studied after Soxhlet extraction.

Table 3.3. Thermal properties for irradiated PCO samples (25-1000 kGy) studied after Soxhlet extraction.

Sample	T_{m1} (ºC)	ΔH_{m1} (J/g)	T_c (ºC)	ΔH_c (J/g)	T_{m2} (ºC)	ΔH_{m2} (J/g)	Crystallinity (%)	T_d (ºC)
PCO-25	58.0	67.8	32.8	-62.3	55.5	69.2	30.1	463.4
PCO-50	56.3	71.5	31.9	-62.5	56.0	63.3	27.5	463.4
PCO-75	58.8	57.3	30.1	-60.7	53.2	68.5	29.8	466.8
PCO-100	58.2	56.2	29.7	-56.6	52.0	62.9	27.4	465.2
PCO-125	59.6	55.5	27.4	-55.8	54.8	59.9	26.0	466.3
PCO-150	58.7	55.5	28.3	-56.2	52.3	63.3	27.5	470.5
PCO-175	55.4	62.5	27.3	-63.2	51.1	68.4	29.7	465.2
PCO-200	57.7	56.6	27.5	-54.1	51.0	64.1	27.9	471.8
PCO-300	57.9	53.8	29.7	-61.2	53.0	62.1	27.0	461.6
PCO-500	57.0	51.1	33.3	-53.1	52.7	51.6	22.4	462.5
PCO-750	55.8	47.4	37.2	-51.5	52.0	40.7	17.7	463.2
PCO-1000	56.5	47.2	40.3	-46.2	50.3	38.8	16.9	462.8

Although practically negligible variations, these results point to about 200 kGy as a critical radiation dose regarding macromolecular structure and related thermal stability.

3.1.4.3. Differential Scanning Calorimetry

Thermal properties of all samples were measured by Differential Scanning Calorimetry (DSC 822e from Mettler Toledo) to identify thermal actuation temperatures. The transition temperature of shape memory effect (T_{trans}) was defined from melting temperature measured in the second heating cycle (T_{m2} in Table 3.2). Samples in aluminium pans were characterized under constant nitrogen flow (50 mL·min^{-1}) before and after Soxhlet extraction. First, samples were heated from −100 to 150 ºC at a rate of 10 ºC·min^{-1}, followed by a cooling scan from 150 to −100 ºC at a rate of −10 ºC·min^{-1}. Subsequently, a second heating scan to 150 ºC was conducted at the same heating rate. In all cases samples around 5-10 mg were used.

The curves for all the studied samples before Soxhlet extraction are represented in Figure 3.11, Figure 3.12 and Figure 3.13, while corresponding melting temperatures (T_m), melting enthalpies (ΔH_m), crystallization temperatures (T_c), crystallization enthalpies (ΔH_c) and crystallinity are listed in Table 3.2.

The crystallinity of each sample was calculated by equation 3.3, where the enthalpy of a 100% crystalline polycyclooctene was 230 J·g^{-1} [31]. As can be observed in Table 3.2, the crystallinity decreases as the radiation dose increases, i.e. gamma radiation diminishes the crystalline regions and increases the amorphous character of the PCO irradiated samples.

$$\%\,crystallinity = \frac{\Delta H_{m2}\,(PCO\ sample)}{\Delta H_m\,(100\%\ crystalline\ PCO)} \times 100 \qquad (3.3)$$

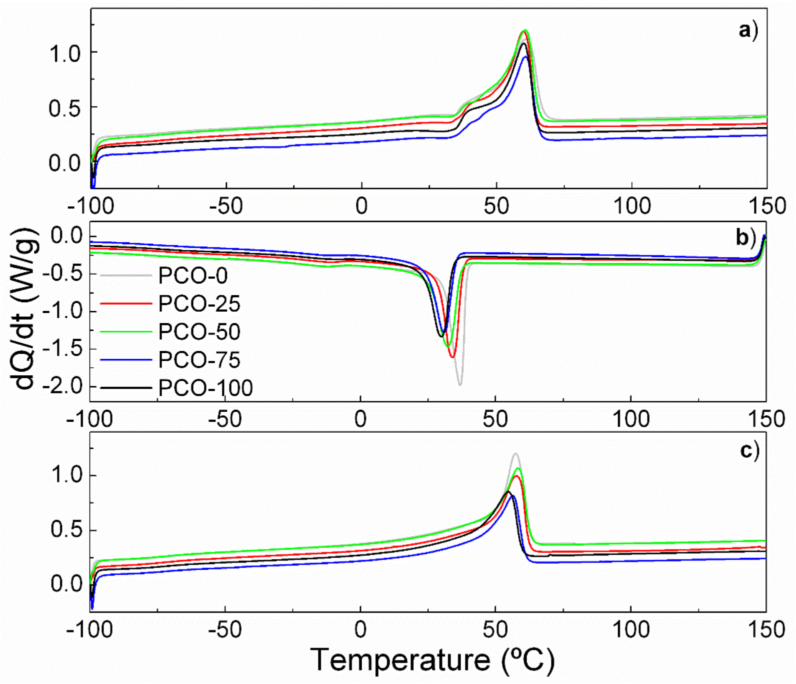

Figure 3.11. DSC curves for irradiated PCO samples (0-100 kGy) before Soxhlet extraction: a) first heating, b) cooling and c) second heating scan.

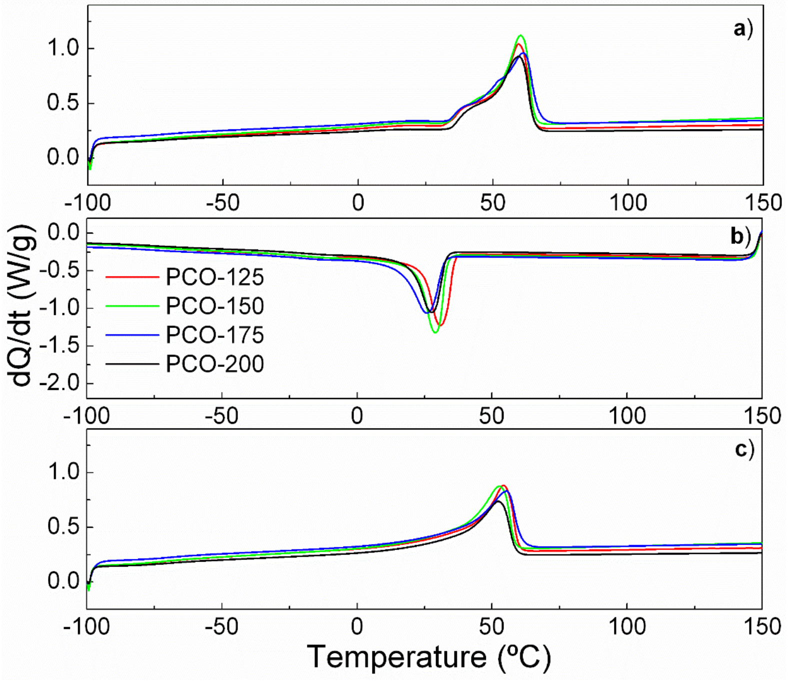

Figure 3.12. DSC curves for irradiated PCO samples (125-200 kGy) before Soxhlet extraction: a) first heating, b) cooling and c) second heating scan.

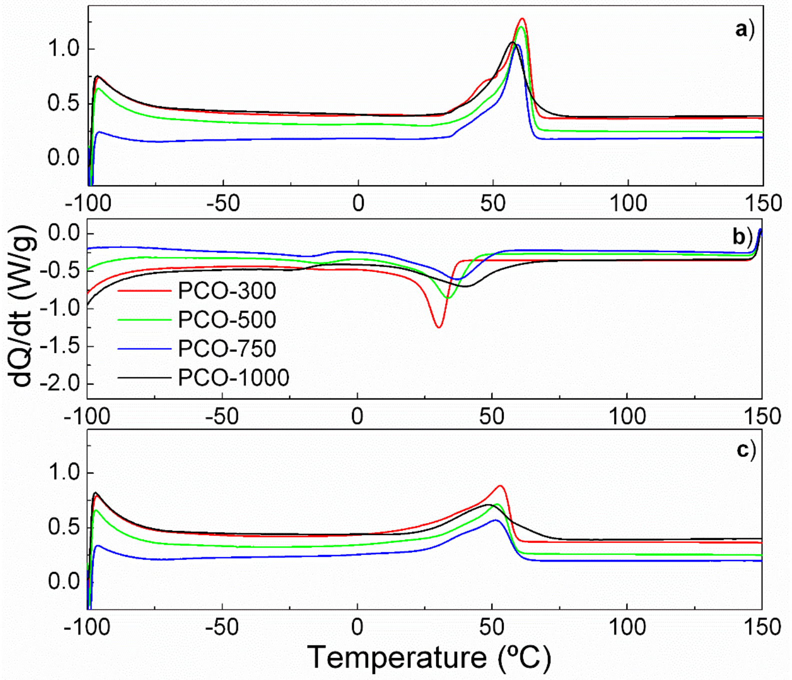

Figure 3.13. DSC curves for irradiated PCO samples (300-1000 kGy) before Soxhlet extraction: a) first heating, b) cooling and c) second heating scan.

From the first scan, it appears that radiation has no pronounced influence on T_m and ΔH_m. It is well known that, although crosslinking is the most important effect of polymer irradiation, both chain scission and crosslinking occur in the radiation process. Therefore, there are two kinds of molecular change induced by radiation in a polymer [1]: an increase in molecular weight due to the formation of a network structure (crosslinking effect), and a decrease in molecular weight due to the main-chain bond scission (scission effect). Both effects occur, primarily, in the amorphous region, while some may take place in the interphase between the crystalline and amorphous regions [2]. Therefore, as crosslinking is the most important effect of polymer irradiation in the PCO irradiated samples studied in this work, according the p_0/q_0 value obtained from the gel content determination, great changes in T_{m1} and ΔH_{m1} values with increasing radiation dose have not been expected.

However, from the second heating scan, an increase in the radiation dose provokes a pronounced decrease both on T_m and $\varDelta H_m$. This decrease is also more pronounced for radiation doses above 500 kGy. The irradiated PCO samples recrystallized during the DSC cooling scan in presence of the crosslinks formed in the irradiation process (as seen in Table 3.1 PCO samples are more crosslinked as radiation dose rises). Then, during the recrystallization process, crosslinks between polymer chains act as defect centres, which restrict chain mobility of PCO chains, inhibiting chain reorganization and causing the observed decrease in crystallinity and related T_m and $\varDelta H_m$ values (Table 3.2). Thus, the restricted mobility of polymeric chains to form crystals provokes this crystallinity reduction from higher crosslinking, as reported in literature [32].

In conclusion, apart from slight differences between the first and second heating process due to changes in thermal history, the DSC analysis demonstrates the impact of the crosslinking degree on crystallinity of the irradiated PCO samples, with decreases in melting enthalpies and melting temperatures as the radiation dose increases (Table 3.2), in good agreement with prior literature [32].

The degree of crystallinity thus decreases with increased density of crosslinks due to more restricted mobility and conformational rearrangement of polymeric chains to form crystals. Then, the melting temperature of the irradiated PCO samples, and consequently the T_{trans} of shape memory features, could be shifted by controlling the crosslinking density from the specific radiation dosage (Table 3.2). On the other hand, the glass transition temperatures (T_g) for these specimens are below -50 ºC and are not influenced by the curing degree, as studied and corroborated by next DMTA analysis.

Thermal properties (T_m, $\varDelta H_m$, T_c, $\varDelta H_c$ and crystallinity values) of the irradiated PCO samples were also analysed by DSC after Soxhlet extraction, where not crosslinked parts from PCO irradiated samples are dissolved in the selected solvent (cyclohexane), and the residue corresponds mainly to the crosslinked fraction [33]. The results are listed in Table 3.3 and represented in Figure 3.14, Figure 3.15 and Figure 3.16.

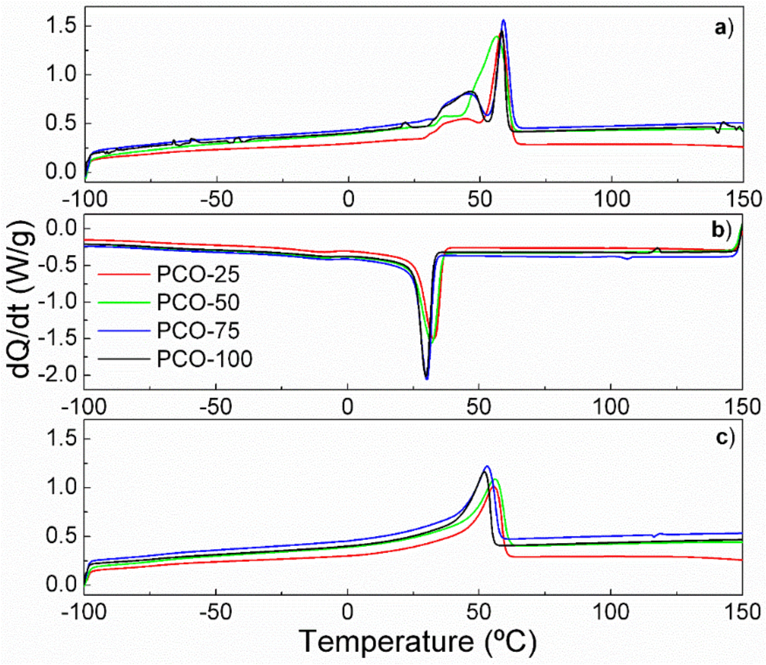

Figure 3.14. DSC curves for irradiated PCO samples (25-100 kGy) after Soxhlet extraction: a) first heating, b) cooling and c) second heating scan.

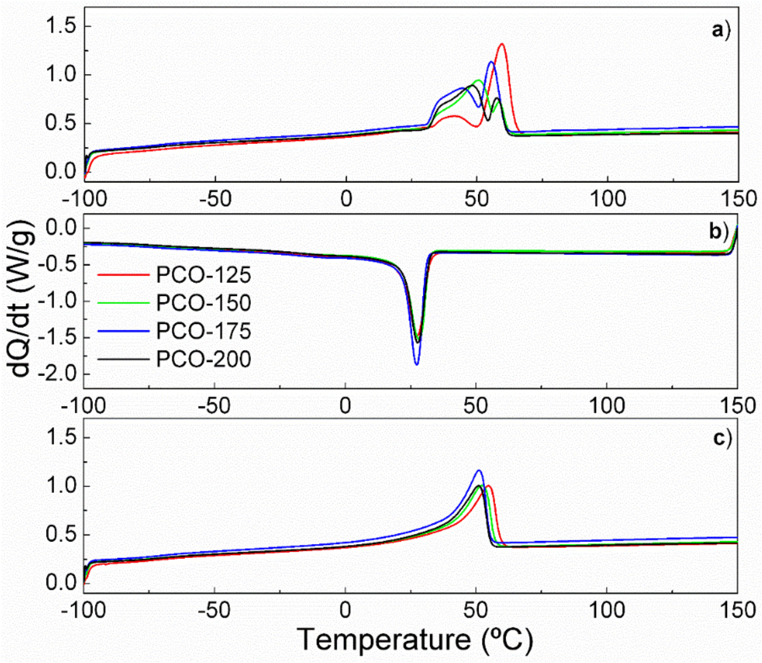

Figure 3.15. DSC curves for irradiated PCO samples (125-200 kGy) after Soxhlet extraction: a) first heating, b) cooling and c) second heating scan.

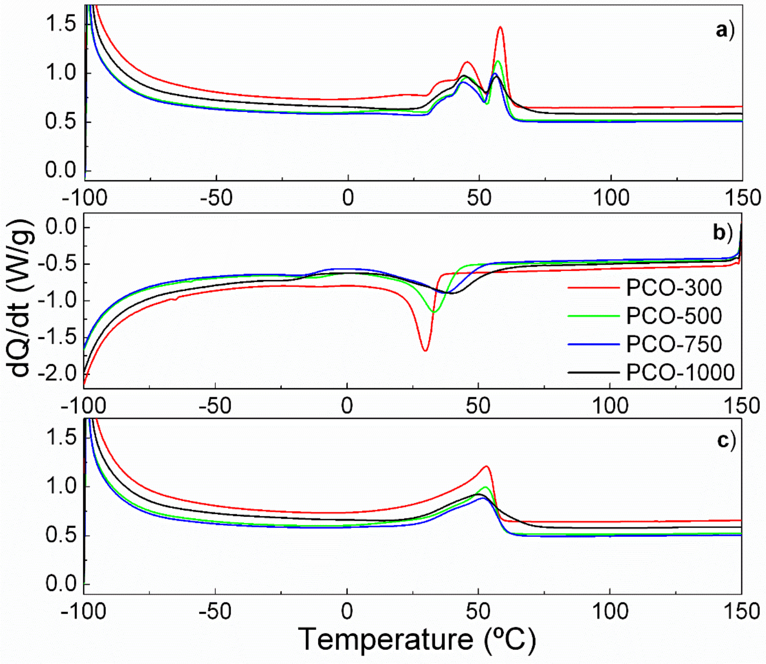

Figure 3.16. DSC curves for PCO irradiated samples (300-1000 kGy) after Soxhlet extraction: a) first heating, b) cooling and c) second heating scan.

As before Soxhlet extraction, T_m and ΔH_m values decrease in both scans as radiation dose increases from higher crosslinking density, as well as there are any differences between T_m and ΔH_m values measured in the first and in the second heating process due to changes in thermal history. However, the radiation dose has minor influence on T_m and ΔH_m in the first heating scan, probably from non-controlled crystallization process after Soxhlet extraction than that of in the second scan after cooling stage, although a more pronounced decrease is observed for radiation doses above 500 kGy in both scans.

3.1.4.4. Dynamic Mechanical Thermal Analysis

Dynamic mechanical thermal analysis was performed in flexion mode using a Polymer Laboratories MK-II DMTA. Rectangular samples (10 mm × 35 mm × 1.5 mm) were directly cut from the irradiated PCO sheets and measured using the dual cantilever test from -100 to 150 ºC, at a deformation frequency of 10 Hz, a strain of 64 µm and a heating rate of 2 ºC min^{-1}. A non-irradiated PCO sample was also measured in the same conditions. Since the dynamic mechanical method (DMTA) is highly sensitivity in detecting changes in internal molecular mobility, it was used to confirm the results obtained by DSC and to measure the glass transition temperatures (T_g) for these specimens.

Flexion storage (E') modulus and tan δ ($tan\delta = E''/E'$) for all PCO samples are depicted in Figure 3.17, Figure 3.18 and Figure 3.19, where a similar behaviour in E' and tan δ is observed for all analysed samples. At temperatures below -50 ºC, the PCO samples have a high storage modulus (vitrified state) owing stiff amorphous and crystalline domains in the polymeric network. Thus, although the balance between crystalline domains and crosslinked phase varies with the radiation dose, the mechanical response is not substantially affected.

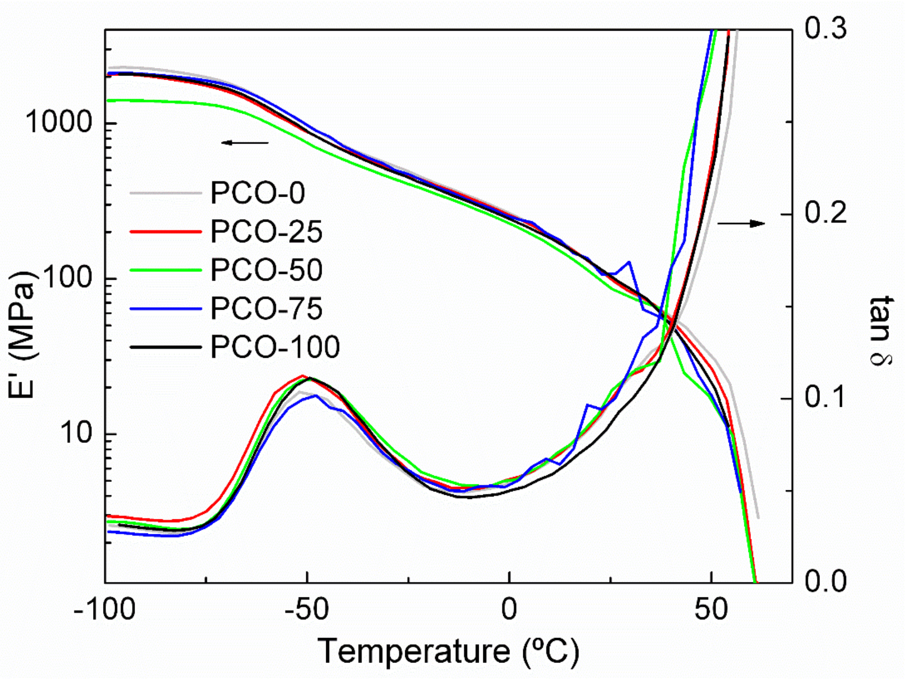

Figure 3.17. Flexion storage (E') modulus and tan δ for irradiated PCO samples (0-100 kGy) before Soxhlet extraction.

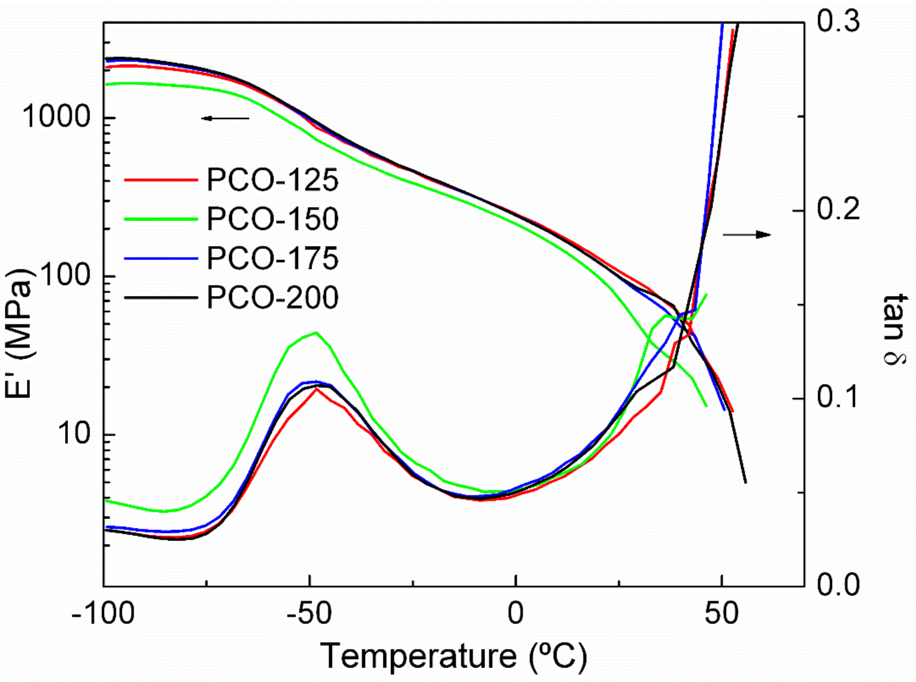

Figure 3.18. Log flexion storage (*E*′) modulus and tan *δ* for irradiated PCO samples (125-200 kGy) before Soxhlet extraction.

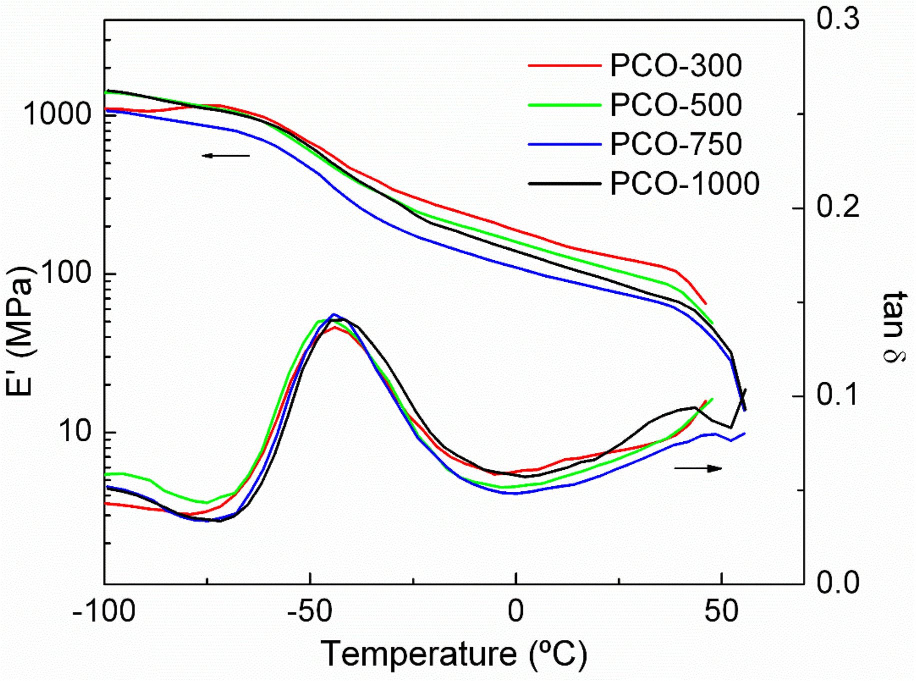

Figure 3.19. Log flexion storage (*E*′) modulus and tan *δ* for irradiated PCO samples (300-1000 kGy) before Soxhlet extraction.

As temperature increases, the storage modulus drops progressively, whereas $\tan\delta$ shows a peak, which is attributable to the glass transition (T_g) of the PCO samples around -50 ºC. At approximately 50 ºC the melting of the sample takes place, where the storage modulus drops sharply and $\tan\delta$ rises indefinitely.

For all the PCO samples tested, a well-defined melting zone associated with the crystalline domains is observed. It was originally expected that gamma-irradiation might affect the crystallinity of these materials, especially for branched polymers [34]. The gel fraction results indicates that significantly large insoluble fractions were generated in the irradiated samples. However, DMTA and DSC results show that the onset temperatures of the glass and melting transitions practically remain stable with radiation, which could be explained by potentially predominant chain scission and crosslinking in the amorphous area first [35].

On the one hand, smaller polymer chains from scission process are characterised by higher mobility to organised macromolecular structure with promoted crystalline phase. On the other hand, the crosslinking process leads to longer and more subdivided molecules that hamper the organization of the structure towards extended amorphous phase. Finally, as the irradiation dose increases, the energy could achieve levels to induce the chain scission or crosslinking in polymeric chains within the crystalline phase, which could affect the crystal thickness or crystallinity.

3.1.5. Conclusions

The effect of gamma irradiation on thermal and mechanical properties as an efficient means of crosslinking semicrystalline polycyclooctene (PCO) was investigated. Thus, a commercial polycyclooctene (PCO) was irradiated with a gamma source of ^{60}Co at different doses (25-1000 kGy), and the gel fraction for each sample was determined by Soxhlet extraction. This insoluble fraction of each irradiated PCO sample is directly related to the degree of crosslinking reached for each sample in the radiation process. The probability of crosslinking or chain scission with radiation dose was analysed by applying the Charlesby-Pinner equation from gel content, which demonstrated that crosslinking process is predominant, fact necessary to obtain shape memory polymers.

Thermal properties were evaluated before and after Soxhlet extraction by means of TGA, DTG and DSC, showing that the thermal stability of all PCO samples is quite similar independently of radiation dose. It is possible to affirm that crosslinking process is predominant comparing with scission one in PCO samples irradiated with gamma radiation up to 1000 kGy.

The investigation of the thermal properties by DSC shows minor changes in the melting temperature (T_m) and melting enthalpy ($\mathit{\Delta} H_m$) with irradiation doses in the first heating scan, which could be attributed to the immobilization of the generated free radicals in the crystalline region with hindered chain mobility. However, for the second heating scan, a decrease in T_m and $\mathit{\Delta} H_m$ with the increasing radiation dose was observed. During the recrystallization process, crosslinks between polymer chains act as defect centres, which restrict chain mobility of PCO chains and, therefore, the T_m and $\mathit{\Delta} H_m$ values determined from the second heating scan are lower.

The mechanical properties were measured by DMTA in flexion mode. The DMTA results confirm the results obtained by DSC for all non-irradiated and irradiated PCO samples before Soxhlet extraction. Furthermore, the analysis allows measuring respective glass transition temperatures (T_g) for PCO samples, which are below −50 ºC and does not show particular influence from the curing degree.

3.2. Shape memory properties

3.2.1. Introduction

Shape-memory materials are stimuli-responsive materials. They have the capability of changing their shape upon application of an external stimulus [36,37]. There are different types of shape memory materials, including Shape Memory Alloys (SMA), Shape Memory Ceramics (SMC), and Shape Memory Polymers (SMP) [38]. Therefore, shape memory polymers (SMP) are those capable of recovering their original shape after previous deformation into a different one (temporary shape) when designed with appropriate molecular structure. In a way, they ’remember’ the programmed shape when processed (permanent shape) on the basis of entropy changes. Besides, they come back to it several times (deformation cycles) [39], also from different temporary shapes [40]. Shape memory polymers can be categorized into thermo-responsive SMP, chemo-responsive SMP and photoresponsive SMP, according to the nature of stimulus [38,41].

The shape memory effect can be induced under appropriate stimulus, such as temperature [37,42–44]. Generally, shape memory effect in thermo-responsive SMPs consists of heating up the sample, deforming, and cooling the sample to fix the temporary shape. Thus, the shape memory effect is induced by heating the sample above a transition temperature to restore the permanent shape. Additionally, as a complement to heating induced shape memory effect, cooling for shape recovery has been demonstrated in a shape memory hybrid (SMH) [45]. Shape memory effect in polymers can be applied to obtain QR codes [46,47], actuators [48], or devices with potential use in minimally invasive biomedical applications [49].

A reported way to obtain shape memory polymers is crosslinking the macromolecular chains of the polymer, by a radical initiator, like a peroxide [50,51], or by ionizing radiation, like electron beam [5,7] or gamma rays [9,10]. Gamma rays generate free radicals which are able to pull out a hydrogen atom from the polymer, so polymeric macroradicals can react and recombine to obtain a crosslinked network [13]. Different polymers have been crosslinked by gamma radiation, like polyamides [18], poly(ethylene oxide) [22], poly(vinylidene fluoride) [52], and polyethylene [9,15].

In this scenario, ionizing energy could replace thermo-chemical processes in the crosslinking of shape memory polymers due to being faster and more controllable. Furthermore, this technology emerges as an alternative process to mould geometries that are impractical by chemical reactions due to limited strength of molten material, flowing like a viscous liquid, i.e avoiding lack of integrity of the moulded profile during thermal procedures [53]. Then, some examples could be shape memory films and small diameter wires by nearly instantaneous crosslinking process with ionizing energy in continuous processes.

In the present section, the expected thermal-induced shape memory behaviour from radiation crosslinking is evaluated both qualitatively and quantitatively for all samples (from 25 to 1000 kGy). On the one hand, shape memory behaviour is qualitatively evaluated by following shape recovery capabilities with a digital camera. On the other hand, in order to quantify the shape memory properties, a thermo-mechanical cycle is performed by Thermo-Mechanical Analysis (TMA). To perform a deeper shape memory analysis, the PCO-200 sample is selected and it is subjected to different thermo-mechanical cycles varying different parameters such as the deformation force, the heating and cooling rates in order to view how these changes affect the shape memory properties of the sample.

As seen in section 2.1, another way to evaluate the shape memory behaviour of a polymer is by following the recovery of an indented surface. In this way, several marks (holes and scratches with different known forces) have been performed in a selection of gamma irradiated polycyclooctene samples (samples irradiated at 50, 100, 150, 200 and 300 kGy). The depth of the marks has been analysed by confocal microscopy and surface profilometry, whereas the width has been calculated using optical microscopy. The recovery of the original surface has been followed by heating under an optical microscope.

3.2.2. Materials

3.2.2.1. Polycyclooctene (PCO)

This work has been performed employing the same commercially available polycyclooctene Vestenamer® 8012 (from Evonik Industries), already described at section 2.1.2.1.

3.2.3. Preparation of samples

All the irradiated PCO samples were prepared as explained in section 3.1.3.

3.2.4. Experimental section

3.2.4.1. Qualitative shape memory behaviour

Thermally-induced shape memory behaviour of all irradiated PCO samples were qualitatively evaluated by digitally monitoring the shape recovery process. A rectangular strip (10 mm x 35 mm x 1.5 mm) of the irradiated PCO samples was deformed in an elbow-shaped strip at a temperature 10 ºC above T_m (immersed in a water bath at 70 ºC) and cooled down to fix the temporary shape below T_m (in a water bath at 30 ºC -Figure 3.20-). Finally, this new geometry was heated again above T_m (T = 70 ºC), and the shape recovery process was registered by a digital camera.

Figure 3.20. Original and temporary shapes of a gamma irradiated PCO sample.

Demonstration of the thermal-induced shape memory effect is shown in Figure 3.21, Figure 3.22 and Figure 3.23, where shape recovery of previously elbow-shaped bent strips (10 mm × 35 mm × 1.5 mm) of irradiated PCO samples under 25, 200 and 1000 kGy radiation doses is documented. In contrast, non-irradiated PCO sample does not show shape memory properties due to a lack of temporary shape stabilizing crosslinks and subsequent flowing like a viscous liquid.

Table 3.4 shows the recovery time measured for all the irradiated PCO samples. As can be seen, the recovery time decreases as the gamma radiation dose increases due to the promoted rubbery elasticity from increased degree of crosslinking. From lack of shape memory capabilities of non-irradiated PCO, the limited chain crosslinking for PCO-25 and PCO-50 samples (21.3 and 47.6 wt% gel content, respectively -Table 3.1-) results in relatively weak shape memory behaviour with a non 100% complete recovery ratio. However, when the gel content is above 84 wt% (radiation doses higher than 75 kGy, Table 3.1) the related crosslinking degree growths enough, the PCO samples shows excellent shape memory behaviour.

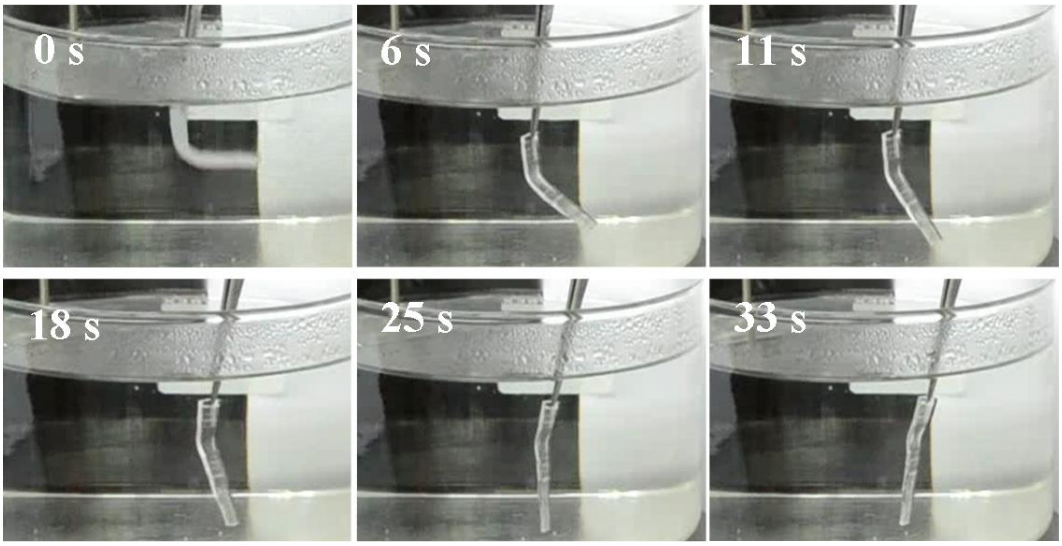

Figure 3.21. Shape memory recovery process of elbow-shaped bent strip for 25 kGy irradiated PCO sample.

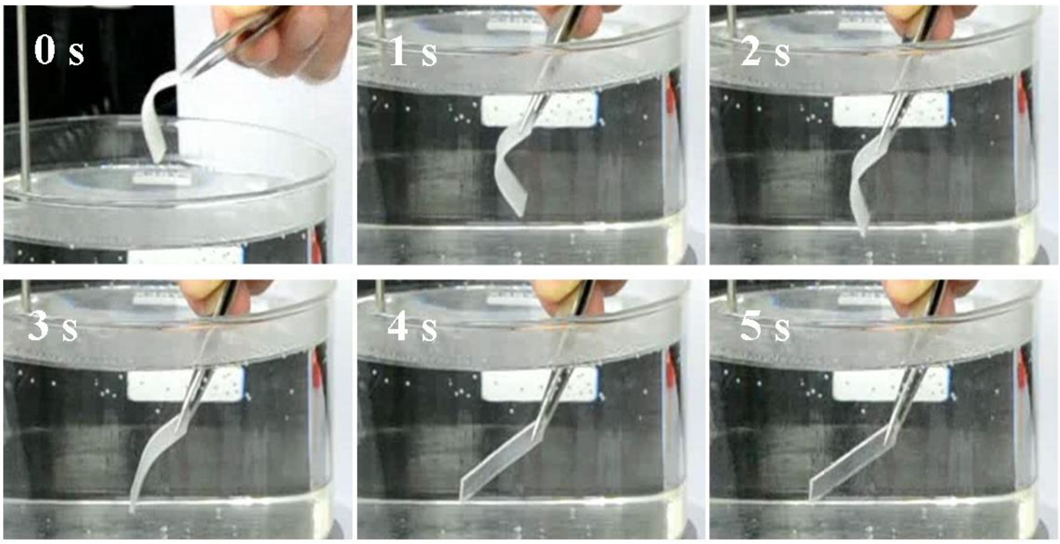

Figure 3.22. Shape memory recovery process of elbow-shaped bent strip for 200 kGy irradiated PCO sample.

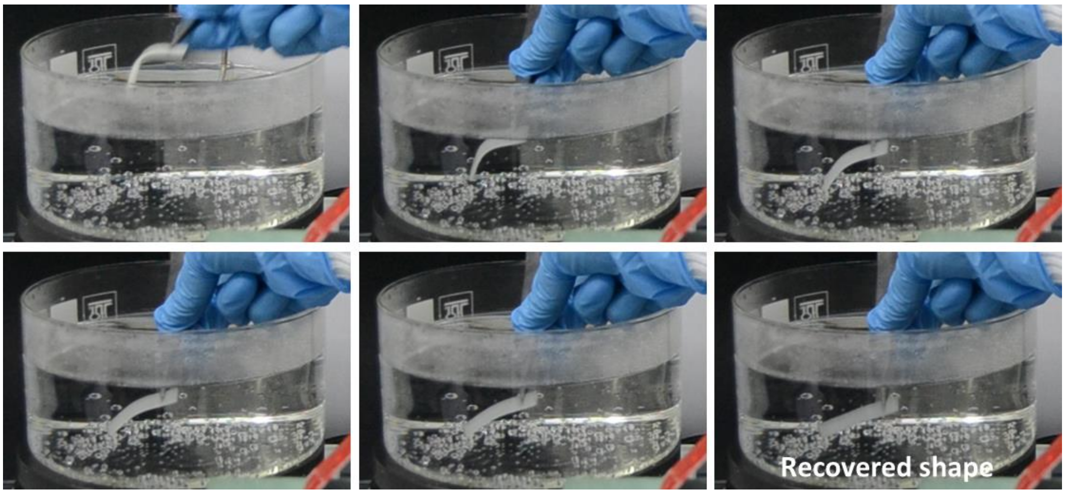

Figure 3.23. Shape memory recovery process of elbow-shaped bent strip for 1000 kGy irradiated PCO sample.

Table 3.4. Recovery times for all irradiated PCO samples.

Sample	Recovery time (s)	Remarks
PCO-25	33	Partial recovery
PCO-50	13	Partial recovery
PCO-75	8	Total recovery
PCO-100	7	Total recovery
PCO-125	6	Total recovery
PCO-150	6	Total recovery
PCO-175	5	Total recovery
PCO-200	5	Total recovery
PCO-300	4	Total recovery
PCO-500	3	Total recovery
PCO-750	3	Total recovery
PCO-1000	3	Total recovery

3.2.4.2. Quantitative shape memory behaviour

Shape memory behaviour on irradiated samples was quantitatively evaluated according to Garle *et al*. [54] by means of Thermo-Mechanical Analysis (TMA), employing a Mettler Toledo DMA-1 in the temperature range of 30-80 ºC at a rate of 4 ºC min^{-1}. The cross-section area of the samples was 4 mm × 1.5 mm, and the experiment was performed using two different initial clamp distances of 10 mm and 20 mm, respectively. The performed test was the same for all PCO irradiated samples (25 to 1000 kGy), recording the increase of the sample length as a function of temperature (see Figure 3.24). First, the sample was heated until 80 ºC (a temperature 20 ºC higher than transition temperature, Table 3.2) with the minimum force (F = 0.001 N) in order to allow relaxation of the polymer chains, so initial conditions are fixed (sample dimensions and temperature). Then, sample was stretched applying 1 N force, cooled at 4 ºC/min until 30 ºC and maintained at this temperature during 5 minutes. After this, the applied stress was reduced to the preload value (0.001 N) in order to fix the temporary shape. In the final step, the sample was heated again at 4 ºC min^{-1} and primary shape was recovered.

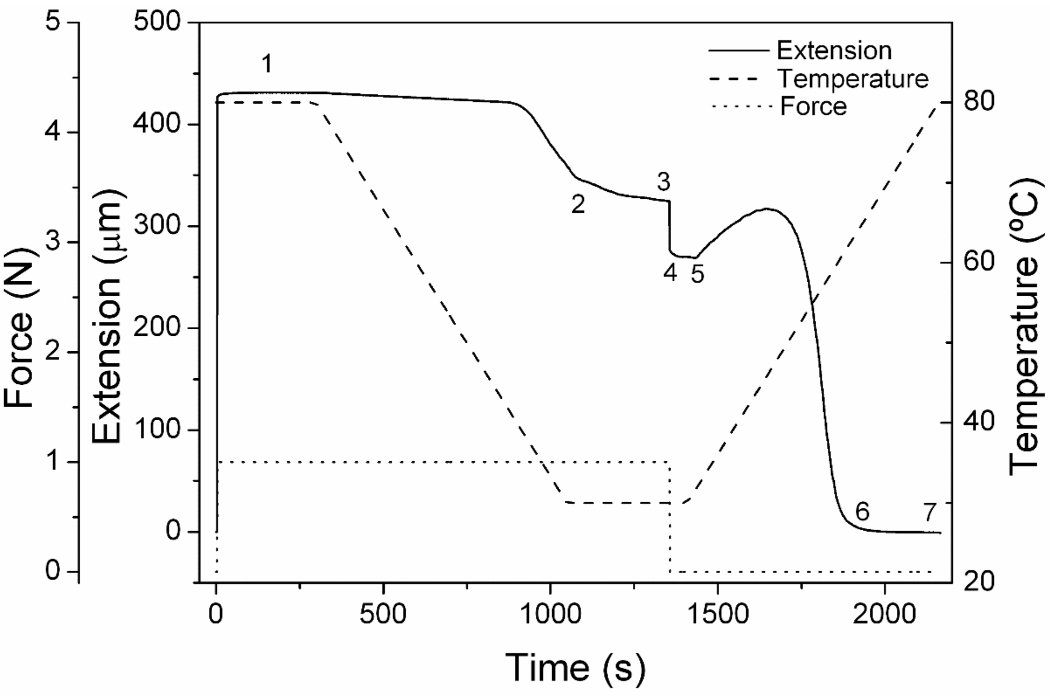

Figure 3.24. Extension, temperature and force of the cyclic thermo-mechanical experiment.

As explained in section 2.4.4.2, in these cyclic thermo-mechanical tests (Figure 3.24), shape-memory behaviour is usually quantified by parameters such as the strain fixity ratio, R_f, and the strain recovery ratio, R_r [40]. For each number of cycles (N), R_f quantifies the ability to fix a mechanical deformation, ε_m, resulting in a temporary shape, ε_u(N); whereas R_r quantifies the ability to restore the mechanical deformation of the permanent shape ε_p(N) after application of a certain deformation, ε_m, as it builds the ratio between the change in strain recorded during shape-memory effect $\varepsilon_m - \varepsilon_p$(N) and the change in strain in the course of programming given by $\varepsilon_m - \varepsilon_p$(N-1). From equations 3.4 and 3.5, it is observed that ideally R_f and R_r should be 100%.

$$R_f(\%) = \left(\frac{\varepsilon_u(N)}{\varepsilon_m(N)}\right) \times 100 \qquad (3.4)$$

$$R_r(\%) = \left(\frac{\varepsilon_m(N) - \varepsilon_p(N)}{\varepsilon_m(N) - \varepsilon_p(N-1)}\right) \times 100 \qquad (3.5)$$

In the performed mechanical tests (Figure 3.24), ε_u is the strain obtained after releasing the applied load (Point 4), ε_m is the strain before the load was released (Point 1), and ε_p is the final strain after heating and without load, i.e., after maximum recovery of the deformation (Point 6).

The obtained results are represented in Figure 3.25 and Figure 3.26 for all the PCO irradiated samples, with a sample free length of 10 mm and 20 mm, respectively. Moreover, Table 3.5 shows the corresponding strain fixity ratio, R_f, and the strain recovery ratio, R_r, calculated from equations 3.4 and 3.5, respectively, for all the PCO irradiated samples when 20 mm free length specimens are employed.

The obtained results show two interesting facts. On the one hand, the strain fixity ratio, R_f, decreases as the radiation dose increases (Table 3.5), and the strain recovery ratio, R_r, is higher when crosslink density grows. On the other hand, in Figure 3.25 it can be observed that, above 300 kGy dose, the employed fixing force (1 N) cannot counteract the contraction stress under cooling ($R_f < 0$). Increasing the sample free length to 20 mm (Figure 3.26), this problem disappears.

From Figure 3.25 and Figure 3.26 it seems that deformation (Extension 1 in Figure 3.24) depends on radiation dose (crosslink density) for the same applied stress, i.e. Extension 1 tends to be shorter as the radiation dose increases. As the radiation dose increases, the crosslink density is higher, so the strength of the network increases, decreasing the extensibility [55,56].

Next, the PCO sample is cooled down maintaining stress and thermal contraction takes place (Extension 2) so that it is higher as the received radiation dose increases. Extension 2 is associated to the contraction of the sample, following Hooke's law. Therefore it is determined by the value of the Young's modulus (equation 3.6), where σ is the stress, ε is the strain, F is the applied force, A is the area of the sample (width × thickness), dl is the change in length (the displacement), and l_0 is the initial length of the sample.

$$E = \frac{\sigma}{\varepsilon} = \frac{F/A}{dl/l_0} \tag{3.6}$$

The sample becomes more rigid when is cooling down, taking place the crystallization (the Young's modulus grows). Then, if the strain is constant in the cooling step, the stress grows [57]. However, when the force is maintained constant, deformation decreases [54], and here, as the applied force is considerable low (1 N), the polymer partially recovers the undergone strain during the cooling process.

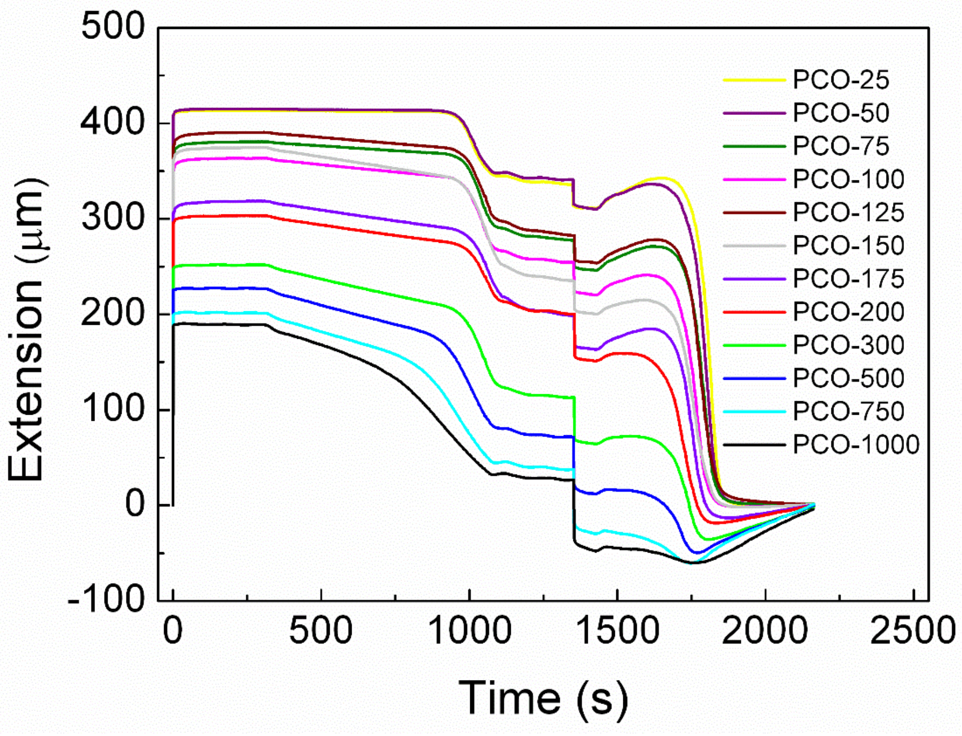

Figure 3.25. Thermo-mechanical cycle for PCO irradiated samples with 10 mm free length.

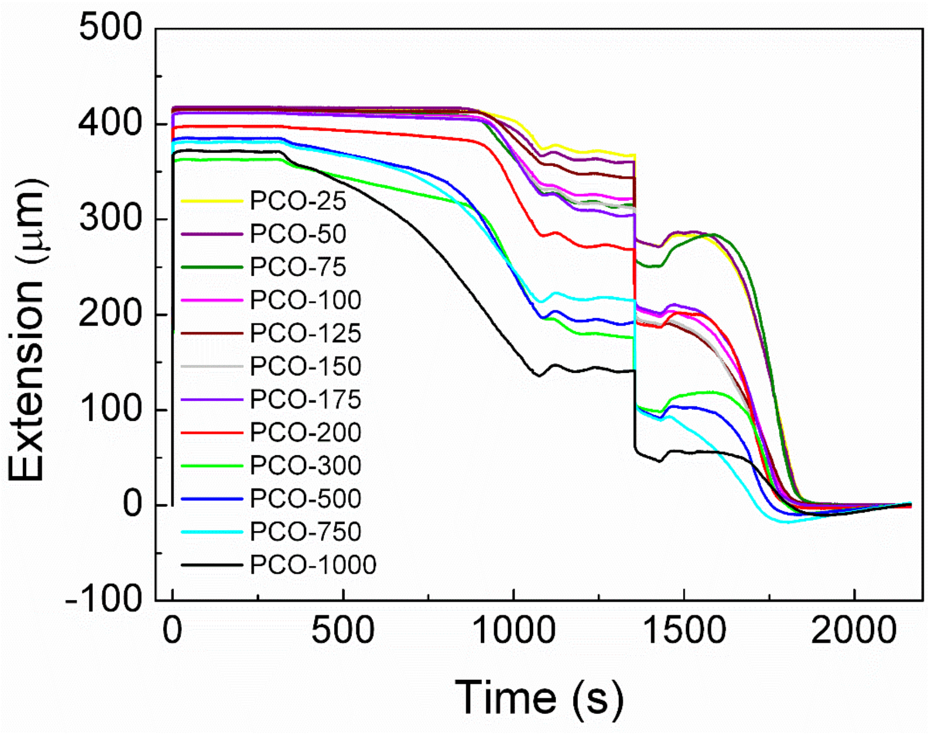

Figure 3.26. Thermo-mechanical cycle for PCO irradiated samples with 20 mm free length.

Table 3.5. Values obtained in the recovery process for all PCO irradiated samples with 20 mm free length.

Sample	**R_f (%)**	**R_r Ext 6 (%)**	**R_r Ext 7 (%)**
PCO-25	70.7	99.0	99.0
PCO-50	66.4	99.3	99.4
PCO-75	64.2	99.8	100.0
PCO-100	51.4	100.0	100.0
PCO-125	48.8	100.0	100.0
PCO-150	49.0	100.0	100.0
PCO-175	52.0	100.0	100.0
PCO-200	52.0	100.0	100.0
PCO-300	29.7	100.0	100.0
PCO-500	28.0	100.0	100.0
PCO-750	28.7	100.0	100.0
PCO-1000	15.7	100.0	100.0

During the cooling process crystallisation takes place, leading to an ordered crystalline phase instead of the amorphous one, being unit cells more stable than amorphous chains. Furthermore, the crystalline phase is stiffer than the amorphous one [58]. All these factors indicate that the larger the crystalline content of the polymer, the lower the contraction. Then, as the received dose increases, crystallinity diminishes, and thermal contraction is higher, resulting in a lower value of Extension 2.

Extension 3 is the result of keeping the sample at 30 ºC during 5 min. When the stress is removed the sample fixes its temporary shape (Extension 4). In these semicrystalline systems, fixation is directly associated to the mechanical strength of the crystalline phase counteracting entropy driven recovery of the deformed sample, so as radiation dose increases and crystallinity decreases, the fixation capability drops. Finally, the sample is maintained stress-free at 30 ºC during 1 min (Extension 5) before the system is heated again to proceed to the recovery process, where PCO samples recovered the original shape. Remnant deformation, Extension 6-7, is used to calculate the recovery ratio (R_r in Table 3.5). In these covalent crosslinked polymer networks, recovery process is related to crosslinking density and associated rubbery elasticity. Thus, higher recovery ratios are achieved from higher crosslink densities.

From data on Table 3.5, it can be concluded that the shape fixity ratio (R_f) decreases as radiation dose increases (more crosslinks) due to the lack of chain mobility after the deformation and cooling process [59]. Moreover, the recovery ratio (R_r) is higher when crosslink density grows from enhanced rubbery elasticity.

The shape fixity values (R_f) are not too high (among 16–70% on Table 3.5). It seems that this fact is directly related to the test procedure developed (the TMA measurement employed in this work). Several factors can be considered: a) the cooling step was performed maintaining the force constant and considerable low (1 N), b) the sample was cooled down slowly (4 ºC min^{-1}) and c) the sample was maintained at 30 ºC during 5 min. Therefore, during the shape memory fixation process (cooling step and isotherm at 30 ºC) the synergy of all these factors lead the samples to undergo a thermal process contraction which decreases the Extension 4 values used to calculate R_f. However, Table 3.5 also shows that R_f drops sharply from a radiation dose up to 200 kGy (from 52% for PCO-200 to 29% from PCO-300) for highly crosslinked systems.

Besides, Table 3.5 shows that all the irradiated samples are characterized by recovery ratios near 100%, including those irradiated at lower doses (PCO-25 and PCO-50), which, a priori, could seem to be in discrepancy with the qualitative data shown in section 3.2.4.1. Although the initial and final temperatures of both experiments are the same, the thermo-mechanical cycle is completely different considering the different deformation mode and thermal treatment. On the one hand, a tensile test with low stress (0.17 MPa) is applied in this section, so the associated deformation is very small and related recovery capacity is improved. In the qualitative experiments, the samples were bent and achieved deformation was considerable higher, with related lower recoverability. On the other hand, in those experiments, both a hot and a cold bath were used, where few second based recovery process occurred. However, here the experiments were performed with a heating ramp, which could allow polymer chains reordering as the temperature increases, together with higher time for recovery process.

In any case, the results in Table 3.5 demonstrate good shape memory behaviour for all the PCO irradiated samples from crosslinking process being predominant comparing with scission one for all the radiation doses employed, as it was concluded by the Charlesby-Pinner equation from gel content determination (the minimum dose for gelation found by extrapolating in the linear fit $s + s^{1/2} = 2$ is for the PCO samples 22 kGy).

Once demonstrated the shape memory ability of all the PCO irradiated samples studied (25 to 1000 kGy) over a thermo-mechanical cycle, shape memory behaviour during several cycles was studied. All the samples were tested performing ten times the same described TMA procedure in order to check the reproducibility of the shape memory behaviour for repetitive cycles. The obtained results are shown in Figure 3.27, Figure 3.28 and Figure 3.29, for PCO-25, PCO-200 and PCO-1000, respectively. In these figures it can be appreciate that there are practically no changes between cycles.

Furthermore, Figure 3.30 provides the 3D shape memory cycles for the same three samples, showing the variation of the sample deformation with the applied force and temperature, where outstanding reproducibility is observed for all samples. This figure also shows the mentioned decrease in deformation as the radiation dose (crosslink density) increases.

In Figure 3.30 it can be noted that before the applied stress was reduced to the preload value (0.001 N), the samples are maintained at 30 ºC during 5 min (maintaining the force) relaxing and shrinking slightly. Therefore, a decrease in extension in the final phase of cooling in Figure 3.30 is observed. Moreover, a slight increase in extension in the early phase of heating is seen because when the sample is heated initially undergoes a process of thermal dilatation (the peak about 1700 sec in Figure 3.24). This behaviour can be appreciated in all TMA Figures.

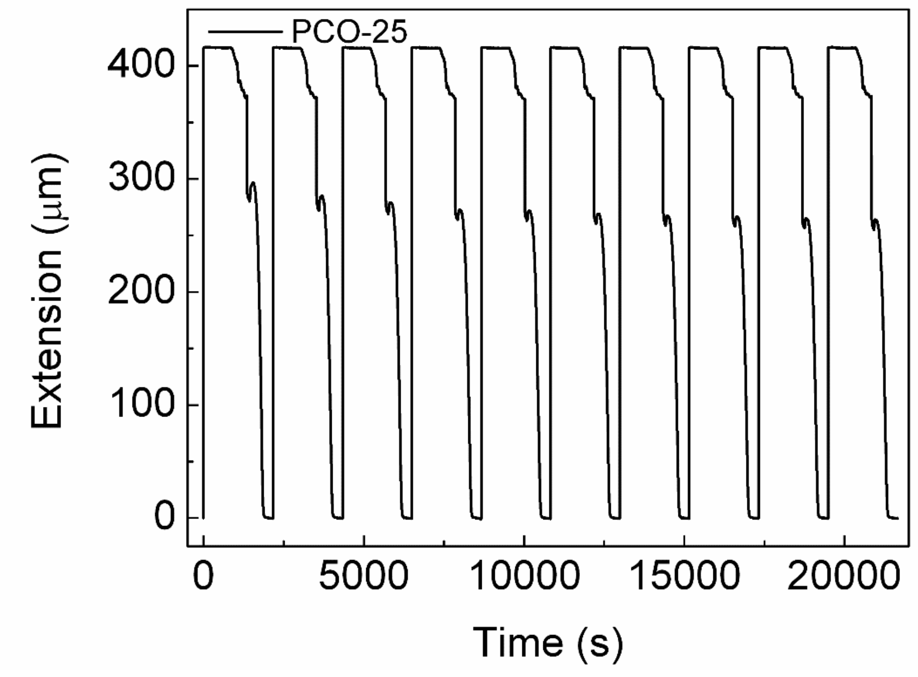

Figure 3.27. Cyclic thermo-mechanical response of irradiated PCO-25 sample during 10 cycles.

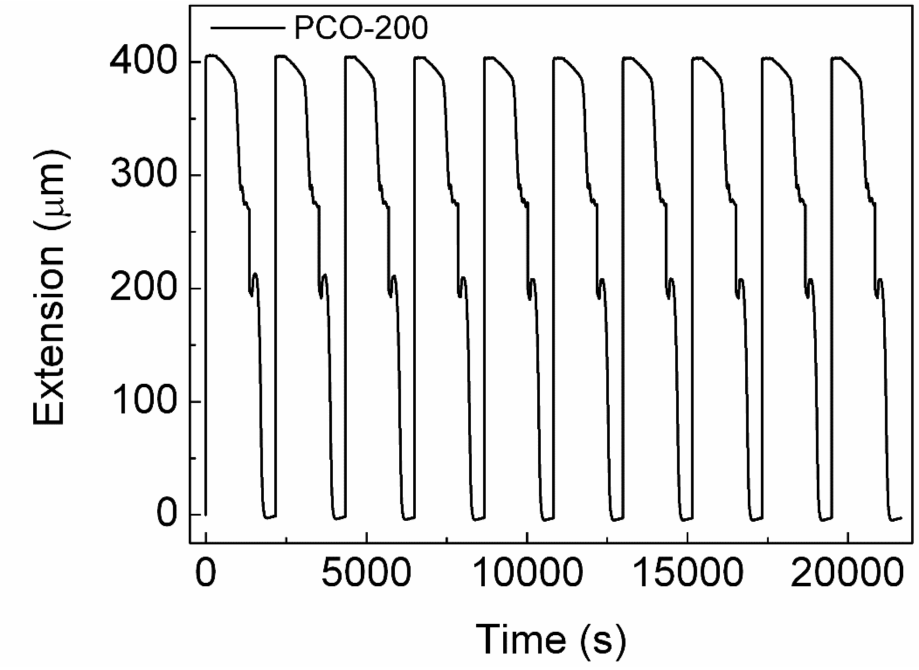

Figure 3.28. Cyclic thermo-mechanical response of irradiated PCO-200 sample during 10 cycles.

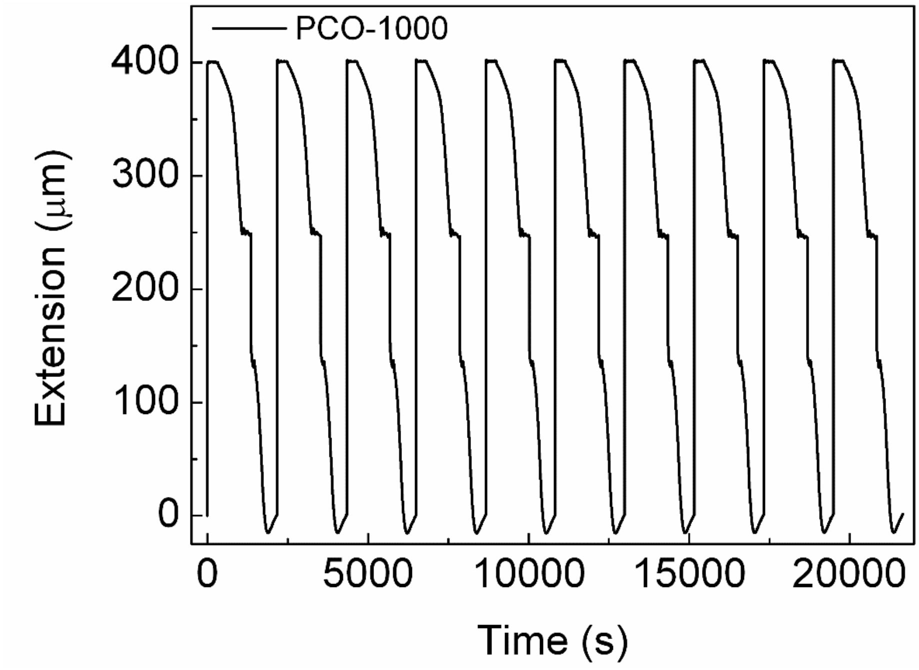

Figure 3.29. Cyclic thermo-mechanical response of irradiated PCO-1000 sample during 10 cycles.

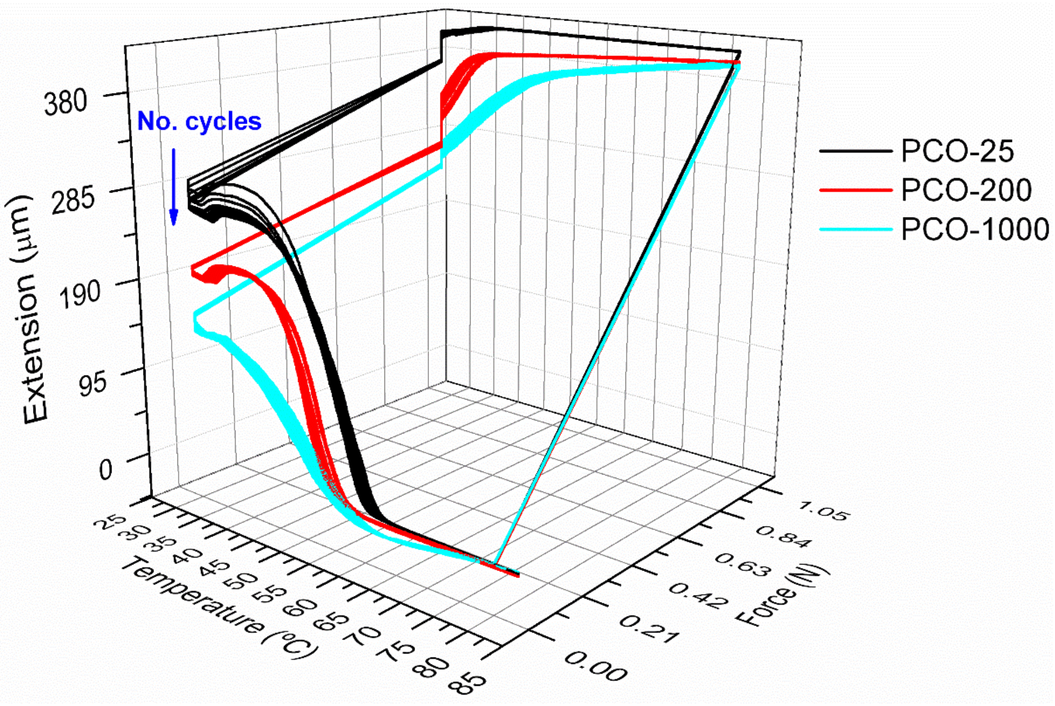

Figure 3.30. Three-dimensional thermo-mechanical cycles for PCO-25, PCO-200 and PCO-1000 samples (10 cycles).

a. PCO-200 sample

As it has been mentioned in the introduction, PCO-200 sample has been chosen in order to perform a deeper shape memory analysis. Thus, the PCO-200 sample has been subjected to different thermo-mechanical cycles varying different parameters such as the deformation force, the heating and cooling rates in order to view how these changes affect the shape memory properties of the sample.

The different experiments performed at PCO-200 sample can be appreciated in Table 3.6. In all TMA thermo-mechanical cycles, samples with 20 mm free length were used. First, the overall rate of the thermo-mechanical cycle was varied, both heating and cooling rate, deforming the sample with 1 N (experiments 1). Figure 3.31 shows no significant differences in the thermo-mechanical cycles when both heating and cooling rate are varied simultaneously from 1 to 4 ºC min^{-1}.

Table 3.6. Experimental conditions to perform shape memory experiments in PCO-200 sample.

Experiment	Force (N)	Cooling rate (°C/min)	Heating rate (°C/min)
1	1	1	1
	1	2	2
	1	3	3
	1	4	4
2	1	4	4
	1	10	4
	1	20	4
3	1	4	4
	1.5	4	4
	2	4	4

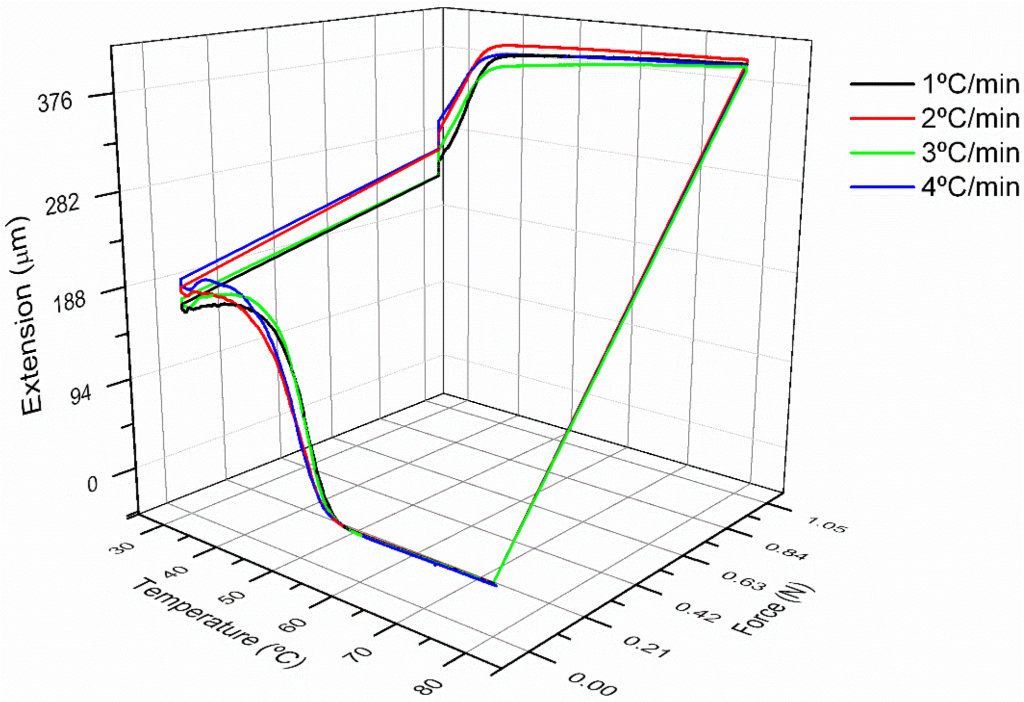

Figure 3.31. Thermo-mechanical cycle of PCO-200 sample varying heating and cooling rates.

Therefore, a second group of experiments was performed by deforming the sample with 1 N and cooling at different rates (4, 10 and 20 ºC min^{-1}). The results are shown in Figure 3.32. It can be observed that the three samples elongate equally due to the same deformation force applied. However, as the cooling process takes place faster (from 4 to 20 ºC min^{-1}), the sample fixes slightly better the temporary shape, which seems to indicate that the cooling speed has little effect on shape fixity.

Finally, the deformation force was varied from 1 to 2 N maintaining the overall rate of the thermo-mechanical cycle constant at 4 ºC min^{-1} (experiments 3 in Table 3.6). These experiments are shown in Figure 3.33, where several thermo-mechanical cycles for PCO-200 sample are represented. Thermo-mechanical cycles demonstrate that higher tensile force involves higher deformation (406 µm for 1 N, 596 µm for 1.5 N and 774 µm for 2 N). The PCO-200 sample was also tested with 2.5 N force, but the achieved deformation exceeded the measurement limit of the equipment (1 mm).

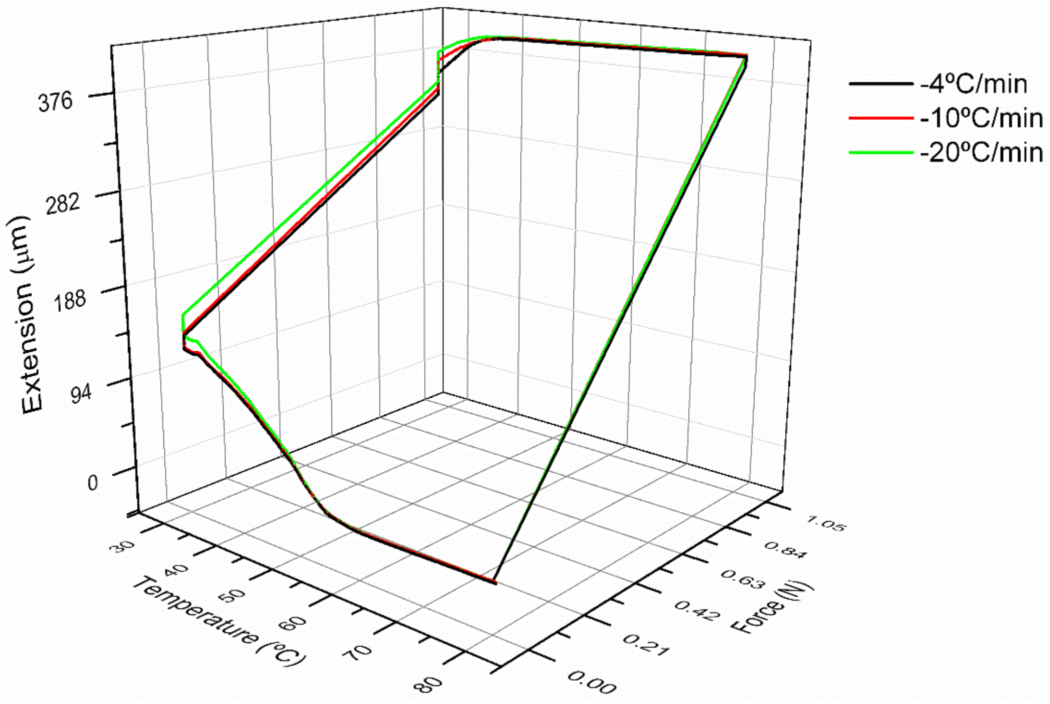

Figure 3.32. Thermo-mechanical cycle of PCO-200 sample cooled at different rates.

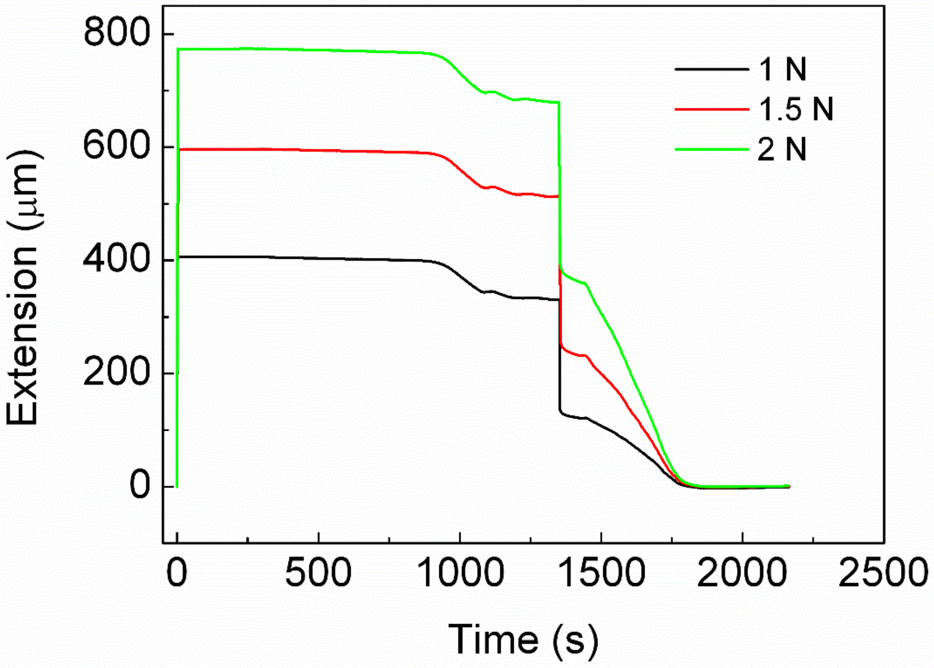

Figure 3.33. Cyclic thermo-mechanical response of PCO-200 sample elongated at different forces.

Next, the sample is cooled down under stress and maintained 5 minutes at 30 ºC. Then, the stress is removed, fixing the temporary shape (about 1350 s), reaching a higher fixation as the deformation force increases. Heating again to 80 ºC without stress, when temperature reaches T_m, PCO-200 sample recovers the primary shape. In all cases, independently of the applied force and thus the generated deformation, the recovery is total.

Therefore, the most remarkable difference between the thermo-mechanical curves with different tensile forces (1, 1.5 and 2 N) lies in the achieved fixing ratio from higher counteracting shrinkage stress in cooling by higher force (2 N).

Previously, the shape memory behaviour during several cycles (ten) was studied for all the PCO irradiated samples. PCO-200 sample was additionally tested performing one hundred times the same described TMA procedure (1 N force, 4 ºC min^{-1} overall rate, 20 mm free length) in order to check the reproducibility of the shape memory behaviour (Figure 3.34).

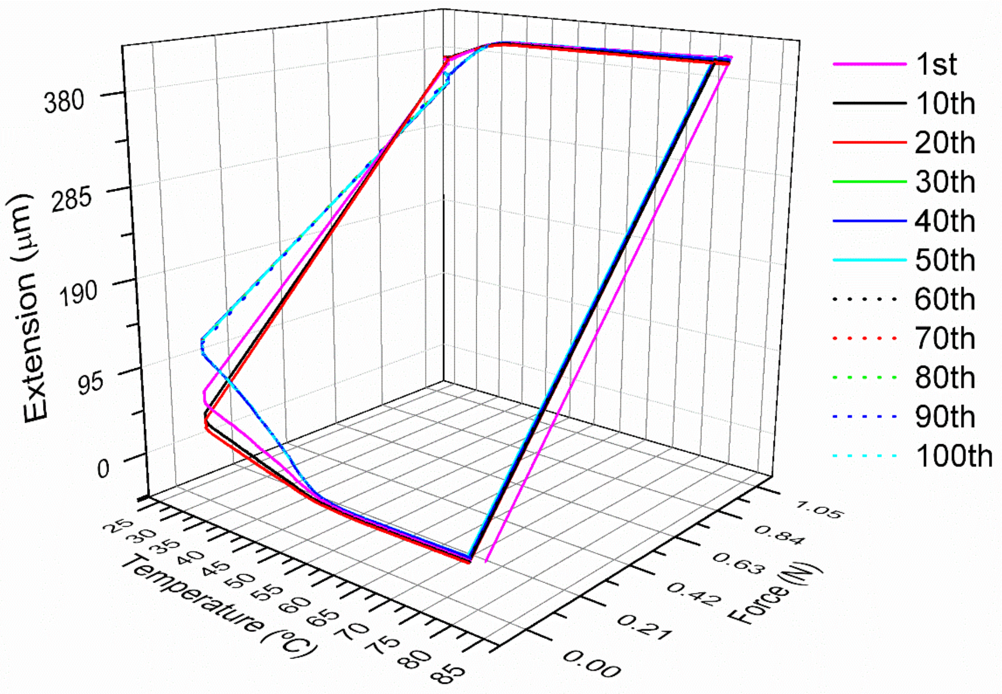

Figure 3.34. 100 TMA cycles performed in a PCO-200 sample

3.2.4.3. Self-repair measurements

As seen in Section 2.1, the ‘reversible plasticity shape memory effect (RP-SME)’ described by Mather *et al.* [60] can be used to repair surfaces. As it explained in section 2.1.4.3, a simple way to demonstrate whether the shape memory behaviour is useful for this is by indenting the surface and following the recovery of the mark by means of temperature. In this way, holes and lines have been performed using a Hardness Test Pencil model 318 from Erichsen. The marks were made in different irradiated samples (PCO-50, PCO-100, PCO-150, PCO-200 and PCO-300) with three known forces (5 N, 10 N and 15 N).

Subsequently, the self-repair properties of the PCO irradiated samples were evaluated using different techniques, as surface profilometry (Alpha-Step-D-100 profilometer from KLA-Tencor), confocal microscopy (LEICA LCS AP2 AOBS) and optical microscopy (LEICA DM 2500). So, the depth of the holes was measured by surface profilometry and confocal microscopy, whereas the depth of the lines was measured only by surface profilometry (due to technique limitations it is quite difficult to measure the depth of the lines by confocal microscopy). Additionally, the width of the lines and the diameter of the holes were determined using optical microscopy.

As the Shore D hardness measures the resistance of plastics toward indentation, it has been also determined as explained in section 2.1.4.2. Table 3.7 summarizes different parameters as the Shore D hardness, the indentation force (5, 10, 15 N), the indentation mark (hole or line) and the dimensions of them (depth, diameter or width) measured by the different techniques (surface or confocal profilometry, and optical microscopy).

Table 3.7 show that the hardness of the PCO irradiated specimen increases with radiation dose, that is, with the crosslinking percentage. As explained in section 2.1.4.2, hardness of semicrystalline polymers depends on numerous microstructural parameters (crystallinity, conformation, defects...), but is often correlated to the degree of crystallinity, which as shown in Table 3.2 also decreases with increasing radiation dose.

The depth values obtained both for holes and for lines show that indentation depth increases with applied force for all samples. In the case of the holes, where the depth has been measured by two different techniques, the same trend is observed. On the other hand, considering the hardness as a measurement of the resistance of the samples towards indentation, it could be expected a direct relationship among the hole or line depth and the hardness. However, as explained before, the relationship between morphological characteristics and hardness in semicrystalline polymers is extremely complex and depends on many variables [61]. This fact together with the method used to do the marks on the PCO irradiated samples (the Hardness Test Pencil), makes difficult the comparison among the different samples.

Table 3.7. Measurements for the different performed marks in PCO irradiated samples.

Sample	Shore D hardness	Force (N)	Hole			Line	
			Depth (µm)		Diameter (µm)	Depth (µm)	Width (µm)
			Surface profilometry	Confocal profilometry	Optical microscopy	Surface profilometry	Optical microscopy
PCO-50	38.8	5	22.5	17.5	589.1	17.6	568.8
		10	46.6	36.9	744.3	59.7	886.2
		15	73.7	61.3	845.8	54.3	761.1
PCO-100	37.2	5	21.8	16.8	582.9	15.0	525.8
		10	43.7	35.3	754.2	69.4	591.7
		15	76.7	67.6	879.0	94.1	774.4
PCO-150	41.8	5	24.7	19.6	634.0	12.9	458.8
		10	42.4	35.8	752.4	65.5	666.5
		15	83.6	66.5	870.4	143.5	640.7
PCO-200	42.9	5	27.1	19.5	624.3	21.3	513.5
		10	44.6	32.6	736.6	77.6	742.7
		15	78.0	56.1	860.0	132.8	691.4
PCO-300	44.9	5	20.6	16.2	604.4	13.7	526.0
		10	41.0	28.2	721.6	54.4	709.9
		15	65.4	49.9	841.3	132.9	678.7

Figure 3.35 shows the hole profiles corresponding to all indented PCO samples (PCO-50, PCO-100, PCO-150, PCO-200, PCO-300) measured by surface profilometry; whereas Figure 3.36, Figure 3.37 and Figure 3.38 show as example the 3D plots for the holes made with different forces (5, 10 and 15 N, respectively) on the PCO-100 sample (measured by confocal profilometry).

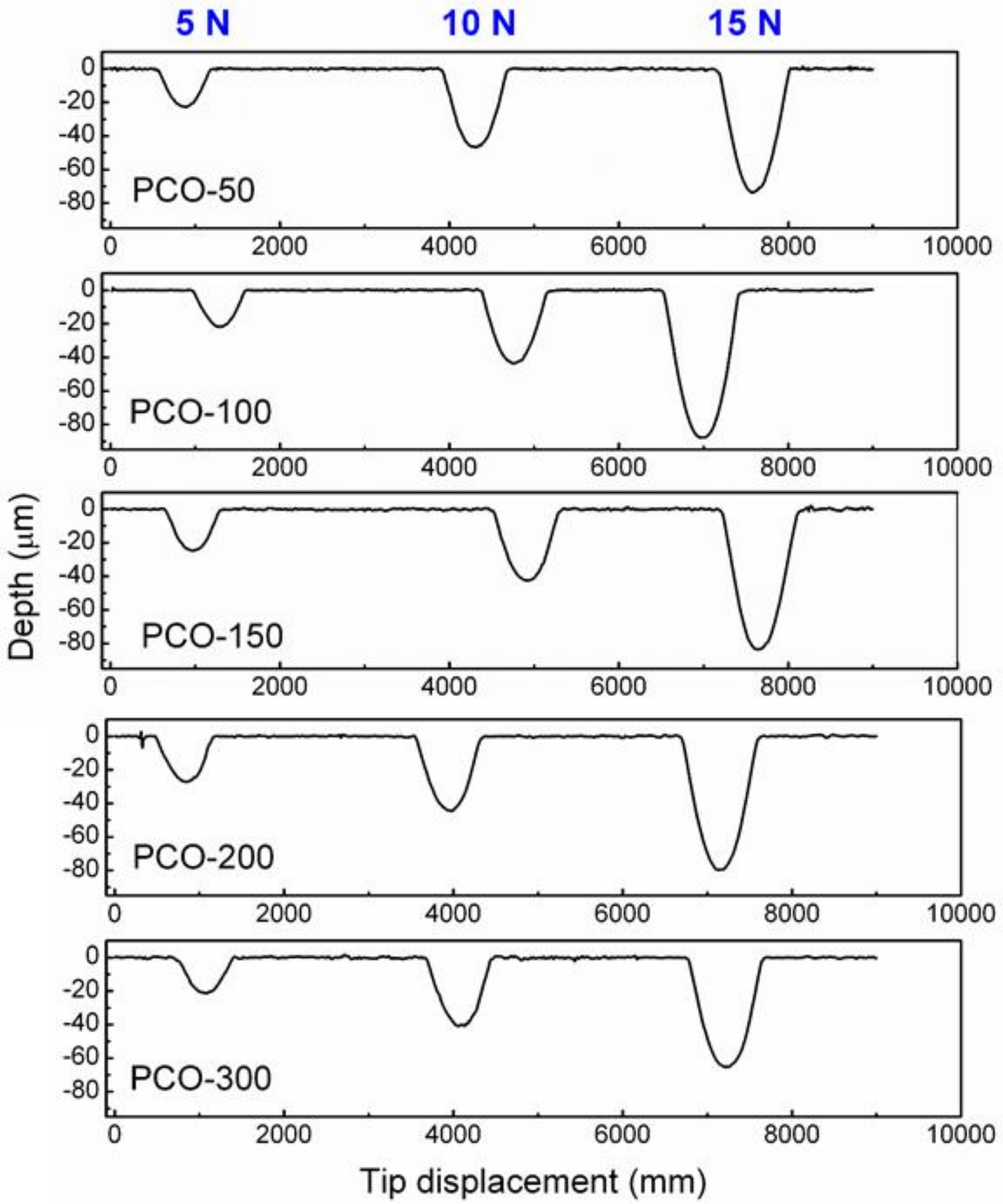

Figure 3.35. Measured profiles of holes by surface profilometry.

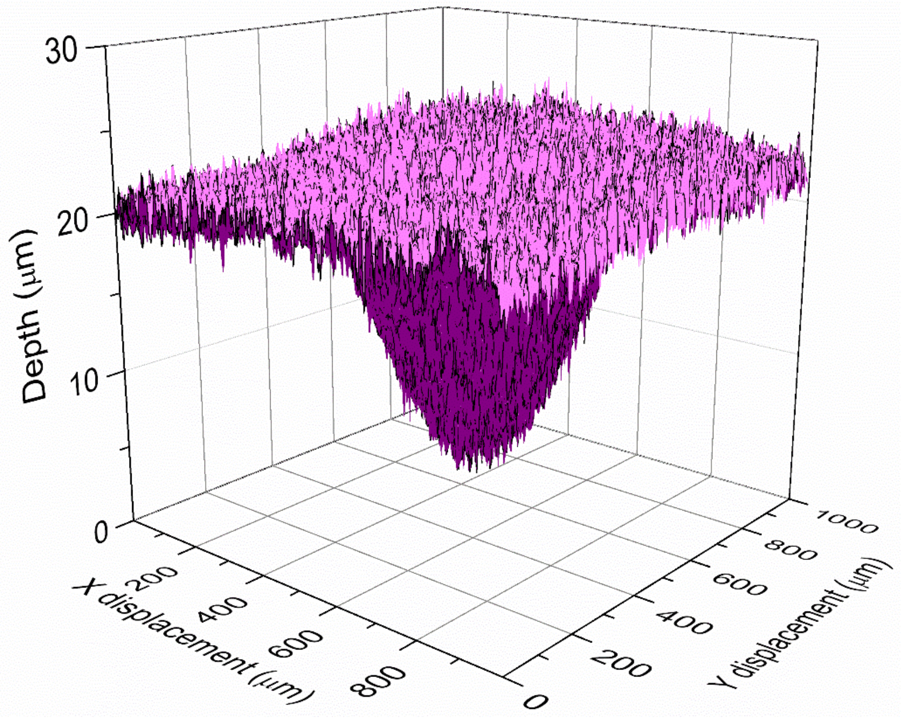

Figure 3.36. Confocal measurement of 5 N hole in PCO-100 sample.

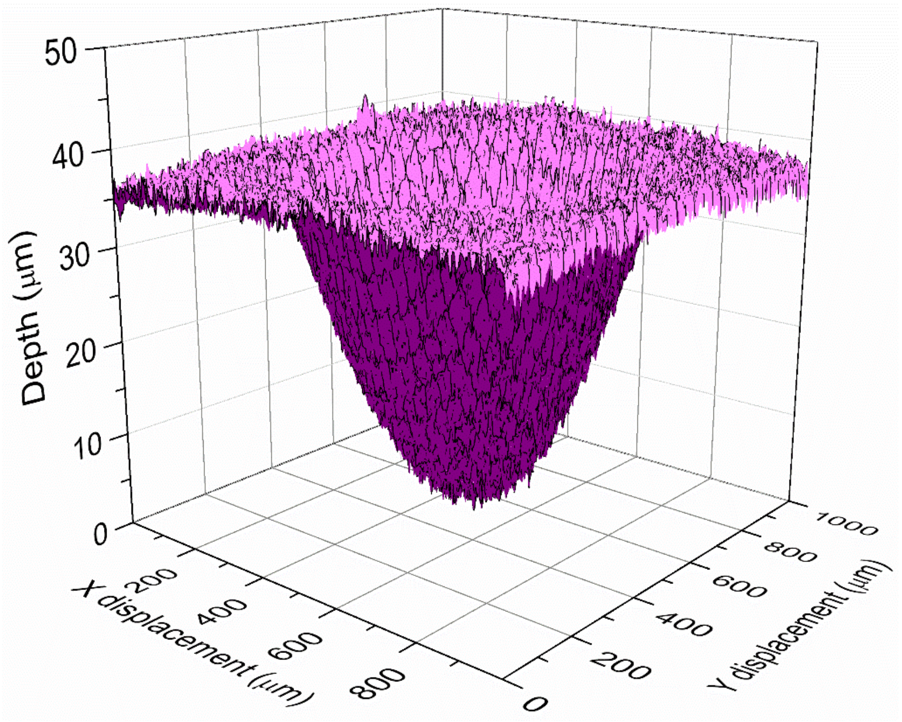

Figure 3.37. Confocal measurement of 10 N hole in PCO-100 sample.

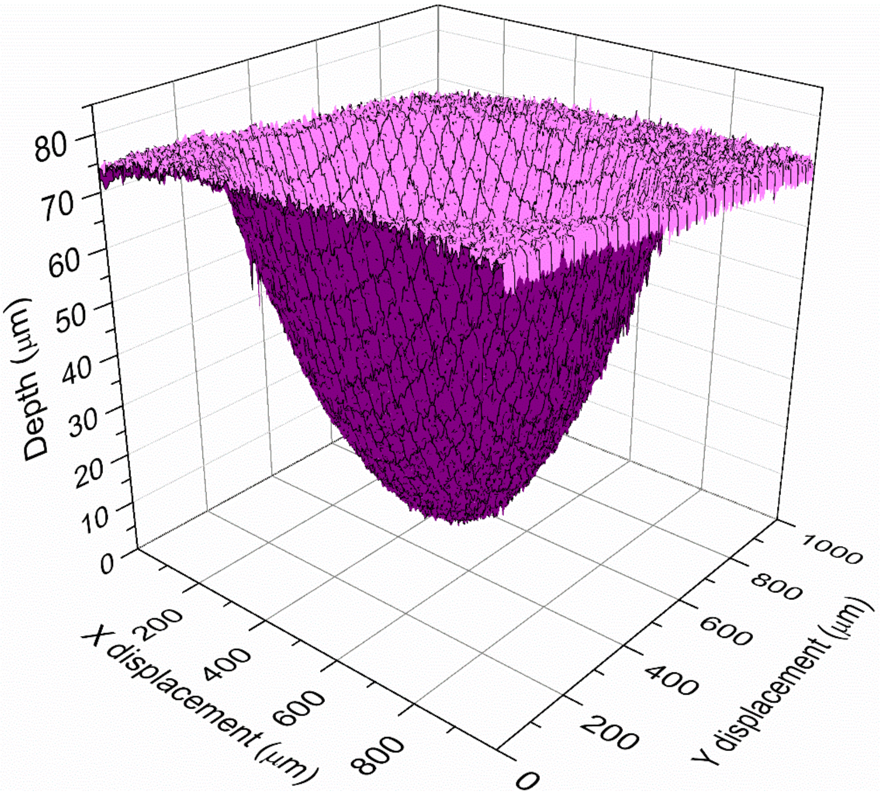

Figure 3.38. Confocal measurement of 15 N hole in PCO-100 sample.

Figure 3.39 shows the line profiles corresponding to the tested samples, where can be observed, for 10 and 15 N force, that the material rises when the lines were performed. This fact is due to the manner in which the lines were made (once the required spring tension is set, the Test Pencil was held upright and placed its point on the test surface to draw a line), and also it will recover when the self-repairing behaviour takes place.

On the other hand, the hole diameters and line widths have been measured by optical microscopy. The obtained results are summarized on Table 3.7. Figure 3.40 shows the diameters of the different holes for PCO-150 sample, whereas in Figure 3.41 the width of the different lines in the same sample is represented. All PCO irradiated samples follow the same pattern, diameters or widths among 600 μm for 5 N, 750 μm for 10 N and among 850 μm for 15 N forces. In the case of lines, the width values are lower than in holes but, as it has been explained previously, the material rises when marking the lines, causing difficulties to the accurate measurements. In summary, it can be seen that generally marks are wider with the applied force.

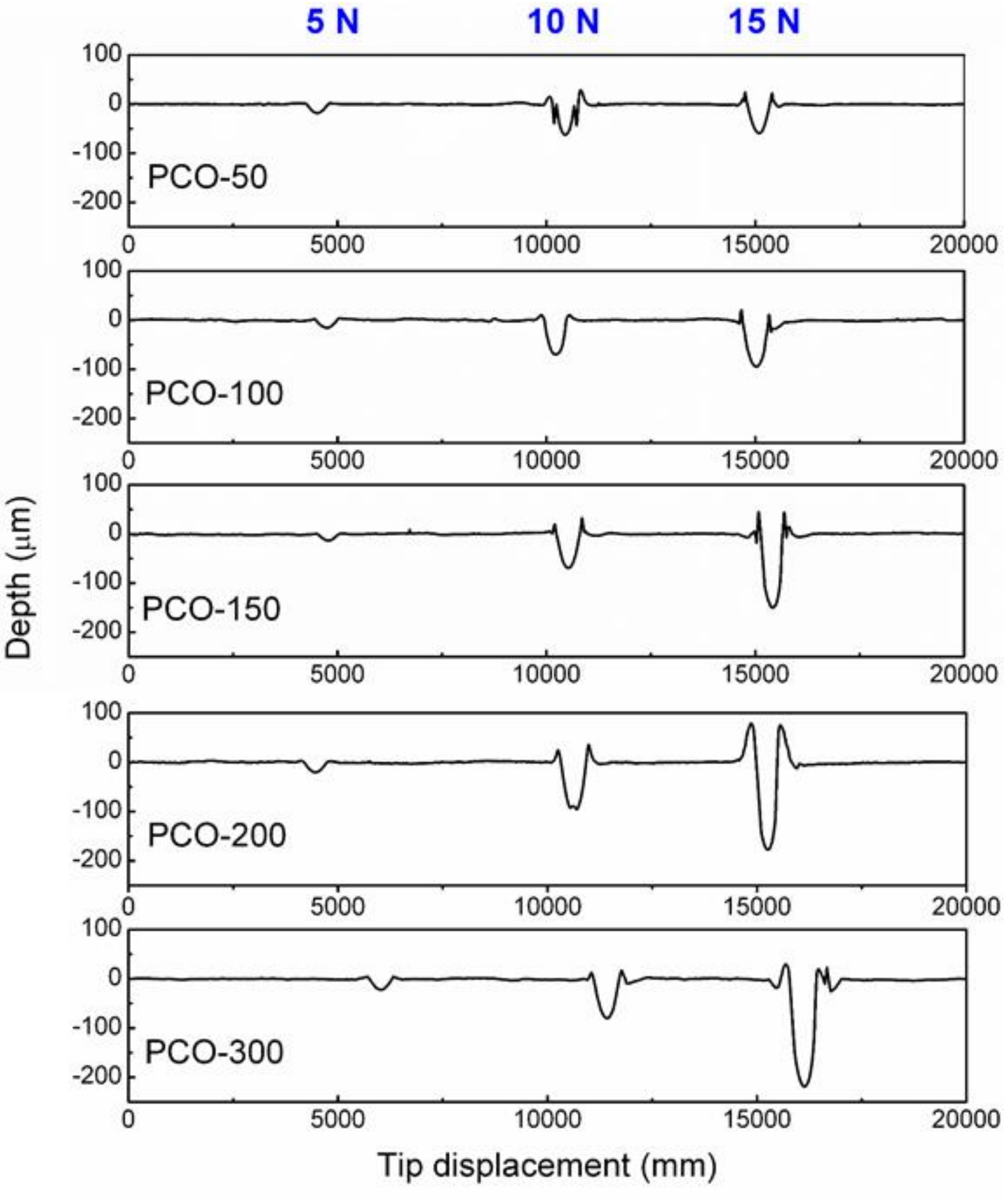

Figure 3.39. Measured profiles of lines by surface profilometry.

Figure 3.40. Diameters of the holes in PCO-150 sample with a) 5 N, b) 10 N, c) 15 N.

Figure 3.41. Widths of the lines in PCO-150 sample with a) 5 N, b) 10 N, c) 15 N.

Finally, the thermal induced self-repair effect was followed *in situ* by optical microscopy (Nikon Eclipse L-150 equipped with an Imaging source camera) recording the recovery of the samples. The samples were put at room temperature under the microscope, and they were heated using the Linkys 32 program. With IC Capture program, the recovery of the samples was recorded as the temperature was increasing (above its transition temperature, T_{trans}). When recovery process was finished, the sample was slowly cooled to room temperature. The variation in the line and hole depths were also measured following the recovery phase under the same heating process of perpendicular cuts of the performed marks (edgewise views of the marks) on replicas by optical microscopy.

From the different recovery videos, several photos at different times (different temperatures) can be extracted. Figure 3.42 to Figure 3.47 show the evolution of the recovery process for 15 N hole with temperature for some samples (PCO-50, PCO-100 and PCO-200), monitored by optical microscopy. Moreover, the recovery of 15 N line in PCO-300 sample is represented in Figure 3.48 (frontal view) and

Figure 3.49 (side view). Note that the variations in the brightness in photos come from melting process of crystallites.

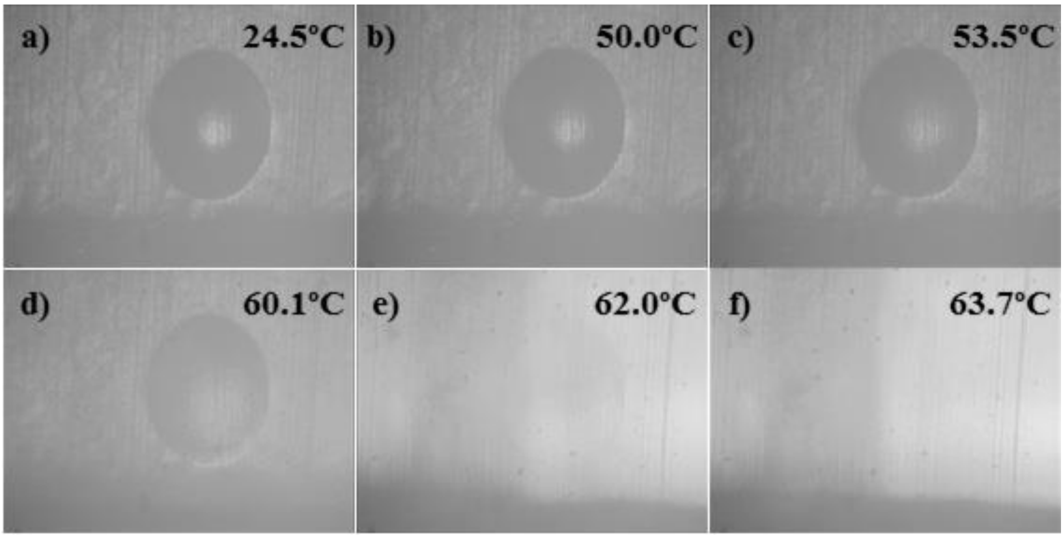

Figure 3.42. Recovery process for 15 N hole in PCO-50 sample (frontal view).

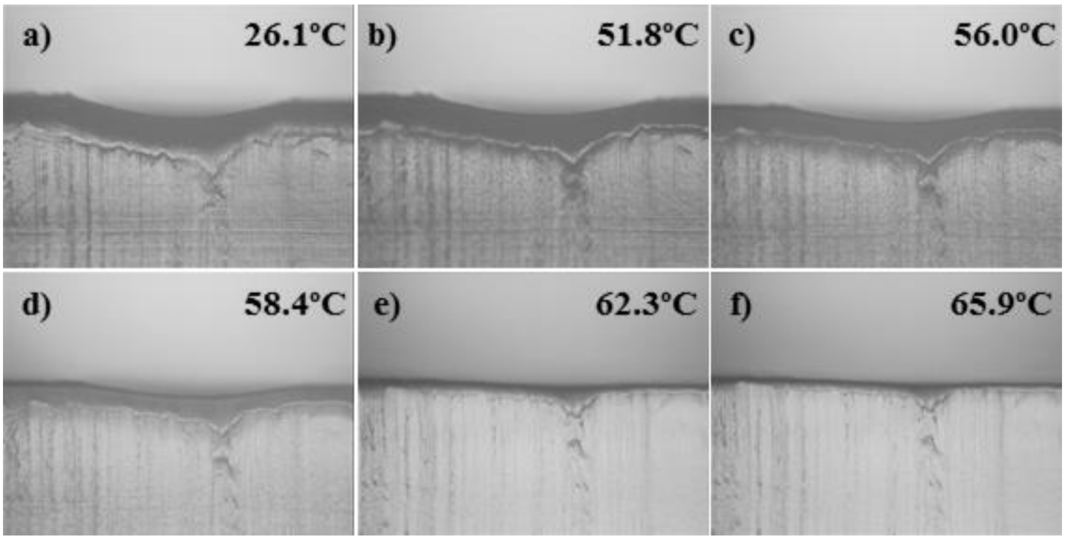

Figure 3.43. Recovery process for 15 N hole in PCO-50 sample (edgewise view).

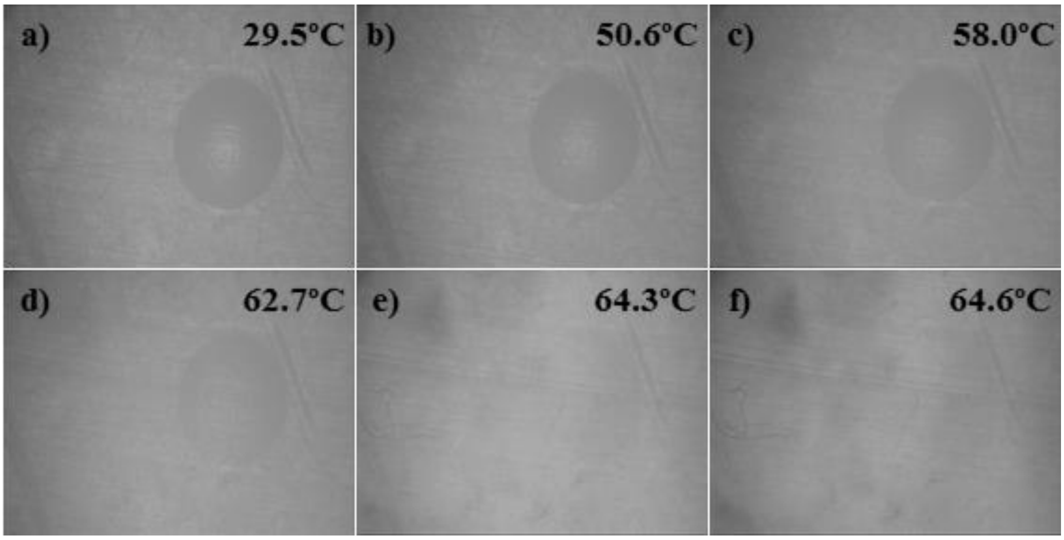

Figure 3.44. Recovery process for 15 N hole in PCO-100 sample (frontal view).

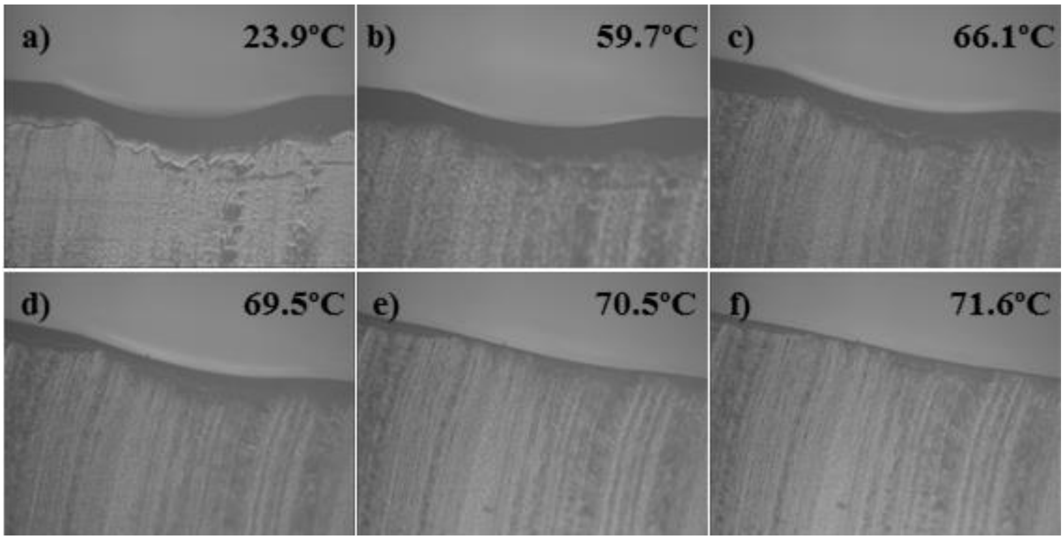

Figure 3.45. Recovery process for 15 N hole in PCO-100 sample (edgewise view).

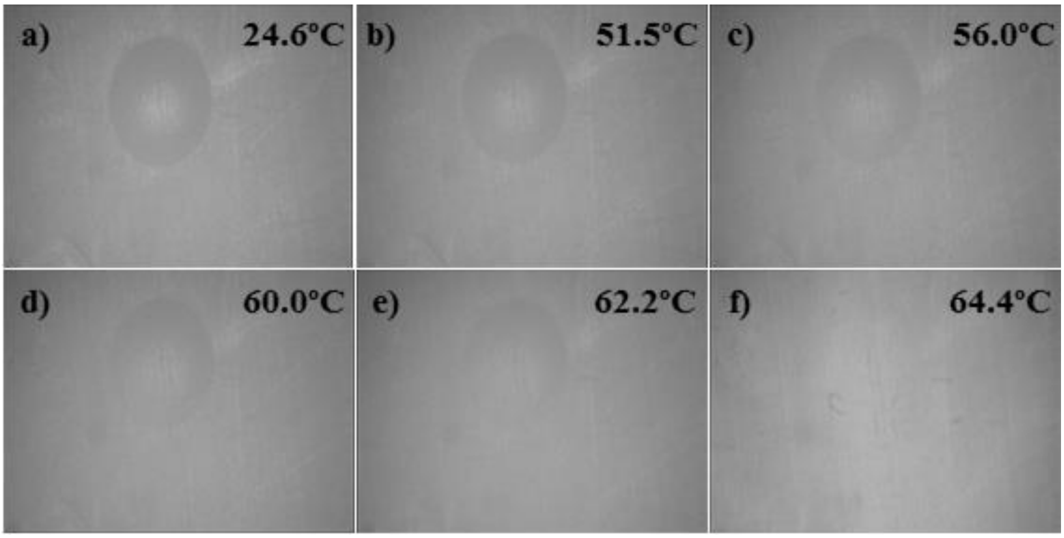

Figure 3.46. Recovery process for 15 N hole in PCO-200 sample (frontal view).

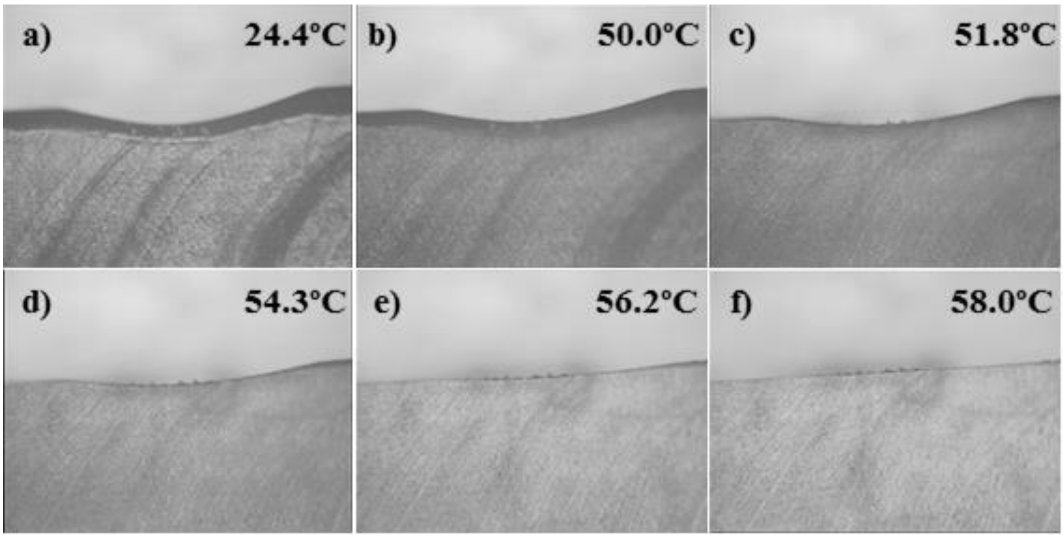

Figure 3.47. Recovery process for 15 N hole in PCO-200 sample (edgewise view).

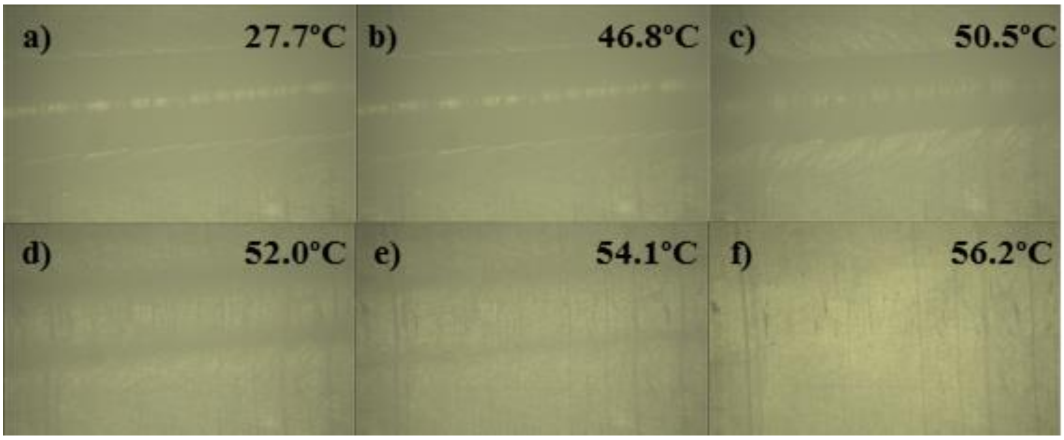

Figure 3.48. Recovery process for 15 N line in PCO-300 sample (frontal view).

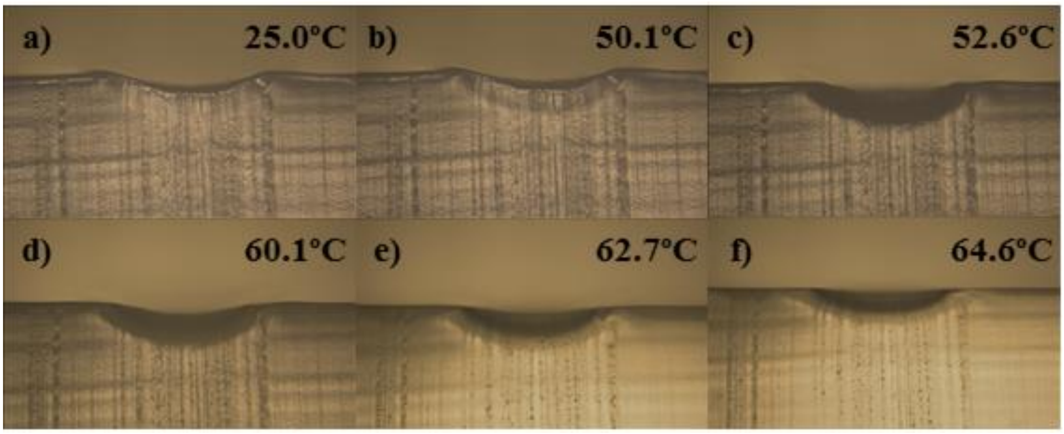

Figure 3.49. Recovery process for 15 N line in PCO-300 sample (side view).

In conclusion and as expected, heating the PCO gamma irradiated samples at a temperature higher than its T_{trans}, the deformations made on the surface disappear, independently of the shape (hole/line) or the employed force (5 N, 10 N, 15 N).

3.2.5. Conclusions

Shape memory behaviour of polycyclooctene irradiated with different amount of gamma rays has been evaluated both qualitative and quantitatively. Qualitative analysis demonstrated promoted shape memory response from high enough crosslinkings at radiation doses above 75 kGy. Besides, the quantitative analysis using TMA showed that, although the strain fixity ratio (R_f) decreases as radiation increases, all the irradiated samples were characterized by recovery ratios near 100%. Finally, the good reproducibility of the shape memory was demonstrated by performing 10 TMA cycles to each sample.

Moreover, different possible conditions to perform the thermo-mechanical cycles in order to evaluate the shape memory properties have been tested in the PCO-200 sample, showing a good shape memory behaviour in all cases.

Additionally, the surface of different samples was marked with different forces and the depth was analysed by surface and confocal profilometry. The recoverability of the initial state when they were heated was demonstrated by optical microscopy.

In summary, ionizing energy is presented as an excellent means of crosslinking and providing shape memory performance in PCO. This opens the opportunity to produce shape memory components over a wide range of profile gauges in continuous moulding process with faster rates and avoiding heat and time consume. Besides, from DSC data, the macromolecular response of PCO with radiation seems to be totally different from chemical crosslinking processes (radical initiator), and the structure and behaviour of network of crystallites with radiation dose for reversible shape memory response should vary. If this phenomenon is extended to all semicrystalline elastomers, further studies should be performed under radiation doses due to two-way reversible shape memory behaviour being affected by kinetics of crystallization. Then, radiation could be a new way to shift the reversibility range without altering the chemical structure of the polymer.

3.3. Free volume measurements

3.3.1. Introduction

As explained in Chapter 1, polycyclooctene (PCO) is a semicrystalline polymer that demonstrates outstanding shape memory properties by crosslinking the macromolecular chains. The melting temperature of the macromolecular network is the shape memory transition temperature [51,62], and the required chemically crosslinked structures can be obtained using a monofunctional peroxide or by ionizing radiation as gamma rays. In particular, the peroxide (or the gamma rays) originates free radicals which are able to pull out an hydrogen atom from the polymer, so polymeric macroradicals can react and recombine to obtain a crosslinked network [13]. However, in these semicrystalline systems, the increase in crosslink density originates, in general, a decrease in the crystallization temperature of the polymer, so crystallites become smaller and can be dispersed in the crosslinked matrix [63]. Thus, the balance between the elasticity, due to the crosslinked structure, and the thermal induced molecular switching of polymer chains with temperature above and below melting temperature, determines the shape memory response [37]. Therefore, it is expected a direct relation between crosslinks and mobility of the chains, where the effect of free volume hole size within the polymer can play an important role in the crosslinked structure, crystallinity and overall shape memory effect.

In particular, it is important to consider the effect of the free volume in these polymers, i.e. the volume that is not occupied by the molecules themselves [64]. Free volume holes play a key role in the mechanical, thermal, relaxation and diffusion properties of polymers [65] and positron annihilation lifetime spectroscopy (PALS) is a unique technique for measuring the subnanoscopic free volume hole sizes in polymers.

As it demonstrated throughout this chapter, ionising radiation is an alternative to crosslink macromolecular chains instead of using peroxides. This technique has different advantages when compared to peroxides, such the reduction of volatile organic compounds, higher purity and lower toxicity [66].

This section shows a preliminary approach to link free volume holes and shape memory properties. In particular, (i) it is established the structure-free volume-shape memory property relationship, in order to physically explain the shape recovery at the nanoscale for the design and rationally control the macroscopic shape memory properties of these materials; and (ii) it is verified the non-cytotoxic nature of the gamma irradiated polycyclooctene, in contrast with the same material crosslinked with dicumyl peroxide. To do so, the cytotoxicity of crosslinked PCO samples using both peroxide (PCO-1) and gamma radiation (PCO-25, PCO-200) are studied in collaboration with the Department of Physics of the University of Minho (Braga, Portugal).

Thus, to analyse the relation between free volume hole size and shape memory, PALS was used to probe the changes in the mean free volume holes' size as a function of temperature. Already in 1996 Ito *et al*. [67] studied the free volume properties of different shape memory polymers measured by PALS. But in the present study free volume hole size values were further compared with the gel fraction and shape recovery of different PCO irradiated samples (25, 50, 75 and 200 kGy). Finally, thermo-mechanical analysis (TMA) was used to test the shape memory properties of the samples.

Additionally, it seems interesting to measure the free volume of a sample at the different stages of the shape memory process. The subnanoscopic free volume holes can be measured *in situ* by PALS, so it is possible to analyse the free volume properties at different processes: (i) when the original sample is heated from 10 ºC to 70ºC (ii) when the deformed sample is heated from 10 ºC to 70 ºC, allowing the recovery of the original shape (that is, *in situ* measurements of the free volume during the recovery process), and (iii) the recovered shape at 10 ºC and room temperature (25 ºC). PALS measurements have been made in collaboration with the Department of Electricity and Electronics of the University of the Basque Country.

3.3.2. Materials

3.3.2.1. Polycyclooctene (PCO)

This work has been performed employing the same commercially available polycyclooctene Vestenamer® 8012 (from Evonik Industries), explained already described at section 2.1.2.1.

3.3.2.2. Dicumyl peroxide (DCP)

Likewise, the dicumyl peroxide used was the same aforementioned at section 2.1.2.2.

3.3.3. Preparation of samples

The sample crosslinked with peroxide (PCO-1) was prepared as explained in section 2.1.3, whereas the samples crosslinked by gamma radiation (PCO-25, PCO-50, PCO-75, PCO-200) were obtained as seen in section 3.1.3.

3.3.4. Experimental section

3.3.4.1. Cytotoxicity Assay

The indirect cytotoxicity evaluation of the samples was conducted according to the ISO 10993-5 standard test method. Briefly, the extraction media were prepared by immersing the samples (13 mm of diameter) in a 24-well tissue culture polystyrene plate with DMEM (containing 1 g.L^{-1} glucose (Gibco) supplemented with 10% FBS (Biochrom) and 1% P/S (Biochrom)), at 37 ºC in a 95% humidified air containing 5% CO_2 and incubated for 24 h. A 20% of Dimethylsulfoxide (DMSO, Sigma

Aldrich) was used as a positive control and the cell culture medium was employed as negative control.

At the same time, the MC3T3-E1 pre-osteoblast cells were seeded in the 96-well tissue culture polystyrene plate at the density of 3×10^4 cells.mL^{-1} and incubated for 24 h to allow cell attachment on the plate. After 24 h, the culture medium from the 96-well tissue culture polystyrene plate was removed and the as prepared extraction media were added to the wells (100 µL). Afterward, the cells were incubated for 24 h and 72 h and after each time, the evaluation of the cell viability was quantified with 3-(4,5-dimethylthiazol-2-yl)-2,5-diphenyltetrazolium bromide (MTT) assay.

The MTT assay measures the mitochondrial activity of the cells, which reflects the viable cell number. At each time point, the medium of every well was removed and fresh medium containing 10% MTT solution (stock solution of 5 mg MTT.mL^{-1} in PBS; Sigma Aldrich) was added. The viable cells with active metabolism convert MTT into a purple coloured formazan product. After 2 h of incubation, the MTT crystals were dissolved with DMSO and the optical density was measured at 570 nm.

All quantitative results were obtained from four replicate samples and controls and were analysed as the average of viability ± standard deviation (SD). The percentage of cell viability was calculated from equation 3.7:

$$Cell\ viability\ (\%) = \frac{Absorbance\ of\ sample}{Absorbance\ of\ neg.control} \times 100 \qquad (3.7)$$

This study evaluates and compares the cytotoxicity of four different PCO samples: pure PCO (not crosslinked), PCO-1 (sample crosslinked with 1 wt% of dicumyl peroxide), and the gamma irradiated samples PCO-25 (dose: 25 kGy) and PCO-200 (dose: 200 kGy), chosen as they are the samples irradiated at the lowest dosage (PCO-25) and the most characterized sample (PCO-200). The effects of polymer extract medium on the metabolic activity of MC3T3-E1 pre-osteoblast cells were evaluated using the MTT assay after 24 h and 72 h (Figure 3.50). According to the

ISO standard 10993-5, when the cell viability reduction is more than 30%, the samples are considered cytotoxic. So, the sample PCO-1 is cytotoxic, whereas raw material and irradiated samples are non-cytotoxic.

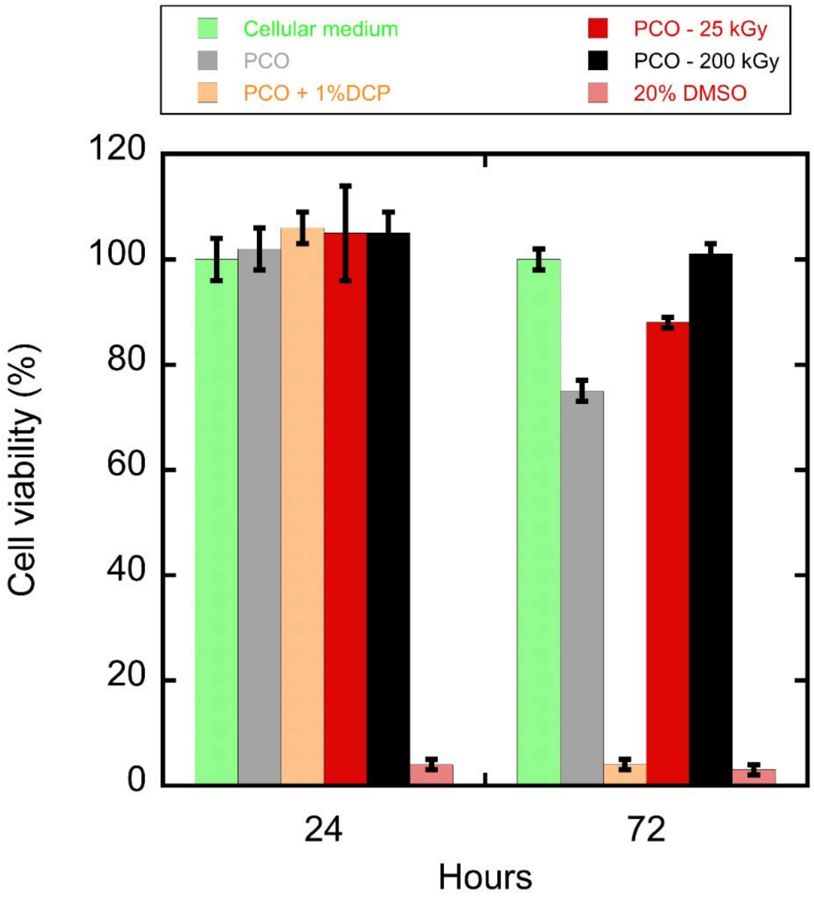

Figure 3.50. Cell viability after 24 h and 72 h exposure to extract medium of the different test specimens, negative control (cellular medium) and positive control (20% DMSO).

In this manner, thermo-active gamma irradiated PCO emerges as a non-cytotoxic alternative contrasting to cytotoxic shape memory PCO crosslinked via dicumyl peroxide (as shown in Figure 3.50) due to its metabolic activation into alkoxy radicals [68]. The absence of residual peroxide and related decomposition products opens biomedicine related potential applications of this shape memory polymer, such as their use as cell culture or smart scaffolds for tissue engineering [69].

3.3.4.2. Shape Memory Behaviour

As previously seen, PCO is a thermally induced shape memory polymer, where the transition temperature corresponds with the melting temperature (T_m). Therefore, in order to evaluate the shape memory behaviour, a cyclic thermo-mechanical experiment was designed in the stress-controlled mode, according to Garle *et al.* [54], in the same way as explained in section 3.2.4.2. Only the irradiated samples were studied by this technique as raw PCO sample (PCO-0) flows like a viscous liquid above the melting temperature and does not demonstrate shape memory capabilities.

Samples shaped as strips, cut from the irradiated PCO sheets, with a cross-section area of 4 x 1.5 mm^2 and initial clamps distance of 20 mm was employed. TMA was conducted on a Mettler Toledo DMA-1 in the temperature range of 30-80 ºC at a heating rate of 4 ºC min^{-1}. Note that the margin of error for displacement measurements is deemed to be null as the technical resolution is 2 nm and the sensitivity is 30 nm. The increase of the sample length was recorded as a function of temperature. The temperature range was selected taking into account the melting temperatures listed in Table 3.2.

Samples were heated until 80 ºC with just a minimum force (F = 0.001 N). This temperature was selected as it is 20 ºC above the transition temperature at which the shape memory effect occurs (T_{trans}), which is defined as the temperature of the maximum melting peak ($T_{trans} = T_m$) from calorimetric analysis (Table 3.2). When initial sample dimensions and temperature were fixed, deformation took place by applying 1 N force. Maintaining this force, the sample was cooled down (4 ºC min^{-1}) and maintained at 30 ºC during 5 min. After this, the applied stress was reduced to the preload value (0.001 N) to fix the temporary shape. In the final step, the sample was heated again (4 ºC min^{-1}) and primary shape was recovered.

The mechanical tests are performed according to Figure 3.24. The thermo-mechanical cycles for irradiated samples are represented in Figure 3.51, and the corresponding extension values at different stages of the experiment (from 1 to 5 -Figure 3.24-) are listed in Table 3.8.

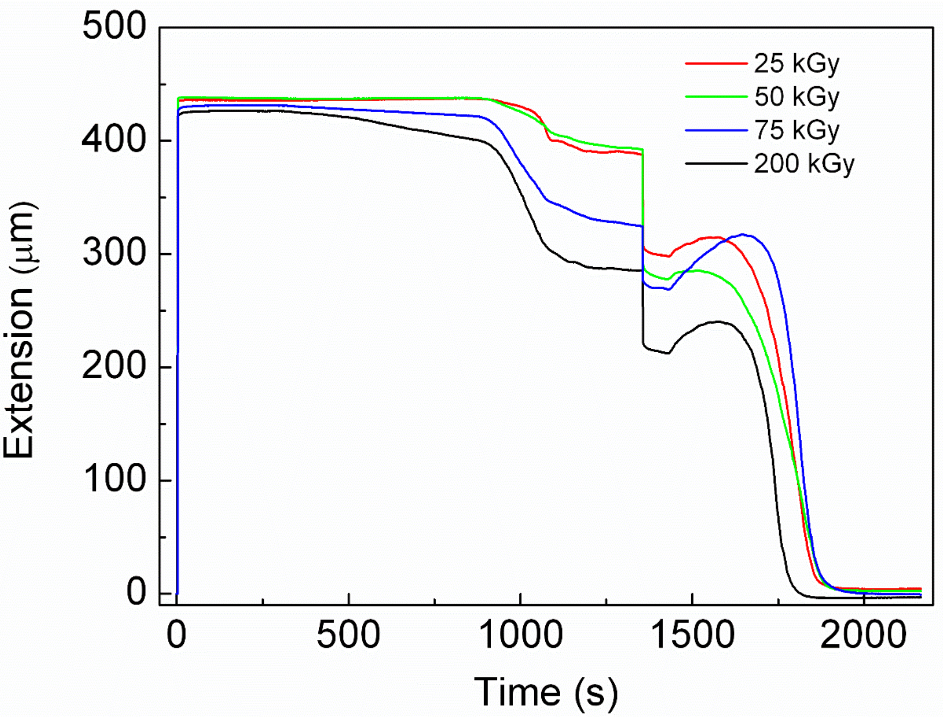

Figure 3.51. Cyclic thermo-mechanical response of irradiated PCO samples showing extension for each sample as a function of time, illustrating the shape programming and recovery for the first cycle.

Table 3.8. Extension values for all samples at different steps of the thermo-mechanical cycle. The error is ± 0.1 µm in all cases.

Sample	Ext. 1 (µm)	Ext. 2 (µm)	Ext. 3 (µm)	Ext. 4 (µm)	Ext. 5 (µm)
PCO-25	436.0	422.4	388.0	308.1	299.0
PCO-50	437.9	417.7	392.6	290.8	278.8
PCO-75	431.0	359.4	324.7	276.6	270.0
PCO-200	426.0	320.2	285.8	221.5	213.6

As explained at section 3.2.4.2, extension 1 is shorter as the irradiation dose increases (higher crosslinking density). When cooling maintaining the stress, the deformation diminishes as the received dose increases, the sample contracts more (thermal contraction is higher) [54], resulting in a lower value of extension 2. Furthermore, as the applied force is considerable low (1 N), the polymer partially recovers the undergone strain. Later, the sample is kept at 30 ºC for 5 min, and deformation stabilizes (extension 3). Then, the stress is removed and temporary shape is fixed (extension 4), showing a lower final stress as crosslink density increases. The sample is maintained stress-free at 30 ºC during 1 min (extension 5) before the recovery process begins. In Table 3.8 it can be seen, on the one hand, that the strain values for PCO-25 and PCO-50 samples are quite similar and, on the other hand, that extension at the different points (E1-E5) decreases as the radiation dose increases.

Finally the sample is heated until 80 ºC, so when temperature reaches T_m the recovery process takes place and the primary shape is recovered. Table 3.9 shows different values obtained in this step, as well as the final recovery temperatures (T_f), and the final extension (remnant extension, extension 6). Moreover, the fixity ratio (R_f) and shape recovery ratio (R_r) were calculated employing equations 3.4 and 3.5. These same parameters have also been evaluated at the end of the TMA tests (80 ºC, point 7). The shape memory cycles in a way (3D plot) can be observed in Figure 3.52.

In these covalent crosslinked polymer networks, recovery process is related to crosslinking density and associated rubbery elasticity. As a consequence, higher crosslink density leads to higher recovery ratios, i.e. lower values of extension 6. Additionally, the extension at final temperature (80 ºC) (extension 7), is also lower as crosslinking increases, so slight differences between recovery values employing extension 6 or extension 7 can be appreciated. Considering that the frozen molecular segments could move and improve the shape memory effect when recovery time is sufficient at a temperature higher than T_{trans} [70], recovery ratio is higher at this final stage at 80 ºC.

In summary, an increment in radiation dose involves a drop in crystallinity and related shape memory transition temperature (Table 3.2). In this way, shape fixity ratio (R_f) decreases as radiation dose increases due to depending on the lack of chain mobility and crystallization process [59], and recovery ratio (R_r) is higher when crosslink density grows from enhanced rubbery elasticity (Table 3.8 and Table 3.9).

In particular, Table 3.9 shows that the shape fixity values (R_f) measured using equation 3.4 are not too high (among 52-70%), and the recovery ratio is practically 100% for all samples, including those irradiated at lower doses (PCO-25 and PCO-50), which could be related to the procedure, as explained in section 3.2.4.2. In any case, samples PCO-75 and PCO-200 have a total shape recovery (100%) at extension 7. These samples exhibit the same total recovery in the previous qualitative results as in the actual quantitative work. Further, PCO-25 and PCO-50 samples had a partial shape recovery in the qualitative study. In the present work these samples neither arise the 100% of the recovery (99.04% and 99.45% with an error of 0.02% at extension 7).

Furthermore, Figure 3.53 shows the linear correlation between the gel fraction (Table 3.1) and the shape recovered after the first cycle obtained by TMA. Considering the thermo-mechanical properties and the associated shape memory response, the gel fraction above 20% and the shape recovery after the first cycle are linearly correlated, as shown in Figure 3.53. Furthermore, as the gel fraction was previously attributed to the radiation crosslinking, the gamma radiation crosslinking can be considered as a rational parameter to design and control a macro-scale shape recovery. An increase in the gamma radiation dose leads to a growth both in the gel fraction and in the shape recovery percentage.

It is important to mention that this linear correlation of the gel fraction and the shape recovery ratio arises in a small interval (around 1% of the recovery). Of course, this relation is not linear if we include the not irradiated PCO sample (0% gel fraction, no shape memory). Only irradiated samples (samples with shape memory) exhibit this linear correlation. The resolution is good enough to show and support the differences in the recovery ratio between the samples as the interval is 50 times larger than the error.

Table 3.9. Values obtained in the recovery process for all samples.

Sample	R_f (%)	T_f (ºC)	Ext. 6 (μm)	R_r (%)	T (ºC)	Ext.7 (μm)	R_r (%)
PCO-25	70.66 ± 0.03	65.7	4.5 ± 0.1	98.97 ± 0.02	80.0	4.2 ± 0.1	99.04 ± 0.02
PCO-50	66.41 ± 0.03	65.5	3.1 ± 0.1	99.29 ± 0.02	80.0	2.4 ± 0.1	99.45 ± 0.02
PCO-75	64.18 ± 0.03	67.3	1.0 ± 0.1	99.77 ± 0.02	80.0	0.0 ± 0.1	100.00 ± 0.02
PCO-200	52.00 ± 0.03	60.3	0.0 ± 0.1	100.00 ± 0.02	80.0	0.0 ± 0.1	100.00 ± 0.02

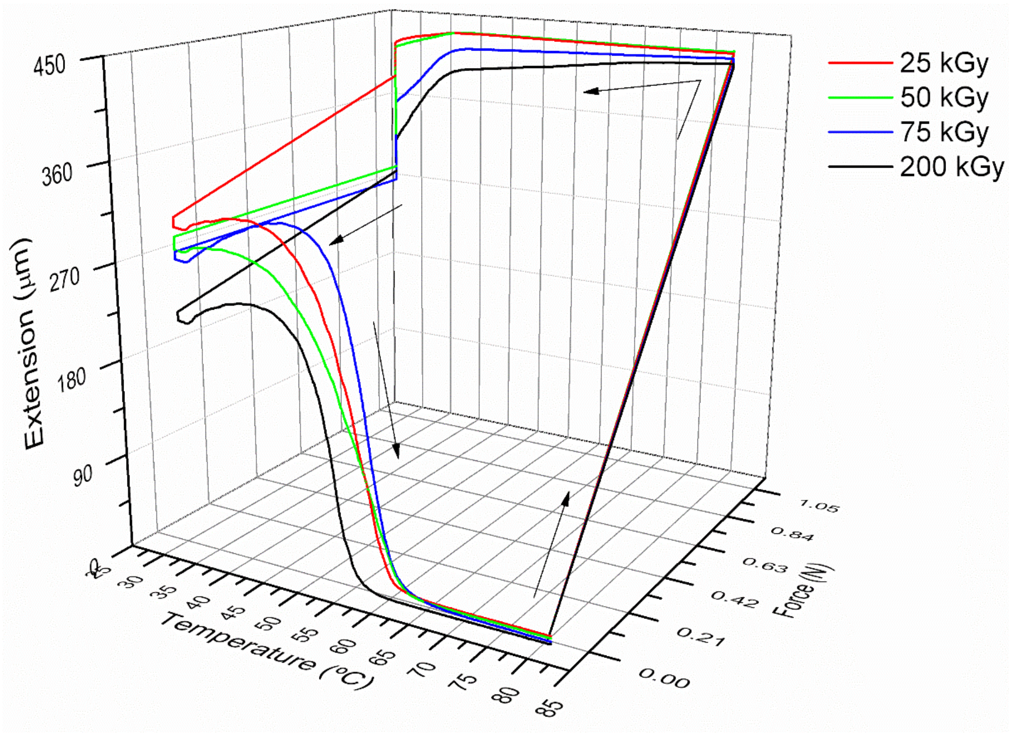

Figure 3.52. Three-dimensional thermo-mechanical cycle to evaluate the shape memory properties for irradiated PCO samples (first cycle).

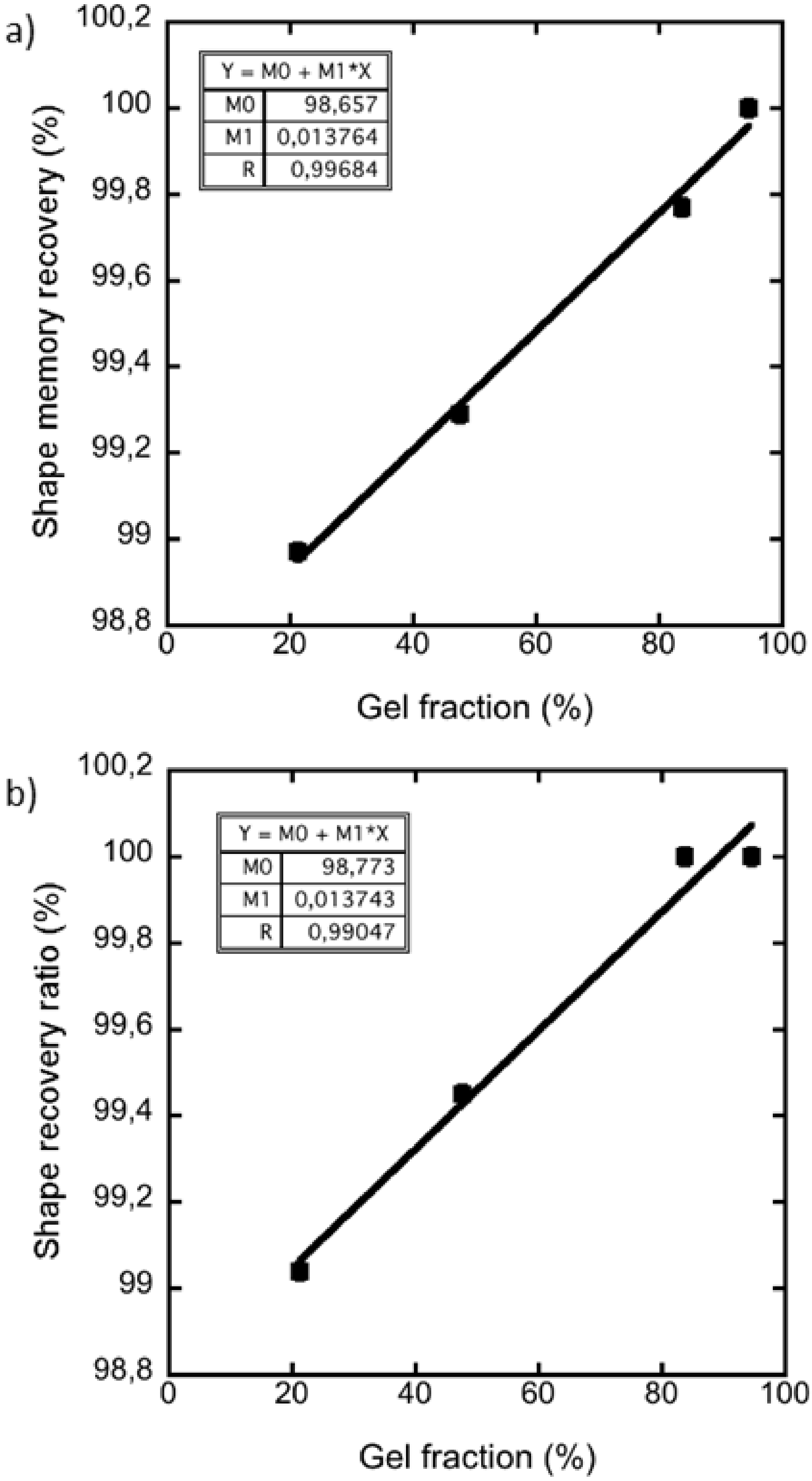

Figure 3.53. Linear correlation (R=0.99) of the percentage of the shape recovered after the first shape memory recovery cycle at extension 6 (a, up) and at extension 7 (b, down), and the gel fraction of the samples. Note that the error of the recovery is ± 0.02%.

3.3.4.3. Positron Annihilation Lifetime Spectroscopy

The PALS equipment consists in a fast-fast coincidence system from ORTEC with two BC-422 Saint Gobain plastic scintillators and two H1949-50 Hamamatsu photo multipliers suited in a vertical position inside a FFD-1402 Radiber S.A. refrigerator. The ^{22}Na source of around 15 µCi sealed with two CS Hyde Kapton foils (7.5 µm) was set between two identical samples. PALS measurements were carried out at different temperatures ranging from 10 ºC to 80 ºC controlled by an 3508 programmable temperature control system from Eurotherm equipped with a variable SALICRU power supply, a FIREROD® cartridge heater of 100 W supplied from WATLOW EUROPE, and a PT-100 CS5 (1|5) temperature sensor from TC S.A. The heater and temperature sensor were installed in a sample holder (designed and fabricated in the Nuclear Techniques Laboratory of the University of the Basque Country - UPV/EHU) of pure aluminium. The spectra of the investigated samples were analysed with LT_Polymers program [71]. About 2.5 x 10^6 counts/spectrum were collected with a resolution function of around 0.270 ns. From each spectrum, the source contribution was subtracted (19.8%, 0.382 ns) and three lifetime components were obtained. The longest-lived lifetimes exhibited distributions and were assigned to ortho-Positronium (o-Ps) lifetimes, τ_{o-Ps}. As usually, these o-Ps lifetimes were used to calculate the size of the free volume holes by using the Tao-Eldrup spherical quantum model [72,73] (equation 3.8).

$$\tau_{o-Ps}^{-1}[ns] \ = 2(ns^{-1})\left[1-\frac{R}{R_0}+\frac{1}{2\pi}sin\left(\frac{2\pi R}{R_0}\right)\right] \tag{3.8}$$

In equation 3.8, $R_0 = R + \Delta R$, R being the estimated mean free volume hole radius, and ΔR an empirical parameter fitted to be 1.66 Å [74]. The mean free volume hole size was evaluated with a spherical approximation.

Mean o-Ps lifetimes obtained by PALS are shown in Figure 3.54. As expected, the o-Ps lifetimes increase with increasing temperature. For example, the mean o-Ps lifetime of the not irradiated PCO increases from 2.55 ± 0.02 ns at 10 ºC to 2.77 ± 0.01 ns at 80 ºC; in the case of the sample irradiated at 200 kGy, this value increases from 2.72 ± 0.02 ns at 10 ºC to 2.84 ± 0.02 ns at 80 ºC. Interestingly, a gap is highlighted between samples with 'partial' shape recovery (red and green) and with 'total' shape recovery (blue and black). At 10 ºC, the mean o-Ps lifetime of the sample irradiated at 200 kGy (total shape recovery) is around 6% larger than the sample irradiated at 25 kGy (partial shape recovery). At 80 ºC, this value is around 2.5% bigger for the sample irradiated at 75 kGy (total shape recovery) compared with the sample irradiated at 50 kGy (partial shape recovery).

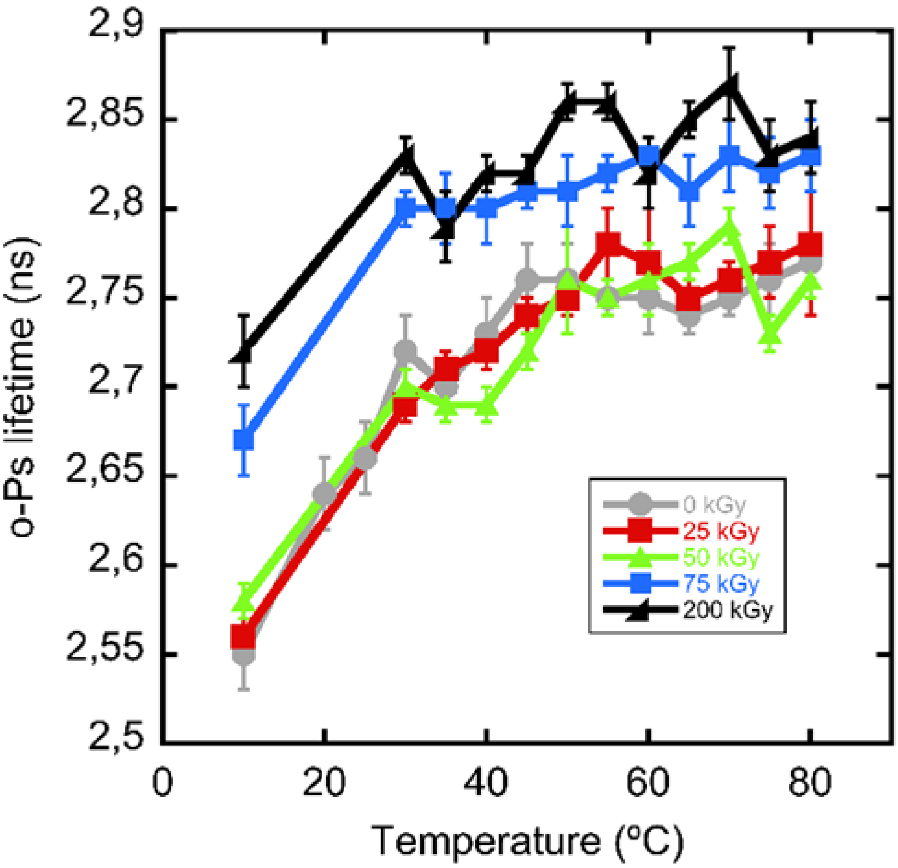

Figure 3.54. Temperature dependence of the mean ortho-Positronium lifetime (o-Ps lifetime) obtained by PALS for gamma-irradiated PCO samples at different doses.

The mean free volume hole size of the samples obtained by PALS at different temperatures versus the gel fraction inside samples (wt%) is shown in Figure 3.55.

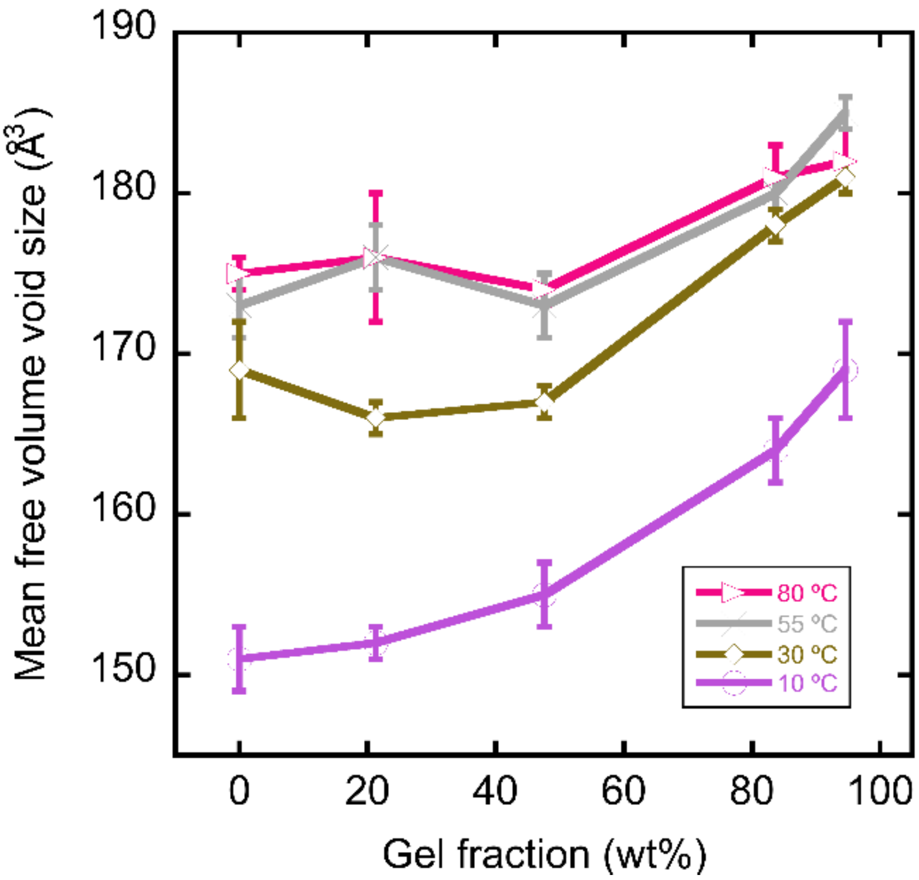

Figure 3.55. Mean free volume hole size of the samples obtained by PALS at different temperatures versus the gel fraction inside samples (wt%).

The mean free volume hole size increases when increasing the gel fraction. A similar trend is found when comparing the mean free volume hole size of the samples obtained by PALS at different temperatures versus the percentage of the shape recovered after the first shape memory recovery cycle obtained by TMA (Figure 3.56).

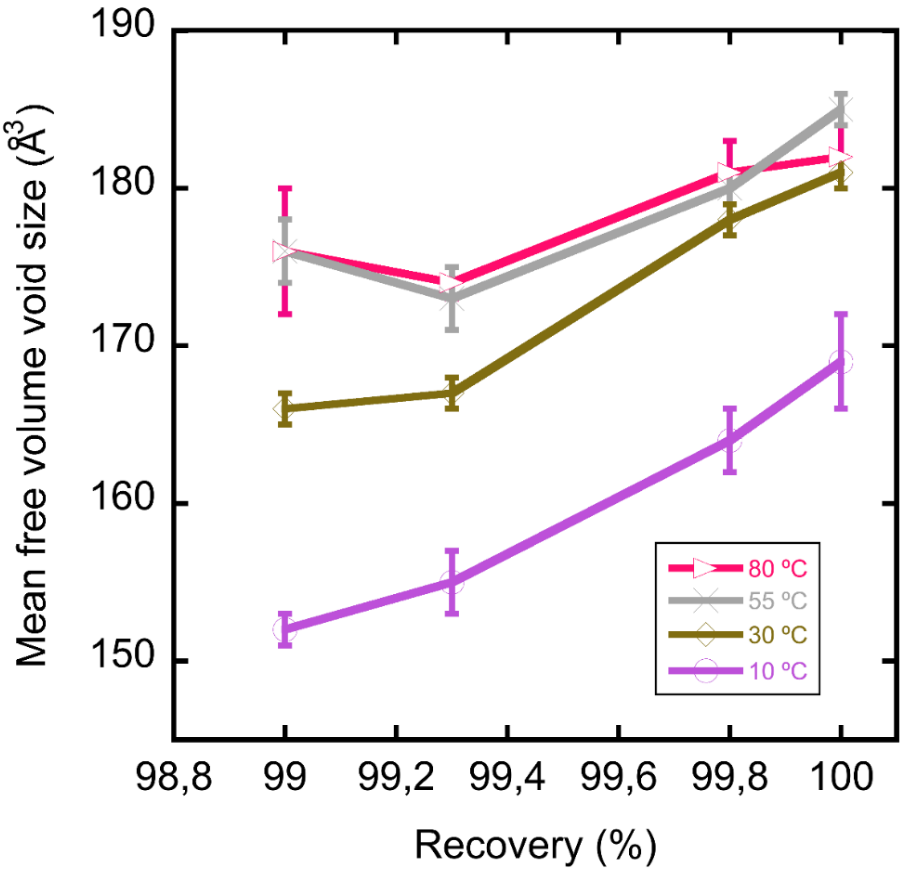

Figure 3.56. Mean free volume hole size of the samples obtained by PALS at different temperatures versus the percentage of the shape recovered (Recovery (%)) after the first shape memory recovery cycle.

The underlying physicochemical mechanism can be explained as follows: to begin with, the mean free volume hole size increases with the radiation dose. The crosslinking increases the free volume hole sizes due to the insufficient PCO chain packing. In this way, the PCO chains can move faster and efficiently to strain for the shape recovery when the temperature increases, as shown in Figure 3.54, Figure 3.55 and Figure 3.56. Furthermore, Figure 3.54 highlights an abrupt increase in the ortho-positronium lifetime (free volume hole size) between the samples with partial macroscale recovery (50 kGy) and total macroscale recovery (75 kGy). It can be concluded that the free volume hole size is a subnanoscale parameter directly affecting the shape memory properties of these SMPs. Therefore, it has been presented a robust study in structure-free volume-shape memory properties in gamma irradiated PCO, although the general link between the molecular scale free volume holes and the micro/macroscale shape memory properties in polymers needs to be confirmed in other SMPs.

3.3.4.4. *In situ* measurements of free volume during recovery process

These measurements were performed on a PCO-200 sample obtained as explained in section 3.1.3, in order to give it shape memory properties. Free volume measurements were performed using two squares of 1 cm^2 cut from the PCO-200 irradiated sheet.

The mean free volume hole size and distribution of the sample were measured *in situ* using the PAL spectrometer explained in section 3.3.4.3. The described PALS system was employed to measure the free volume in the sample at the original shape at 10 ºC, 25 ºC, 40 ºC, 55 ºC and 70 ºC. Then, a temporal shape was gave to the sample by stretching it at 80 ºC with 3 N force (employing the Mettler Toledo DMA-1 used to make the thermo-mechanical analysis), and cooling down at 20 ºC min^{-1} maintaining the stress in order to fix the temporal shape (an 11% was the reached deformation). The free volume of this temporary shape was measured again by PALS at the same temperature values ranging from 10 ºC to 70 ºC. When the transition temperature of the shape memory effect was reached (the transition temperature of the shape memory effect, T_{trans}, is 51.8 ºC), the sample starts to recover its original shape. The free volume of the recovered-shape sample was measured again at 10 ºC and 25 ºC. The measured sample was the same for the three shapes (original, deformed and recovered) during the shape recovery cycle.

The results of this PALS study (Table 3.10) show that for each measurement – of the original, deformed and recovered samples – over the course of the heat treatment, the intensity of the o-Ps signal (I_3) increases. Raw lifetime data are also showed in the Table 3.10. As usual, from the longest-lived component τ_3, the mean size of the free volume holes was obtained (plotted in Figure 3.57). From the third component, the distribution of the o-Ps lifetime (σ_3) was obtained the free volume hole size distribution σ_{V_f} as well, showed in Table 3.10. It is important to note that no extra o-Ps lifetime (σ_4) was detected in any case; the fits were excellent for the obtained positron spectra (see χ^2 values in Table 3.10).

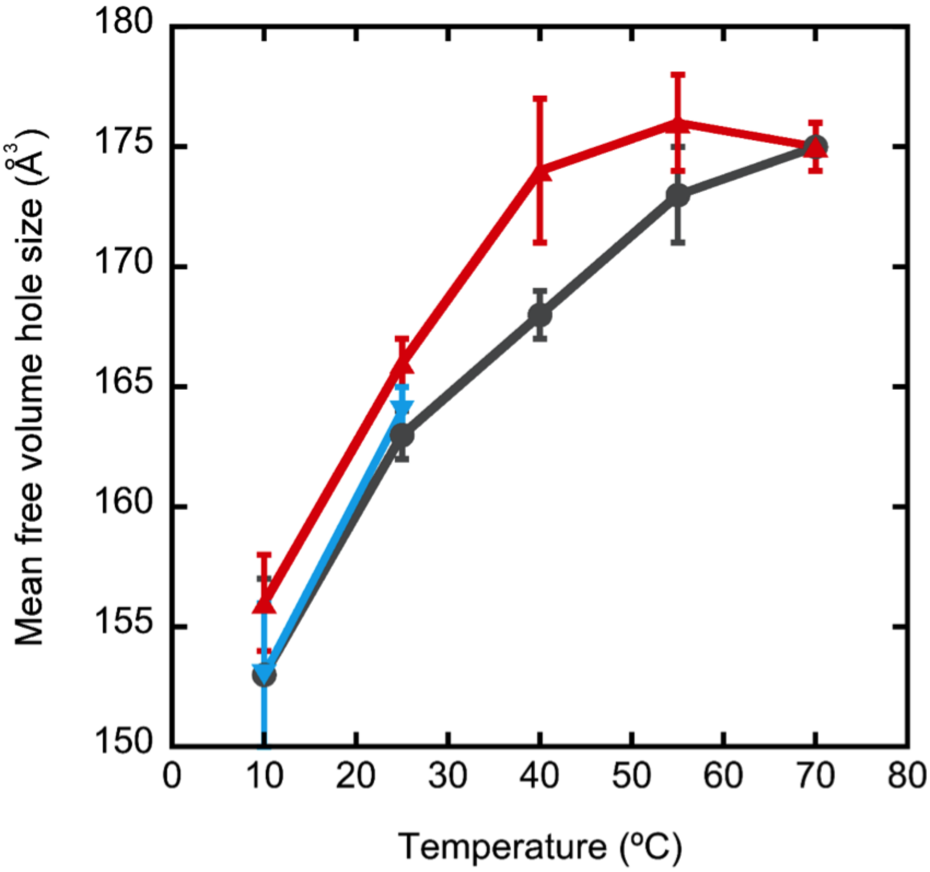

Figure 3.57. ***In situ*** **measured mean free volume hole size of the original (grey), deformed (red) and recovered sample (blue) versus the temperature of the heat treatment during the shape recovery process of the gamma-irradiated polycyclooctene.**

Table 3.10. Data obtained by *in situ* measurements of PALS during the shape recovery process of PCO-200 sample.

Sample	T (ºC)	χ^2 (a.u.)	I_3 (%)	τ_3 (ns)	σ_3 (ns)	V_f (Å^3)	σ_{V_f} (Å^3)
Original	10	1.02	33.7±0.8	2.57±0.03	0.45±0.06	153±4	49±7
	25	0.99	35.2±0.3	2.66±0.01	0.36±0.01	163±1	39±1
	40	1.05	36.2±0.5	2.71±0.01	0.23±0.04	168±1	25±4
	55	0.93	44.9±0.8	2.75±0.02	0.29±0.04	173±2	32±4
	70	1.01	44.7±0.2	2.77±0.01	0.27±0.05	175±1	30±6
Deformed	10	0.99	37.5±0.2	2.59±0.02	0.34±0.07	156±2	40±8
	25	1.06	39.0±0.3	2.69±0.01	0.17±0.06	166±1	19±6
	40	1.11	40.9±0.4	2.76±0.03	0.40±0.30	174±3	40±30
	55	1.06	43.4±0.2	2.78±0.02	0.22±0.06	176±2	24±7
	70	1.06	43.7±0.2	2.77±0.01	0.26±0.03	175±1	28±4
Recovered	10	1.04	37.6±0.8	2.57±0.02	0.42±0.03	153±3	46±3
	25	1.02	36.5±0.1	2.67±0.01	0.30±0.03	164±1	35±4

The measured mean sizes of the free volume holes are plotted in Figure 3.57. From this data, it is highlighted that:

-As expected, the mean free volume hole size values increase with the temperature in the original sample (see the grey line in Figure 3.57). The free volume holes are enlarged around a 14% during the heat treatment from 10 ºC to 70 ºC.

-When the sample is deformed, the mean size of the free volume holes increases at all the temperature values analysed comparing with the original sample (compare the red line *versus* the grey line in Figure 3.57). The most remarkable difference is reached at 40 ºC; at this point, the mean free volume hole size in the deformed shape is 174 ± 4 Å^3, while for the original shape is 168 ± 1 Å^3. A reasonable explanation for this might be that the deformation alters the molecular organization of the monomeric units at the subnanoscale. This disorder may provoke larger free volumes within the polymer.

-Very interestingly, when the deformed sample starts to recover its original shape, the sizes of the free volume holes gets closer to the original shape ones: at 55 ºC the mean free volume hole size of the deformed sample starting to recovery is 176 ± 2 Å^3 comparing to the 173 ± 2 Å^3 measured for the original sample (note at this stage that the T_{trans} = 51.8 ºC).

-Even more surprisingly, when the sample is totally recovered (see red triangle at 70 ºC in Figure 3.57), the values are almost the same as the ones obtained for the original shape (grey dot at 70 ºC): 175 ± 1 Å^3. Moreover, after cooling the recovered sample at 10 ºC the mean free volume hole size is similar to the corresponding value for the original sample: 153 ± 3 Å^3 versus 153 ± 4 Å^3 at 10 ºC (see blue triangle and grey dot at 10 ºC in Figure 3.57). Even these values are similar at room temperature: 164 ± 1 Å^3 versus 163 ± 1Å^3 (see blue triangle and grey dot at 25 ºC in Figure 3.57). Furthermore, the values of the free volume hole size distribution are also very similar, which means that the difference in size between the free volume holes present in the sample when recovered and the original shape are quite similar.

From the positron annihilation lifetime spectra we obtain the mean lifetime (τ) and standard deviation (σ_r). Fitting the lifetime spectrum in a log-normal distribution, and using the Mathematica software, it is possible to obtain the probability density functions (pdf) by using the command PDF[LogNormalDistribution[[μ,σ], x], where $\mu = ln\tau - \sigma^2/2$ and $\sigma = \sqrt{\ln(\sigma_r^2/\tau^2 + 1)}$. A probability density function (pdf), also named density, of the continuous free volume hole size variables, is a function used to describe the relative tendency for this variable to take on a certain value. In order to understand how does the free volume change inside the polymer during the shape recovery, we also determined the probability density functions (pdf) of the measured free volume hole sizes and distributions. We have plotted the probability density functions versus the mean volume of the holes of the original (in grey) and the deformed (in red) samples at the same temperature: 40 ºC in Figure 3.58a. Figure 3.58b shows the pdf versus the mean free volume hole sizes of the original (grey), deformed (red) and recovered (blue) shapes at room temperature. Results highlight that when the sample is deformed, the free volume holes are larger but more similar between them due to the sharpness of the pdf at 25 ºC (in red). Then, when the temperature reaches 40 ºC, the difference in size of the free volume holes between the original and the deformed shape is even larger: the free volume holes are even bigger. Figure 3.58a reflects a wider pdf for the deformed shape than for the original shape. This means that the size of the free volume holes is more heterogeneous in the case of the deformed sample at 40 ºC. But, finally, when the shape is totally recovered (see the blue line in Figure 3.58b), its pdf is very close from the pdf of the original shape (in grey). These results may be explained by the fact that the macroscopic shape is recovered when the internal structure and organisation is recovered through the motion of the monomeric units of polymer chains via free volume holes (note that the volume of the monomeric fraction is closer to the volume of cyclooctene monomer, that is, around 216 Å^3). At the final stage, when the macroscopic shape is totally recovered, the subnanoscopic free volume properties are very similar to those in the original shape because the organisation of the polymer chains is recovered.

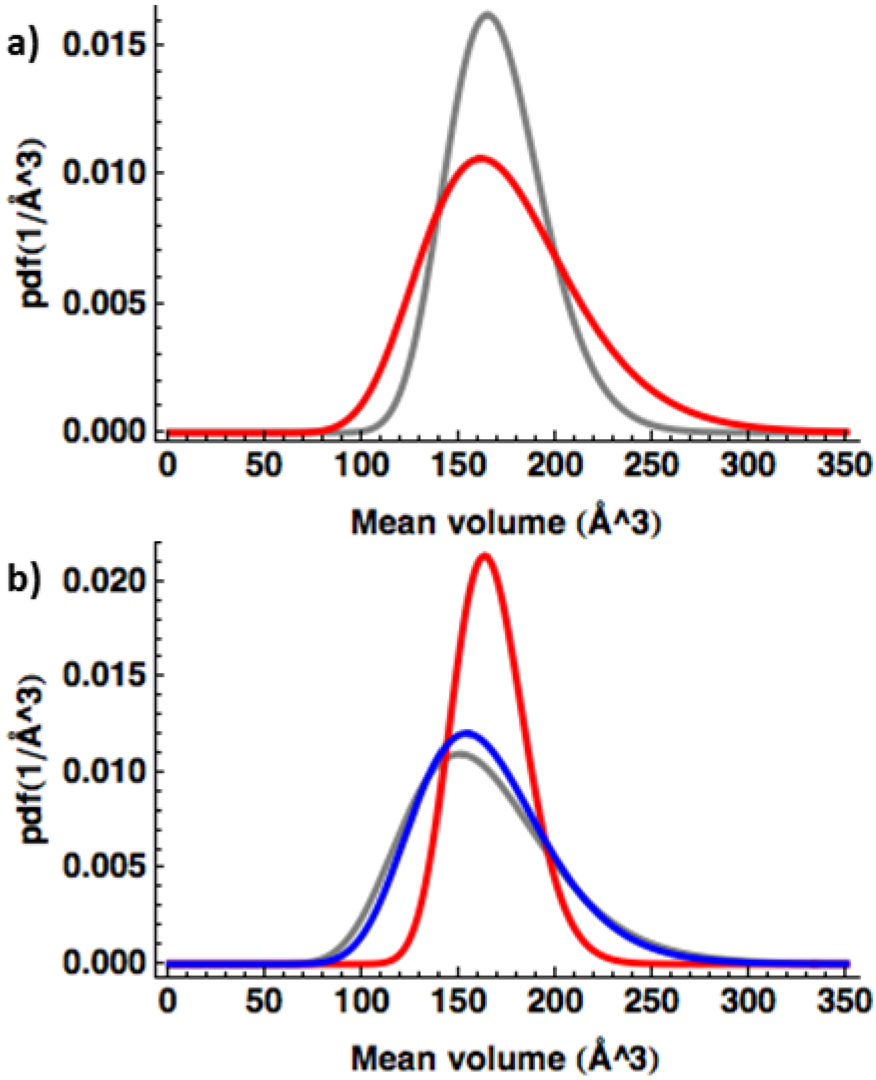

Figure 3.58. Obtained probability density functions (pdf) of the mean free volume hole size of the original sample (in grey), the deformed sample (in red) and the recovered sample (in blue) at (a) 40 ºC and (b) 25 ºC.

As far as authors know, this is the first *in situ* measurement of the free volume properties during the shape recovery process. The obtained results give light to the poorly understood physicochemical link existing between the free volume and shape memory properties [67]. The present findings confirm that the size of free volume holes is associated with the shape recovery. The deformation of the original sample reflects the disorder of the structure of the polymer at the nanoscale. Surprisingly, the analysed sample recovers not only the macroscopic original shape, but also the molecular organization, reflected in the recovery of the original subnanoscopic mean free volume hole size and distribution.

This finding has important implications in shape memory polymer physics for improving the shape memory polymer properties. If the subnanoscale free volume is tuned (by gamma-irradiation, different crosslinking, additions, etc.), desired macroscopic properties of shape memory could be reached. However, further research should be done in different shape memory polymers in order to totally uncover the link between the free volume and shape memory properties.

3.3.5. Conclusions

The shape recovery and free volume hole sizes in gamma irradiated polycyclooctene (PCO) samples has been analysed, as a non-cytotoxic alternative to peroxide based crosslinked PCO. It has been proven that in fact there is a physicochemical link between free volume holes and shape memory properties. The results indicate that the subnanoscale free volume holes caused by gamma irradiation in PCO samples allow the movement of polymer chains facilitating the recovery to the original macroscopic shape. Further, it is shown that the gamma irradiated PCO samples are non-cytotoxic; this is a first step towards developing biomedical applications based on these materials.

Positron annihilation lifetime spectroscopy has been employed to study how the free volume changes during shape recovery process in a gamma-irradiated polycyclooctene shape memory polymer. During the macroscopic shape recovery in a PCO-based shape memory polymer the subnanoscopic free volume molecular re-organisation is achieved. This study highlights that the local free volume plays a fundamental role in the macroscopic shape memory properties by permitting the molecular re-organization.

3.4. References

1. Bhattacharya, A. Radiation and industrial polymers. *Prog. Polym. Sci.* **2000**, *25*, 371–401.

2. Luo, S.; Netravali, A. N. Effect of 60Co γ- radiation on the properties of poly (hydroxybutyrate- co- hydroxyvalerate). *J. Appl. Polym. Sci.* **1999**, *73*, 1059–1067.

3. Chmielewski, A. G.; Haji-Saeid, M.; Ahmed, S. Progress in radiation processing of polymers. *Nucl. Instruments Methods Phys. Res. Sect. B Beam Interact. with Mater. Atoms* **2005**, *236*, 44–54.

4. Zahran, A. R. R.; Kandeil, A. Y.; Higazy, A. A.; Kassem, M. E. Ultrasonic and thermal properties of γ-irradiated low-density polyethylene. *J. Appl. Polym. Sci.* **1993**, *49*, 1291–1297.

5. Cerrada, M. L.; Benavente, R.; Fernández-García, M.; Pérez, E.; Campos, J. M.; Ribeiro, M. R. Crosslinking in metallocene ethylene-co-5,7-dimethylocta-1,6-diene copolymers initiated by electron-beam irradiation. *Polymer (Guildf).* **2009**, *50*, 1095–1102.

6. Gheysari, D.; Behjat, A. Radiation crosslinking of LDPE and HDPE with 5 and 10 MeV electron beams. *Eur. Polym. J.* **2001**, *37*, 2011–2016.

7. Gheysari, D.; Behjat, A.; Haji-Saeid, M. The effect of high-energy electron beam on mechanical and thermal properties of LDPE and HDPE. *Eur. Polym. J.* **2001**, *37*, 295–302.

8. Abdel-Aziz, M. M.; Basfar, A. A. Aging of ethylene-propylene diene rubber (EPDM) vulcanized by γ-radiation. *Polym. Test.* **2000**, *19*, 591–602.

9. Barkhudaryan, V. G. Effect of γ-radiation on the molecular characteristics of low-density polyethylene. *Polymer (Guildf).* **2000**, *41*, 575–578.

10. Shyichuk, A.; Shyichuk, I.; Wu, G.; Katsumura, Y. Quantitative analysis of the temperature effect on the radiation crosslinking and scission of polyethylene macromolecules. *J. Polym. Sci. Part A Polym. Chem.* **2001**, *39*, 1656–1661.

11. Kurtz, S. M.; Muratoglu, O. K.; Evans, M.; Edidin, A. A. Advances in the processing, sterilization, and crosslinking of ultra-high molecular weight polyethylene for total joint arthroplasty. *Biomaterials* **1999**, *20*, 1659–1688.

12. Premnath, V.; Harris, W. H.; Jasty, M.; Merrill, E. W. Gamma sterilization of UHMWPE articular implants: an analysis of the oxidation problem. *Biomaterials* **1996**, *17*, 1741–1753.

13. Tamboli, S. M.; Mhaske, S. T.; Kale, D. D. Crosslinked polyethylene. *Indian J. Chem. Technol.* **2004**, *11*, 853–864.

14. Barkhudaryan, V. G. Alterations of molecular characteristics of polyethylene under the influence of γ-radiation. *Polymer (Guildf).* **2000**, *41*, 2511–2514.

15. Basfar, A. A. Flammability of radiation cross-linked low density polyethylene as an insulating material for wire and cable. *Radiat. Phys. Chem.* **2002**, *63*, 505–508.

16. Elshereafy, E.; Mohamed, M.; El-Zayat, M. M.; El Miligy, A. A. Gamma radiation curing of nitrile rubber/high density polyethylene blends. *J. Radioanal. Nucl. Chem.* **2012**, *293*, 941–947.

17. Abdel Tawab, K.; Magida, M. M.; Ibrahim, S. Effect of ionizing radiation on the morphological, thermal and mechanical properties of polyvinyl alcohol/polyethylene glycol blends. *J. Polym. Environ.* **2011**, *19*, 440–446.

18. Feng, W.; Hu, F. M.; Yuan, L. H.; Zhou, Y.; Zhou, Y. Y. Radiation crosslinking of polyamide 610. *Radiat. Phys. Chem.* **2002**, *63*, 493–496.

19. Ferro, W. P.; de Andrade e Silva, L. G. Ionizing radiation effect studies on polyamide 6.6 properties. *Radiat. Phys. Chem.* **2004**, *71*, 269–271.

20. Abdou, S. M.; Mohamed, R. I. Characterization of structural modifications in poly-tetra-fluoroethylene induced by electron beam irradiation. *J. Phys. Chem. Solids* **2002**, *63*, 393–398.

21. Pugmire, D. L.; Wetteland, C. J.; Duncan, W. S.; Lakis, R. E.; Schwartz, D. S. Cross-linking of polytetrafluoroethylene during room-temperature irradiation. *Polym. Degrad. Stab.* **2009**, *94*, 1533–1541.

22. Jurkin, T.; Pucić, I. Poly(ethylene oxide) irradiated in the solid state, melt and aqueous solution—a DSC and WAXD study. *Radiat. Phys. Chem.* **2012**, *81*, 1303–1308.

23. Clough, R. L. High-energy radiation and polymers: A review of commercial processes and emerging applications. *Nucl. Instruments Methods Phys. Res. Sect. B Beam Interact. with Mater. Atoms* **2001**, *185*, 8–33.

24. Charlesby, A.; Pinner, S. H. Analysis of the Solubility Behaviour of Irradiated Polyethylene and Other Polymers. *Proc. R. Soc. A Math. Phys. Eng. Sci.* **1959**, *249*, 367–386.

25. Ivanov, V. S. *Radiation Chemistry of Polymers*; VSP: Utrecht, 1992.

26. Zhu, G.; Liang, G.; Xu, Q.; Yu, Q. Shape-memory effects of radiation crosslinked poly(ϵ-caprolactone). *J. Appl. Polym. Sci.* **2003**, *90*, 1589–1595.

27. Li, F.; Zhu, W.; Zhang, X.; Zhao, C.; Xu, M. Shape memory effect of ethylene–vinyl acetate copolymers. *J. Appl. Polym. Sci.* **1999**, *71*, 1063–1070.

28. Cleland, M. R.; Parks, L. A.; Cheng, S. Applications for radiation processing of materials. *Nucl. Instruments Methods Phys. Res. Sect. B Beam Interact. with Mater. Atoms* **2003**, *208*, 66–73.

29. Charlesby, A. Use of high energy radiation for crosslinking and degradation. *Radiat. Phys. Chem.* **1977**, *9*, 17–29.

30. Silverman, J. Basic concepts of radiation processing. *Radiat. Phys. Chem.* **1977**,

9, 1–15.

31. Schneider, W. A.; Müller, M. F. Crystallinity of trans-polyoctenamer: characterization and influence of sample history. *J. Mol. Catal.* **1988**, *46*, 395–403.

32. Han, C.; Bian, J.; Liu, H.; Dong, L. Effect of γ-radiation on the thermal and mechanical properties of a commercial poly (butylene adipate- co- terephthalate). *Polym. Int.* **2009**, *58*, 691–696.

33. Khonakdar, H. A.; Jafari, S. H.; Wagenknecht, U.; Jehnichen, D. Effect of electron-irradiation on cross-link density and crystalline structure of low- and high-density polyethylene. *Radiat. Phys. Chem.* **2006**, *75*, 78–86.

34. Vachon, C.; Gendron, R. Effect of gamma-irradiation on the foaming behavior of ethylene-co-octene polymers. *Radiat. Phys. Chem.* **2003**, *66*, 415–425.

35. Lee, S. M.; Choi, S. W.; Nho, Y. C.; Song, H. H. Modification of microstructures and physical properties of ultra high molecular weight polyethylene by electron beam irradiation. *J. Polym. Sci. Part B Polym. Phys.* **2005**, *43*, 3019–3029.

36. Huang, W. M.; Ding, Z.; Wang, C. C.; Wei, J.; Zhao, Y.; Purnawali, H. Shape memory materials. *Mater. Today* **2010**, *13*, 54–61.

37. Lendlein, A.; Kelch, S. Shape-memory polymers. *Angew. Chemie Int. Ed.* **2002**, *41*, 2034–2057.

38. Otsuka, K.; Wayman, C. M. *Shape memory materials*; Cambridge University Press: Cambridge, 1999.

39. Rousseau, I. A. Challenges of shape memory polymers: A review of the progress toward overcoming SMP's limitations. *Polym. Eng. Sci.* **2008**, *48*, 2075–2089.

40. Behl, M.; Lendlein, A. Shape-memory polymers. *Mater. Today* **2007**, *10*, 20–28.

41. Huang, W. M.; Zhao, Y.; Wang, C. C.; Ding, Z.; Purnawali, H.; Tang, C.; Zhang, J. L. Thermo/chemo-responsive shape memory effect in polymers: A sketch of working mechanisms, fundamentals and optimization. *J. Polym. Res.* 2012, *19*.

42. Liu, C.; Qin, H.; Mather, P. T. Review of progress in shape-memory polymers. *J. Mater. Chem.* **2007**, *17*, 1543–1558.

43. Serrano, M. C.; Ameer, G. A. Recent insights into the biomedical applications of shape-memory polymers. *Macromol. Biosci.* 2012, *12*, 1156–1171.

44. Pretsch, T. Review on the functional determinants and durability of shape memory polymers. *Polymers (Basel).* 2010, *2*, 120–158.

45. Wang, C. C.; Huang, W. M.; Ding, Z.; Zhao, Y.; Purnawali, H. Cooling-/water-responsive shape memory hybrids. *Compos. Sci. Technol.* **2012**, *72*, 1178–1182.

46. Pretsch, T.; Ecker, M.; Schildhauer, M.; Maskos, M. Switchable information carriers based on shape memory polymer. *J. Mater. Chem.* **2012**, *22*, 7757.

47. Fritzsche, N.; Pretsch, T. Programming of temperature-memory onsets in a semicrystalline polyurethane elastomer. *Macromolecules* **2014**, *47*, 5952–5959.

48. Imai, S.; Sakurai, K. An actuator of two-way behavior by using two kinds of shape memory polymers with different Tgs. *Precis. Eng.* **2013**, *37*, 572–579.

49. Singhal, P.; Small, W.; Cosgriff-Hernandez, E.; Maitland, D. J.; Wilson, T. S. Low density biodegradable shape memory polyurethane foams for embolic biomedical applications. *Acta Biomater.* **2014**, *10*, 67–76.

50. Alonso-Villanueva, J.; Cuevas, J. M.; Laza, J. M.; Vilas, J. L.; León, L. M. Synthesis of poly(cyclooctene) by ring-opening metathesis polymerization: Characterization and shape memory properties. *J. Appl. Polym. Sci.* **2010**, *115*, 2440–2447.

51. Liu, C.; Chun, S. B.; Mather, P. T.; Zheng, L.; Haley, E. H.; Coughlin, E. B. Chemically cross-linked polycyclooctene: synthesis, characterization, and shape

memory behavior. *Macromolecules* **2002**, *35*, 9868–9874.

52. Medeiros, A. S.; Gual, M. R.; Pereira, C.; Faria, L. O. Thermal analysis for study of the gamma radiation effects in poly(vinylidene fluoride). *Radiat. Phys. Chem.* **2015**.

53. Drobny, J. G. *Ionizing Radiation and Polymers*; Elsevier, 2013.

54. Garle, A.; Kong, S.; Ojha, U.; Budhlall, B. M. Thermoresponsive semicrystalline poly(ε-caprolactone) networks: exploiting cross-linking with cinnamoyl moieties to design polymers with tunable shape memory. *ACS Appl. Mater. Interfaces* **2012**, *4*, 645–657.

55. Cui, Y.; Tan, M.; Zhu, A.; Guo, M. Strain hardening and highly resilient hydrogels crosslinked by chain-extended reactive pseudo-polyrotaxane. *RSC Adv.* **2014**, *4*, 56791–56797.

56. Zhao, T.; Tan, M.; Cui, Y.; Deng, C.; Huang, H.; Guo, M. Reactive macromolecular micelle crosslinked highly elastic hydrogel with water-triggered shape-memory behaviour. *Polym. Chem.* **2014**, *5*, 4965.

57. Tobushi, H.; Okumura, K.; Hayashi, S.; Ito, N. Thermomechanical constitutive model of shape memory polymer. *Mech. Mater.* **2001**, *33*, 545–554.

58. Barot, G.; Rao, I. J. Constitutive modeling of the mechanics associated with crystallizable shape memory polymers. *Zeitschrift für Angew. Math. und Phys. ZAMP* **2006**, *57*, 652–681.

59. Cuevas, J. M.; Laza, J. M.; Rubio, R.; German, L.; Vilas, J. L.; León, L. M. Development and characterization of semi-crystalline polyalkenamer based shape memory polymers. *Smart Mater. Struct.* **2011**, *20*, 035003.

60. Rodriguez, E. D.; Luo, X.; Mather, P. T. Linear/network poly(ε-caprolactone) blends exhibiting Shape Memory Assisted Self-Healing (SMASH). *ACS Appl. Mater. Interfaces* **2011**, *3*, 152–161.

61. Deslandes, Y.; Rosa, E. A.; Brisse, F.; Meneghini, T. Correlation of microhardness and morphology of poly (ether-ether-ketone) films. *J. Mater. Sci.* **1991**, *26*, 2769–2777.

62. Chung, T.; Romo-Uribe, A.; Mather, P. T. Two-way reversible shape memory in a semicrystalline network. *Macromolecules* **2008**, *41*, 184–192.

63. Oshima, A.; Ikeda, S.; Seguchi, T.; Tabata, Y. Improvement of radiation resistance for polytetrafluoroethylene (PTFE) by radiation crosslinking. *Radiat. Phys. Chem.* **1997**, *49*, 279–284.

64. Jean, Y. C.; Mallon, P. E.; Schrader, D. M. *Principles and applications of positron & positronium chemistry*; World Scientific Publishing, Singapore, 2003.

65. Jean, Y. C.; Van Horn, J. D.; Hung, W. S.; Lee, K. R. Perspective of positron annihilation spectroscopy in polymers. *Macromolecules* **2013**, *46*, 7133–7145.

66. Makuuchi, K.; Cheng, S. *Radiation processing of polymer materials and its industrial applications*; John Wiley & Sons, 2012.

67. Ito, K.; Abe, K.; Li, H. L.; Ujihira, Y.; Ishikawa, N.; Hayashi, S. Variation of free volume size and content of shape memory polymer — polyurethane — upon temperature studied by positron annihilation lifetime techniques and infrared spectroscopy. *J. Radioanal. Nucl. Chem.* **1996**, *211*, 53–60.

68. Fuchs, J. *Environmental stressors in health and disease*; CRC Press, 2001.

69. Lendlein, A. *Shape-memory polymers*; Springer Science & Business Media, 2010.

70. Hu, J. *Shape memory polymers and textiles*; Woodhead Publishing Limited and CRC Press LLC: Cambridge, 2007.

71. Kansy, J. Microcomputer program for analysis of positron annihilation lifetime spectra. *Nucl. Instruments Methods Phys. Res. Sect. A Accel. Spectrometers, Detect. Assoc. Equip.* **1996**, *374*, 235–244.

72. Eldrup, M.; Lightbody, D.; Sherwood, J. N. The temperature dependence of positron lifetimes in solid pivalic acid. *Chem. Phys.* **1981**, *63*, 51–58.

73. Tao, S. J. Positronium Annihilation in Molecular Substances. *J. Chem. Phys.* **1972**, *56*, 5499.

74. Nakanishi, H.; Wang, S.; Jean, Y. Microscopic surface tension studies by positron annihilation. In *International Symposium on Positron Annihilation Studies of Fluids*; Sharma, S. C., Ed.; World Scientific Publishing: Singapore, 1988; p. 292.

CHAPTER 4

Polycyclooctene (PCO) blended with ionomers

4.1. Thermal, mechanical, and shape memory behavior: PCO/Surlyn 8940 and PCO/Surlyn 1705 blends

4.1.1. Introduction

The term ‘ionomer’ was apparently coined by the DuPont Co. to describe those materials based on a hydrocarbon backbone containing pendant acid groups which are partially or completely neutralized with metal ions to form salts [1]. The hydrocarbon backbone is always the majority component, where the concentration of the salt groups may vary (maximum of 15-20% ionic groups) [2].

The best-known (and commercially most important) ionomer is the zinc, sodium or other metal salt of a copolymer of ethylene and methacrylic acid, commercialized by DuPont as Surlyn®. The neutralization of the acid results in the formation of ionic groups within the resulting polymer matrix. The hydrophilic ionic groups are separated from the hydrophobic polymer matrix, forming small ionic domains called ‘ionic clusters’ [3,4]. These ionic groups are attached to the macromolecular chains, so they cannot go off by themselves, allowing to these thermoplastic polymers to act in a similar way to a crosslinked polymer [5]. It has been demonstrated that the physical crosslinking between acid functional groups and salt ions (ionic crystallites) show an order-disorder transition of first order below the melting point of crystallites of polyethylene regions [3], associated to the self-healing mechanism of these systems [6]. In this manner, Tadano *et al.* [3] proposed a model where the crystal-like order inside the clusters is destroyed when a certain temperature (T_{ord}) is reached when the sample is heated, obtaining a disordered state; continuing heating, the polyethylene crystallites are melted, but the disordered ionic clusters still exist; when cooling, the polyethylene regions are crystallised, but to recover the order in the clusters it is not enough to cool the system to room temperature, it is necessary to keep the sample below T_{ord}, allowing the slowly process of reordering of the clusters (relaxation process) (Figure 4.1).

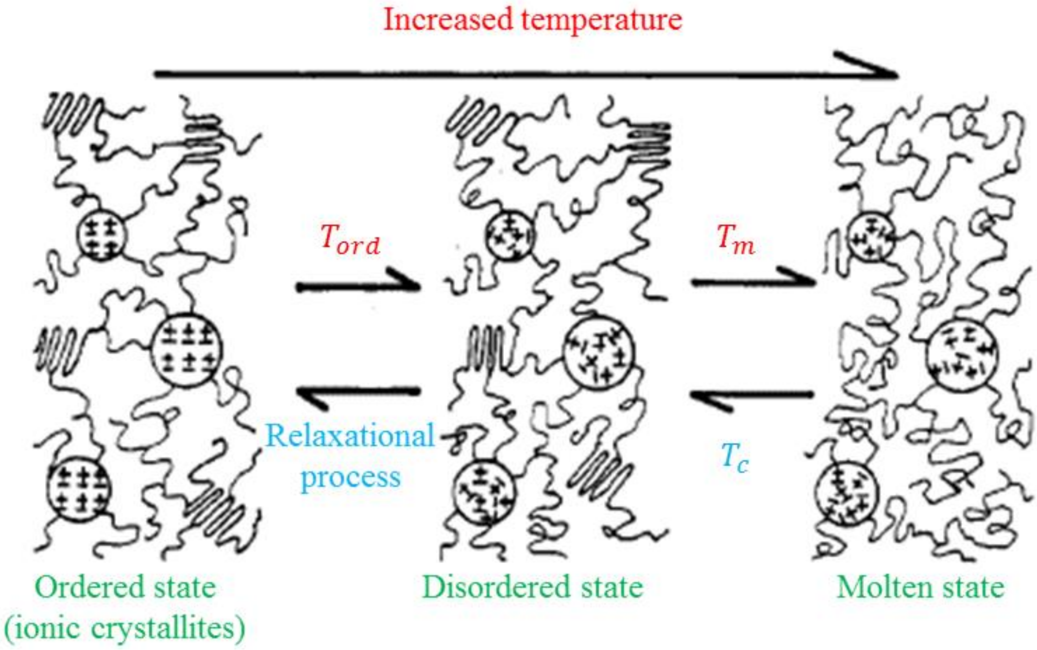

Figure 4.1. Model proposed by Tadano *et al.* for the order-disorder transition of ionic clusters.

Looking for a polymeric system with shape memory and self-healing properties, and as a preliminary test, it looks reasonable to blend the PCO used along this thesis with an ionomer. Of course, it is necessary to crosslink the PCO chains, for example using dicumyl peroxide (DCP). In this way, two Surlyn ionomers were selected (Surlyn 1705 and Surlyn 8940), and ionomer/PCO 50/50 blends were performed. At the same time, 50/50 blends containing different amounts of DCP (2 and 3 wt%) were prepared. The samples were characterised by Thermogravimetric Analysis (TGA), Differential Scanning Calorimetry (DSC), and Dynamic Mechanical Thermal Analysis (DMTA). Additionally, the shape memory behaviour of the samples was analysed following the procedures explained in Chapter 3: qualitative analysis recording the shape recovery with a digital camera; thermo-mechanical cycle performed by Thermo-Mechanical Analysis (TMA); and recovery of the original surface after been indented with different forces.

4.1.2. Materials

4.1.2.1. Polycyclooctene (PCO)

This work has been performed employing the same commercially available polycyclooctene Vestenamer® 8012 (from Evonik Industries), already described at section 2.1.2.1.

4.1.2.2. Surlyn ionomers

Surlyn ionomers are obtained from polyethylene-methacrylic acid, where part of the methacrylic acid groups have been neutralised with a specific cation, such as lithium, sodium, zinc, or magnesium.

In this work, two different ionomers supplied by DuPont were used as received in pellet form. The ionomers used are poly(ethylene-co-methacrylic acids) (EMAA), were a percentage of methacrylic acid groups have been neutralised with zinc (Surlyn 1705) or with sodium (Surlyn 8940). Figure 4.2 show the chemical structure of both Surlyn ionomers.

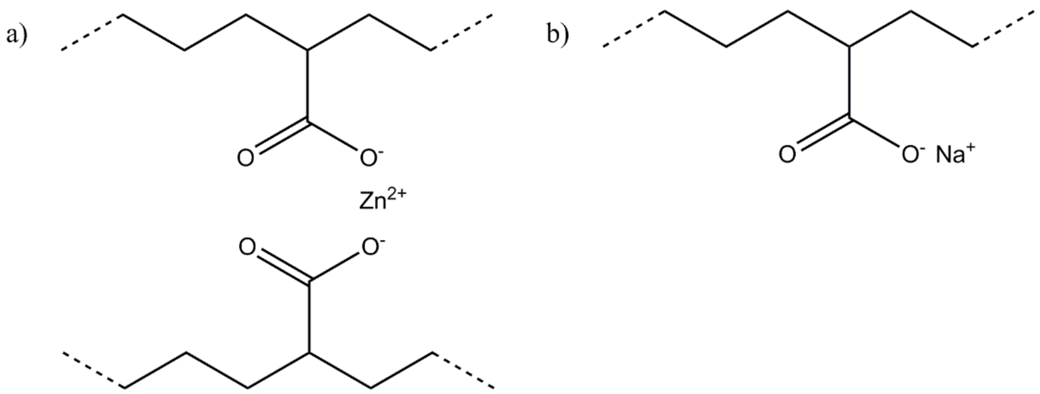

Figure 4.2. Chemical structure of Surlyn (EMAA) ionomers: a) Zn^{2+} ionomer (Surlyn 1705); b) Na^{+} ionomer (Surlyn 8940).

4.1.2.3. Dicumyl peroxide (DCP)

The dicumyl peroxide used was the same aforementioned at section 2.1.2.2.

4.1.3. Preparation of samples

Polycyclooctene/ionomer-based shape memory formulations were prepared by a melt-blending protocol quite similar to that mentioned at section 2.1.3. To obtain the different formulations, specific amounts of ionomer/PCO/DCP were blended according to Table 4.1 in a Haake Rheomix 600 mixing chamber. The ionomer or the 50/50 mix of ionomer+PCO (depending on the formulation) was inserted to the mixer at 92ºC. After 8 minutes, the DCP (2 or 3 wt% referred to the relationship ionomer/PCO or 3 wt% in the case of both ionomers) was added, mixing the components during 4 minutes more. As can be seen in Table 4.1, both ionomers have been mixed with 3% DCP in order to check the influence of the peroxide in these molecules.

Table 4.1. Developed samples.

Sample	Ionomer (wt%)*	PCO (wt%)*	DCP (wt%)*
Surlyn 1705	100	--	--
Surlyn 1705 + 3% DCP	97	--	3
Surlyn 1705 + PCO	50	50	--
Surlyn 1705 + PCO + 2% DCP	49.5	49.5	1
Surlyn 1705 + PCO + 3% DCP	49.25	49.25	1.5
Surlyn 8940	100	--	--
Surlyn 8940 + 3% DCP	97	--	3
Surlyn 8940 + PCO	50	50	--
Surlyn 8940 + PCO + 2% DCP	49.5	49.5	1
Surlyn 8940 + PCO + 3% DCP	49.25	49.25	1.5

* Weight percentages refer to the global relationship Surlyn/PCO/DCP.

Subsequently, the samples were made by compression moulding, in a 50 mm × 50 mm × 1.5 mm mould, between two Teflon sheets, at 160ºC during 20 minutes. After this, the specimens were cooled to room temperature in the mould maintaining the pressure, obtaining in this manner the final sample sheets that will be characterized by the analytical techniques cited above (TGA, DSC, DMTA). Shape memory effect by TMA and self-healing behaviour will be also analysed on these samples.

4.1.4. Experimental section

4.1.4.1. Thermogravimetric Analysis

The TGA measurements were performed from 25 to 800 ºC with a heating rate of 10 ºC min^{-1} under nitrogen atmosphere. The analyses were carried out with a Mettler Toledo TGA/SDTA 851e thermobalance. The temperatures (T_d) at the maximum degradation rate (dw/dt) were obtained from DTG curves.

The analysis was performed before and after compression moulding. Table 4.2 collects the degradation temperatures for the pellets and the mixtures, whereas the values after compression moulding are detailed in Table 4.3 (note that S1705 corresponds to Surlyn 1705 ionomer and S8940 to Surlyn 8940 ionomer). The TGA curves for all developed samples are represented in Figure 4.3 (Surlyn 1705 mixtures), Figure 4.4 (Surlyn 1705 moulded compressed samples), Figure 4.5 (Surlyn 8940 mixtures), and Figure 4.6 (Surlyn 8940 moulded compressed samples).

All samples decompose in one main breakdown stage at temperatures above 400 ºC, (Figure 4.3 to Figure 4.6), but in the TGA curves of the samples with peroxide a slight decrease in the mass percentage below 200 ºC can be noted. This weight loss stage can be associated with residual peroxide and decomposition products of the DCP [7]. Anyway, all the developed samples present a good thermal stability up to 400 ºC, and as it can be seen the behaviour of the blends is similar, independently of the employed ionomer.

Table 4.2. Thermal properties for studied samples before compression moulding (pellets and blends).

Sample	T_{m1-PCO} (ºC)	T_{m1-S} (ºC)	T_{c-PCO} (ºC)	T_{c-S} (ºC)	T_{m2-PCO} (ºC)	T_{m2-S} (ºC)	T_d (ºC)
S1705	--	96.9	--	61.5	--	96.1	462.3
S1705 + 3% DCP	--	96.6	--	66.7	--	92.1	465.0
S1705 + PCO	59.5	95.3	36.4	66.1	57.8	94.5	461.5
S1705 + PCO + 2% DCP	57.7	93.9	36.2	66.7	56.0	93.5	463.8
S1705 + PCO + 3% DCP	57.6	93.5	35.6	66.8	55.3	93.3	465.4
S8940	--	103.3	--	79.4	--	102.0	467.4
S8940 + 3% DCP	--	99.6	--	78.3	--	98.0	463.8
S8940 + PCO	59.7	100.2	36.5	79.4	57.2	98.0	465.9
S8940 + PCO + 2% DCP	59.2	98.4	36.0	79.4	55.9	97.0	466.3
S8940 + PCO + 3% DCP	58.5	98.2	35.9	79.4	55.9	97.4	463.0

Table 4.3. Thermal properties for studied samples after being compressed.

Sample	T_{m1-PCO} **(ºC)**	T_{m1-S} **(ºC)**	T_{c-PCO} **(ºC)**	T_{c-S} **(ºC)**	T_{m2-PCO} **(ºC)**	T_{m2-S} **(ºC)**	T_d **(ºC)**
S1705	--	96.1	--	61.8	--	94.4	467.7
S1705 + 3% DCP	--	90.1	--	61.8	--	88.6	466.1
S1705 + PCO	58.1	94.6	37.0	65.6	56.5	93.8	461.7
S1705 + PCO + 2% DCP	54.0	93.0	31.5	62.4	54.3	92.3	465.4
S1705 + PCO + 3% DCP	49.7	91.7	26.5	60.7	49.0	91.2	464.9
S8940	--	101.2	--	78.8	--	100.0	467.2
S8940 + 3% DCP	--	92.1	--	71.1	--	92.0	467.6
S8940 + PCO	56.8	96.5	37.6	80.4	55.8	96.7	467.2
S8940 + PCO + 2% DCP	52.2	96.2	32.7	77.9	51.5	95.4	465.3
S8940 + PCO + 3% DCP	47.9	94.5	25.1	75.2	48.2	96.0	466.1

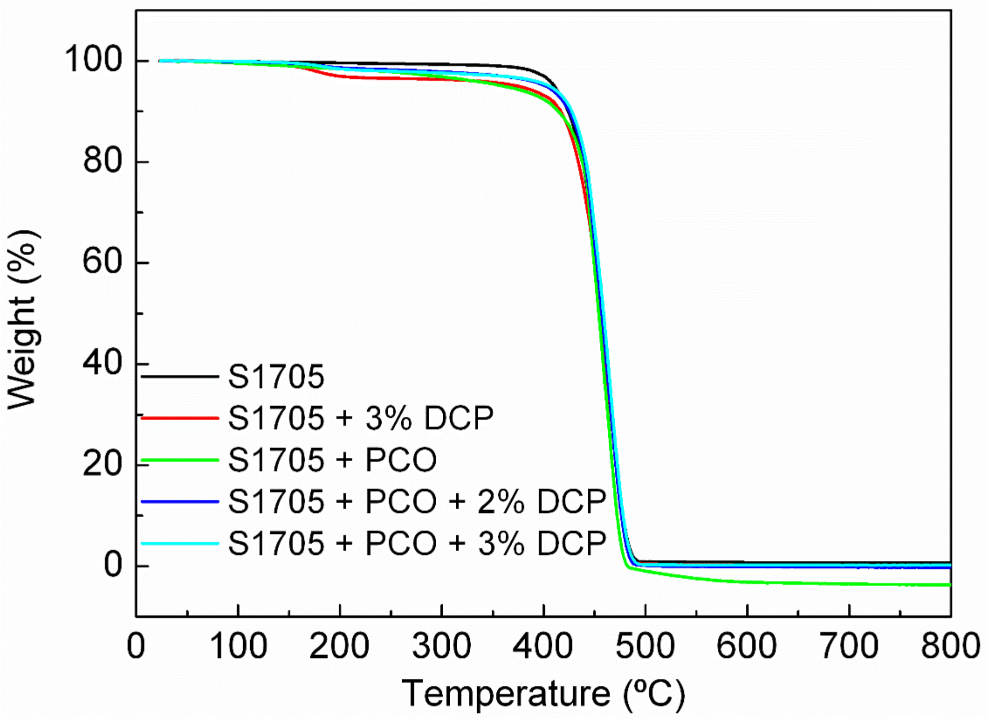

Figure 4.3. TGA of the samples containing Surlyn 1705 ionomer before compression moulding.

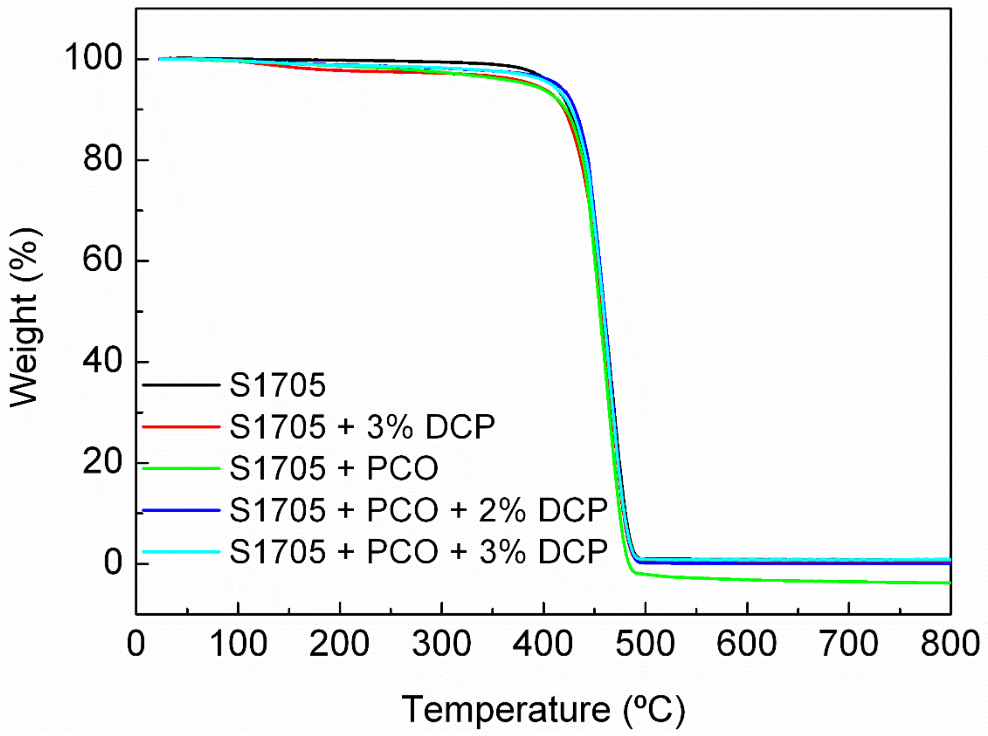

Figure 4.4. TGA of the samples containing Surlyn 1705 ionomer after compression moulding.

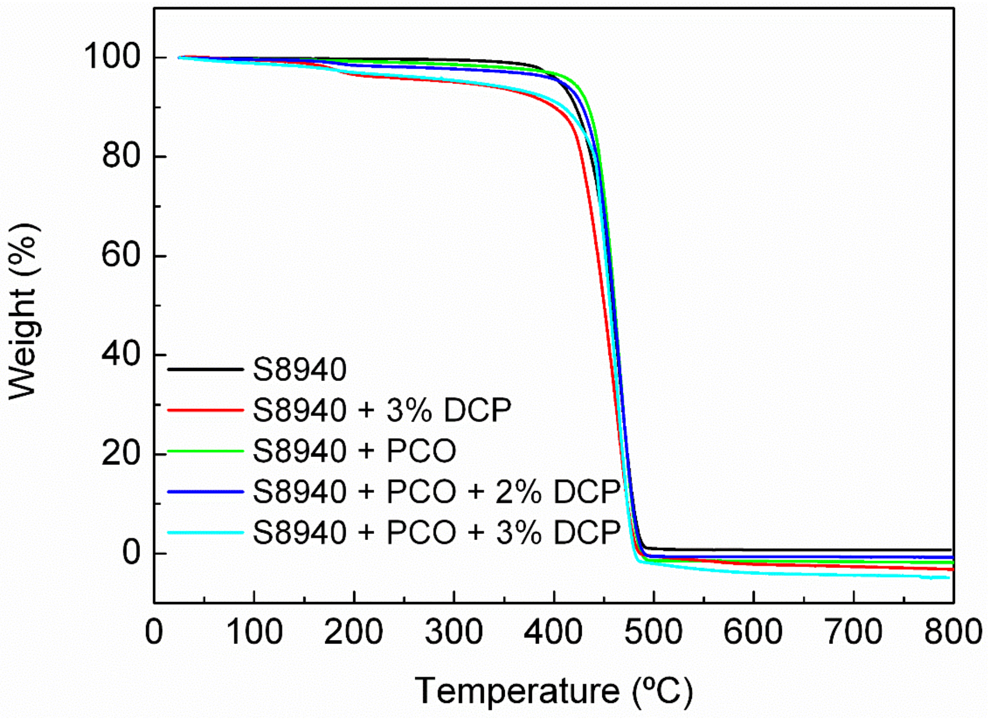

Figure 4.5. TGA of the samples containing Surlyn 8940 ionomer before compression moulding.

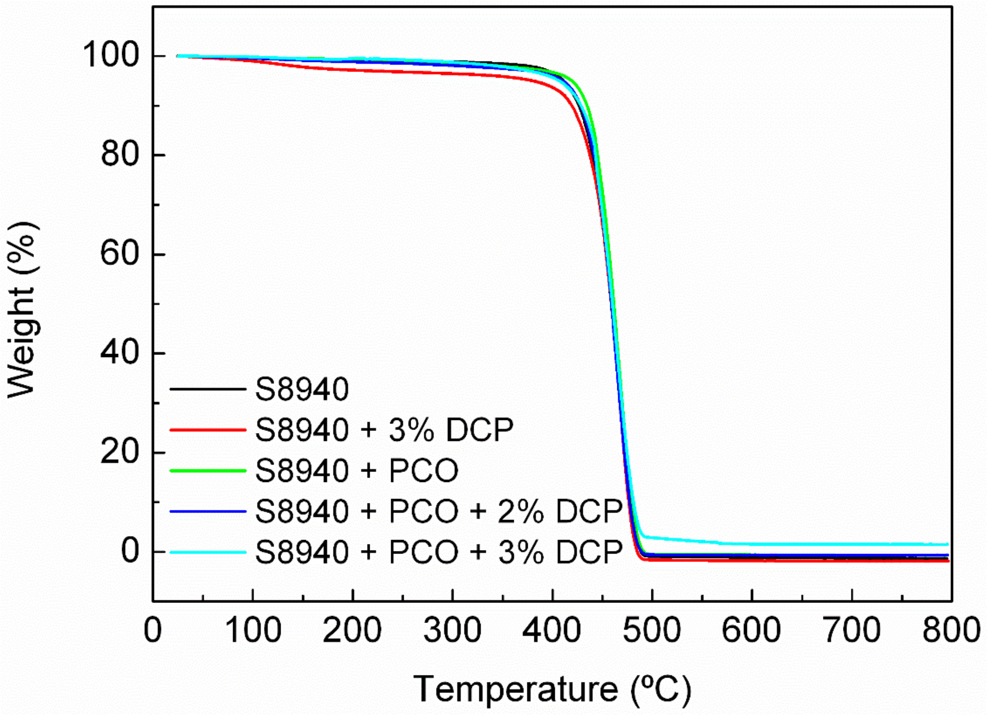

Figure 4.6. TGA of the samples containing Surlyn 8940 ionomer after compression moulding.

Figure 4.7 shows the TGA curves for the two pure ionomers, where practically no differences on the degradation process can be observed. The only appreciable difference consists in the remnant weight at the end of the process, i.e. the inorganic part (metal ions) that does not suffer degradation process at 800ºC. Therefore, this non-degraded residue is slightly higher for the Surlyn 1705 ionomer (Zn atomic weight 65.38) than for the Surlyn 8940 ionomer (Na atomic weight 22.99).

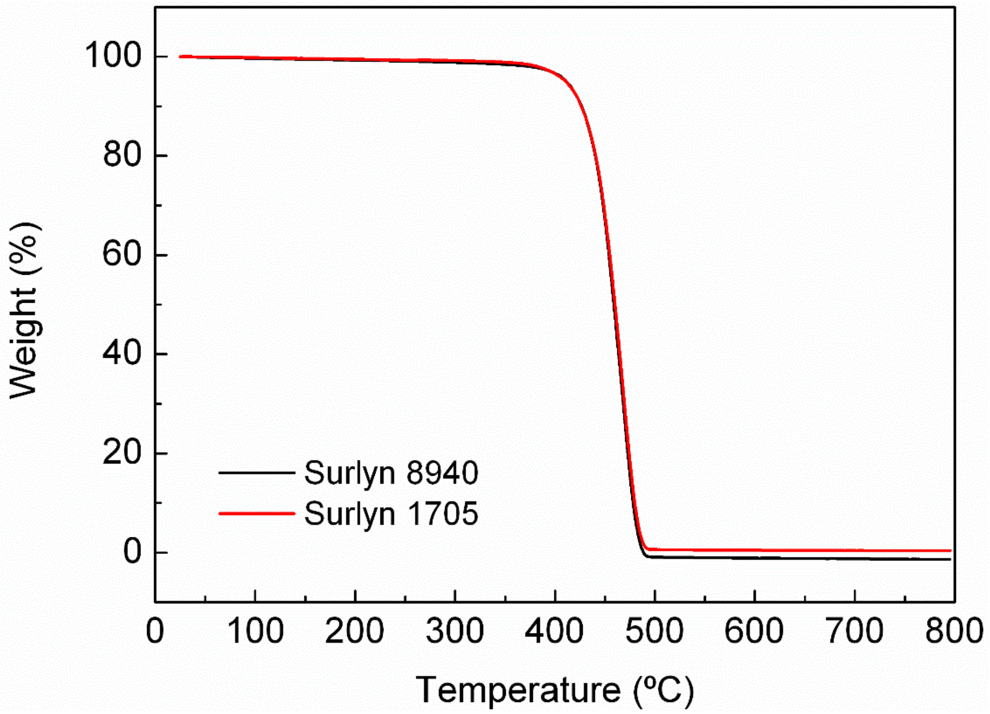

Figure 4.7. TGA curves of Surlyn 8940 and Surlyn 1705 samples after compression moulding process.

4.1.4.2. Differential Scanning Calorimetry

Thermal properties of the samples were measured by Differential Scanning Calorimetry (DSC 822e from Mettler Toledo) to identify thermal actuation temperatures. Samples in aluminium pans were characterized under constant nitrogen flow (50 mL·min^{-1}), heating from −100 ºC to 150 ºC at a rate of 10 ºC·min^{-1}, cooling from 150 ºC to −100 ºC at a rate of −10 ºC·min^{-1}, and heating again at 10 ºC·min^{-1} until 150 ºC. As in the TGA, this analysis was performed for the ionomer pellets and the blends obtained by extrusion process (Table 4.2) and also for the samples performed by compression moulding (Table 4.3). The DSC curves for all developed samples are represented in Figure 4.8 (Surlyn 1705 mixtures), Figure 4.9 (Surlyn 1705 moulded compressed samples), Figure 4.10 (Surlyn 8940 mixtures), and Figure 4.11 (Surlyn 8940 moulded compressed samples).

For all samples, small differences can be seen between first and second heating due to thermal history. However, for the pure ionomers, it is important to mention that in the first heating a weak peak appears before melting, whereas in the second heating it does not exist. This peak is known as order-disorder transition (T_{ord}) because the ionic clusters lose order and strength [8], and can be clearly seen in Figure 4.12, where the DSC curves of the two pure ionomers (together with the corresponding PCO curve) after compression moulding are represented. It can be observed that, although the melting temperature for the two ionic specimens is quite similar (96 ºC for S1705 and 101ºC for S8940 in the first heating, and 94ºC for S1705 and 100 ºC for S8940 in the second heating), the crystallization peak varies in around 20 ºC (62ºC for S1705 and 79ºC for S8940).

Observing the characteristic temperatures before the compression process (Table 4.2) it can be seen that the differences between samples are not significant. However, when they are compressed (Table 4.3) the behaviour changes in those samples with peroxide due to the crosslinking process, and a diminution in the temperatures is certified (Figure 4.9 and Figure 4.11). The samples containing the polymer and the ionomer present two melting and two crystallization peaks, indicating that the blends are immiscible (clearly seen in Figure 4.13). Additionally, as the amount of peroxide increases, the melting temperature of the two peaks decreases, due to the increase of crosslinks, causing a restriction of the mobility of the polymer chains, which provokes a diminution of the melting temperature, as is in concordance with previous studies [9] (as can be noted in Figure 4.9 and Figure 4.11, but it is easier to see in Figure 4.14).

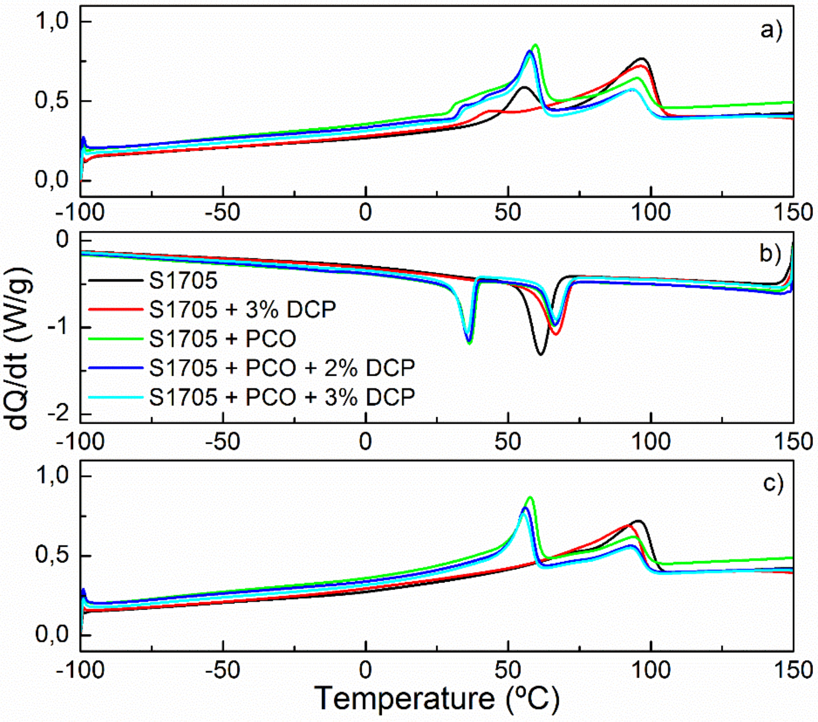

Figure 4.8. DSC of the samples containing Surlyn 1705 ionomer before compression moulding: a) first heating, b) cooling and c) second heating scan.

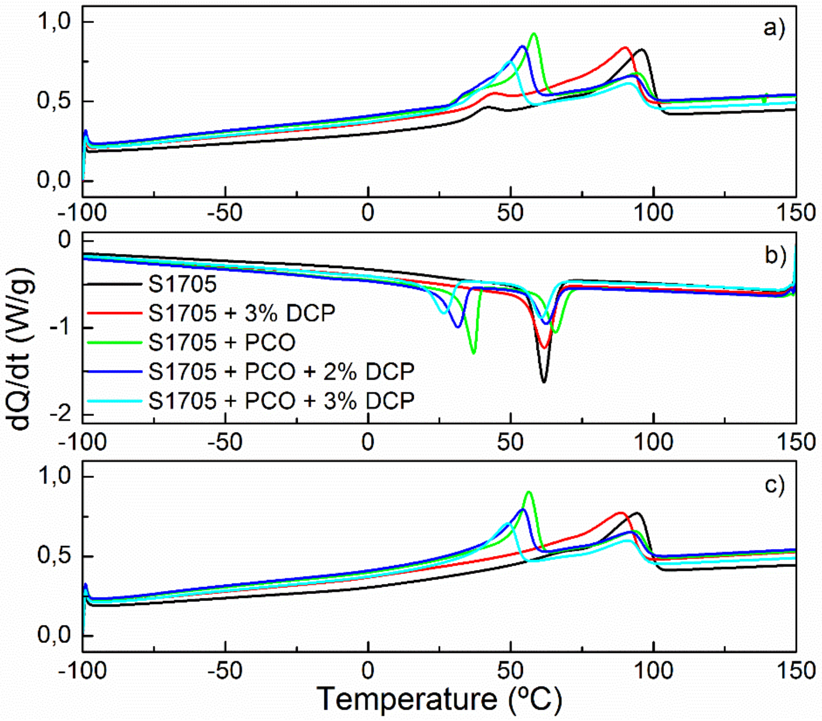

Figure 4.9. DSC of the samples containing Surlyn 1705 ionomer after compression moulding: a) first heating, b) cooling and c) second heating scan.

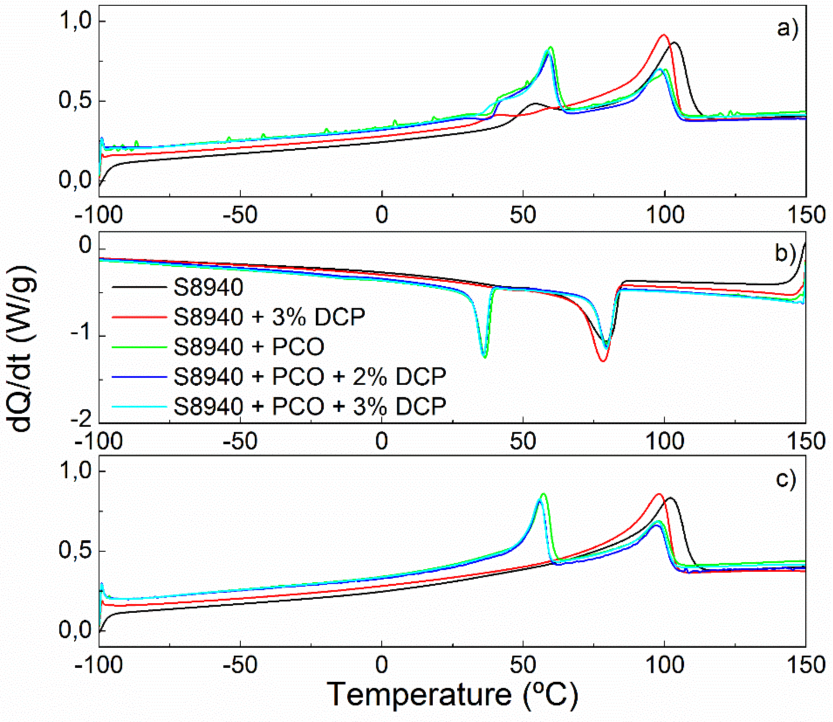

Figure 4.10. DSC of the samples containing Surlyn 8940 ionomer before compression moulding: a) first heating, b) cooling and c) second heating scan.

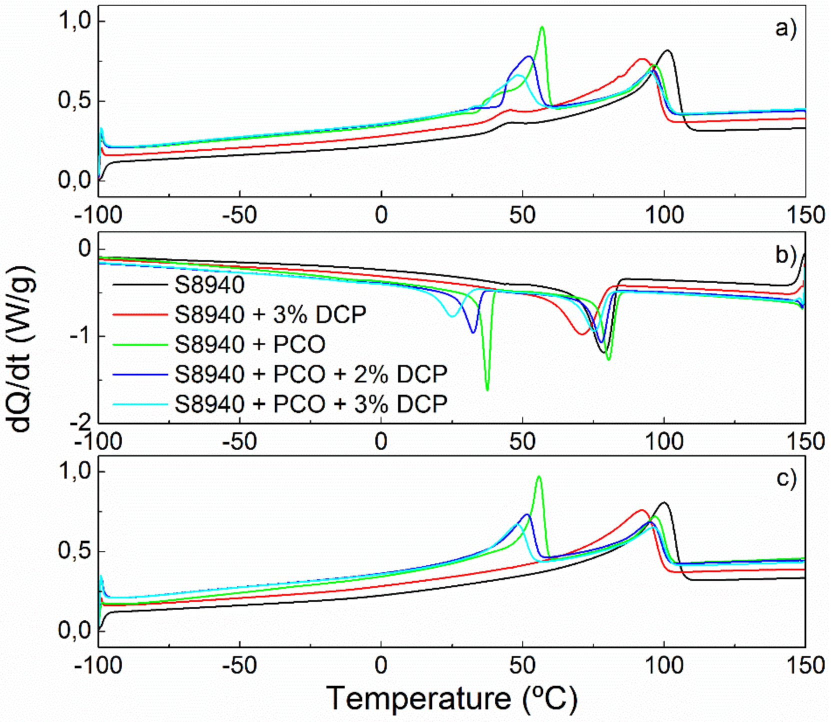

Figure 4.11. DSC of the samples containing Surlyn 8940 ionomer after compression moulding: a) first heating, b) cooling and c) second heating scan.

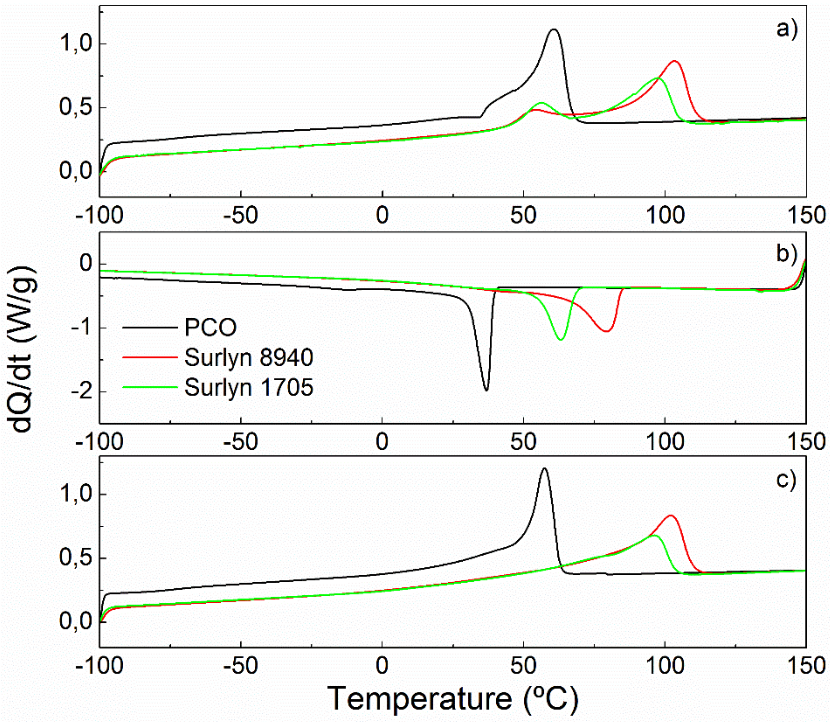

Figure 4.12. DSC curves for PCO, Surlyn 8940 and Surlyn 1705 samples after compression moulding: a) first heating, b) cooling and c) second heating scan.

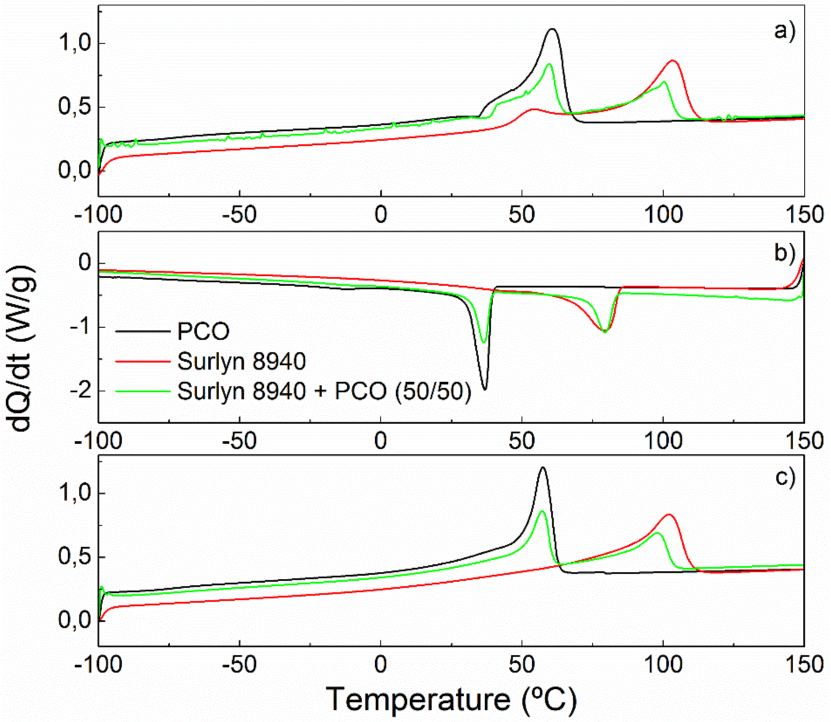

Figure 4.13. Comparison between PCO, Surlyn 8940 and the 50/50 blend after compression moulding: a) first heating, b) cooling and c) second heating scan.

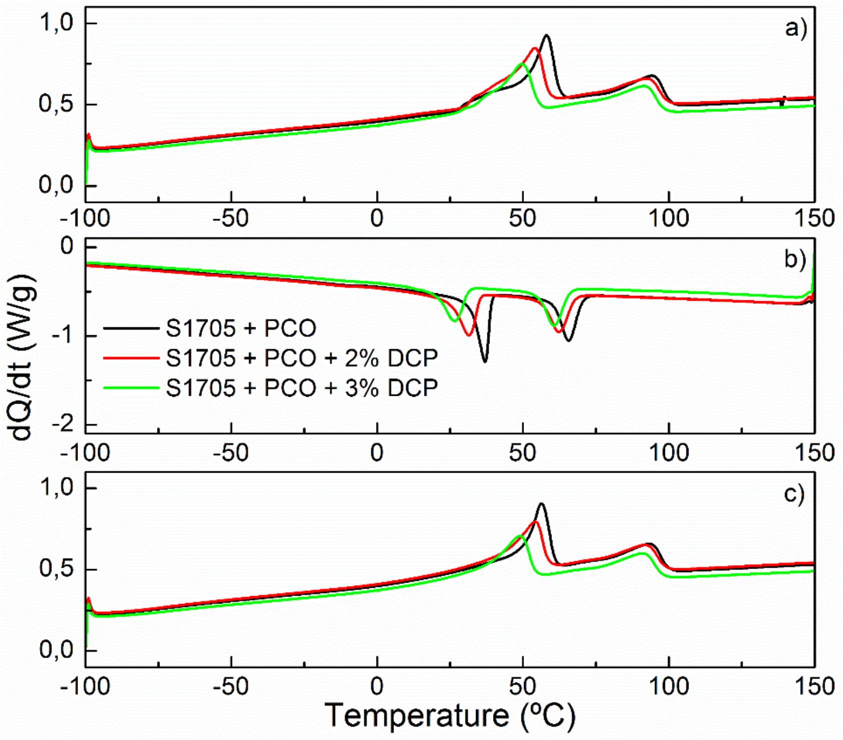

Figure 4.14. DSC curves of Surlyn 1705 + PCO blends after compression moulding: a) first heating, b) cooling and c) second heating scan.

As the ionomers had demonstrated shape memory properties [10,11] and, additionally, these Surlyn + PCO systems present two separated transition temperatures (see T_{m-PCO} and T_{m-S} on Table 4.3), they are susceptible to show triple-shape memory behaviour [12,13], so this effect will be analysed.

4.1.4.3. Dynamic Mechanical Thermal Analysis

Dynamic mechanical thermal analysis were performed in a Polymer Laboratories MK-II DMTA, in flexion mode, in 10 mm × 35 mm × 1.5 mm strips (cut from the compression manufactured samples). The samples were measured using the dual cantilever test from -100 to 150 ºC, at a deformation frequency of 10 Hz, a strain of 64 µm and a heating rate of 2 ºC min^{-1}. This technique is highly sensitivity for detect changes in internal molecular mobility, so it is useful to confirm the results obtained by DSC and to measure the glass transition temperatures (T_g) for these specimens.

The evolution of flexural storage modulus (E') and $\tan\delta$ with temperature are shown in Figure 4.15 (comparison between Surlyn 8940 and Surlyn 8940 + 3% DCP samples) and Figure 4.16 (comparison between Surlyn 8940 + PCO blends). Similar behaviour can be observed for Surlyn 1705 ionomer (Figure 4.17 and Figure 4.18, respectively).

When we compare the ionomer sample with and without peroxide (Figure 4.15 for Surlyn 8940 and Figure 4.17 for Surlyn 1705), we can observe that initially both samples show a similar behaviour, where high values of storage modulus are observed due to the samples are in a vitrified state ($T < T_g$). When the T_g of the sample is reached, a drop in the E' curve is observed, resulting in a peak in the $\tan\delta$ analysis (around 50ºC). At temperatures above the glass transition temperature, the modulus continues dropping progressively until about 100ºC, which corresponds to the melting temperature of the crystallites, as shown in section 4.1.4.2. At this temperature, the main difference between these two systems is clear: while E' in the sample without peroxide (Surlyn ionomers) drops and $\tan\delta$ rises indefinitely; the sample with a 3 wt% of peroxide shows a *plateau* both in E' as in $\tan\delta$, indicating that this sample is crosslinked [7,14]. Therefore, it can be concluded that the dicumyl peroxide is able to crosslink the ionomer chains.

Analysing the Surlyn + PCO blends (Figure 4.16 and Figure 4.18 for Surlyn 8940 and Surlyn 1705, respectively), the behaviour is similar for that described above, beginning with high values of E', and dropping at about -50 ºC, which corresponds to the glass transition temperature of the PCO portion [15], observing a peak in $\tan\delta$ curve. Then, the modulus continues dropping progressively until near 50 ºC, temperature associated to the glass transition of the ionomer, as seen before. Reaching this point, the sample without peroxide follows the same trend observed before in both Surlyn ionomers, that is, the modulus drops and the $\tan\delta$ rises indefinitely. In contrast, those samples with peroxide show a stabilisation of the modulus and $\tan\delta$ values, indicating that the samples are crosslinked.

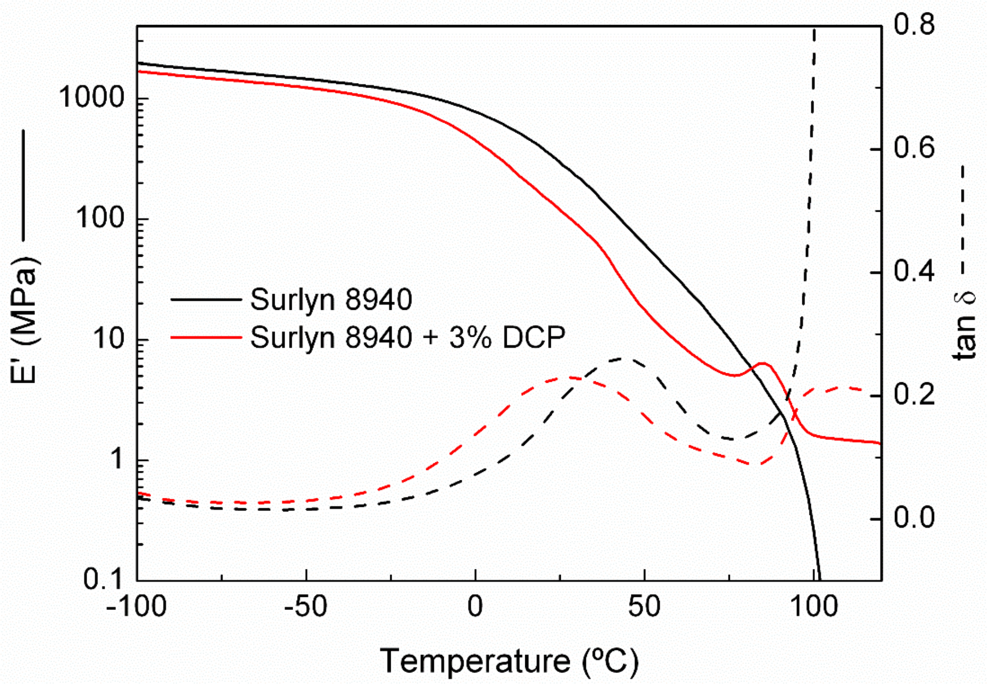

Figure 4.15. Flexion storage (E') modulus and tan δ for Surlyn 8940 and Surlyn 8940 + 3% DCP samples.

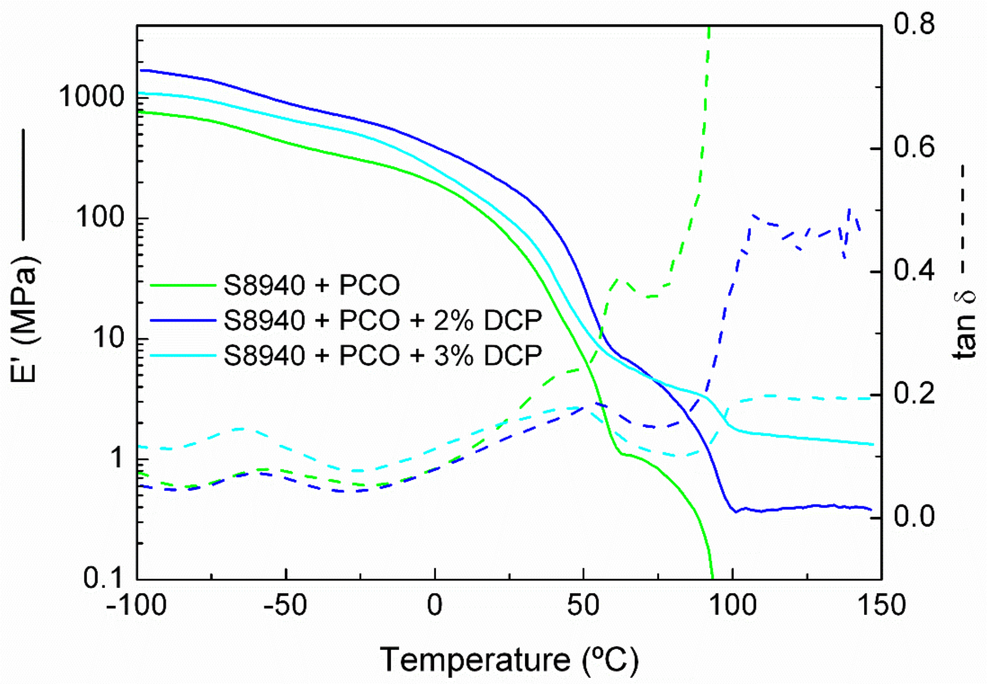

Figure 4.16. Flexion storage (E') modulus and tan δ for Surlyn 8940 + PCO blends.

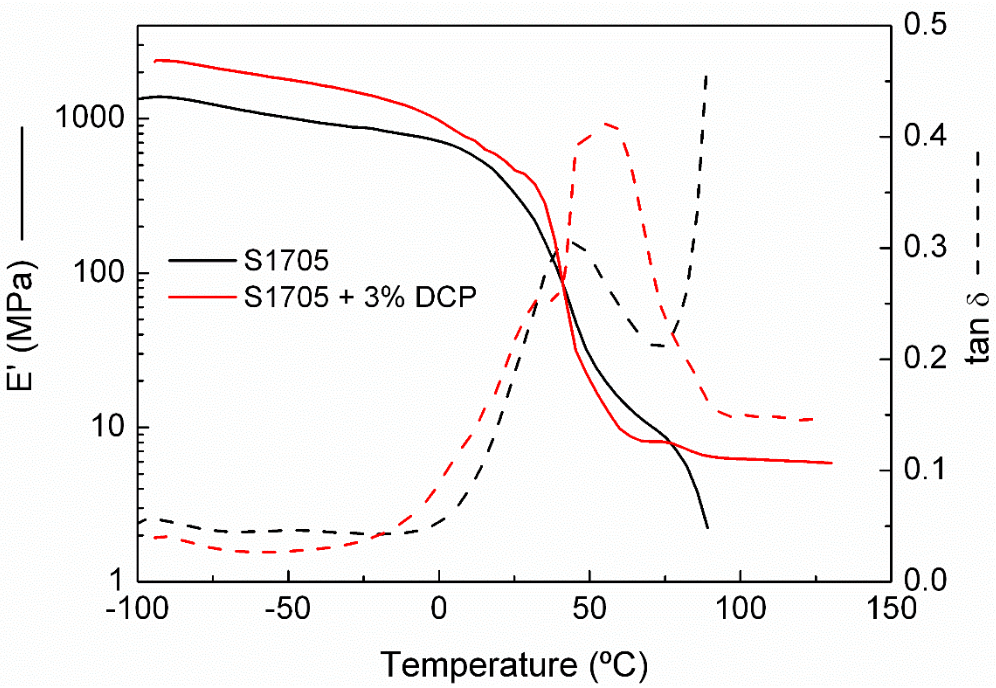

Figure 4.17. Flexion storage (E') modulus and tan δ for Surlyn 1705 and Surlyn 1705 + 3% DCP samples.

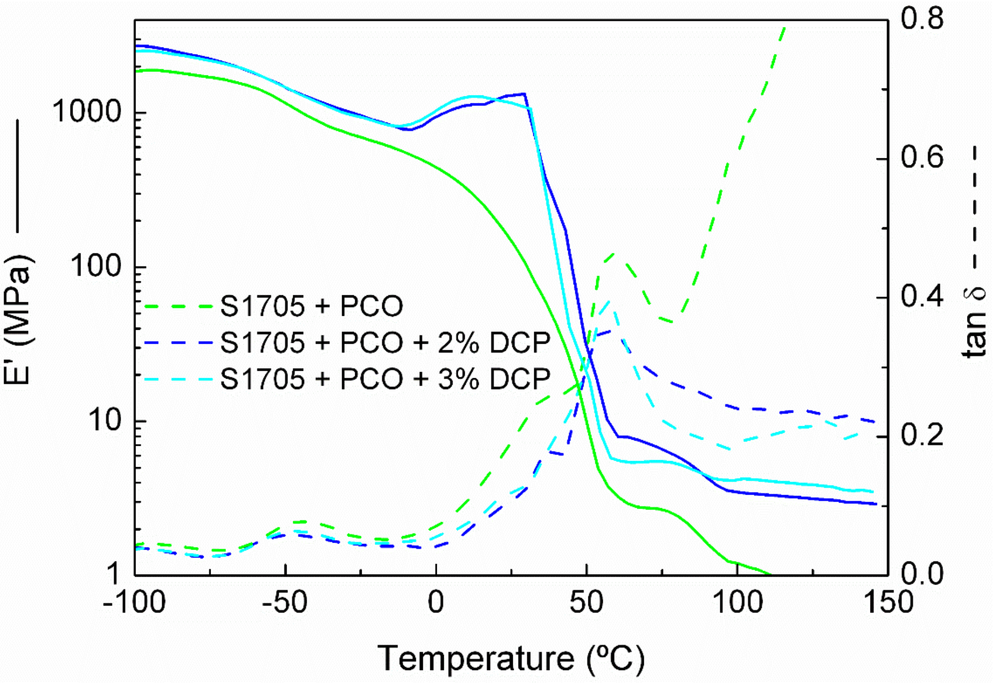

Figure 4.18. Flexion storage (E') modulus and tan δ for Surlyn 1705 + PCO blends.

4.1.4.4. Shape memory behaviour

As seen in section 3.2.4, the shape memory behaviour can be analysed qualitatively (with a digital camera), quantitatively (by TMA cycles), or studying the self-repair capabilities of the samples.

a. Qualitative analysis

These experiments were made taking into account those ones made in section 3.2.4.1, i.e. using almost the same protocol aforementioned in that section. For Surlyn, Surlyn + 3% DCP, and Surlyn + PCO samples, 10 mm x 35 mm x 1.5 mm specimens were bended at a temperature higher than T_{trans}, and this temporary shape was fixed cooling down the system below its T_{trans}. The recovery process was effectuated by heating again the sample at a temperature above T_{trans}. This experiment has been performed for all the samples taking 90ºC as T_{trans} (near the melting temperature of both ionomers, showed at Table 4.3). As example, Figure 4.19 shows this process for Surlyn 1705. Because the original sample at room temperature is transparent, the sample was green painted in order to see the changes of shape.

As commented at section 4.1.4.2, those samples containing ionomer, polycylooctene and peroxide (crosslinked samples) are able to show triple-shape memory effect. To check this, a new experiment was tested according to the explanation in section 1.5.1.2. First, the sample in its original shape (I shape) was heated at higher temperature (90 ºC, near the melting temperature of the ionomer), partially bended at this temperature and put at middle temperature (60 ºC, higher than T_{trans} of PCO) to fix one of the temporary shapes (L shape), and at the same time deform to give the second temporary shape, which is fixed in a cool bath at 20 ºC (U shape). When the sample is heated again at 60 ºC, it is partially recovered (L shape) and when is heated at 90 ºC the sample recovers the original shape (I shape). This permanent shape is cooled again at 20 ºC, allowing to the sample to crystallize. As an example, Figure 4.20 shows the process for one of the samples

(Surlyn 9520 + PCO + 3% DCP). In order to see the different changes of shape, the sample was painted green on one side and red on the other.

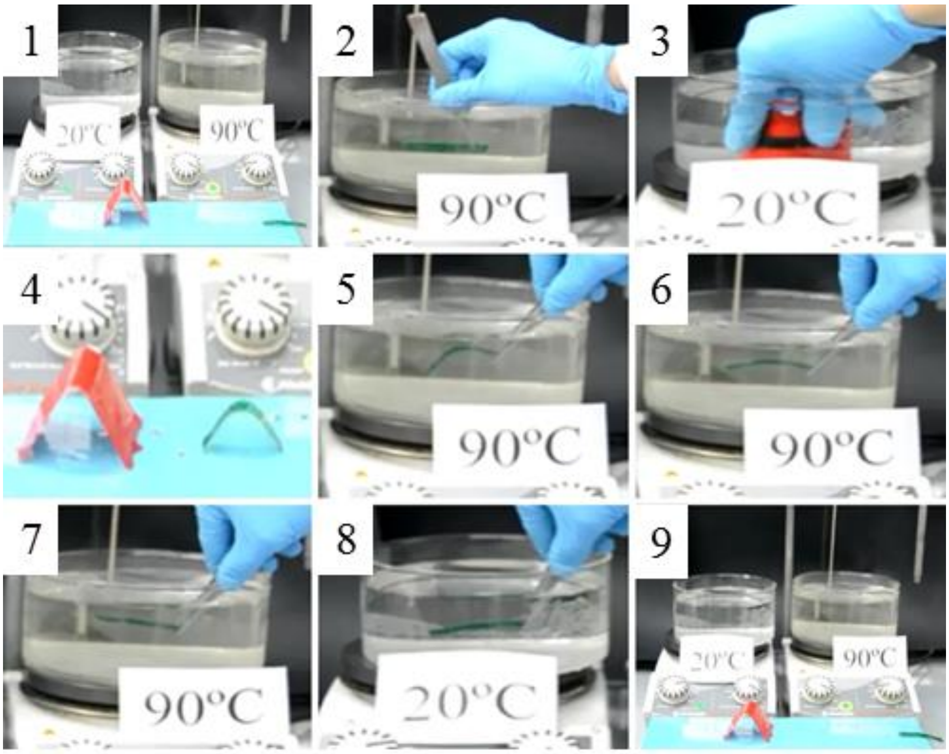

Figure 4.19. Dual shape memory effect of Surlyn 1705 (fixation of the temporary shape + recovery of the original one).

b. Quantitative analysis

Shape memory properties of all developed samples were quantitatively analysed with thermo-mechanical cycles performed in the temperature range of 30-100ºC at a rate of 4 ºC min^{-1} employing a Mettler Toledo DMA-1. Rectangular samples of about 20 mm × 4 mm × 1.5 mm were used.

As explained in section 4.1.4.4a, two kind of experiments can be done. The dual shape memory experiment has been done in Surlyn, Surlyn + 3% DCP and Surlyn + PCO samples (using both ionomers: Surlyn 8940 and Surlyn 1705). In the case of Surlyn + PCO + DCP samples, the triple-shape memory behaviour was characterised.

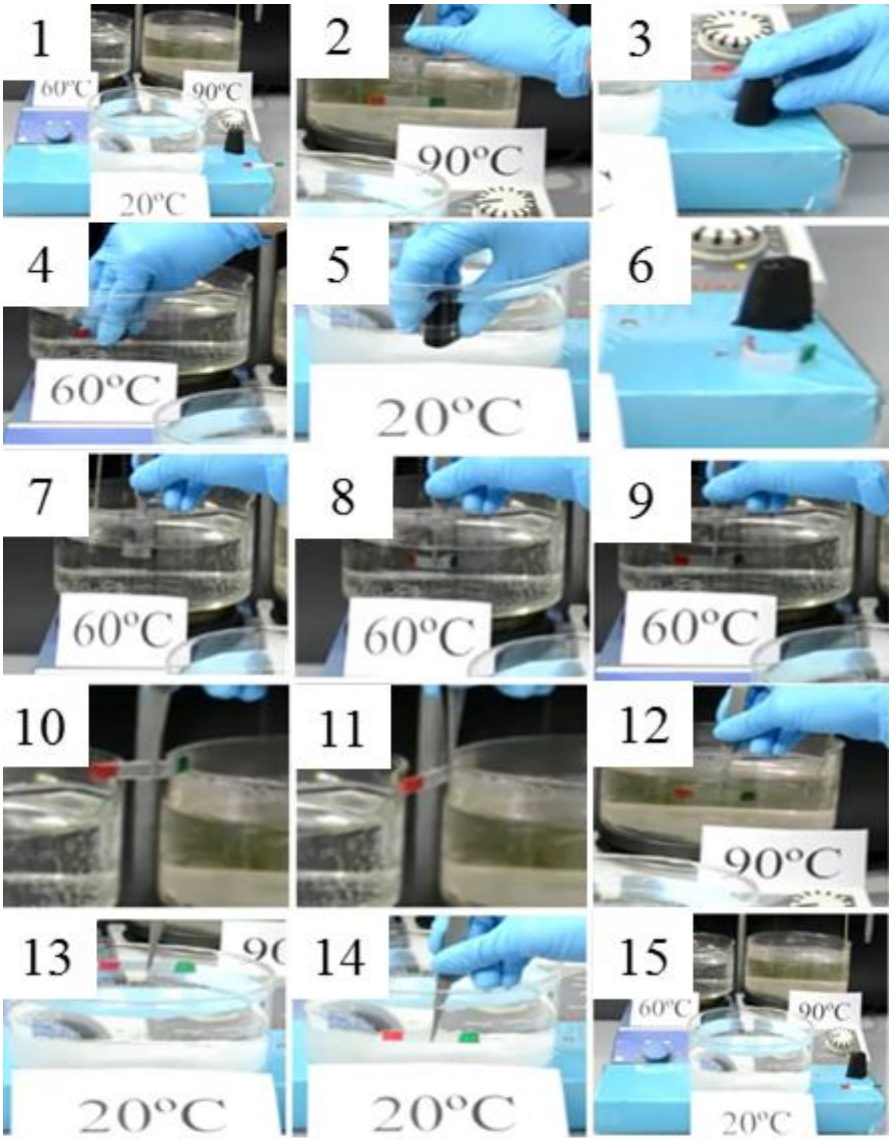

Figure 4.20. Triple shape memory effect of Surlyn 1705 + PCO + 3% DCP (fixation of the L temporary shape + fixation of the U temporary shape + recovery of the L temporary shape + recovery of the original I shape).

The followed procedure to characterise the dual shape memory behaviour (Figure 4.21) consists in heat the sample with a minimum force (F = 0.001 N) at a temperature above the transition temperature (T_m), and then stretched it with a selected X force (1 N or 2 N), deforming it. This stress was maintained during 5 minutes (1). Then the sample was cooled maintaining the force (2) and keeping at low temperature 5 minutes in order to fix the deformation (3). The force was unloaded until a minimum value (0.001 N), fixing the temporary shape (4), and maintained at low temperature without force (5) before heating the sample until $T > T_{trans}$ in order to recover the original shape (6).

As it has been previously mentioned, these dual shape memory experiments were performed for the following samples: both ionomers, ionomer + 3 wt% DCP blends, and ionomer + PCO blends, using first 1 N force, as seen in section 3.2.4.2. The result can be seen in Figure 4.22 as an example for Surlyn 1705 ionomer. As the elongation and the fixation are not too high, it was decided to make the same experiment using a higher force (2 N), showing the result as well in Figure 4.22. In view of obtained results, from here all thermo-mechanical performed cycles have been carried applying a 2 N force. Figure 4.23 show the thermo-mechanical cycles for Surlyn samples deformed at 2 N force. No significant differences are observed in Figure 4.23, both ionomers deform and recover its original shape equally, although the fixation and the recovery processes are a bit different for each of them.

Figure 4.24 and Figure 4.25 show the comparison in the thermo-mechanical cycles between ionomer, ionomer + DCP and ionomer + PCO blends. For example, between Surlyn 1705 and the blend with PCO there are not too much differences (Figure 4.24), but the influence of the crosslinker (DCP) is clear: when the force is applied, the sample without DCP elongates a little bit more than the sample with peroxide. Additionally, when the cooling begins, the Surlyn sample contracts (typical behaviour in stress-control mode, as seen in section 3.2.4.2), but in Surlyn 1705 + 3% DCP sample the deformation increases (the sample dilates). In any case, the original shape is clearly recovered in all cases. A similar behaviour is observed for Surlyn 8940 samples in Figure 4.25.

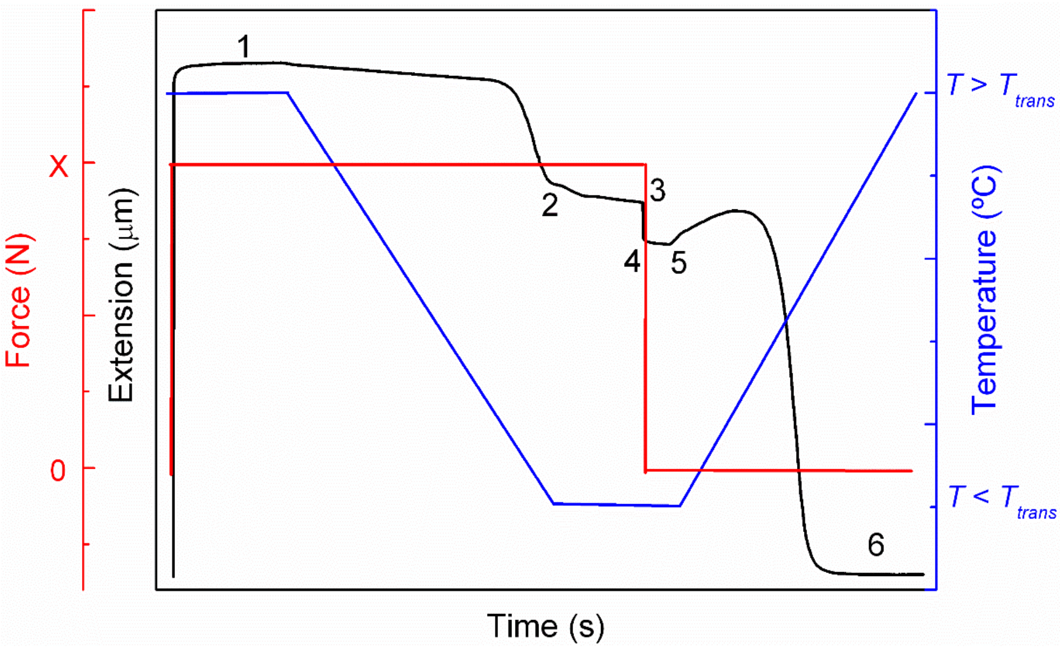

Figure 4.21. Thermo-mechanical procedure to quantify the dual shape memory effect.

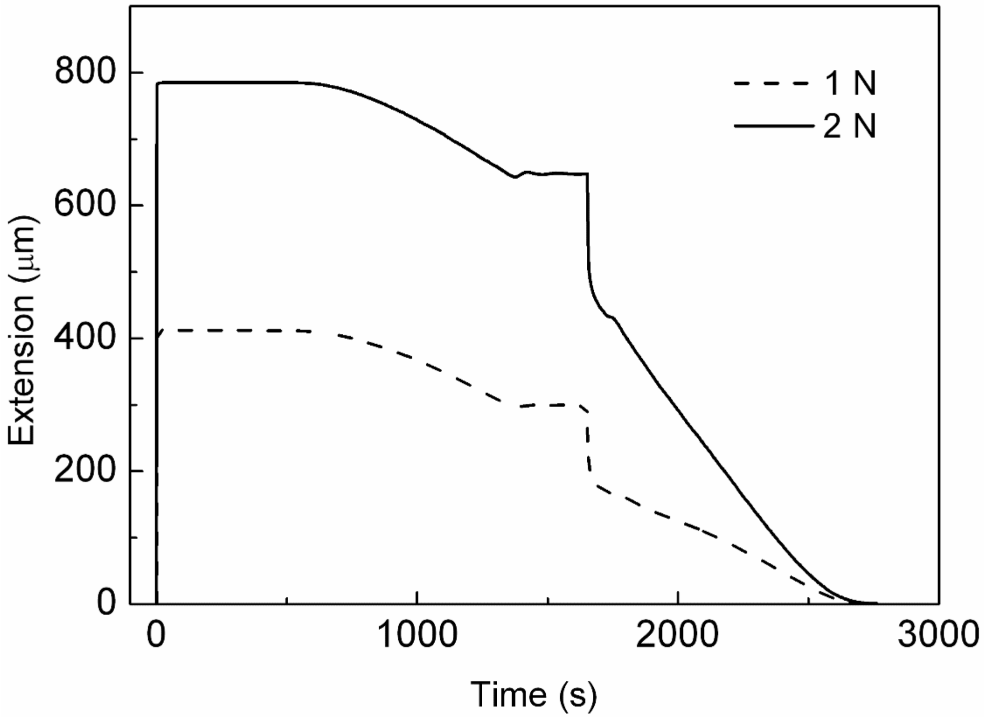

Figure 4.22. Thermo-mechanical cycles of Surlyn 1705 sample elongated at different forces (dual shape memory effect).

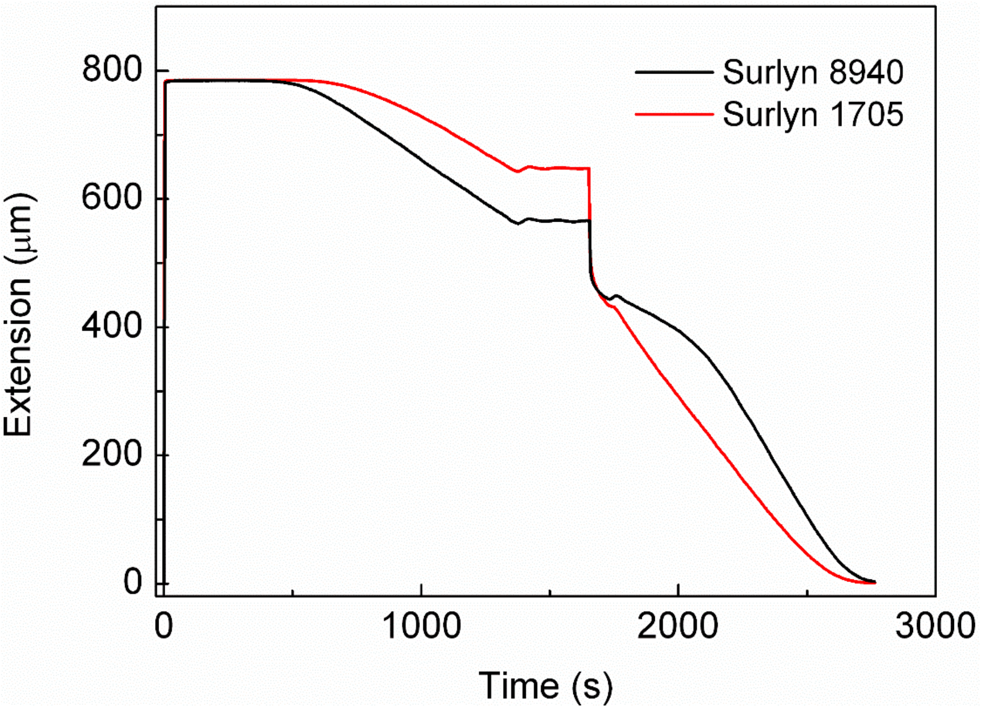

Figure 4.23. Thermo-mechanical cycles of Surlyn 8940 and Surlyn 1705 samples (dual shape memory effect).

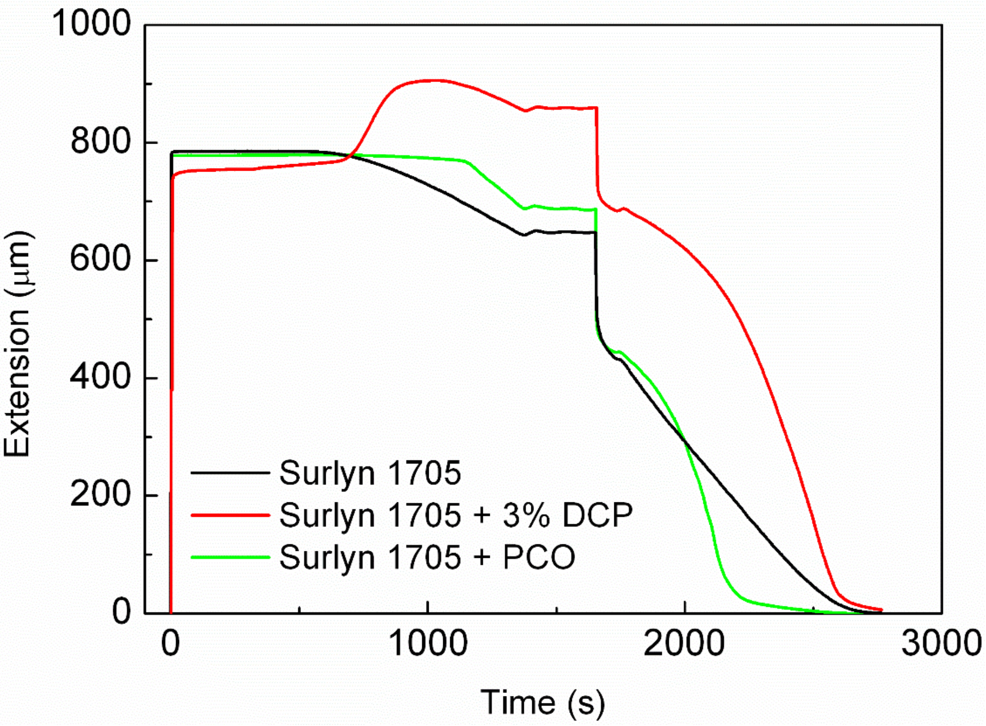

Figure 4.24. Thermo-mechanical cycles of Surlyn 1705, Surlyn 1705 + 3% DCP and Surlyn 1705 + PCO (dual shape memory effect).

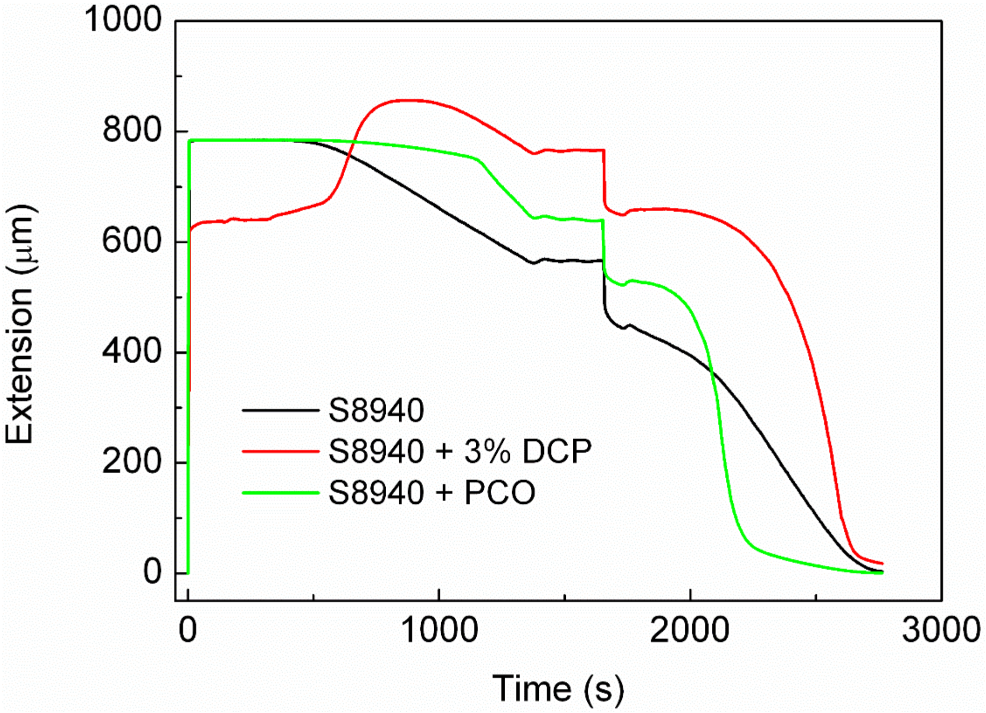

Figure 4.25. Thermo-mechanical cycles of Surlyn 8940, Surlyn 8940 + 3% DCP and Surlyn 8940 + PCO (dual shape memory effect).

The procedure to evaluate Surlyn + PCO + DCP samples is represented in Figure 4.26. First, it is necessary to remember that these systems present triple-shape memory effect because they consist in two separate phases: ionomer part and PCO part. Each phase owns its characteristic transition temperature, where the transition temperature of the ionomer is higher than the PCO one. According to this, the sample was first heated without force (0.001 N) at a temperature above the transition temperature of the ionomer, and then stretched with a selected X force (2 N). After 5 minutes at this temperature (1), the sample was cooled with constant stress until a temperature lower than transition temperature of the ionomer but higher than the PCO one (i.e., 70 ºC) (2) and maintained at this temperature 5 minutes. The force was unloaded until a minimum value (0.001 N), and after maintain the conditions for 5 minutes, the first temporary shape was fixed (3). Subsequently, the sample was elongated applying a $Y > X$ force (2.5 N), maintaining this stress for 5 minutes (4). The next step consisted in cool down the system until a temperature lower than the lowest transition temperature (i.e., 30 ºC) (5) and maintain at low temperature during 5 minutes (6). When the force was removed, the second temporary shape was fixed (7). After a minute at low temperature without force (8), the sample was heated until $T_{high} > T > T_{low}$ (9) and maintained 5 minutes at that temperature to allow the total recovery of the first temporary shape (10). Finally, the sample was heated again until $T > T_{high}$ in order to recover the original shape (11).

The triple-shape memory behaviour of the Surlyn 1705 + PCO + DCP and the Surlyn 8940 + PCO + DCP blends (2% and 3% DCP) is represented in Figure 4.27 and Figure 4.28, respectively. As can be seen, the fixation of the first temporary shape due to the ionomer (between 1000 and 1300 s) is not so good, probably because 70 ºC is a temperature enough high at which the ionomer macromolecules still have some mobility, so it is more difficult to fix the temporary shape at this temperature. At this temperature, the sample is again deformed, obtaining the second temporary shape when cooling and removing the force (around 2600 s). Without force, the sample is heated and when 70 ºC are reached, the sample recovers the shape given at that temperature (the extension between 3300 and 3500 s is almost similar to that at 1300 s). If heating continues up to 100 ºC, the recovery is complete, i.e. the extension of the sample is equal to that at the initial point of the experiment.

The reproducibility of the shape memory behaviour for all developed samples (Table 4.1) was tested performing the same described TMA procedure over ten times. As an example, Figure 4.29 shows the obtained results for Surlyn 8940 + PCO sample, where the length sample is represented versus the experiment time. The results can also be represented in a 3D graph, as it can be seen as an example in Figure 4.30 for Surlyn 8940 sample, where the variation of the sample deformation with the applied force and temperature is represented. The reproducibility of the triple-shape memory behaviour of Surlyn 8940 + PCO + 3% DCP is shown in Figure 4.31 in a 3D graph (the initial point of the experiment is marked with an asterisk, and the letters (a, b, c, d,...) serve as guide to follow the triple-shape memory experiment). Practically no changes between cycles can be observed for all samples.

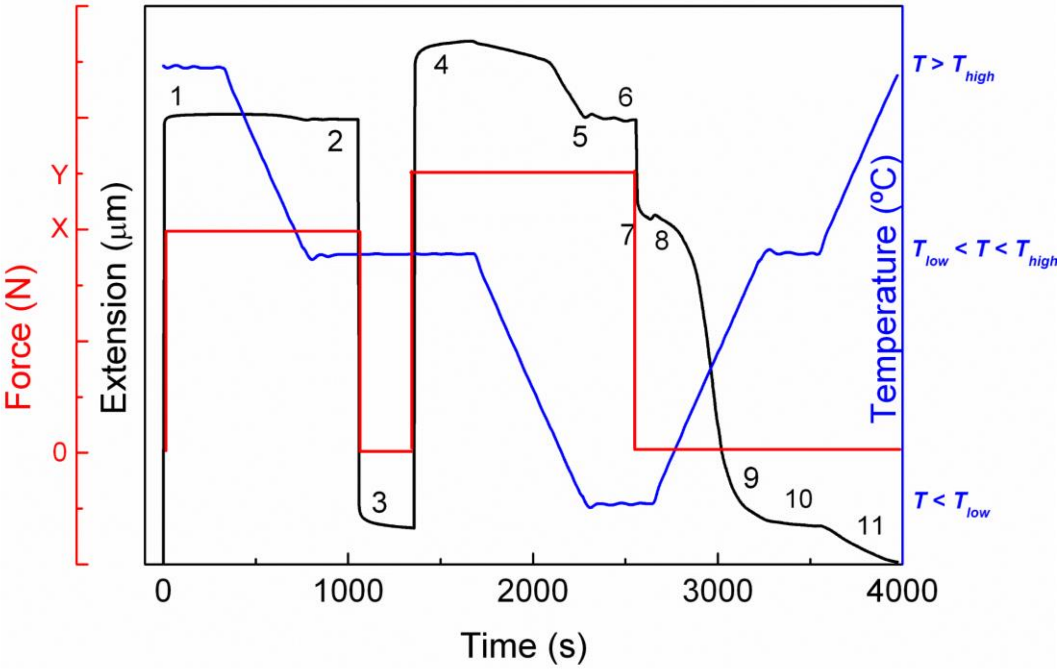

Figure 4.26. Thermo-mechanical procedure to quantify the triple shape memory effect.

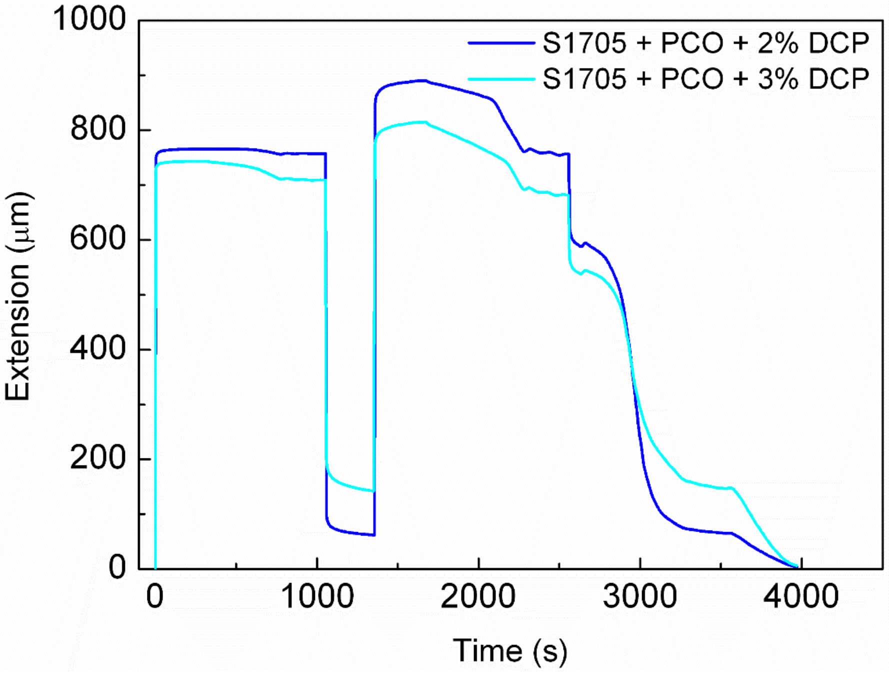

Figure 4.27. Thermo-mechanical cycles of Surlyn 1705 + PCO + 2% DCP and Surlyn 1705 + PCO + 3% DCP (triple-shape memory effect).

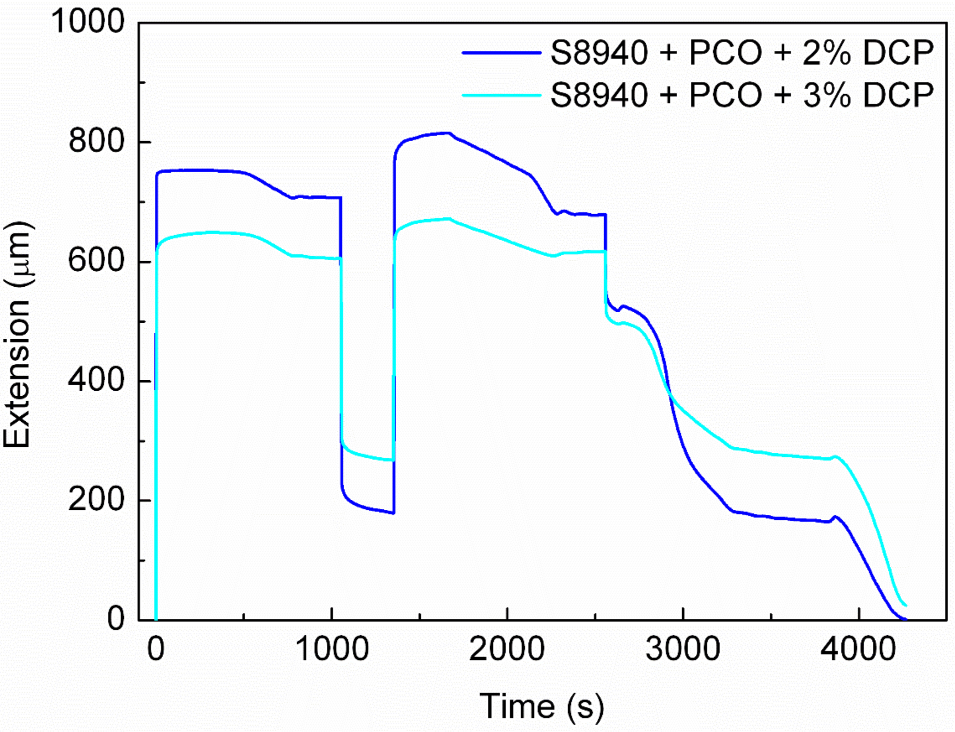

Figure 4.28. Thermo-mechanical cycles of Surlyn 8940 + PCO + 2% DCP and Surlyn 8940 + PCO + 3% DCP (triple-shape memory effect).

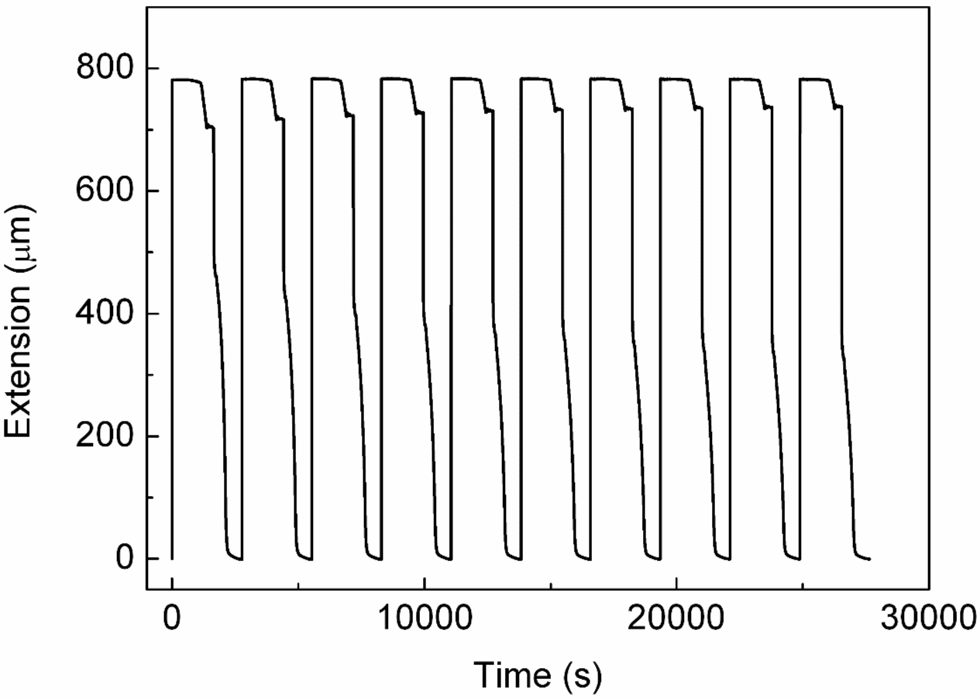

Figure 4.29. Thermo-mechanical response of Surlyn 8940 + PCO sample over 10 cycles (dual shape memory effect).

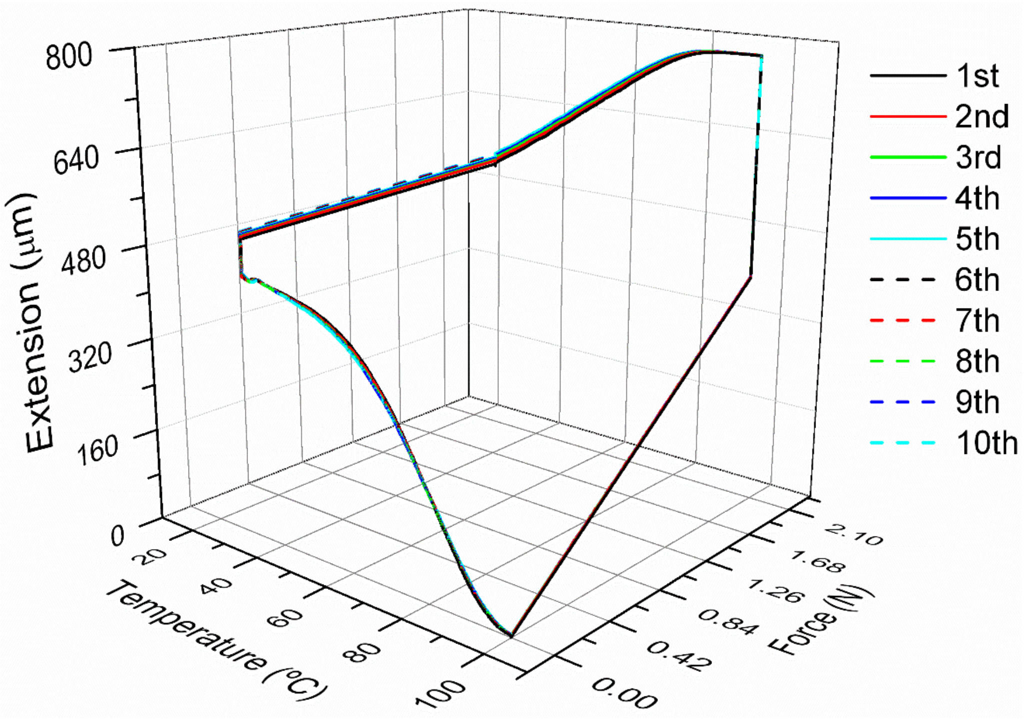

Figure 4.30. Three-dimensional representation of the thermo-mechanical response of Surlyn 8940 sample over 10 cycles (dual shape memory effect).

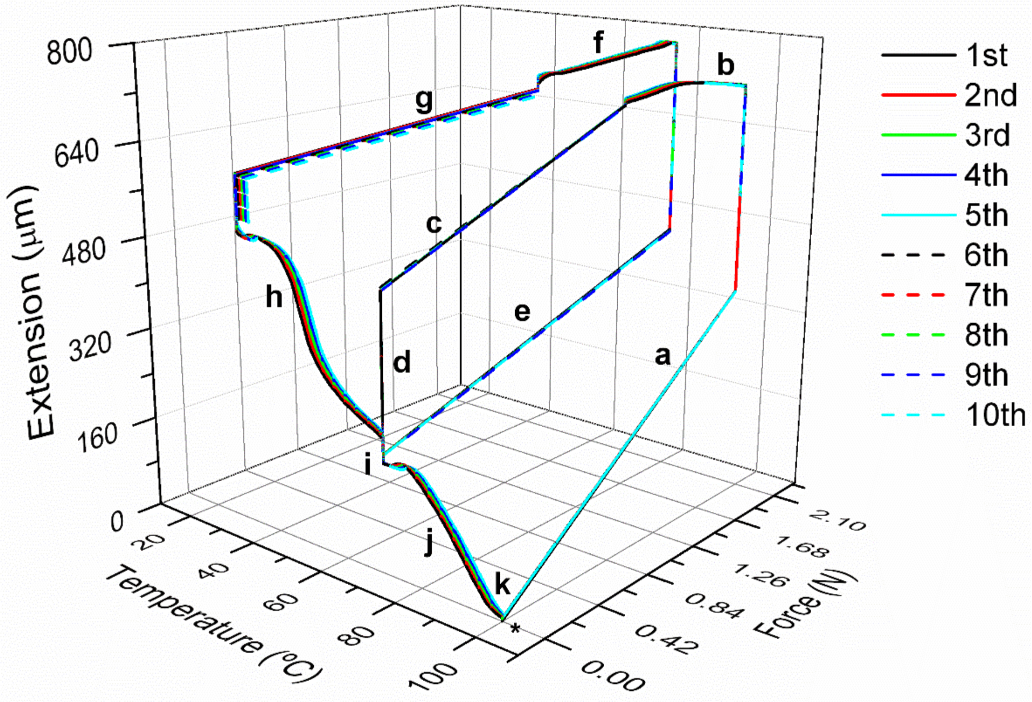

Figure 4.31. Three-dimensional representation of the thermo-mechanical response of Surlyn 8940 + PCO+ 3% DCP sample over 10 cycles (triple-shape memory effect).

c. Self-repair measurements

Self-repair properties of selected blends (Surlyn 1705, Surlyn 1705 + PCO, Surlyn 1705 + PCO + 3% DCP, and the analogues with the Surlyn 8940 ionomer) were evaluated as explained in section 3.2.4.3.

Non-contact confocal optical 3D microscopy (LEICA LCS AP2 AOBS), profilometry (Alpha-Step-D-100 profilometer from KLA-Tencor) and optical microscopy (LEICA DM 2500) were used in order to evaluate the dimensions of the marks. Moreover, the thermal induced self-repair effect was followed *in situ* by optical microscopy (Nikon Eclipse L-150 equipped with and Imaging source camera) recording the recovery of the samples.

Samples were previously marked with a Hardness Test Pencil model 318 from Erichsen, with three different known forces (5 N, 10 N, 15 N). Both holes and lines were performed and analysed. It is not too easy to measure the depth of the lines by confocal microscopy due to technique limitations, so the depth of these marks was only measured by surface profilometry.

Table 4.4 collects the data extracted from the different marks in the samples: the Shore D hardness of the samples; the depth of the holes measured by surface profilometry and confocal microscopy with the three different forces, as well as their diameters (measured with a LEICA DM 2500 optical microscope); and the depth of the lines measured by surface profilometry, and their corresponding widths analysed by optical microscopy.

As explained in section 2.1.4.2, hardness of semicrystalline polymers depends on numerous microestructural parameters, and it is often correlated to the yield stress, being a direct relationship between yield stress and degree of crystallinity [16]. From the previous results obtained in section 2.1.4.2, it is expected a diminution in Shore D hardness value when the ionomers were blended with PCO, and a greater drop when the ionomer/PCO blend was crosslinked with DCP and the crystallinity decrease (as it has been observed previously). This tendency can be seen in Table 4.4.

Table 4.4. Measurements for the different performed marks.

Sample	Shore D hardness	Force (N)	Hole			Line	
			Depth (µm)		Diameter (µm)	Depth (µm)	Width (µm)
			Surface profilometry	Confocal profilometry	Optical microscopy	Surface profilometry	Optical microscopy
S1705	47.5	5	--	--	--	--	452.0
		10	7.2	5.9	--	6.2	538.1
		15	11.1	8.5	--	12.4	659.1
S1705 + PCO	47.1	5	23.6	19.9	576.6	13.3	560.1
		10	51.8	40.6	872.8	34.4	767.7
		15	77.2	59.6	880.3	60.0	813.0
S1705 + PCO + 3% DCP	36.5	5	24.6	21.4	721.1	18.7	581.5
		10	46.3	35.4	831.6	45.8	757.0
		15	105.9	81.2	935.2	71.1	721.4
S8940	43.1	5	--	4.6	--	--	830.8
		10	15.9	13.4	--	9.4	786.4
		15	20.9	16.7	--	50.9	730.1
S8940 + PCO	39.0	5	20.8	16.2	572.4	15.7	528.8
		10	47.6	37.7	768.8	80.7	689.0
		15	68.7	55.8	874.8	147.0	812.8
S8940 + PCO + 3% DCP	34.1	5	19.9	15.9	651.1	11.7	634.1
		10	41.0	32.4	822.3	36.2	776.9
		15	81.6	64.4	906.8	58.7	685.0

Table 4.4 shows that the marks are deeper as the applied force indentation increases. The depth of the holes has been measured by two different techniques (surface profilometry and confocal microsocopy), but the observed trend is the same, demonstrating that both techniques are appropriated for this type of measurements. In base of this result, and due to the limitation of confocal microscopy for measuring depth lines, these marks have been analysed by profilometry technique.

Attending to the hardness, which is a measurement of the resistance of the samples towards indentation, very different behaviour have been observed based on the nature of the samples (see sections 2.1.4.3.a and 3.2.4.3). In principle, it could be expected higher indentation marks as the hardness of the sample decreases. In fact, it can be observed in Table 4.4 that, generally, higher hardness involves lower indentation marks and so, lower depths deformations. That could be the reason why, for both Surlyn, it has not been possible measure the 5 N marks depth.

Figure 4.32 and Figure 4.33 show the line profiles for the samples developed with Surlyn 1705 and Surlyn 8940, respectively; whereas the hole profiles corresponding to the Surlyn 1705 and Surlyn 8940 samples are represented in Figure 4.34 and Figure 4.35 (surface profilometry measurements). It can be observed, for 10 and 15 N force, that the material rises when the lines were performed. As explained along all the work, this could be due to the followed process to make the lines.

At the same time, and as an example, the surface of the holes in Surlyn 8940 + PCO sample measured by confocal microscopy are represented in Figure 4.36 to Figure 4.38 for the different indentation forces, 5, 10 and 15 N, respectively.

As in section 3.2.4.3., optical microscopy has been employed to measure hole diameters and line widths, summarizing the results on Table 4.4. Generally marks are wider with the applied force, as it has been observed previously by profilometry, showing results among 600, 700 and 900 μm for 5, 10 and 15 N force, respectively. As example, Figure 4.39 and Figure 4.40 show photographs of the diameters of the holes in Surlyn + PCO + 3% DCP samples, whereas Figure 4.41 and Figure 4.42 represent the line width measurements in the same samples.

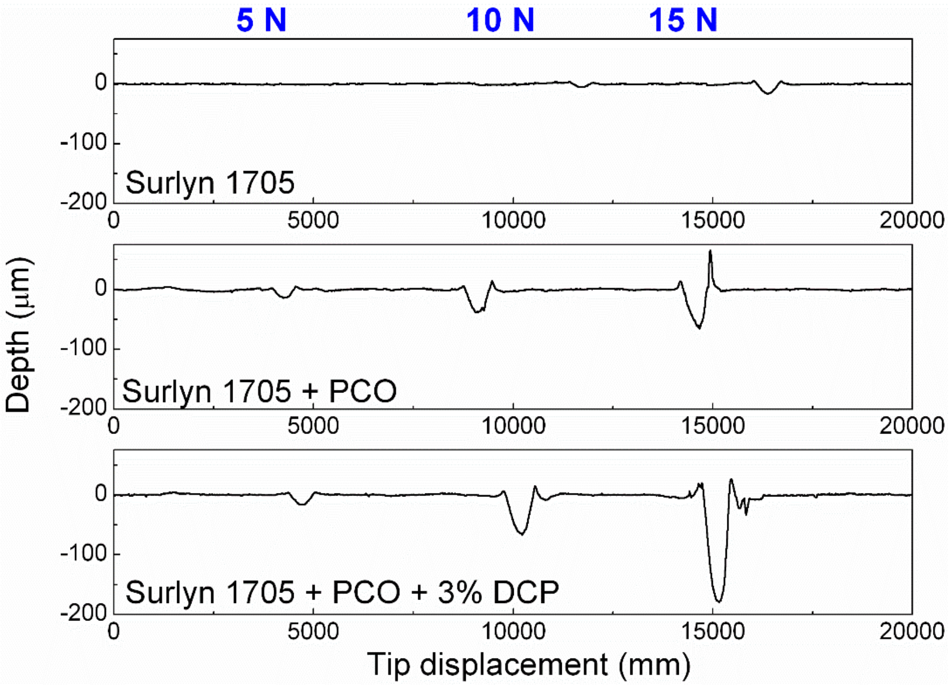

Figure 4.32. Measured profiles of lines by surface profilometry in the samples made with Surlyn 1705.

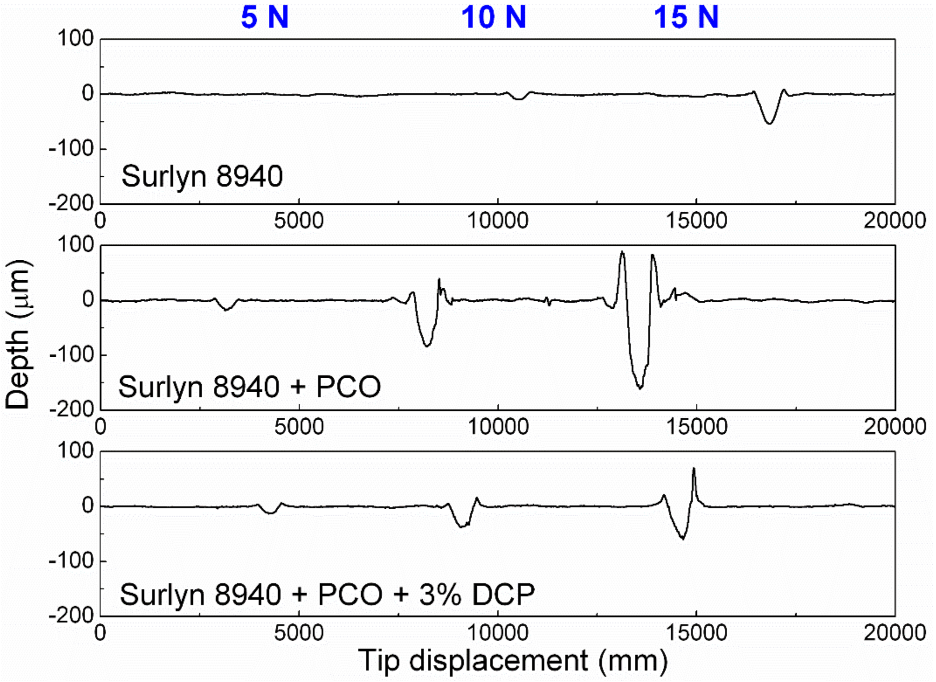

Figure 4.33. Measured profiles of lines by surface profilometry in the samples made with Surlyn 8940.

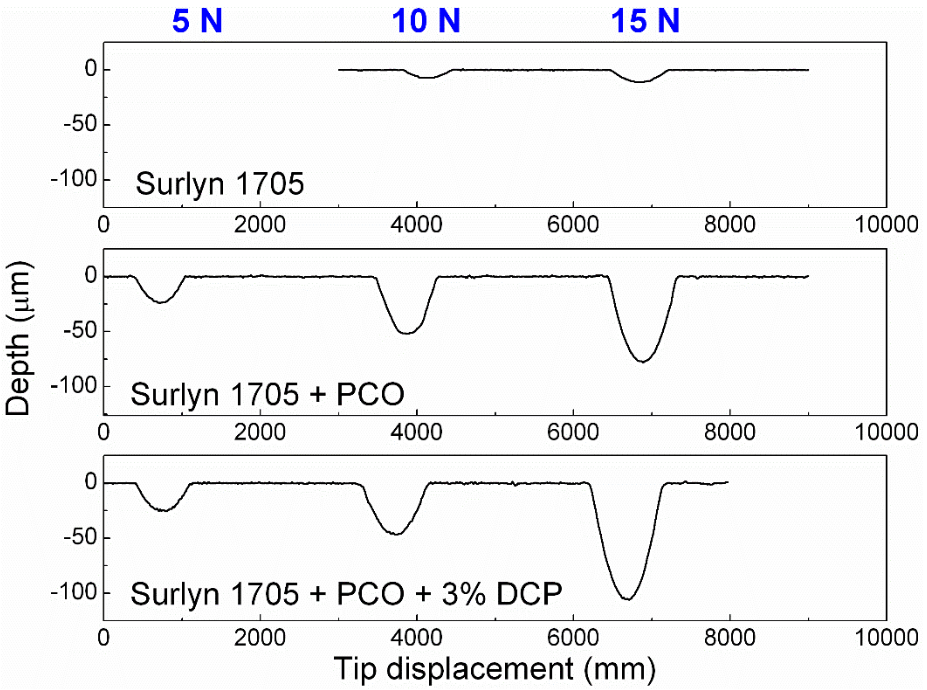

Figure 4.34. Measured profiles of holes by surface profilometry in the samples made with Surlyn 1705.

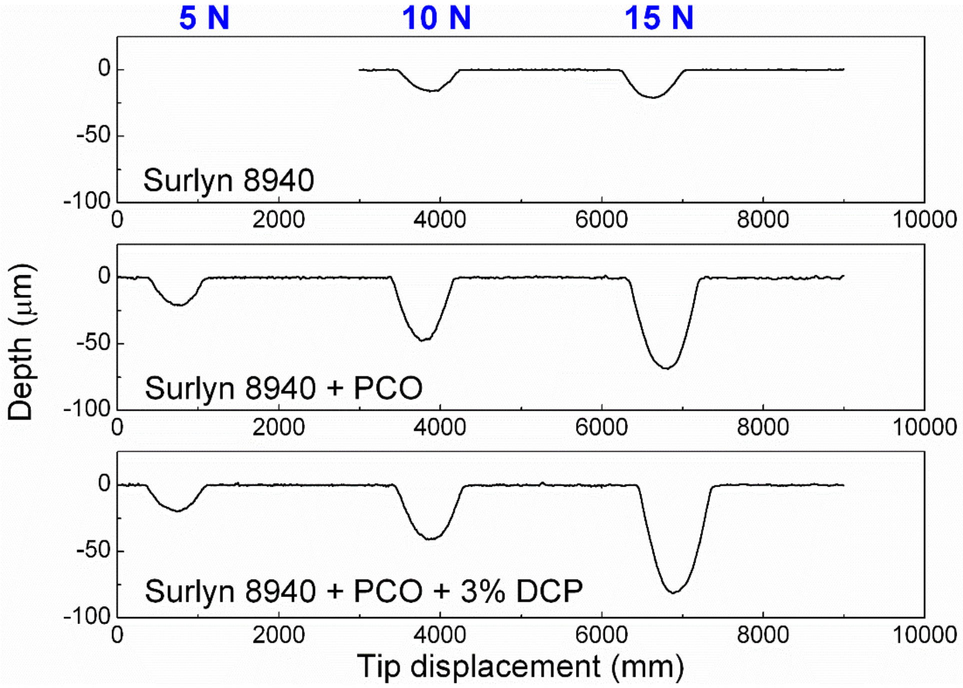

Figure 4.35. Measured profiles of holes by surface profilometry in the samples made with Surlyn 8940.

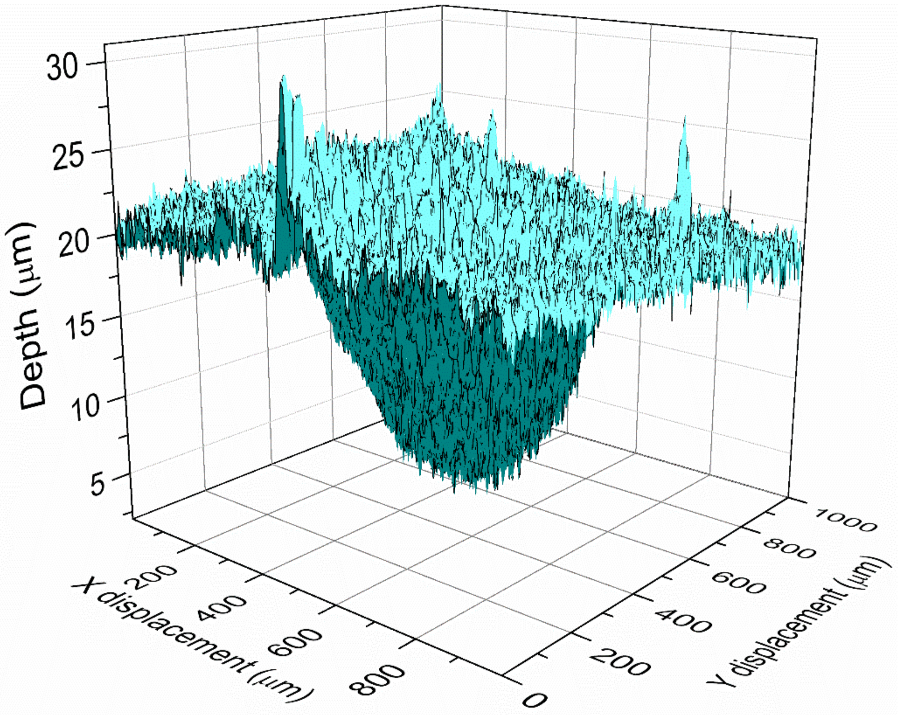

Figure 4.36. Confocal measurement of 5 N hole in Surlyn 8940 + PCO sample.

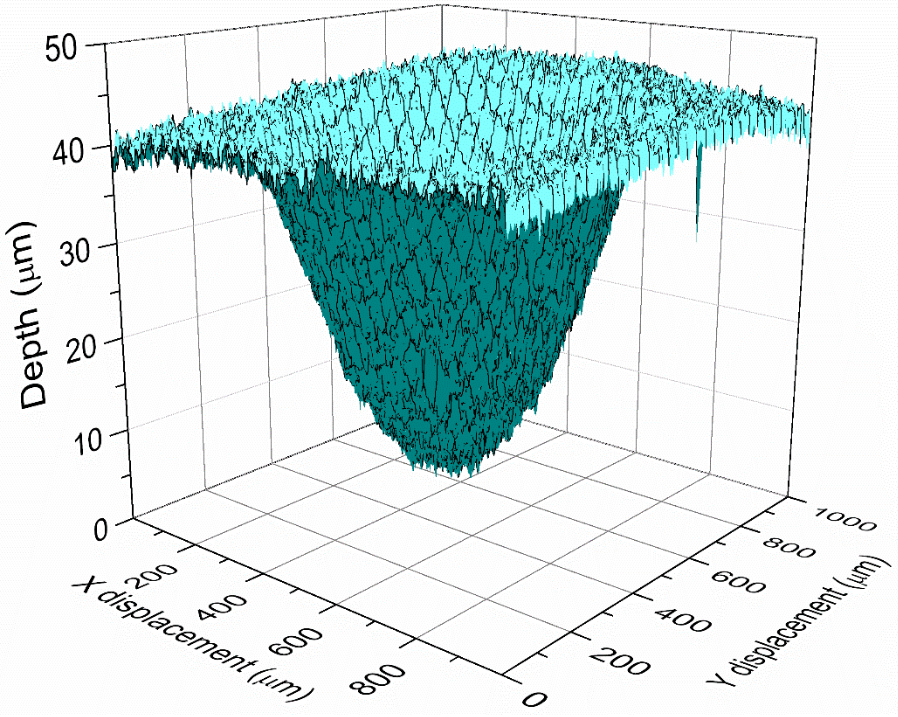

Figure 4.37. Confocal measurement of 10 N hole in Surlyn 8940 + PCO sample.

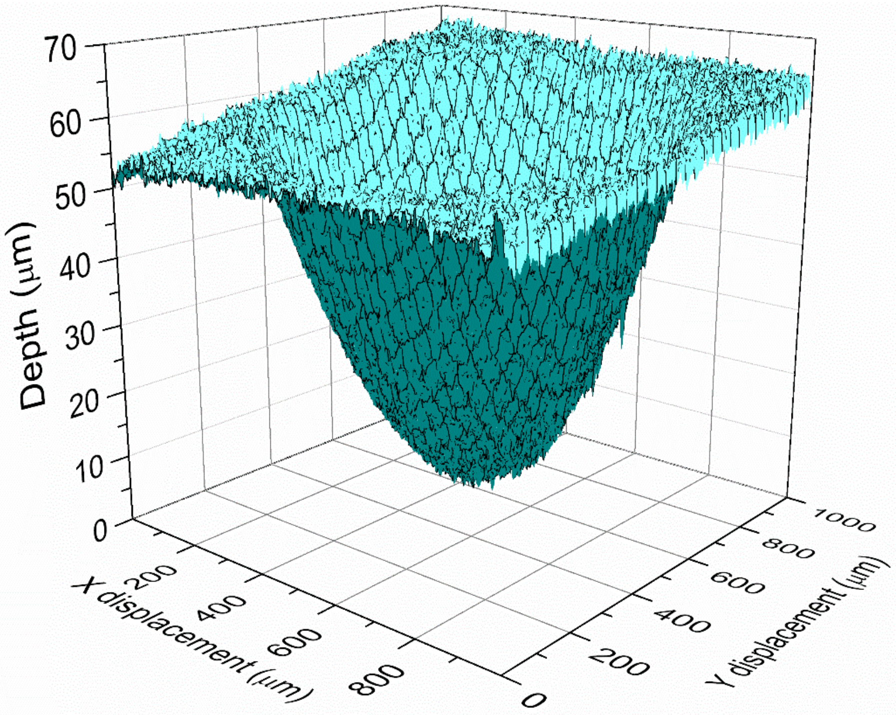

Figure 4.38. Confocal measurement of 15 N hole in Surlyn 8940 + PCO sample.

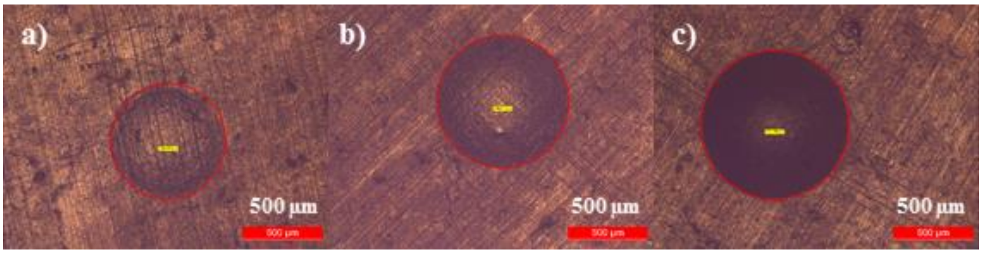

Figure 4.39. Diameters measured by optical microscopy of the holes in Surlyn 1705 + PCO + 3% DCP sample with a) 5 N, b) 10 N, c) 15 N.

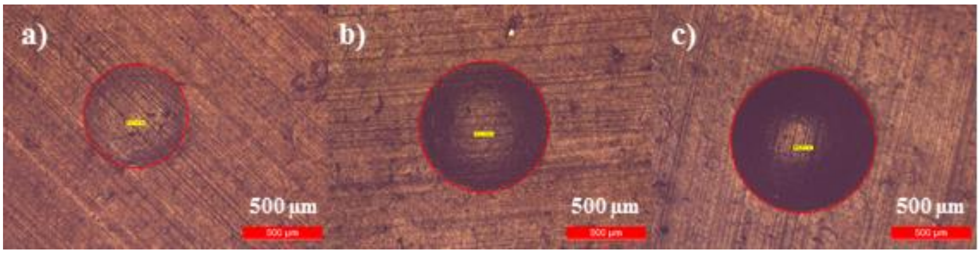

Figure 4.40. Diameters measured by optical microscopy of the holes in Surlyn 8940 + PCO + 3% DCP sample with a) 5 N, b) 10 N, c) 15 N.

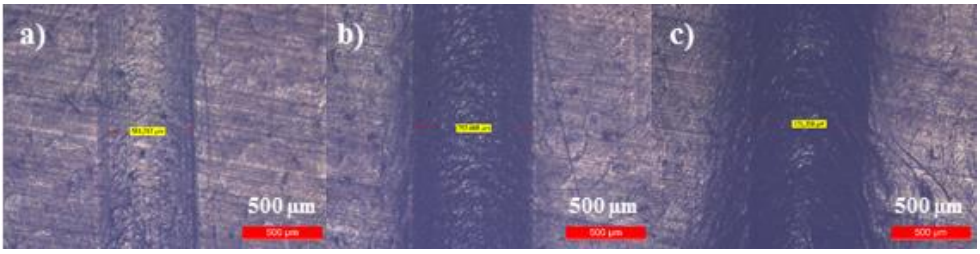

Figure 4.41. Widths measured by optical microscopy of the lines in Surlyn 1705 + PCO + 3% DCP sample with a) 5 N, b) 10 N, c) 15 N.

Figure 4.42. Widths measured by optical microscopy of the lines in Surlyn 8940 + PCO + 3% DCP sample with a) 5 N, b) 10 N, c) 15 N.

Finally, the evolution of the recovery process with temperature was monitored by optical microscopy in the same way that made in section 3.2.4.3. (i.e. the sample was placed at room temperature on a heating surface and series of photos of the mark were taken when temperature was increasing, cooling to room temperature when recovery process was finished). As an example, Figure 4.43 to Figure 4.46 show the evolution of the recovery process of the ionomer + PCO + 3% DCP samples through this procedure.

In conclusion, these kind of systems are capable of recover the original state when enough temperature is applied, as it was checked for PCO+DCP samples (section 2.1) and for irradiated PCO ones (section 3.2).

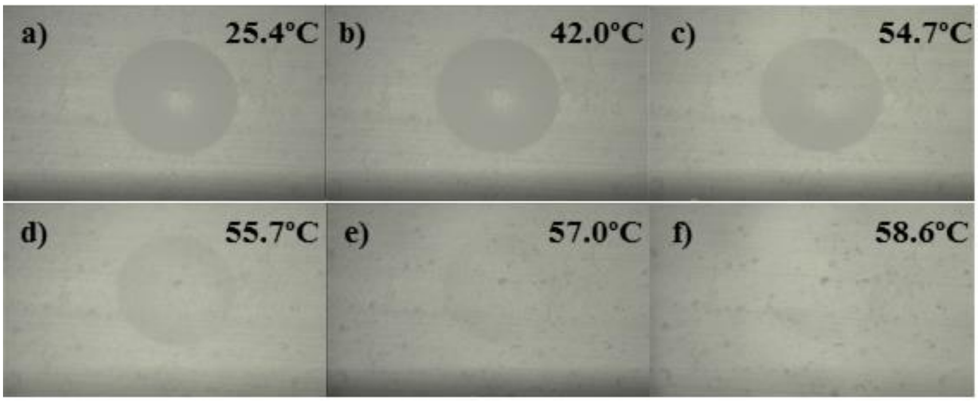

Figure 4.43. Recovery process for 15 N hole in Surlyn 8940 + PCO + 3% DCP sample (frontal view).

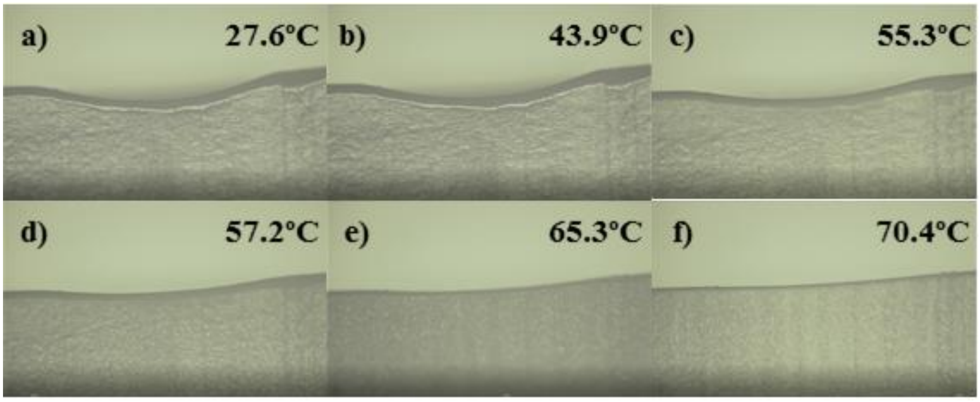

Figure 4.44. Recovery process for 15 N hole in Surlyn 8940 + PCO + 3% DCP sample (edgewise view).

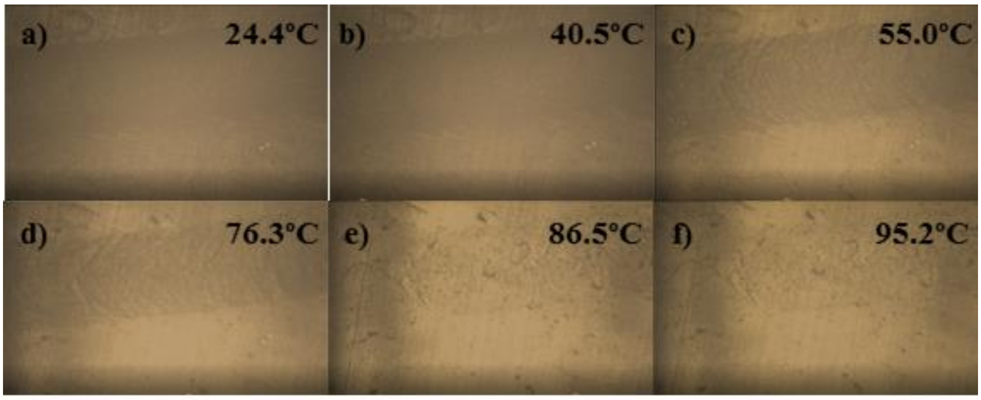

Figure 4.45. Recovery process for 15 N line in Surlyn 1705 + PCO + 3% DCP sample (frontal view).

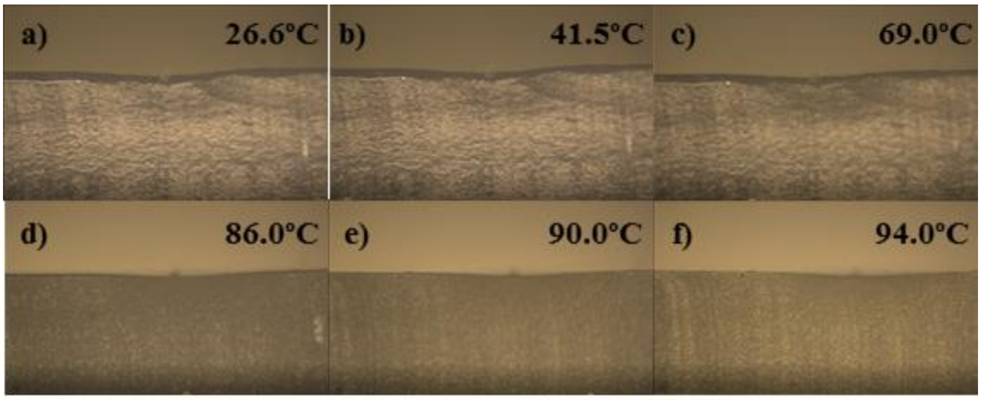

Figure 4.46. Recovery process for 15 N line in Surlyn 1705 + PCO + 3% DCP sample (side view).

4.1.5. Conclusions

Different samples were prepared by blending ionomer (Surlyn 8940/Surlyn 1705), polycyclooctene (PCO), and dicumyl peroxide (DCP). The samples were analysed by Differential Scanning Calorimetry (DSC) and Thermogravimetric Analysis (TGA) before and after manufacturing the materials by compression moulding, showing that the crosslinking occurs during the compression moulding, not during the extruding process. The DSC measurements of those samples with peroxide after the compression moulding showed a diminution in the melting temperature, indicating that the crosslinking process had taken place. These results are in concordance with the measurements performed by Dynamic Mechanical Thermal Analysis (DMTA).

The shape memory behaviour of these samples were evaluated both qualitative (monitoring the shape recovery process) and quantitatively (by Thermo-Mechanical Analysis, TMA). Those samples consisting on Surlyn + PCO + DCP showed triple-shape memory behaviour, analysed as well by recording the recoverability in hot water and by cyclic thermo-mechanical analysis. Performing 10 TMA cycles to each sample served to demonstrate the good reproducibility of the shape memory effect in these systems.

Finally, thermal-activated self-repair features of a series of Surlyn samples (Surlyn 1705 and Surlyn 8940, Surlyn + PCO blends and Surlyn + PCO + 3% DCP blends) were demonstrated by evaluating the recovery of plastic deformations performed with different indentation forces.

4.2. Shape memory and self-healing properties: PCO/Surlyn 9520 blends

4.2.1. Introduction

All materials may suffer natural or artificial degradation processes when they are exposed to mechanical, chemical or thermal stresses, so they can deteriorate over time. In this way, scratches or surface and internal cracks can be formed. Particularly, the long-time degradation processes in structural materials results in microcracks, causing a failure. Therefore, repairing is essential to improve reliability and lifetime of materials [17].

Self-healing is defined as the ability of a material to heal (recover/repair) damages automatically and autonomously (i.e. without any external intervention). However, it is accepted as self-healing systems those in which the human intervention during healing is minimal. Taking this into account, self-healing could be a solution to avoid a catastrophic damage in the materials, reducing the first point of damage.

In polymers, self-healing process can be extrinsic or intrinsic. Extrinsic healing is based on the incorporation of an external healing agent, which can be: a liquid stored in microcapsules [18], hollow fibres [19], or microvascular networks [20]; or a solid, usually thermoplastic particles dispersed along the polymer matrix [21,22]. This kind of self-healing process takes place by releasing the healing agent autonomously once the material suffers the damage. Intrinsic healing is related with physical or chemical reversible interactions, such as hydrogen bonds [23], reversible covalent bonds (for example based on Diels-Alder reaction [24] or disulfides [25]), or ionic supramolecular clusters (where ionomers are one of the most studied systems) [8,26], among others. In the intrinsic healing, although the self-healing properties fall on the polymer itself, it is necessary an external trigger to perform the self-healing action.

From the point of view of the future application, intrinsic healing process has a clear advantage over extrinsic one. Since no healing agent is spent, one can break and heal the sample several times [27]. On the contrary, as the healing efficiency in these systems is related to the mobility of the chains and to the amount of reversible bonds, the fractured surfaces must be in contact before healing occurs, which is sometimes complicated to do if the piece is a part of a large engineering structure. To solve this, it has been thought about the possibility of obtain a system with shape memory and self-healing properties, trying to use the shape memory effect to put into contact the two fractured zones of the piece before the self-healing process takes place.

Evaluating the different possibilities of self-healing systems, the use of ionomers, briefly explained at section 4.1.1, has been chosen. Additionally, the decision was made taking into account the previously obtained results. This work has been developed at Novel Aerospace Materials group of Delft University of Technology (TU Delft), employing the Surlyn 9520 ionomer provided by DuPont. This ionomer is, in essence, similar to those employed in section 4.1, which have shown good shape memory properties in the evaluated samples.

In this way, PCO and Surlyn 9520 ionomer were blended in different proportions (30/70, 50/50, and 70/30). Additionally, as the main objective is to have a system with shape memory properties capable of heal, PCO must be crosslinked. Thus, different samples were prepared (Table 4.5), without and with a crosslinking agent (DCP). Without DCP, PCO/Surlyn 9520 blends were prepared in 30/70, 50/50 and 70/30 proportions, as well as both raw materials (PCO and Surlyn). The same samples were made using a 3 wt% DCP as crosslinking agent. Thermogravimetric analysis, differential scanning calorimetry, rheology, and tensile machine were used to characterise all the samples. In order to study the self-healing behaviour, the samples were cut in two parts and put together at high temperature. Additionally, the shape memory behaviour of the samples which heal was analysed following a torsion procedure.

4.2.2. Materials

4.2.2.1. Polycyclooctene (PCO)

This work has been performed employing the same commercially available polycyclooctene Vestenamer® 8012 (from Evonik Industries), already described at section 2.1.2.1.

4.2.2.2. Surlyn 9520

Surlyn 9520 is a poly(ethylene-co methacrylic acid) (EMAA) zinc ionomer from Du Pont, which has 10 wt% of MAA groups, where 72 % are neutralized with Zn^{2+} ions [28].

4.2.2.3. Dicumyl peroxide (DCP)

The dicumyl peroxide used was the same aforementioned at section 2.1.2.2.

4.2.3. Preparation of samples

A series of samples were prepared by mixing the different components in the desired proportions using a twin screw mini-extruder. As mentioned, to obtain the shape memory material it is necessary to crosslink the PCO, so DCP was added. The DCP amount in the PCO + Surlyn 9520 + DCP blends was added according to the polyolefin amount (3 wt% of the PCO weight). Once these samples were appropriately extruded, films of approximately 1 mm thickness were compression moulded at 160ºC under a pressure of 20 MPa during 20 minutes. In those samples with DCP, the crosslinking process takes place in this step (during the compression procedure). The different developed samples are listed in Table 4.5.

Table 4.5. Different developed samples.

Samples without DCP	Samples with DCP
Surlyn 9520	Surlyn 9520 + 3% DCP
PCO / Surlyn 9520 (30/70)	PCO + 3% DCP / Surlyn 9520 (30/70)
PCO / Surlyn 9520 (50/50)	PCO + 3% DCP / Surlyn 9520 (50/50)
PCO / Surlyn 9520 (70/30)	PCO + 3% DCP / Surlyn 9520 (70/30)
PCO	PCO + 3% DCP

4.2.4. Experimental section

4.2.4.1. Thermogravimetric Analysis

Thermal stability of the different samples was evaluated by Thermogravimetric Analysis with a Perkin Elmer TGA 4000 thermobalance. The measurements were carried out from 30 to 600ºC with a heating rate of 10ºC·min^{-1} under nitrogen atmosphere.

TGA analysis was performed for all formulations showed in Table 4.5 without and with peroxide, and the results are showed in Figure 4.47 and Figure 4.48, respectively (note that S9520 corresponds to Surlyn 9520 ionomer). Although all samples decompose in one main breakdown stage at temperatures above 400ºC, in those samples with peroxide the TGA curves show a slight decrease in the mass percentage below 200ºC, which can be associated with residual peroxide and decomposition products of the DCP [7].

The residual mass percentage after polymer degradation was calculated for all the samples, and it is showed in Table 4.6. For all samples, with and without peroxide, the same trend is observed. The residue could be related to the content of Zn^{2+} (present in the ionomer), so as the ionomer content decreases, the residual mass percentage at 600ºC is lower (less ionomer, less proportion of Zn, less residue).

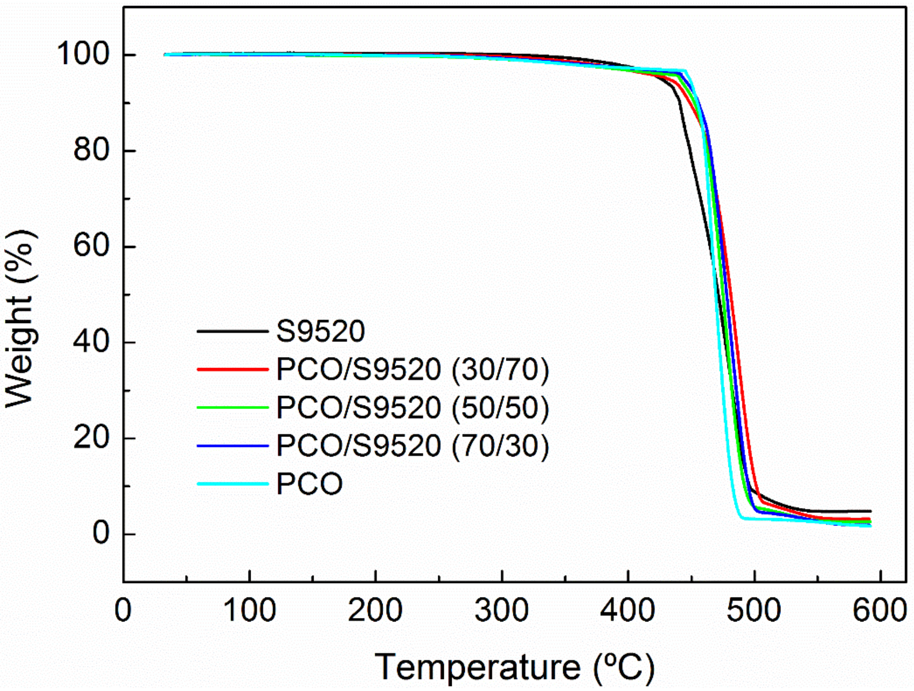

Figure 4.47. TGA of the different samples (without peroxide).

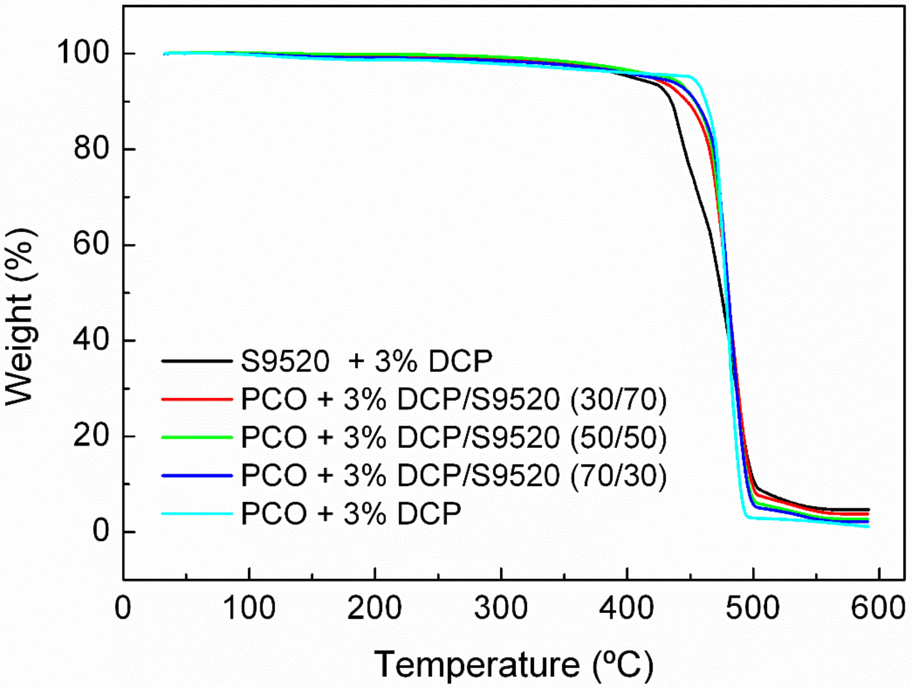

Figure 4.48. TGA of the different samples (with peroxide).

Table 4.6. Residual mass percentage and characteristic temperatures of the samples.

Sample	**Residual mass (%)**	T_{m1} **(°C)**	T_{c1} **(°C)**	T_{m2} **(°C)**	T_{c2} **(°C)**
Surlyn 9520	4.86	--	--	110	81
PCO / Surlyn 9520 (30/70)	3.19	63	43	106	76
PCO / Surlyn 9520 (50/50)	2.66	62	43	103	71
PCO / Surlyn 9520 (70/30)	1.97	64	42	106	76
PCO	1.73	52	41	--	--
Surlyn 9520 +3% DCP	4.67	--	--	87	63
PCO +3% DCP / Surlyn 9520 (30/70)	3.78	49	30	92	64
PCO +3% DCP / Surlyn 9520 (50/50)	2.71	50	29	94	66
PCO +3% DCP / Surlyn 9520 (70/30)	2.20	40	17	91	63
PCO +3% DCP	1.15	33	7	--	--

4.2.4.2. Differential Scanning Calorimetry

To identify thermal actuation temperatures, thermal properties of the samples were measured by Differential Scanning Calorimetry using a Perkin Elmer DSC 8000. Samples in aluminium pans (5-10 mg) were characterized under constant helium flow. First, samples were heated from −100 to 150 ºC at a rate of 20 ºC·min^{-1}, followed by a cooling scan from 150 to −100 ºC at a rate of −20 ºC·min^{-1}. This process (heat-cool) was repeated twice in each sample.

DSC measurement was carried out in all developed samples to identify thermal actuation temperatures, which are shown in Table 4.6. It has to be taken into account that these melting and cooling temperatures are related to the second heating and cooling scans, which are represented in Figure 4.49 for the samples without peroxide and in Figure 4.50 for those samples with DCP. The ionomer presents one melting peak at 110 ºC and one crystallization peak at 81 ºC, whereas the PCO melts at 52 ºC and crystallises at 41 ºC. In this way, the PCO/ionomer blends (without DCP) present two melting peaks at values around 60 ºC and 100 ºC, and two crystallization peaks at 40 ºC and 70 ºC, as shown in Table 4.6 and Figure 4.49.

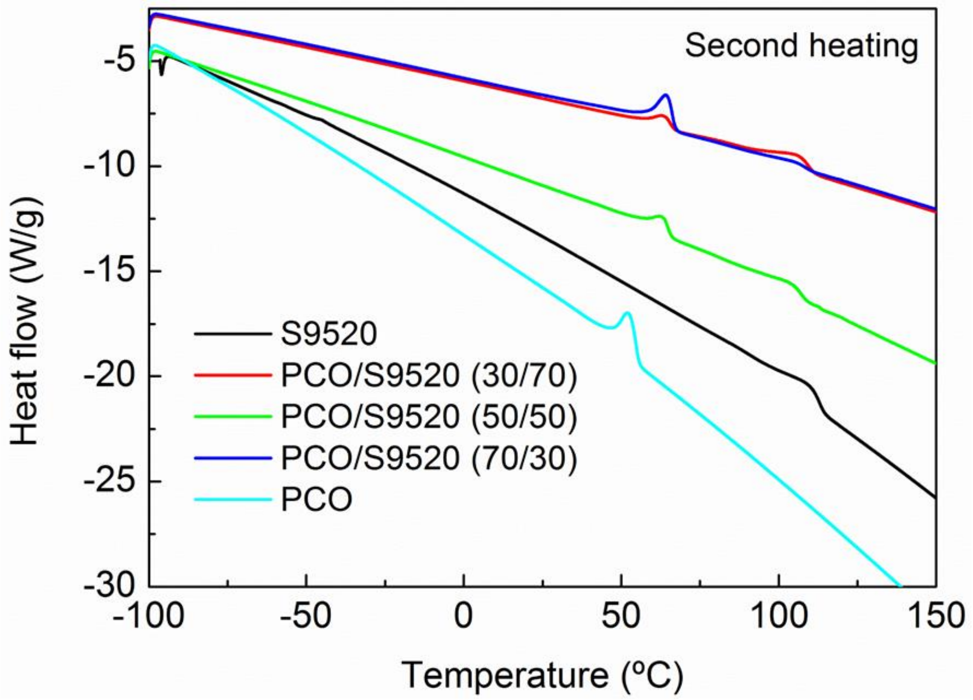

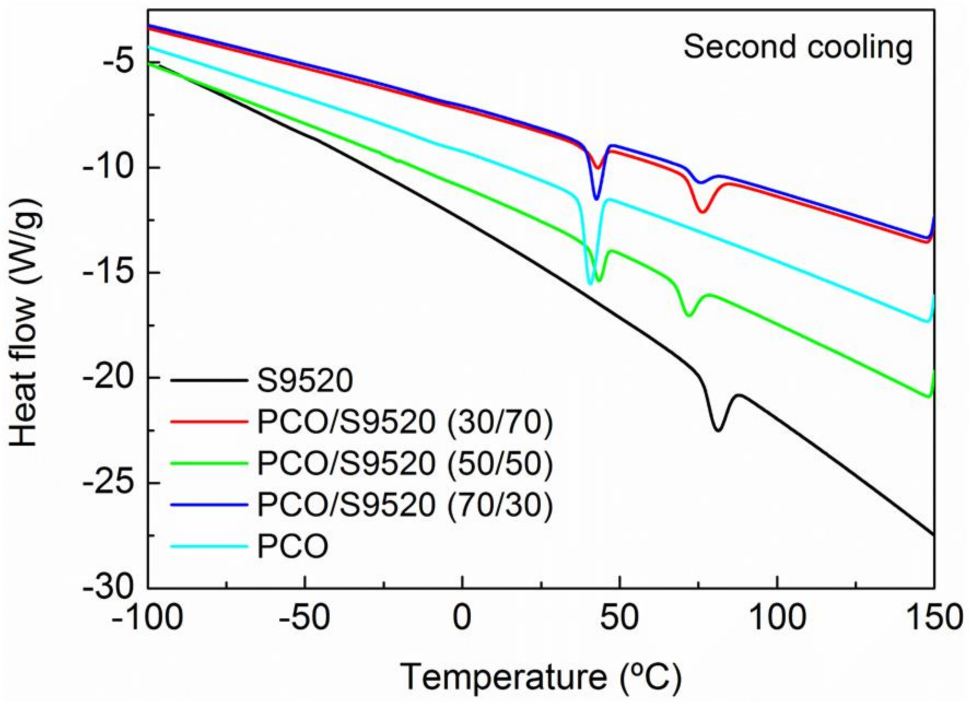

Figure 4.49. DSC of samples without DCP (second heating and second cooling scans).

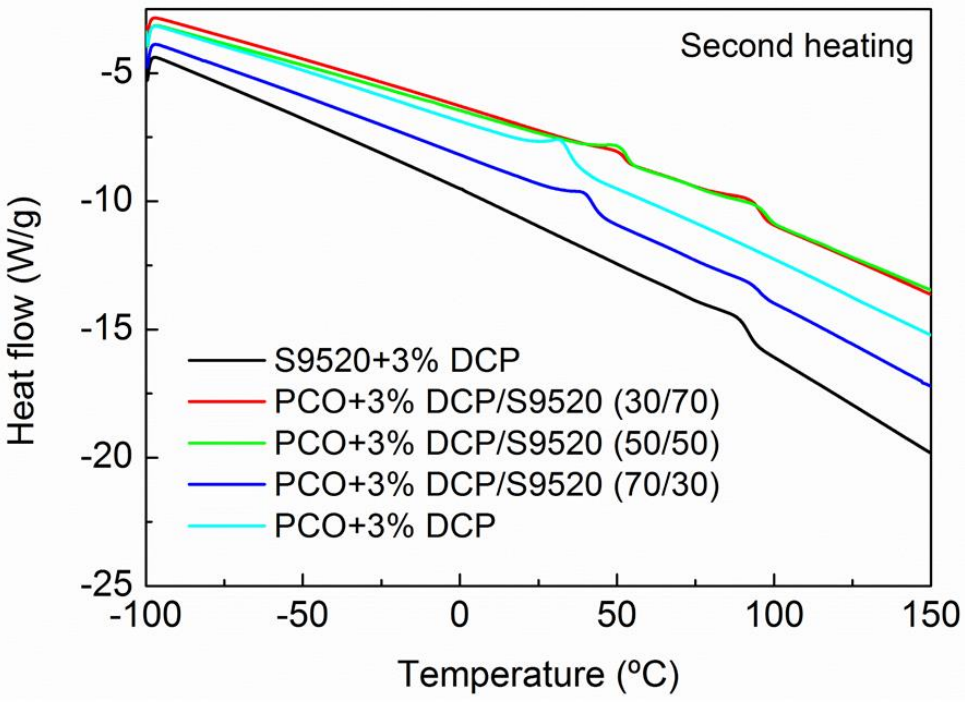

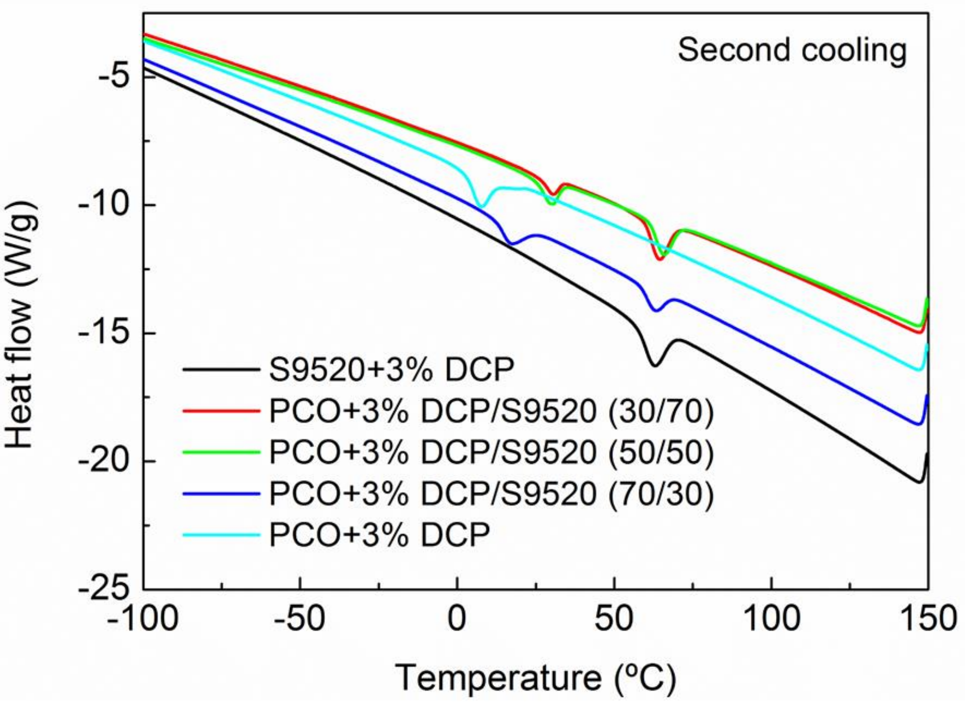

Figure 4.50. DSC of samples with DCP (second heating and second cooling scans).

When the DCP is added (Figure 4.50) the density of crosslinks increases, hindering the mobility of the polymer chains, causing a diminution of the melting temperature, as is in concordance with previous studies [9,29]. So it is demonstrated that the samples containing DCP, even Surlyn 9520 + 3% DCP, are crosslinked, because the melting temperatures decrease comparing with those samples without peroxide. To clearly see the difference between a crosslinked sample and a non-crosslinked one, Figure 4.51 represents the second heating-cooling cycle for PCO/Surlyn9520 and PCO+3%DCP/Surlyn9520 samples in a 30/70 proportion, where can be noted the displacement to lower temperatures for all the peaks when DCP is added.

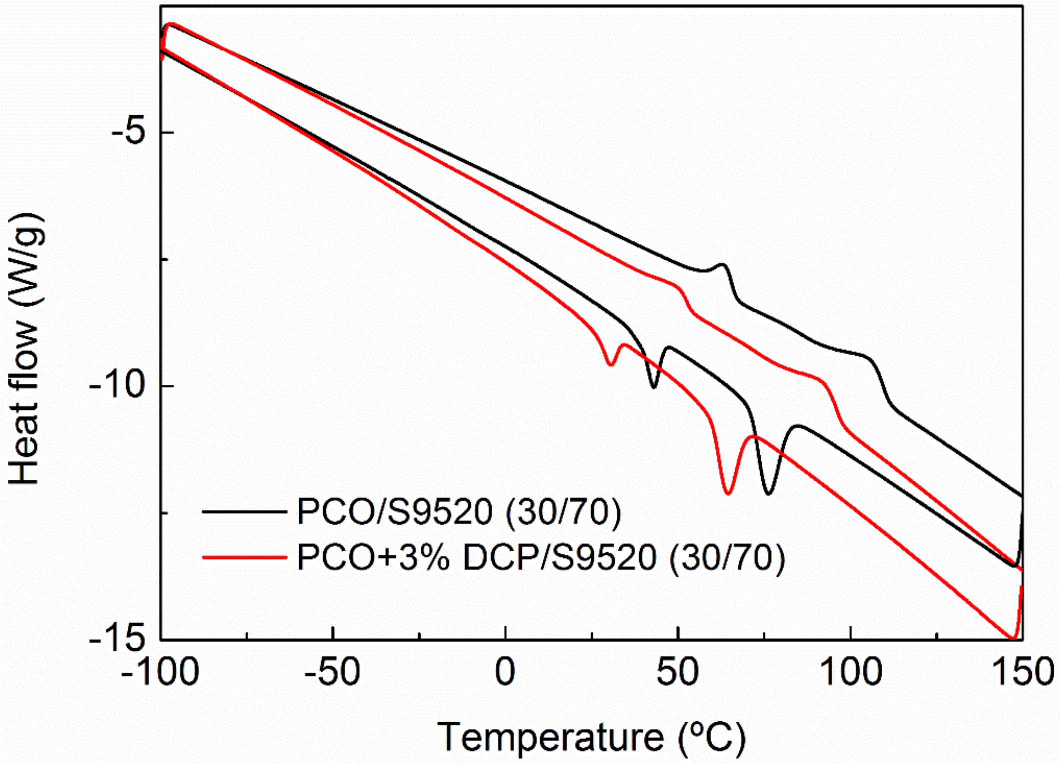

Figure 4.51. Comparison of a formulation without and with peroxide.

4.2.4.3. Rheology

Polymers are viscoelastic materials, i.e. their properties lie between the properties of pure elastic solids and viscous fluids [30]. Rheology helps to measure both the elastic (storage) modulus, G’, and viscous (loss) modulus, G’’. In an oscillatory frequency sweep, the relationship between these moduli indicates which part (elastic or viscous) is dominant at given conditions. In non-crosslinked polymers, the behaviour at a temperature higher than melting temperature is as follows: at higher frequencies (short times) the elastic part (G’) is predominant over the viscous one (G’’); as the frequency decreases (the time increases) G’’ takes importance, the behaviour of the polymer is like a viscous liquid. So there is a point where G’ and G’’ will crossover, and it is when the frequency is equal to the reciprocal relaxation time. In contrast, when the polymers are crosslinked systems, the behaviour is different, consisting in G’ values higher than those of G’’ over all frequency range (crosslinked systems do not flow, so elastic part is predominant over viscous one), not showing therefore crossover between storage and loss moduli [31].

Oscillatory shear rheology measurements were performed in all samples using a Haake Mars III rheometer. An 8 mm diameter (stainless steel) parallel plate geometry was employed, with a constant shear strain γ of 0.3%, which was within the linear viscoelastic regime of the materials. Frequency sweep experiments between 10^2–10^{-2} Hz were performed at different temperatures every 10 ºC, ranging from a temperature above the highest T_m of the sample, to a temperature below the lowest T_m, with an isothermal hold for 5 min prior to each temperature step.

First, it is necessary to evaluate the rheology behaviour of the ionomer and the polyolefin at different temperatures, beginning at a temperature higher than T_m and finishing when the melting has finished. In this way, Surlyn 9520 was evaluated in the range 140-80 ºC, whereas PCO was analysed between 80 ºC and 30 ºC. The results for Surlyn 9520 and PCO are shown in Figure 4.52 and Figure 4.53 respectively. It can be observed that at a temperature above melting point, at high frequency, G’ is higher than G”. But there is a point where there is a crossover between G’ and G”, indicating that at larger times (lower frequencies) the viscous part of the material is predominant to the elastic one. For supramolecular systems, is generally accepted that this crossover is related to the self-healing ability. In this way, supramolecular bond lifetime (τ), which is the characteristic average timescale for the reversible bonds to break and reform (i.e. measures the ionic relaxation timescale) [32], can be calculate as the inverse of the frequency where G' and G'' intersect. It has been proposed that those systems with τ between 10 and 100 s, which is equivalent to frequencies between 0.01 and 0.1 Hz, would show good healing behaviour combined with strong mechanical properties [33,34]. Figure 4.52 shows this behaviour for Surlyn 9520 sample, which is a good-known self-healing system. As it can be seen, at healing temperature (110 ºC), the crossover occurs in the optimum frequency range. Likewise, Figure 4.53 shows a crossover between G' and G'', but in this case the crossover takes place at about 20 Hz ($\tau \approx 0.05$ s). According to Bose *et al.*, different behaviours can be observed depending on the point of the crossover takes place [33]. The different groups are collected in Table 4.7. Thus, the pure PCO tends to melt, and not to self-heal (for $0.01 \text{ s} < \tau < 1$ s, that is, frequencies in the range 1-100 Hz, viscous flow occurs). At temperatures below the melting, the crossover disappears, G' is higher than G" at every frequency, so the elastic behaviour is predominant to the viscous one.

Table 4.7. Correlation of rheological behaviour to the macroscopic scratch healing data [33].

τ (s)	**Result**
0.01-1	Weak mechanical properties Viscous flow
1-10	Weak mechanical properties Elastic recovery
10-100	Strong mechanical properties Good healing
100-1000	Strong mechanical properties Delayed elasticity

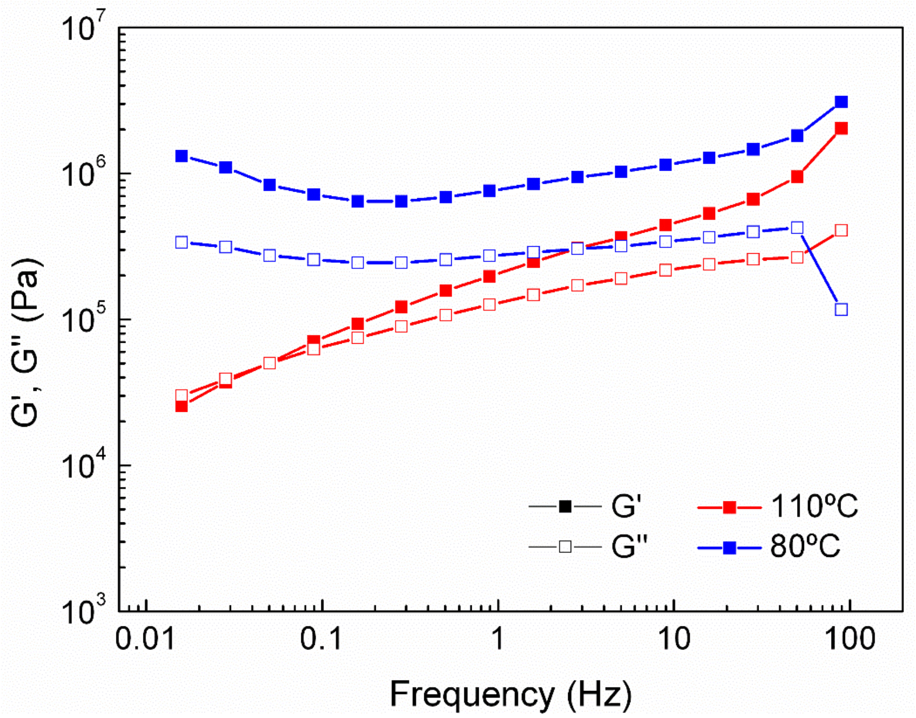

Figure 4.52. Comparison of G' and G'' of Surlyn 9520 plotted as a function of frequency.

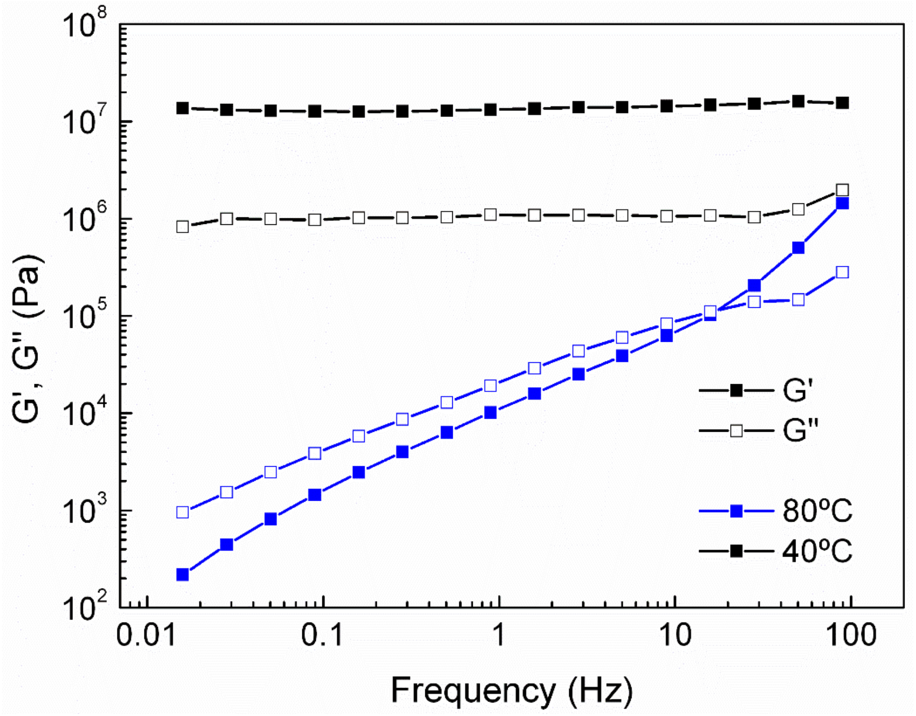

Figure 4.53. Comparison of G' and G'' of PCO plotted as a function of frequency.

The PCO + ionomer blends are analysed between 140ºC and 30ºC, and the same behaviour can be observed (Figure 4.54 for 30/70 composition, Figure 4.55 for 50/50 composition and Figure 4.56 for 70/30 composition). The crossover exists at 110ºC (healing temperature), so these blends are able to heal or to melt, depending on the point where the crossover occurs. Looking at the different figures, and according to the frequency ranges where G' and G'' cross (Table 4.7), the 30/70 ($\tau \approx 25$ s) and the 50/50 ($\tau \approx 22$ s) compositions seem able to heal, whereas the 70/30 sample ($\tau \approx 0.08$ s) melts. Additionally, for this sample it can be seen that the crossover persists at 80ºC in the same melting region ($\tau \approx 0.3$ s), due to the high amount of PCO in the sample.

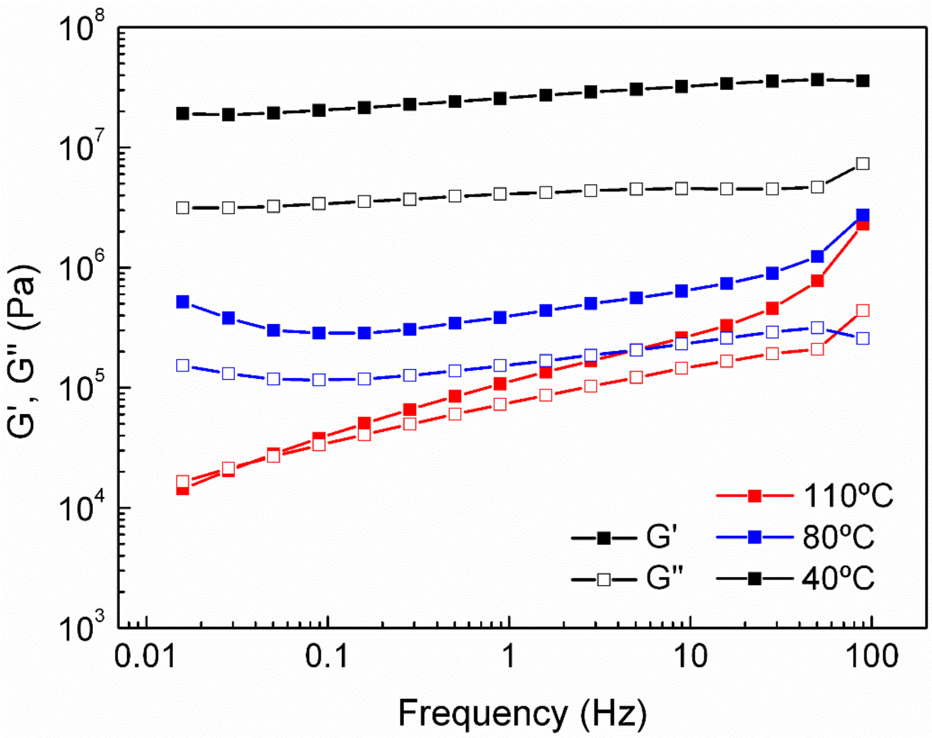

Figure 4.54. Comparison of G' and G'' of PCO/Surlyn 9520 (30/70) plotted as a function of frequency.

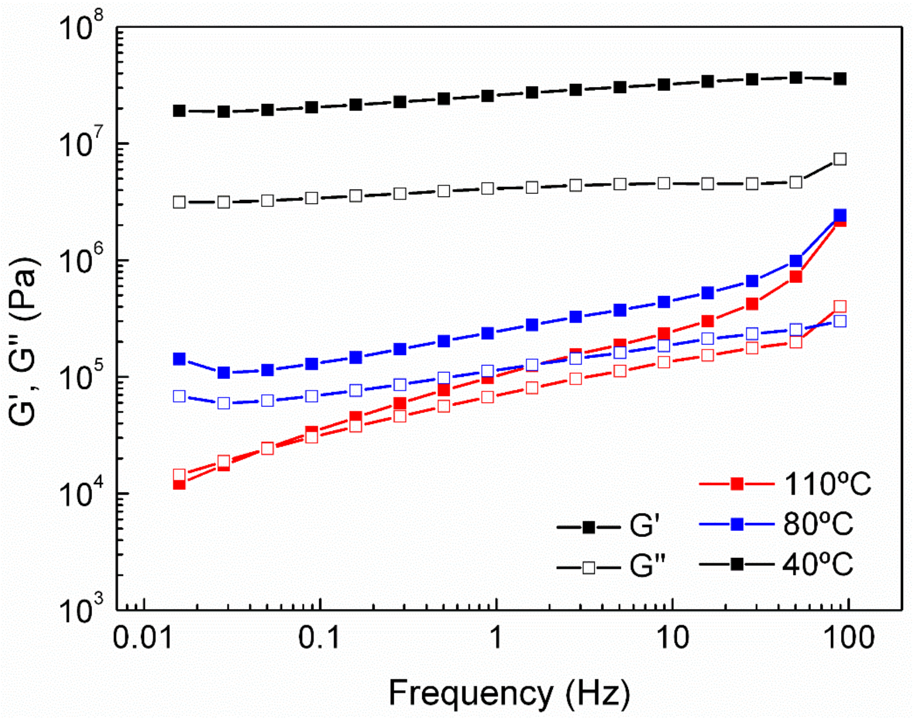

Figure 4.55. Comparison of G' and G'' of PCO/Surlyn 9520 (50/50) plotted as a function of frequency.

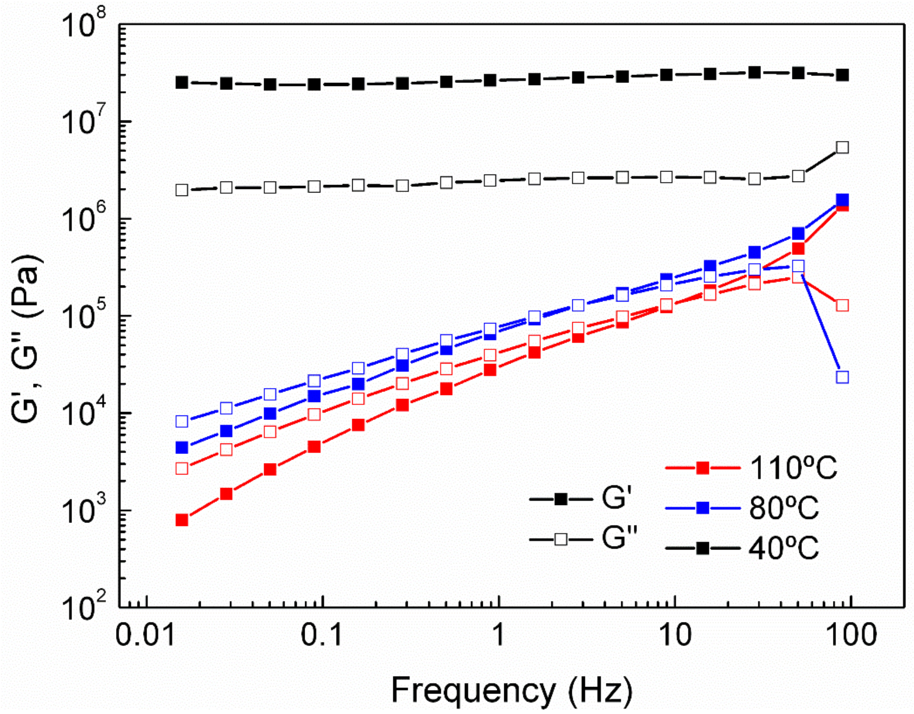

Figure 4.56. Comparison of G' and G'' of PCO/Surlyn 9520 (70/30) plotted as a function of frequency.

When the samples with DCP are analysed a very different behaviour can be seen. PCO + 3% DCP sample, which is a well-known crosslinked system [9,29], was analysed between 80 ºC and 10 ºC, and the results at different temperatures are represented in Figure 4.57. As can be seen, there is no crossover at checked temperatures, which can be attributed to the crosslinks due to the peroxide, in accordance to DSC results. The rest of DCP containing samples (Surlyn 9520 + 3% DCP, and PCO + 3% DCP/Surlyn 9520 blends) were analysed in the range 120-10ºC. The same behaviour can be observed in Figure 4.58, where G’ and G’’ of these samples are represented at 110ºC, which is the healing temperature of the ionomer. The lack of crossover implies an absence of macroscale network mobility, so we could not expect any self-healing process in this kind of samples because they are covalently crosslinked.

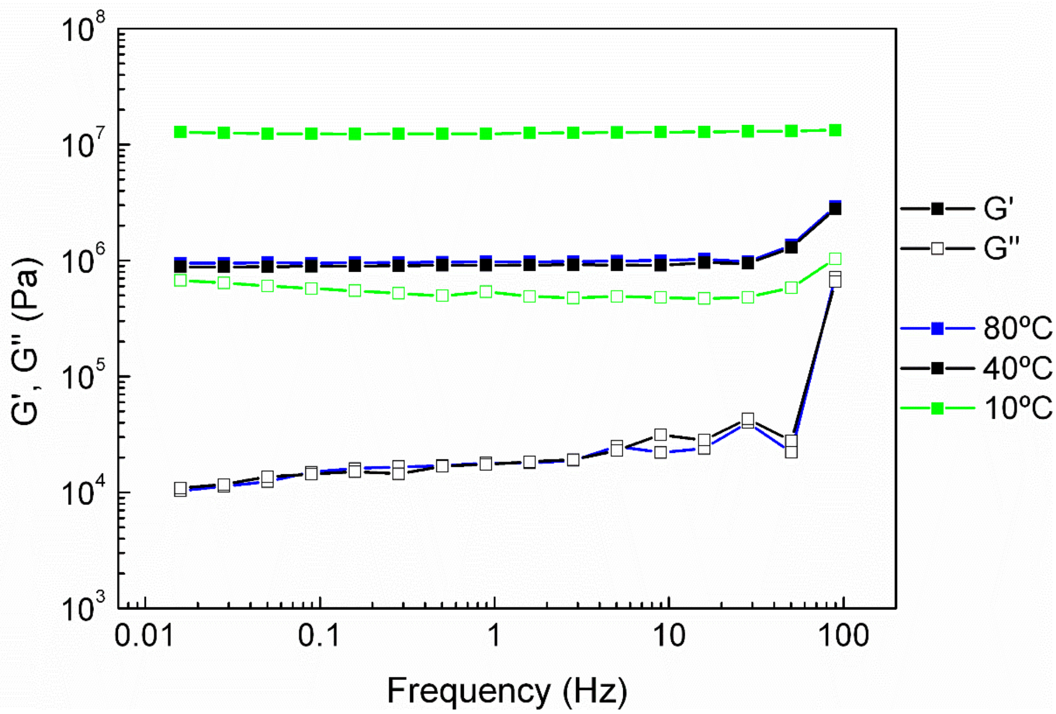

Figure 4.57. G’ and G’’ of PCO + 3% DCP sample at different temperatures.

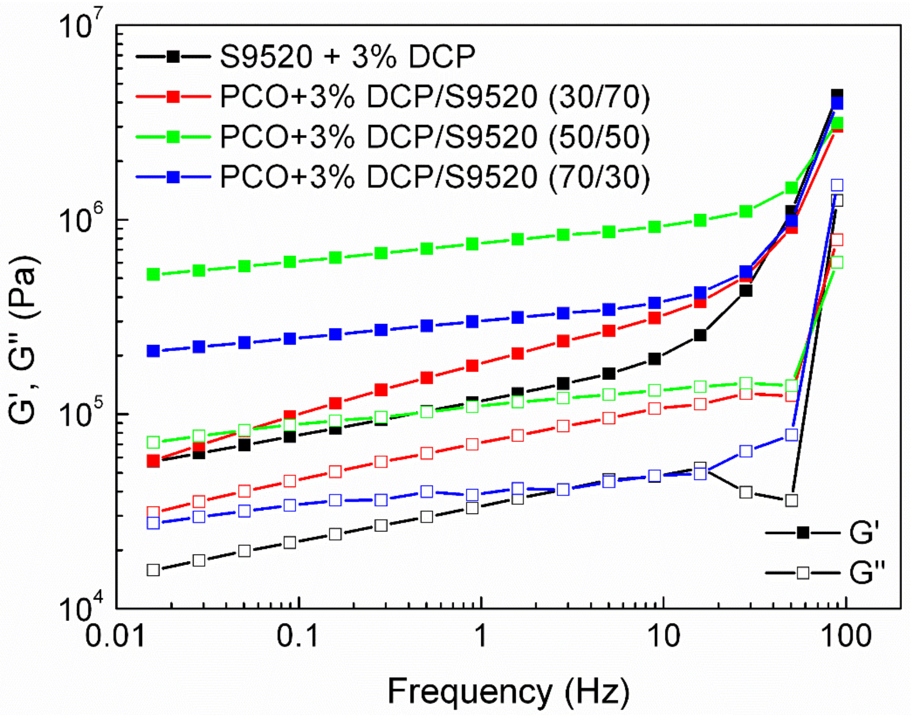

Figure 4.58. G’ and G’’ of different samples containing DCP at 110ºC.

4.2.4.4. Tensile properties

Dog-bone shaped specimens (ASTM D1708) were pressed from all the developed films. Tensile tests, before and after healing, were performed on these specimens using an Instron 3365 universal testing machine equipped with a 1 kN load cell. Tests were performed with a crosshead speed of 10 mm min^{-1} at room temperature.

The tensile properties of all developed blends were tested and the resulting curves are depicted in Figure 4.59. From these curves, different parameters have been calculated for all samples, collected in Table 4.8. When comparing the tensile behaviour of the blends it can be noted that yield strength and ultimate strength of all polymeric systems increases as the fraction of the ionomer phase increases. However, when comparing the non-crosslinked systems with their crosslinked counterparts a less obvious trend is observed. Crosslinking of the systems results in a drop in yield strength for all compositions, but increases the ultimate strength of all blends except for the case of PCO. This behaviour is also observed for the pure ionomer, implying that the DCP is not only capable to crosslink the PCO, but it has an effect on the ionomer as well, confirming the results obtained by DSC.

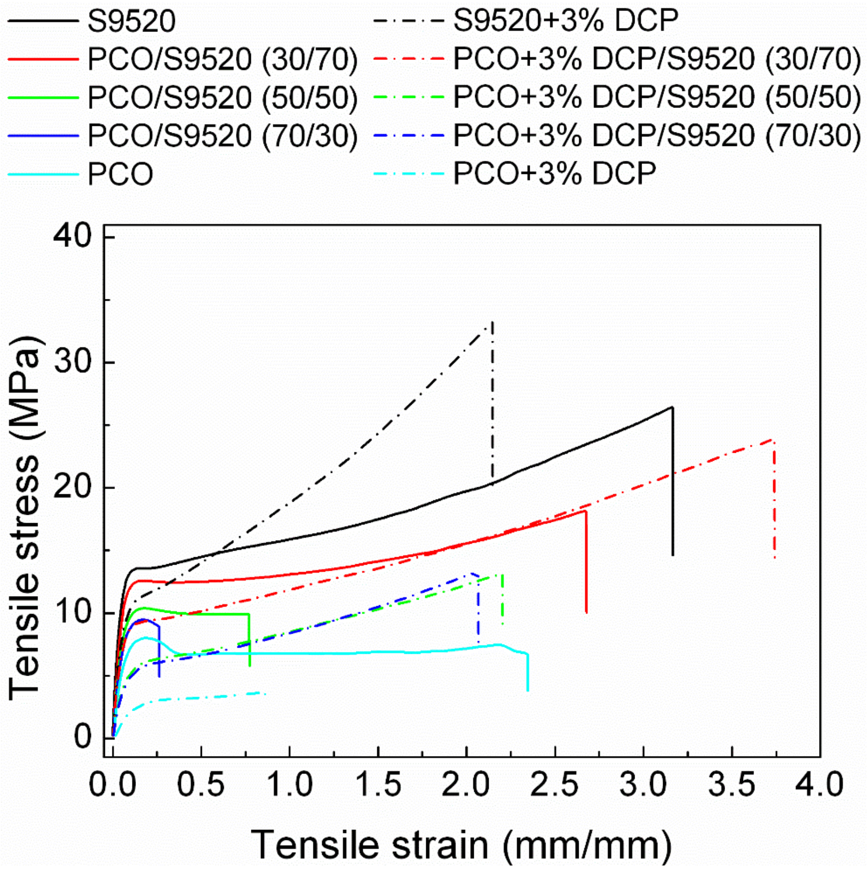

Figure 4.59. Tensile test for all developed samples.

When the toughness of the blends is analysed, it can be observed that for the non-crosslinked blends the strain at break is drastically reduced upon the addition of low amounts (< 50%) of ionomer compared to that of pure PCO. Only the 30/70 PCO/ionomer blend shows a higher strain at break than the pure PCO, but it is even more brittle than the pure ionomer. For the crosslinked blends it is noted that the strain at break increases for all blends compared to the non-crosslinked systems. Only the pure PCO and Surlyn fail at an earlier stage upon the addition of DCP.

Table 4.8. Tensile properties of the developed samples.

Sample	E' (MPa)	Yield strength (MPa)	Ultimate strength (MPa)	Strain at break
S9520	284	13.8	26.5	3.2
PCO/S9520 (30/70)	235	12.5	18.2	2.7
PCO/S9520 (50/50)	200	10.3	10.0	0.8
PCO/S9520 (70/30)	189	9.5	9.2	0.3
PCO	122	8.0	6.9	2.3
S9520+3%DCP	188	11.0	33.4	2.1
PCO+3%DCP/S9520 (30/70)	169	9.2	24.0	3.7
PCO+3%DCP/S9520 (50/50)	86	6.2	13.3	2.2
PCO+3%DCP/S9520 (70/30)	86	5.8	13.3	2.1
PCO+3%DCP	22	3.0	3.8	0.9

4.2.4.5. Self-healing

To evaluate the self-healing behaviour of the substrates, dog-bone shaped samples from the different films were fully fractured by applying a razor blade cut. The fractured interfaces were repositioned together while being constrained with Kapton tape. Specimens were then healed in an oven at 110 ºC (healing temperature of the ionomer) during 16 hours.

The results of this self-healing experiment for all the samples can be seen in Figure 4.60, where an original dog-bone is shown together with a dog-bone of each sample after the process described above. Comparing the tested samples with the original one, it can be seen than only few samples retain their dimensions. For the non-crosslinked samples, the crack visibility diminishes as the amount of PCO increases, but at the same time the viscosity drops to a level at which the specimen can no longer retain its original shape, fact related with the melting of the PCO phase. These results are in concordance with those obtained by rheology.

From rheology it is also anticipated that the crosslinked specimen will not show any healing. Observing the images in Figure 4.60 it can be seen that this is true for all specimens, except for the 30/70 PCO + 3% DCP/Surlyn blend. While the rest of crosslinked samples show no healing in combination with deformation and/or shrinkage of the specimen, the 30/70 PCO + 3% DCP/Surlyn blend is able to heal retaining its original dimensions and shows no visible presence of the razor blade fracture.

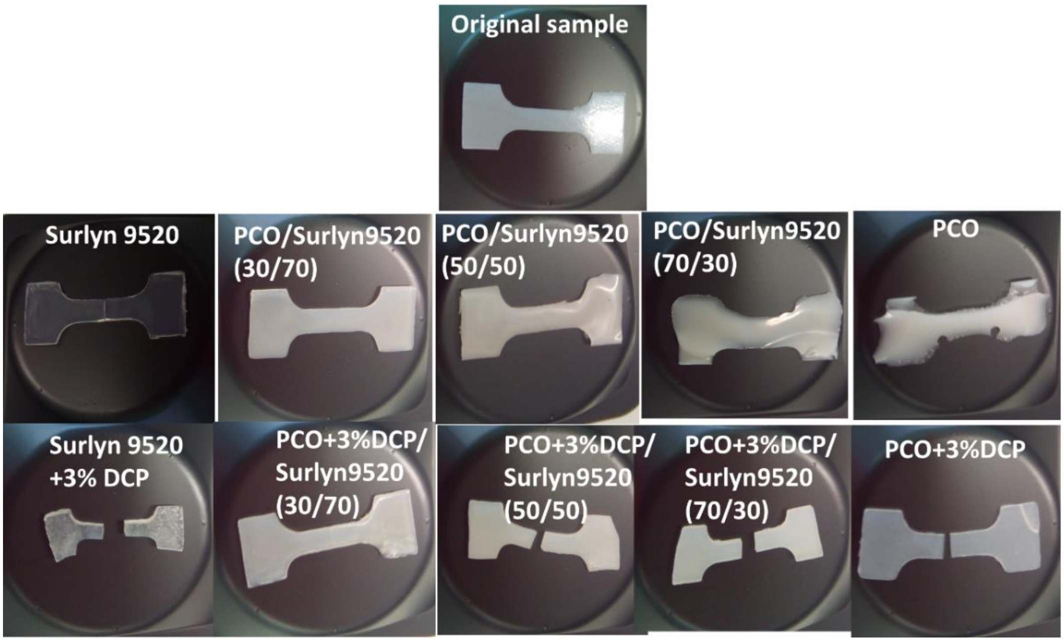

Figure 4.60. Dog-bone shaped samples after self-healing experiment for all developed samples (plus the original sample).

The specimens that retained their original dimensions and showed disappearance of the fracture (Surlyn 9520, 30/70 PCO/Surlyn 9520, and 30/70 PCO+3%DCP/Surlyn 9520) were tested in tensile. The results of these experiments and those of their pristine counterparts are shown in Figure 4.61a. Additionally, a zoom in the interest part has been made, as can be seen in Figure 4.61b.

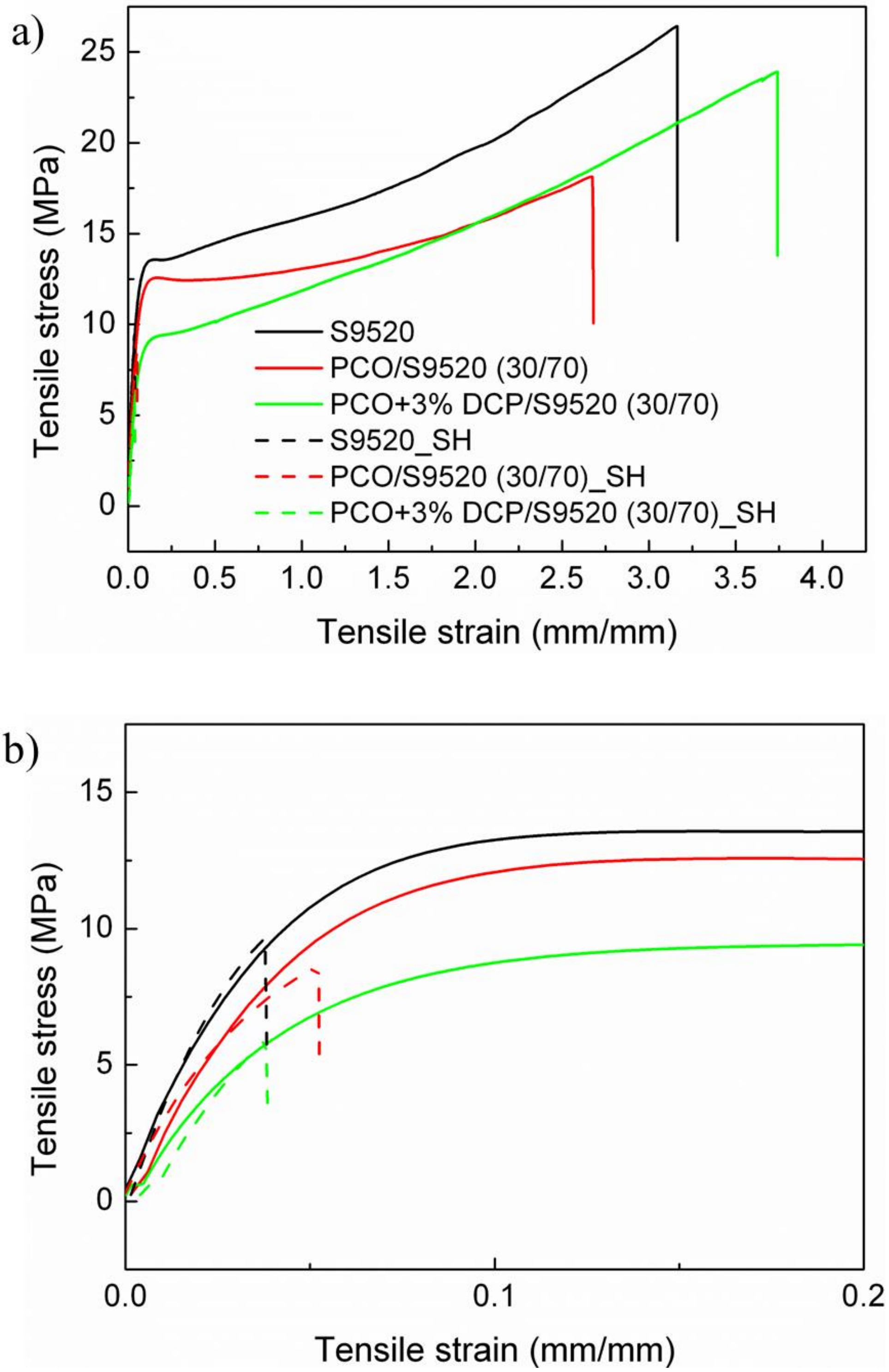

Figure 4.61. Tensile test for the samples that heal (pristine and healed).

From this figure it can be seen a similar behaviour for all healed specimens, failing before reaching their original yield strength at a much lower strain than the corresponding pristine specimen. Since the healed specimens break at their initial damaged site, this is most likely explained due to the fact that the chosen damage mode is too severe to fully restore the cut interface which therefore still acts as a crack initiator. However, Figure 4.61b shows that all the healed specimens have a restoration of polymer stiffness close to 100%, which is a clear indication that a partial healing of the interface has taken place. Additionally, the 30/70 blends show a similar healing response to that of the pure ionomer, which its self-healing properties have been well reported in the last decades [26,35–37].

4.2.4.6. Shape memory

As it has been observed, the 30/70 PCO/ionomer blends (without and with peroxide) have shown self-healing properties, so the next step is to evaluate the shape memory properties of these systems.

The shape memory behaviour was quantified in torsion mode, following the scheme showed in Figure 4.62 [38], where it is explained that first it is necessary to heat the sample (1), and then deform it (2). This temporary shape is fixed by cooling down (3), and removing the stress the sample is heated again, allowing the free recovery (4). The shape memory experiment in torsion mode was made using a Haake Mars III rheometer. The followed protocol is shown in Figure 4.63. The sample was heated at a temperature higher than the transition temperature of the sample [i.e. melting temperature obtained by DSC, (1)] and then put under a torsion of 180º (ε=15%), deforming the sample (2). Then, the sample was cooled at 5 ºC min^{-1} under constant strain conditions until a temperature lower than crystallization temperature of the sample (3). When the sample was unloaded to 0 MPa the temporary shape (ε_u) was achieved (4). To induce the shape recovery, the programmed sample was heated again at a rate of 5 ºC min^{-1} (5), resulting in the recovered shape (6).

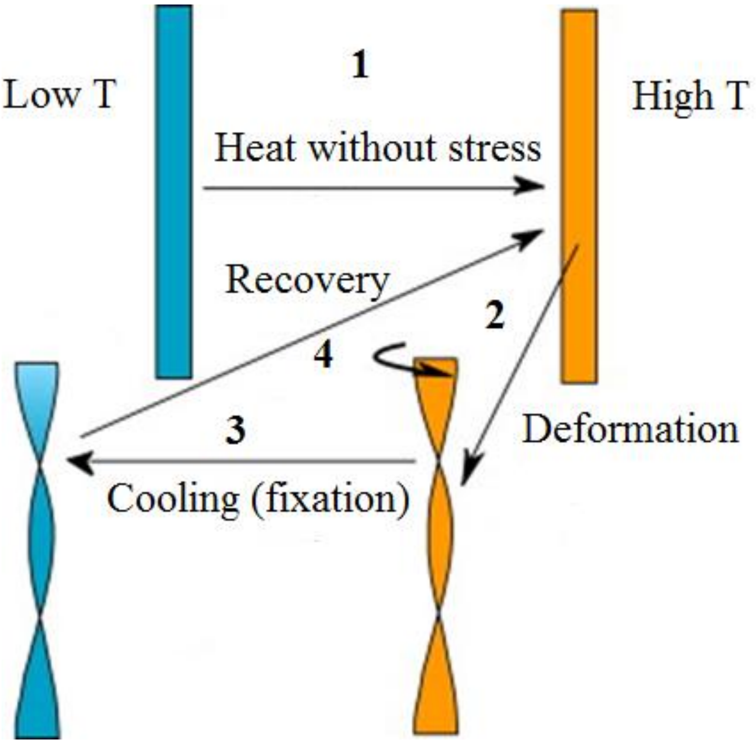

Figure 4.62. Schematic representation of the performed shape memory cycle.

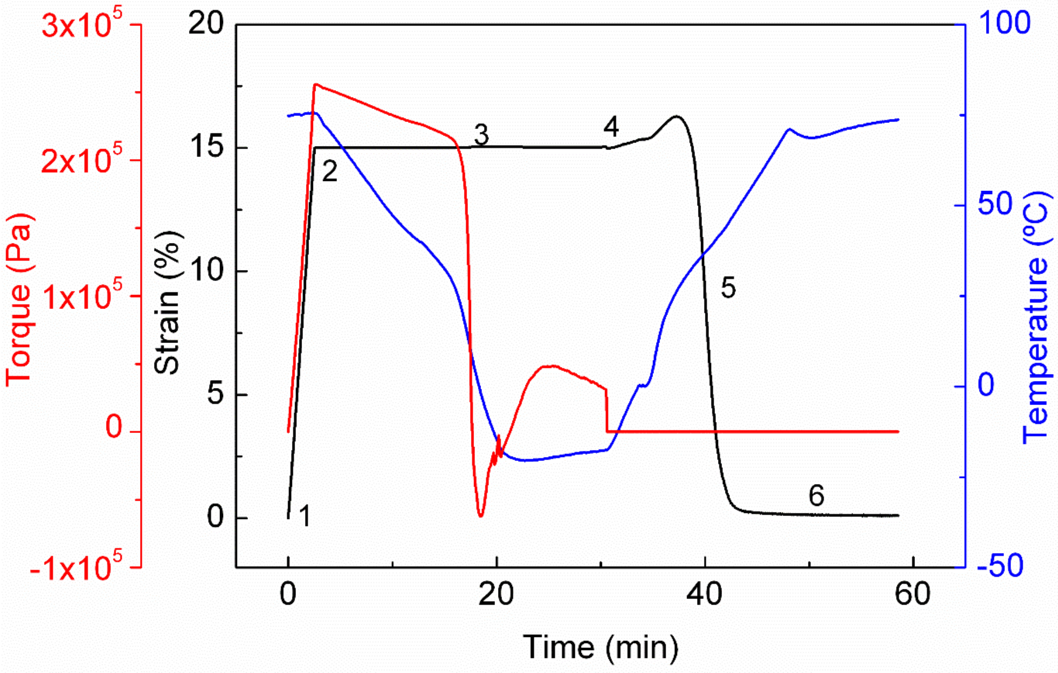

Figure 4.63. Thermo-mechanical procedure to quantify the dual shape memory effect in torsion mode.

PCO + 3% DCP sample has shown shape memory behaviour before [7,14,29], so it is a good sample to evaluate the efficiency and validity of this torsion protocol. The applied temperature profile ranged from -15 ºC till 75 ºC. The result for four consecutive cycles is shown in Figure 4.64. It can be seen that the sample fixes the deformation quite good (steps 2 to 4), and the recovery of the original shape is total. Additionally, a good reproducibility between cycles is observed.

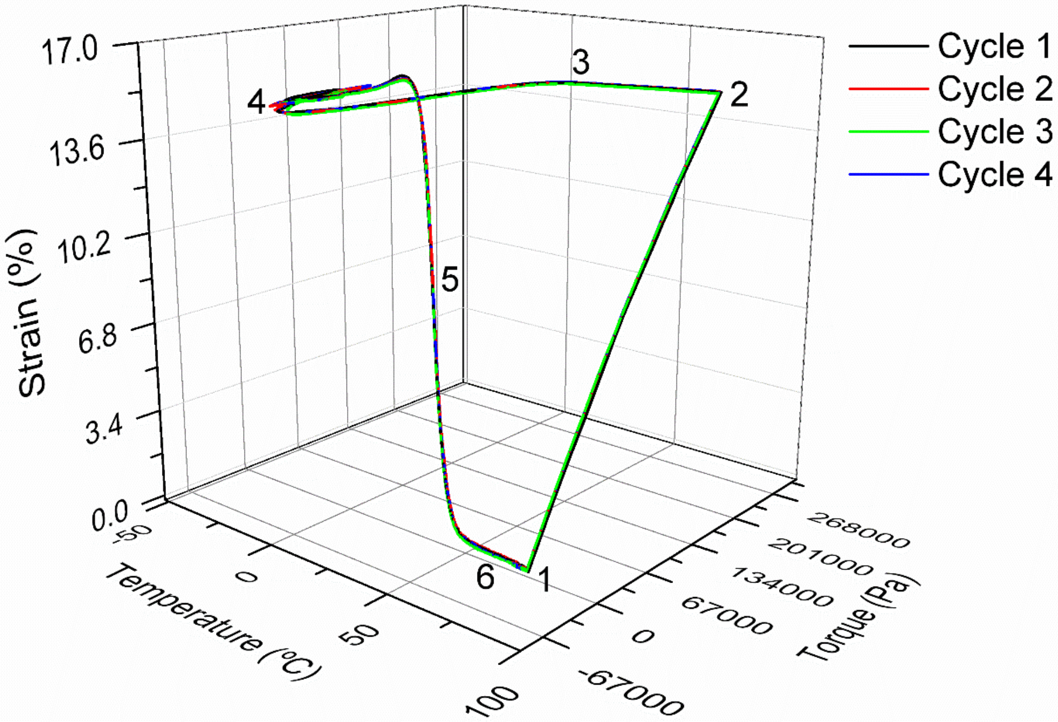

Figure 4.64. Three-dimensional view of four cycles for PCO+3%DCP sample.

Once the efficiency of this shape memory protocol has been demonstrated, the shape memory behaviour of those samples that heal [PCO/Surlyn 9520 (30/70) and PCO+3%DCP/Surlyn 9520 (30/70)] is analysed in order to know if a system with shape memory and self-healing properties has been obtained.

First, the shape memory experiment for PCO+3%DCP/Surlyn 9520 (30/70) sample was performed taking into account the melting temperatures obtained by DSC for this sample. This experiment was made at two different heating temperatures: 75 ºC, which is a temperature higher than the transition temperature of the PCO (49 ºC) but lower than the melting temperature of the ionomer (92 ºC); and 110 ºC, which is a temperature higher than the melting point of the Surlyn 9520. In both cases, the cooling was performed until the same temperature (0 ºC), as well as at the same heating and cooling rates (5 ºC min^{-1}). The results for the shape memory experiments from 0 ºC to 75 ºC and from 0 ºC to 110 ºC are shown in Figure 4.65 and Figure 4.66, respectively. Comparing the two figures, it can be seen that the recovery of the original shape is better when the experiment is performed at 110 ºC, which indicates that the ionomer plays a slight role in the recovery of the sample. In this way, this temperature is used to test the shape memory behaviour of the sample without crosslinker (without DCP), and the result is shown in Figure 4.67. In this case, it is not observed a recovery of the permanent shape, but the sample continues deforming as the temperature increases when the force is removed. So, the lack of crosslinks hinders the capability of the sample to recover its permanent shape at high temperature.

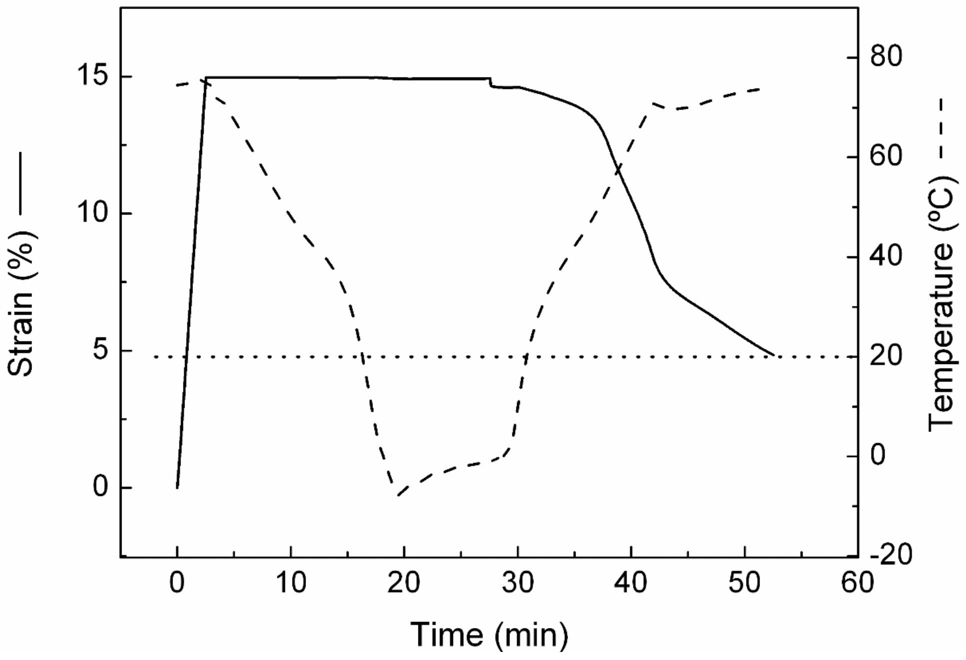

Figure 4.65. Shape memory cycle for PCO+3%DCP/Surlyn 9520 (30/70) sample at 75 ºC.

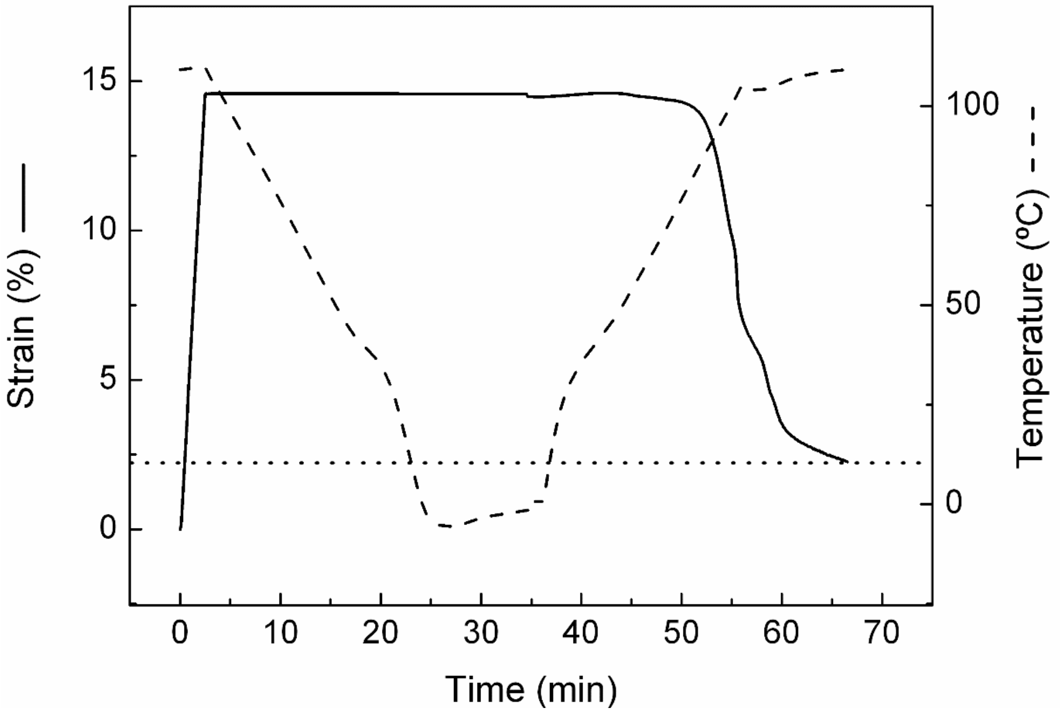

Figure 4.66. Shape memory cycle for PCO+3%DCP/Surlyn 9520 (30/70) sample at 110 ºC

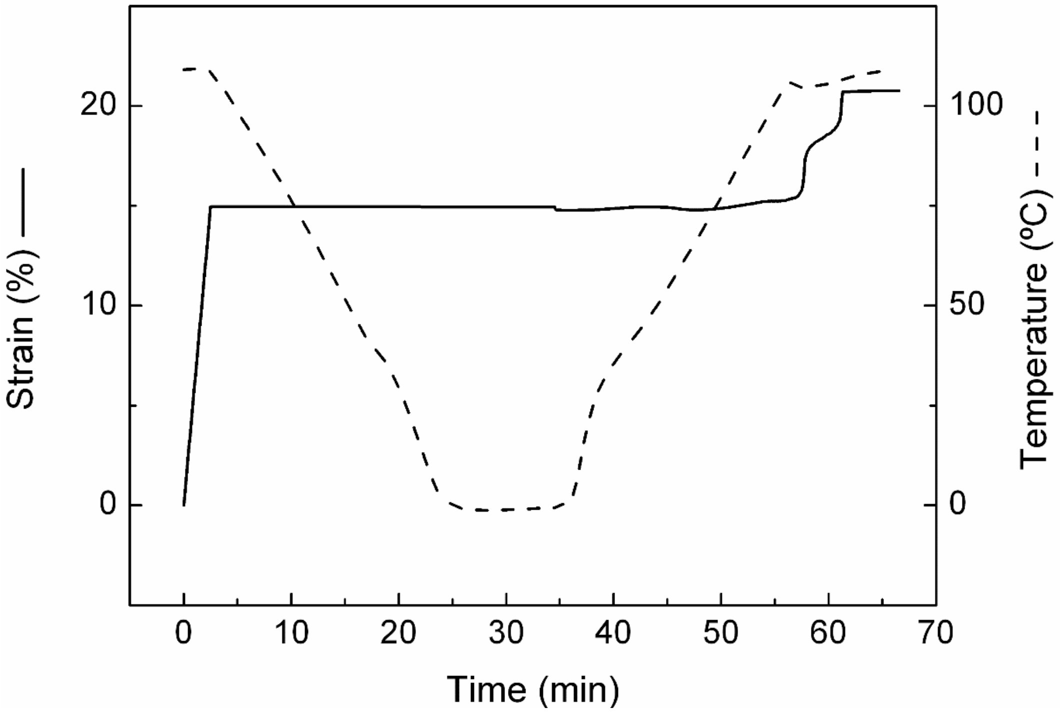

Figure 4.67. First shape memory cycle for PCO/Surlyn 9520 (30/70) sample.

In view of obtained results, it has been thought appropriate to make a triple-shape memory experiment in PCO+3%DCP/Surlyn 9520 (30/70) sample. To do that, a two-step programming process was performed following the protocol shown in Figure 4.68. First, the sample was heated at 110 ºC [a temperature higher than the melting peak of the ionomer in this sample, (1)], and then stretched 180º, i.e. $\varepsilon = 15\%$ (2). Then, the sample was cooled at 5 ºC min^{-1} maintaining the strain constant until 60 ºC (3), which is an intermediate temperature between the crystallization of the ionomer and the transition temperature of the PCO. After 10 minutes at 60 ºC, the first temporary shape was fixed, and a second deformation step was made stretching, again, a 15% (4). Cooling to 0 ºC [a temperature lower than the crystallisation temperature of the PCO, (5)], the second temporary shape was achieved when the sample was unloaded (6). Heating to 110 ºC, the shape recovery process of the sample was observed. Although the programming process is made in two steps, the recovery is performed only in one, but it can be see the recovery of the temporary shape at 60 ºC (7) and then the recovery of the original shape when the 110 ºC are reached (8). The reproducibility of the triple-shape memory effect for four consecutive cycles can be seen in Figure 4.69.

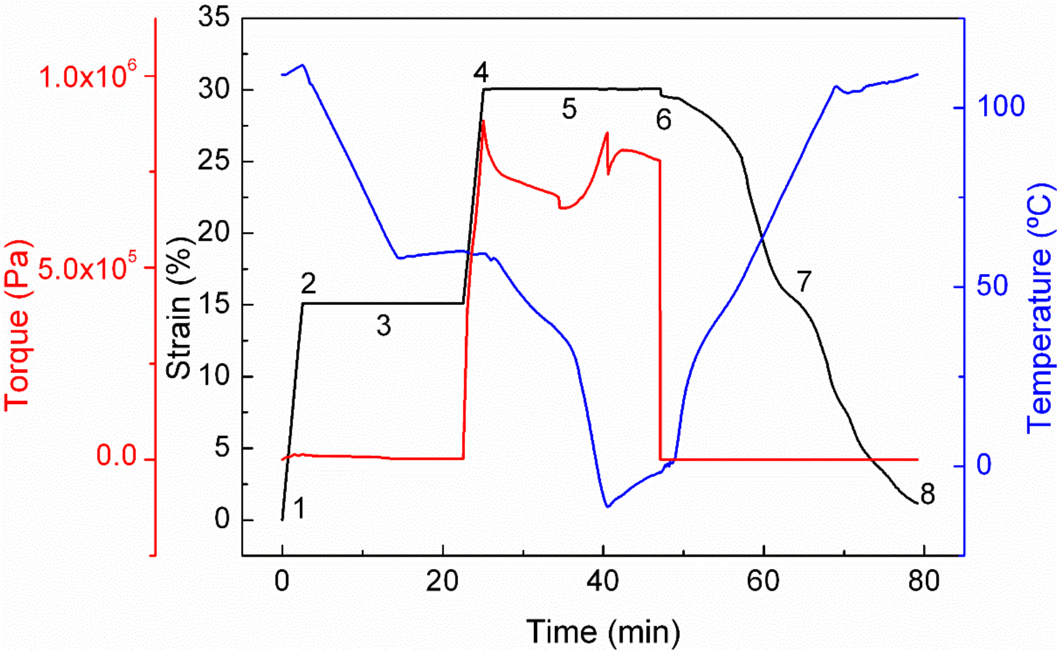

Figure 4.68. Thermo-mechanical procedure to quantify the triple shape memory effect (torsion mode).

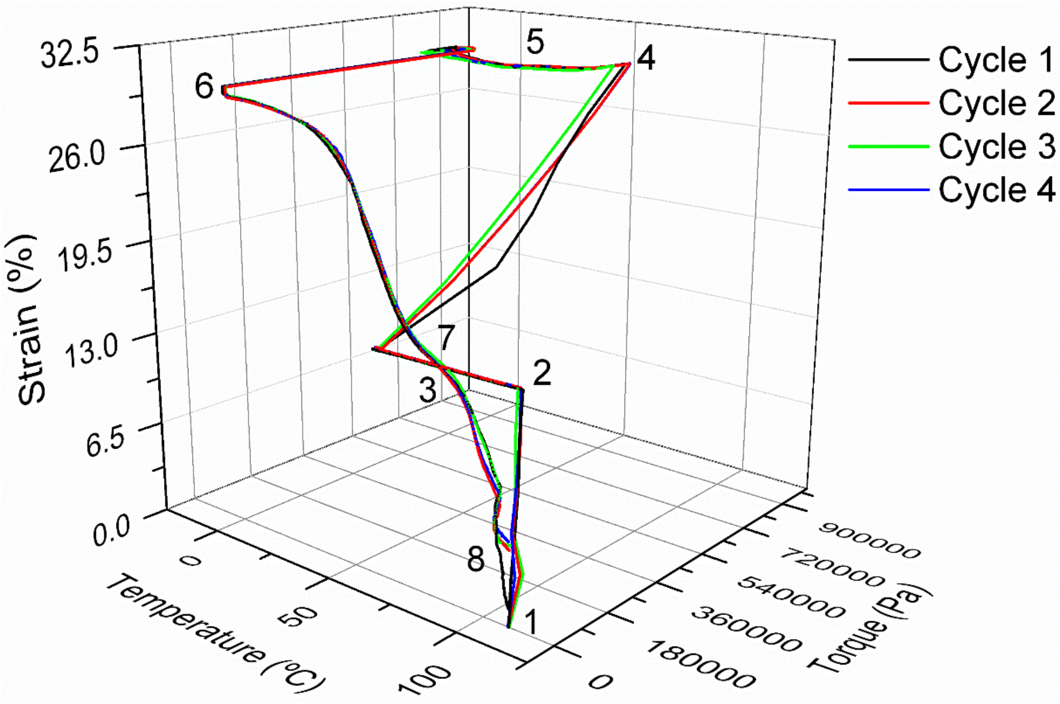

Figure 4.69. Triple shape-memory process for PCO+3%DCP/Surlyn 9520 (30/70) sample (four cycles).

4.2.5. Conclusions

Polycyclooctene (PCO) and Surlyn 9520 were blended in different proportions, and the same blends were prepared by adding a known amount of dicumyl peroxide (DCP). The samples were analysed by Thermogravimetric Analysis (TGA) and Differential Scanning Calorimetry (DSC) in order to evaluate the characteristic temperatures of each sample. The DSC measurements of those samples with peroxide showed a diminution in the melting temperature comparing with the samples without DCP, indicating that the crosslinking process had taken place. These results are in concordance with the measurements performed by rheology not showing crossover between G' and G'', which also shown the possibilities of the samples without DCP to heal or melt depending on the frequency range where the crossover between G' and G'' occurs.

After evaluate the tensile behaviour of all the samples, the self-healing behaviour was tested by cutting and letting at 110 ºC during 16 hours, concluding that the most interesting samples are those PCO/Surlyn at 30/70 proportions, both without and with peroxide, samples which heal. The tensile experiment was again performed in these healed samples, demonstrating the healing efficiency (a near 100% stiffness recovery after healing at standard ionomer healing conditions is obtained). The shape memory behaviour of the formulations which heal was quantitatively evaluated in torsion mode, obtaining as result that the PCO+3%DCP/Surlyn 9520 (30/70) sample shows both dual and triple shape memory behaviour.

In this way, a polymeric system with distinct shape memory and self-healing properties has been developed.

4.3. References

1. MacKnight, W. J.; Earnest, T. R. The structure and properties of ionomers. *J. Polym. Sci. Macromol. Rev.* **1981**, *16*, 41–122.

2. *Ionomers: Synthesis, structure, properties and applications*; Tant, M. R.; Mauritz, K. A.; Wilkes, G. L., Eds.; Springer Netherlands: New York, 1997.

3. Tadano, K.; Hirasawa, E.; Yamamoto, H.; Yano, S. Order-disorder transition of ionic clusters in ionomers. *Macromolecules* **1989**, *22*, 226–233.

4. Tachino, H.; Kuteumizuj, S.; Yano, S. Dynamic Mechanical Relaxations of Ethylene Ionomers. *Macromolecules* **1993**, *26*, 752–757.

5. *Polyelectrolytes: Thermodynamics and Rheology*; Visakh, P. M.; Bayraktar, O.; Picó, G. A., Eds.; Springer International Publishing: Switzerland, 2014.

6. Rhaman, M. A.; Penco, M.; Spagnoli, G.; Grande, A. M.; Di Landro, L. Self-healing behavior of blends based on ionomers with ethylene/vinyl alcohol copolymer or epoxidized natural rubber. *Macromol. Mater. Eng.* **2011**, *296*, 1119–1127.

7. Cuevas, J. M.; Laza, J. M.; Rubio, R.; German, L.; Vilas, J. L.; León, L. M. Development and characterization of semi-crystalline polyalkenamer based shape memory polymers. *Smart Mater. Struct.* **2011**, *20*, 035003.

8. Varley, R. J.; van der Zwaag, S. Towards an understanding of thermally activated self-healing of an ionomer system during ballistic penetration. *Acta Mater.* **2008**, *56*, 5737–5750.

9. Cuevas, J. M.; Rubio, R.; German, L.; Laza, J. M.; Vilas, J. L.; Rodriguez, M.; Leon, L. M. Triple-shape memory effect of covalently crosslinked polyalkenamer based semicrystalline polymer blends. *Soft Matter* **2012**, *8*, 4928–4935.

10. Han, S. Il; Gu, B. H.; Nam, K. H.; Im, S. J.; Kim, S. C.; Im, S. S. Novel

copolyester-based ionomer for a shape-memory biodegradable material. *Polymer* **2007**, *48*, 1830–1834.

11. Weiss, R. A.; Izzo, E.; Mandelbaum, S. New Design of Shape Memory Polymers: Mixtures of an Elastomeric Ionomer and Low Molar Mass Fatty Acids and Their Salts. *Macromolecules* **2008**, *41*, 2978–2980.

12. Zhao, J.; Chen, M.; Wang, X.; Zhao, X.; Wang, Z.; Dang, Z. M.; Ma, L.; Hu, G. H.; Chen, F. Triple shape memory effects of cross-linked polyethylene/polypropylene blends with cocontinuous architecture. *ACS Appl. Mater. Interfaces* **2013**, *5*, 5550–5556.

13. Hoeher, R.; Raidt, T.; Krumm, C.; Meuris, M.; Katzenberg, F.; Tiller, J. C. Tunable Multiple-Shape Memory Polyethylene Blends. *Macromol. Chem. Phys.* **2013**, *214*, 2725–2732.

14. Liu, C.; Chun, S. B.; Mather, P. T.; Zheng, L.; Haley, E. H.; Coughlin, E. B. Chemically cross-linked polycyclooctene: synthesis, characterization, and shape memory behavior. *Macromolecules* **2002**, *35*, 9868–9874.

15. Alonso-Villanueva, J.; Cuevas, J. M.; Laza, J. M.; Vilas, J. L.; León, L. M. Synthesis of poly(cyclooctene) by ring-opening metathesis polymerization: Characterization and shape memory properties. *J. Appl. Polym. Sci.* **2010**, *115,* 2440–2447.

16. Calleja, F. J. B.; Salazar, J. M.; Čačković, H.; Loboda-Čačković, J. Correlation of hardness and microstructure in unoriented lamellar polyethylene. *J. Mater. Sci.* **1981**, *16*, 739–751.

17. Ghosh, S. K. *Self-Healing Materials: Fundamentals, Design Strategies, and Applications*; 2009.

18. White, S. R.; Sottos, N. R.; Geubelle, P. H.; Moore, J. S.; Kessler, M. R.; Sriram, S. R.; Brown, E. N.; Viswanathan, S. Autonomic healing of polymer composites. *Nature* **2001**, *409*, 794–797.

19. Pang, J. W. C.; Bond, I. P. A hollow fibre reinforced polymer composite encompassing self-healing and enhanced damage visibility. *Compos. Sci. Technol.* **2005**, *65*, 1791–1799.

20. Williams, H. R.; Trask, R. S.; Knights, A. C.; Williams, E. R.; Bond, I. P. Biomimetic reliability strategies for self-healing vascular networks in engineering materials. *J. R. Soc. Interface* **2008**, *5*, 735–47.

21. Nji, J.; Li, G. Damage healing ability of a shape-memory-polymer-based particulate composite with small thermoplastic contents. *Smart Mater. Struct.* **2012**, *21*, 025011.

22. Hayes, S. A.; Jones, F. R.; Marshiya, K.; Zhang, W. A self-healing thermosetting composite material. *Compos. Part A Appl. Sci. Manuf.* **2007**, *38*, 1116–1120.

23. Zhang, X.; He, J. Hydrogen-bonding-supported self-healing antifogging thin films. *Sci. Rep.* **2015**, *5*, 9227.

24. Liu, Y.-L.; Chuo, T.-W. Self-healing polymers based on thermally reversible Diels–Alder chemistry. *Polym. Chem.* **2013**, *4*, 2194.

25. Canadell, J.; Goossens, H.; Klumperman, B. Self-healing materials based on disulfide links. *Macromolecules* **2011**, *44*, 2536–2541.

26. Kalista, S. J.; Pflug, J. R.; Varley, R. J. Effect of ionic content on ballistic self-healing in EMAA copolymers and ionomers. *Polym. Chem.* **2013**, *4*, 4910.

27. Garcia, S. J. Effect of polymer architecture on the intrinsic self-healing character of polymers. *Eur. Polym. J.* **2014**, *53*, 118–125.

28. Dolog, R.; Weiss, R. A. Shape memory behavior of a polyethylene-based carboxylate ionomer. *Macromolecules* **2013**, *46*, 7845–7852.

29. García-Huete, N.; Laza, J. M.; Cuevas, J. M.; Gonzalo, B.; Vilas, J. L.; León, L. M. Shape memory effect for recovering surface damages on polymer substrates.

J. Polym. Res. **2014**, *21*, 481.

30. Aho, J.; Boetker, J. P.; Baldursdottir, S.; Rantanen, J. Rheology as a tool for evaluation of melt processability of innovative dosage forms. *Int. J. Pharm.* **2015**, *494*, 623–642.

31. Raghavan, S. R.; Chen, L. A.; McDowell, C.; Khan, S. A.; Hwang, R.; White, S. Rheological study of crosslinking and gelation in chlorobutyl elastomer systems. *Polymer* **1996**, *37*, 5869–5875.

32. Stukalin, E. B.; Cai, L. H.; Kumar, N. A.; Leibler, L.; Rubinstein, M. Self-healing of unentangled polymer networks with reversible bonds. *Macromolecules* **2013**, *46*, 7525–7541.

33. Bose, R. K.; Hohlbein, N.; Garcia, S. J.; Schmidt, A. M.; van der Zwaag, S. Connecting supramolecular bond lifetime and network mobility for scratch healing in poly(butyl acrylate) ionomers containing sodium, zinc and cobalt. *Phys. Chem. Chem. Phys.* **2015**, *17*, 1697–704.

34. Bose, R. K.; Hohlbein, N.; Garcia, S. J.; Schmidt, A. M.; Van Der Zwaag, S. Relationship between the network dynamics, supramolecular relaxation time and healing kinetics of cobalt poly(butyl acrylate) ionomers. *Polymer* **2015**, *69*, 228–232.

35. Vega, J. M.; Grande, A. M.; Van Der Zwaag, S.; Garcia, S. J. On the role of free carboxylic groups and cluster conformation on the surface scratch healing behaviour of ionomers. *Eur. Polym. J.* **2014**, *57*, 121–126.

36. Kalista, S. J.; Ward, T. C.; Oyetunji, Z. Self-Healing of Poly(Ethylene-co-Methacrylic Acid) Copolymers Following Projectile Puncture. *Mech. Adv. Mater. Struct.* **2007**, *14*, 391–397.

37. Schmets, A. J. M.; van der Zaken, G.; van der Zwaag, S. *Self healing materials: an alternative approach to 20 centuries of materials science*; Springer: Dordrecht, The Netherlands, 2007; Vol. 100.

38. Diani, J.; Frédy, C.; Gilormini, P.; Merckel, Y.; Régnier, G.; Rousseau, I. A torsion test for the study of the large deformation recovery of shape memory polymers. *Polym. Test.* **2011**, *30*, 335–341.

CHAPTER 5

Final considerations and conclusions

This chapter is focused in summarize the general considerations derived from this work, since the corresponding scientific and technical conclusions are individually explained in each chapter. First of all, it is necessary to mention that this thesis has been made according to the possibility of transfer the acquired knowledge to the industry, so it has been tried to perform the experimental work in a simple and easily reproducible way, without deepening too much in certain aspects. The main goal of the thesis has been fulfilled according to the planning presented in Chapter 1. In this way, different systems based on a commercial polycylooctene have been prepared, and the shape memory behaviour of the samples has been evaluated.

Therefore, the first step was to complete the study started few years ago with the Doctoral Thesis entitled "Desarrollo y caracterización de la capacidad de memoria de forma en polímeros semicristalinos", where the polycyclooctene was crosslinked with a peroxide in order to provide it shape memory properties. In this sense, it was clearly demonstrated the possibility of develop different thermally-induced shape memory polymeric systems based on a commercially accessible polymer in a relatively easy way, being transferable to industrial processes. In the present thesis, the superficial behaviour of these polymeric systems has been evaluated. On the one hand, self-repair behaviour has been evaluated by making indentations and studying the recovery in order to demonstrate the potential applications of these polymeric systems in aesthetic or functional applications. On the other hand, responsive pillar-shaped structures were developed, where the hydrophobicity/hydrophilicity can be modified by means of shape memory effect, being interesting for their use as switchable wetting surfaces or in areas like tissue engineering.

As expected, and it has been demonstrated in this work, the presence of residual peroxide and its by-products makes these polymer formulations, crosslinked with dicumyl peroxide, cytotoxic systems. Therefore, to extend the possibility of application of these semicrystalline polymers to fields such as biomedicine it was necessary to modify the crosslinking method. Thus, different non-cytotoxic polymer formulations with thermally induced shape memory effect have been developed. Finally, positron annihilation lifetime spectroscopy measurements were performed in order to make a first correlation between free volume and shape memory behaviour. In conclusion, it has been demonstrated that ionizing energies such as gamma radiation can be an excellent way to crosslink semicrystalline polymers to provide shape memory capabilities.

At the last step, polycyclooctene has been mixed with different ionomers, beginning in this way a study consisting in trying to develop polymer blends with self-healing and shape memory properties. These new polymeric materials present potential applications in different fields such as the textile, the automotive and/or the appliance industry. After evaluating the thermal and mechanical behaviour on 50/50 blends, and observing the shape memory behaviour with two different ionomers (Surlyn 1705 and Surlyn 8940), a more extensively study was make using another ionomer (Surlyn 9520), establishing a relationship between the blend ratio and the final mechanical and healing behaviour.

One of the main contributions of the developed work is that it opens new lines of research in this area. Thus, for example, in order to understand the mechanism of the shape memory effect, the study of the crystalline structure of the samples at the different stages of the shape memory process would be of great interest. It is also necessary to find alternatives for a better evaluation of the shape memory behaviour. For example, it would be recommendable to check the maximum deformation force of the systems which allow a good recoverability of the initial properties, in order to determine and delimit the possible applications. Moreover, taking the last results in self-healing field as starting point, it would be interesting to perform puncture, scratch and fatigue experiments on the PCO/Surlyn blends, or even develop new PCO/ionomer formulations.

Contributions

This Doctoral Thesis has led to the following results:

PAPERS

García-Huete, N.; Laza, J. M.; Cuevas, J. M.; Gonzalo, B.; Vilas, J. L.; León, L. M. Shape memory effect for recovering surface damages on polymer substrates. *J. Polym. Res.* **2014**, *21*, 481.

García-Huete, N.; Laza, J. M.; Cuevas, J. M.; Vilas, J. L.; Bilbao, E.; León, L. M. Study of the effect of gamma irradiation on a commercial polycyclooctene I. Thermal and mechanical properties. *Radiat. Phys. Chem.* **2014**, *102*, 108–116.

Axpe, E.; García-Huete, N.; Cuevas, J. M.; Ribeiro, C.; Mérida, D.; Laza, J. M.; García, J. Á.; Vilas, J. L.; Lanceros-Méndez, S.; Plazaola, F.; León, L. M. Connecting free volume with shape memory properties in noncytotoxic gamma-irradiated polycyclooctene. *J. Polym. Sci. Part B Polym. Phys.* **2015**, *53*, 1080–1088.

García-Huete, N.; Cuevas, J. M.; Laza, J. M.; Vilas, J. L.; León, L. M. Polymeric shape-memory micro-patterned surface for switching wettability with temperature. *Polymers (Basel).* **2015**, *7*, 1674–1688.

García-Huete, N.; Axpe, E.; Cuevas, J.M.; Mérida, D.; Laza, J.M.; García, J.A.; Vilas, J.; Plazaola, F.; León, L.M. In situ measurements of free volume during recovery process of a shape memory polymer. *Polymer* **2017**, *109*, 66-70.

García-Huete, N.; Crespo, M.P.; Laza, J.M.; Cuevas, J.M.; Vilas, J.L.; León, L.M. Thermal-activated self-repair features of covalently crosslinked polyalkenamer by gamma radiation (in preparation).

García-Huete, N.; Laza, J.M.; Cuevas, J.M.; Ruiz-Rubio, L.; Vilas, J.L.; León L.M. Ionizing energy as an excellent means providing shape memory performance in polymers: the case of gamma irradiated polycyclooctene (in preparation).

García-Huete, N.; Post, W.; Laza, J.M.; Vilas, J.L.; León, L.M.; García, S.J. Development of a crosslinked polymer blend with shape memory and self-healing properties (in preparation).

CONGRESSES

García-Huete, N.; Laza, J. M.; Cuevas, J. M.; Vilas, J. L.; Bilbao, E.; León, L. M. Study of the effect of gamma irradiation on a commercial polycyclooctene. Thermal and mechanical properties, XIII Reunión del Grupo Especializado de Polímeros GEP, 7-10 Septiembre 2014, Girona (España).

García-Huete, N.; Laza, J. M.; Cuevas, J. M.; Vilas, J. L.; León, L. M. Shape memory behavior of a commercial gamma-irradiated polycyclooctene, MOL2NET-1ST International Conference on Multidisciplinary Sciences, 5-10 Diciembre 2015 (on-line).